biosensors

Special Issue Reprint

Nano-Biosensors for Detection and Monitoring

Edited by
Krishna Kant

mdpi.com/journal/biosensors

MDPI

Nano-Biosensors for Detection and Monitoring

Nano-Biosensors for Detection and Monitoring

Editor

Krishna Kant

MDPI

Basel • Beijing • Wuhan • Barcelona • Belgrade • Novi Sad • Cluj • Manchester

Editor
Krishna Kant
Center for Research in
Nanomaterials and
Biomedicine (CINBIO),
University of Vigo
Vigo, Spain

Editorial Office
MDPI
St. Alban-Anlage 66
4052 Basel, Switzerland

This is a reprint of articles from the Special Issue published online in the open access journal *Biosensors* (ISSN 2079-6374) (available at: https://www.mdpi.com/si/biosensors/nano_biosens_DM).

For citation purposes, cite each article independently as indicated on the article page online and as indicated below:

Lastname, A.A.; Lastname, B.B. Article Title. *Journal Name* **Year**, *Volume Number*, Page Range.

ISBN 978-3-0365-9512-2 (Hbk)
ISBN 978-3-0365-9513-9 (PDF)
doi.org/10.3390/books978-3-0365-9513-9

Contents

About the Editor

Krishna Kant

Krishna Kant works as an associate professor and Marie-Curie Researcher at the University of Vigo, Spain's Center for Research in Nanomaterials and Biomedicine. He is a specialist in the design and manufacture of micro-nano biomedical devices using biosensing and microfluidics. He graduated from Amity University with a master's degree in technology (M.Tech.) in nanobiotechnology in 2009, as well as from Flinders University in Australia with a doctorate in nanotechnology in 2014. His areas of interest include point-of-care diagnostic devices, cell separation, and microfluidics. He has published over 40 peer-reviewed publications. Having received significant grants and prizes, including the MSCA individual fellowship, the Lady Davis fellowship (during his postdoctoral studies), and the ARC fellowship (during his doctorate studies), his research is increasingly being recognized. In addition, he has been granted an EMBO visiting fellowship and other hackathon prizes from different organizations.

biosensors

MDPI

Editorial

Nano-Biosensors for Detection and Monitoring (Volume 1)

Krishna Kant [1,2]

[1] Biomedical Research Center (CINBIO), University of Vigo, 36310 Vigo, Spain; krishna.kant@uvigo.gal
[2] Centre for Interdisciplinary Research and Innovation (CIDRI), University of Petroleum and Energy Studies, Dehradun 248007, India

Nano-biosensing technology is a continuously evolving and expanding field with applications concerning biological substances and sensing platforms, which include the detection of chemical, biological, and environmental elements and welfare. However, sensing biological analytes is of significance in the diagnostic industry. Biosensing analyses are required in areas like pharmaceutical, food industry, and environmental applications. The development of capable biosensors is important, and they can rapidly recognize biological interactions at small scales with maximum precision. Nanomaterials, along with biosensing technology, enhanced the capabilities of biosensors with respect to their high surface area-to-volume ratios and functional capabilities. These types of sensors are usually used as bioreceptors at bio–nano interfaces. Numerous kinds of nanostructures involving nanoparticles, nanotubes, nanowires, and nanocomposites are effectively used to enhance the operation and productivity of sensors. Concurrently, the use of nanostructures and sensing technologies led to the development of biosensors with high specificity and compatibility. Biosensing technology provides the benefits of nanoscience and offers the potential to develop monitoring sensors for the early-stage diagnosis of diseases in an inexpensive manner.

This Special Issue is devoted to and collected advances in a variety of topics: from recognition to engineering and from integration methods to novel sensors. Articles reporting on the newest advances in multiplexed detection report on electrochemical, optical, and magnetic biosensing platforms, in addition to others. An interesting article by Jeong Hee Kim et al. (contribution 1) presented a novel approach for the non-perturbative identification of kidney tissue using Raman spectroscopy and artificial intelligence. The integration of sophisticated and sensitive Raman techniques with AI-based approaches is leading to the development of a model system for accurate detection, and these techniques are used for point-of-care purposes as well. In their approach, they employ Raman spectroscopy and machine learning algorithms, which present the capability for the recognition of amyloids in pathologic lesions. Sara Knežević et.al. (contribution 2) presented a multi-walled carbon nanotube-based sensing approach for the recognition of uric acid. They developed an amperometric, non-enzymatic sensor for the sensitive quantification of uric acid. The developed sensing device presents high reproducibility and a limit of detection up to 64.28 nM. The sensing device is also tested with real-life samples and shows high sensitivity and stability, which makes it a potential candidate for further medical research and clinical application. This Special Issue collected innovative approaches for detection and commercial applications with respect to clinical and environmental samples. The development approaches and recent advancements have also been discussed for nanobiosensors and their detection and monitoring approaches. These arrangements are very crucial for clinical diagnostic applications, and they are required for sample arrangement, sensing, and data administration. Minimizing technology usage via the minimum mandatory sample size is appropriate for the analysis of samples as it would not require skilled users.

Citation: Kant, K. Nano-Biosensors for Detection and Monitoring (Volume 1). *Biosensors* **2023**, *13*, 966. https://doi.org/10.3390/bios13110966

Received: 28 October 2023
Accepted: 31 October 2023
Published: 1 November 2023

Funding: Krishna Kant acknowledges the European Union's Horizon 2020 research and innovation program under the Marie Sklodowska-Curie grant agreement no. (894227).

Acknowledgments: The authors are grateful for the valuable opportunity to serve as Guest Editors of this Special Issue, "Nano-Biosensors for Detection and Monitoring". We are thankful to all authors for their contributions to this Special Issue. We also thank the editorial assistance and publishing staff of *Biosensors* for their support.

Conflicts of Interest: The author declares no conflict of interest.

List of Contributions:

1. Kim, J.H., Zhang, C., Sperati, C.J., Bagnasco, S.M. and Barman, I. Non-Perturbative Identification and Subtyping of Amyloidosis in Human Kidney Tissue with Raman Spectroscopy and Machine Learning. *Biosensors* **2023**, *13*, 466.
2. Knežević, S., Ognjanović, M., Stanković, V., Zlatanova, M., Nešić, A., Gavrović-Jankulović, M. and Stanković, D. La (OH) 3 Multi-Walled Carbon Nanotube/Carbon Paste-Based Sensing Approach for the Detection of Uric Acid—A Product of Environmentally Stressed Cells. *Biosensors* **2022**, *12*, 705.

biosensors

MDPI

Communication

Non-Perturbative Identification and Subtyping of Amyloidosis in Human Kidney Tissue with Raman Spectroscopy and Machine Learning

Jeong Hee Kim [1], Chi Zhang [1], Christopher John Sperati [2], Serena M. Bagnasco [3] and Ishan Barman [1,4,5,*]

[1] Department of Mechanical Engineering, Johns Hopkins University, Baltimore, MD 21218, USA
[2] Division of Nephrology, School of Medicine, Johns Hopkins University, Baltimore, MD 21287, USA
[3] Department of Pathology, School of Medicine, Johns Hopkins University, Baltimore, MD 21218, USA
[4] The Russell H. Morgan Department of Radiology and Radiological Science, School of Medicine, Johns Hopkins University, Baltimore, MD 21218, USA
[5] Department of Oncology, School of Medicine, Johns Hopkins University, Baltimore, MD 21218, USA
* Correspondence: ibarman@jhu.edu; Tel.: +1-410-516-0656

Abstract: Amyloids are proteins with characteristic beta-sheet secondary structures that display fibrillary ultrastructural configurations. They can result in pathologic lesions when deposited in human organs. Various types of amyloid protein can be routinely identified in human tissue specimens by special stains, immunolabeling, and electron microscopy, and, for certain forms of amyloidosis, mass spectrometry is required. In this study, we applied Raman spectroscopy to identify immunoglobulin light chain and amyloid A amyloidosis in human renal tissue biopsies and compared the results with a normal kidney biopsy as a control case. Raman spectra of amyloid fibrils within unstained, frozen, human kidney tissue demonstrated changes in conformation of protein secondary structures. By using t-distributed stochastic neighbor embedding (t-SNE) and density-based spatial clustering of applications with noise (DBSCAN), Raman spectroscopic data were accurately classified with respect to each amyloid type and deposition site. To the best of our knowledge, this is the first time Raman spectroscopy has been used for amyloid characterization of ex vivo human kidney tissue samples. Our approach, using Raman spectroscopy with machine learning algorithms, shows the potential for the identification of amyloid in pathologic lesions.

Keywords: Raman spectroscopy; machine learning; renal amyloidosis; human kidney tissue; amyloid subtyping

Citation: Kim, J.H.; Zhang, C.; Sperati, C.J.; Bagnasco, S.M.; Barman, I. Non-Perturbative Identification and Subtyping of Amyloidosis in Human Kidney Tissue with Raman Spectroscopy and Machine Learning. *Biosensors* **2023**, *13*, 466. https://doi.org/10.3390/bios13040466

Received: 16 March 2023
Revised: 5 April 2023
Accepted: 6 April 2023
Published: 8 April 2023

1. Introduction

Amyloidosis is an uncommon systemic disease caused by irregular protein aggregation and misfolding that leads to the formation of insoluble amyloid deposits [1–4]. Different types of amyloid derive from various amyloid precursor proteins and can infiltrate various organs [1,5]. Although these protein deposits and their sequences vary, amyloid fibrils share a common structure, namely steric zippers, arranged in a periodic fibrillar lattice of β-sheets; this structure can be observed across various modalities, including NMR spectroscopy, cryo-electron microscopy (cryo-EM), and atomic force microscopy (AFM) [6–8].

Recently, Raman spectroscopy has been utilized to study amyloid fibril formation and structural conformations [9–13]. By vibrationally fingerprinting biological samples at a molecular level, Raman spectroscopy identifies various molecules, including proteins and lipids, with high sensitivity and in a nondestructive and label-free manner [14–20]. In addition, its relatively simple setup and the lack of a requirement for a priori knowledge of sample composition make Raman spectroscopy a potential tool to study amyloidosis. Previous studies have shown that Raman spectroscopy is sensitive to differences in structural conformations of different amyloid types [11,12,21–23]. In particular, amide I and

III bands identified β-sheet structures in both amyloid fibrils isolated from patients and synthesized amyloid peptides [9,10,22,24]. However, although these findings established the applicability of Raman spectroscopy to study amyloidosis, synthesized amyloid and isolated amyloid fibrils are overly simplified and disconnected from protocols of clinical detection and diagnosis.

To address this limitation, several researchers have investigated amyloid deposits in tissue with Raman spectroscopy. Animal models have been used to identify biomarkers representative of the amyloid signature within a mixture of biomolecules, coupled with spectral unmixing analysis [25–27]. In addition, others have applied Raman spectroscopy to tissue biopsies of patients that reported changes in the protein signature associated with amyloid [24,28–33]. Although these studies demonstrate Raman spectroscopy's capability to distinguish subtle spectral changes due to amyloid deposits in tissue samples, they were mainly focused on brain tissues to investigate amyloid involvement with disorders such as Alzheimer's disease and Parkinson's disease. However, no previous Raman spectroscopic investigations of renal amyloid deposits exist, despite the fact that the kidney is one of the most commonly involved organs in amyloidoses [5,34].

Here, we employ Raman spectroscopy to examine amyloid deposits for the first time, to the best of our knowledge, in unstained fresh-frozen human kidney tissues. Specifically, we investigated immunoglobulin light chain (AL) and serum amyloid A (AA), which are precursor proteins that give rise to AL amyloidosis and AA amyloidosis, respectively [3,35]. These amyloid diseases represent the two major amyloid diseases with kidney involvement [5,36,37]. We investigated the Raman spectra of AL, AA, and non-amyloidogenic (NA) tissues collected from six patients through analyses of the protein band area and second derivative. Then, using t-distributed stochastic neighbor embedding (t-SNE) and density-based spatial clustering of applications with noise (DBSCAN), we characterized endogenous molecular compositions and structures indicative of amyloid deposits and demonstrated heterogeneity between different amyloid types. In this study, we describe in detail our methodological approach, combining Raman spectroscopy with machine learning techniques to identify and characterize the two major types of amyloidosis in human renal tissue.

2. Materials and Methods

2.1. Sample Preparation

Remnant, de-identified tissues from kidney biopsies performed for diagnostic purposes (IRB approval: IRB00090103) were used for this study, as illustrated in Figure 1. The biopsied tissues of AA, AL, and NA amyloidosis from 6 patients were prepared as a frozen tissue block. Fresh frozen blocks were sectioned by a cryostat, and thin-sliced kidney tissue sections were placed on quartz and glass microscope slides for Raman measurements and histological evaluation, respectively. Tissue sections for Raman measurements remained unstained and were prepared on quartz slides to avoid spectral interference with the biochemical fingerprints of the tissue sample. Consecutive slices from each tissue block were used to detect and identify amyloid fibrils through histological evaluation (Figure 2).

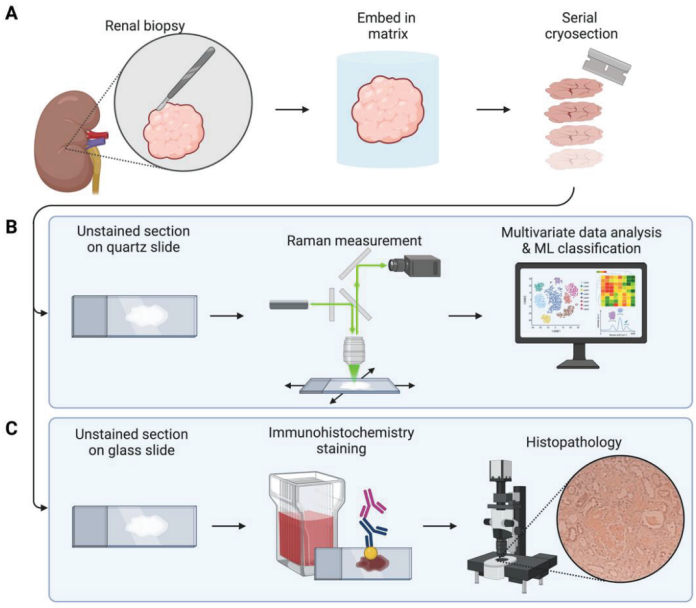

Figure 1. The overall workflow for amyloid identification and subtyping. (**A**) Tissue preparation steps. Biopsied tissues were frozen and sectioned for evaluation. (**B**) Raman spectroscopic data acquisition and analysis. Fresh frozen tissue sections were prepared on quartz slides to minimize spectral interference, and employed for Raman measurements, which were subjected to machine learning analysis. (**C**) Histopathologic validation. Consecutive tissue sections used in (**B**) were utilized for the gold standard, immunohistochemistry evaluation. (Created with BioRender.com (accessed on 23 February 2023)).

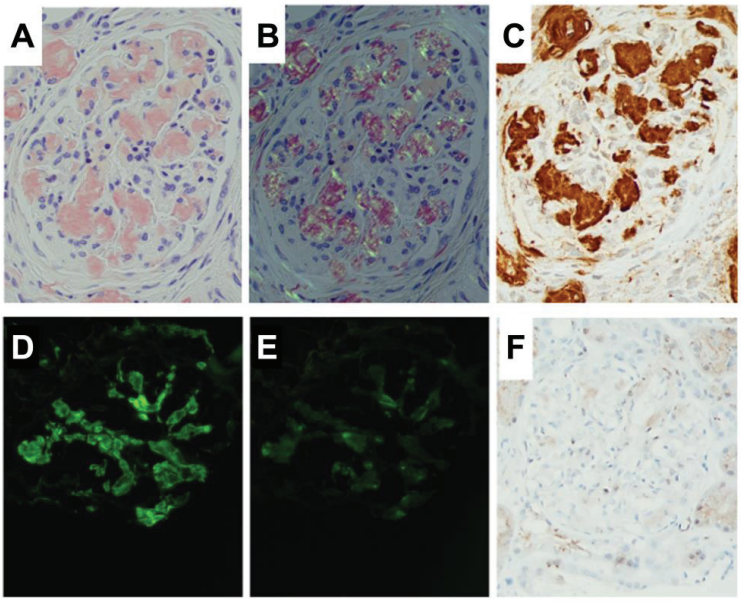

Figure 2. Renal amyloidosis. (**A**) Glomerular and arteriolar deposits of amyloid identified as Congo red-positive material (magnification 400×). (**B**) Glomerular amyloid Congo red-positive deposits

showing birefringence under polarized light (magnification 400×). (**C**) AA amyloidosis: the immunohistochemical stain for amyloid A is strongly positive in the glomerulus and in the arterioles (magnification 400×). (**D**) AL amyloidosis: by immunofluorescence, a glomerulus containing Congo red-positive material (not shown) shows a positive stain for the kappa light chain (magnification 400×). (**E**) The immunofluorescence stain for lambda light chain is negative in the same glomerulus (magnification 400×). (**F**) The immunohistochemical stain for amyloid A is negative in the glomeruli containing deposits of AL amyloid.

2.2. Raman Spectroscopy

A Raman spectroscopy system (Horiba Jobin Yvon-XploRA PLUS) collected Raman spectra of ex vivo kidney tissue samples (Figure 1b). A 532 nm laser was projected onto room-temperature kidney sections, and the resulting Raman scattering between 700 and 3500 cm^{-1} was recorded through a CCD camera. Measurements were taken at various pathological sites, including glomeruli and other structures within the cortical region.

The collected Raman spectra were processed using MATLAB 2018b (MathWorks, Inc., Natick, MA, USA) with baseline and background correction [38], spectral smoothing through a Savitzky-Golay filter [39], and normalization based on water content (3100–3400 cm^{-1}). For multivariate and machine learning analysis, the biological fingerprint region (800–1800 cm^{-1}) was selected, which contains molecular information including proteins, lipids, and other tissue constituents.

2.3. Data Analysis

The collected Raman spectroscopic signals were examined to identify spectral features unique to a particular amyloid type.

Second derivative analysis, which has been used to estimate the contribution of protein secondary structure [29,40], was applied to identify spectral features arising from amyloid fibrils within tissues. Second derivative spectra were obtained by the Savitzky-Golay filter [39], followed by robust locally weighted smoothing.

To further characterize spectral features associated with AL and AA amyloidosis beyond those apparent upon visual inspection, we employed t-Distributed Stochastic Neighbor Embedding (t-SNE), a multivariate analysis technique, and density-based spatial clustering of applications with noise (DBSCAN), an unsupervised machine learning approach. These allowed the unveiling and decomposing of subtle and complex tissue information with greater sensitivity by addressing spectral interference due to background and fluorescence. Both approaches considered Raman spectra collected from both glomerular and non-glomerular regions in AL, AA, and NA tissues. All analyses were performed and visualized using MATLAB and Orange [41].

Briefly, t-SNE is a dimensionality reduction technique that evaluates complicated Raman spectra. By extracting both linear and non-linear features from Raman spectra, it reduces tissue spectra containing information about various biological molecules, from a higher to a lower dimension [42]. We used a perplexity of 15 and an exaggeration of 2 as parameters.

DBSCAN is an unsupervised machine learning approach for data clustering. This machine learning technique is robust to outliers, which makes it a suitable approach for analyzing a large collection of Raman spectra. Core point neighbors and neighborhood distance (Euclidian distance) were determined based on an analysis design from a previous study [43].

3. Results and Discussion

To characterize amyloid deposits, we utilized Raman spectroscopy to collect molecular fingerprints of ex vivo amyloid-infiltrated human kidney tissue samples from patients affected by AL or AA amyloidosis. Raman spectra were measured both within glomeruli with amyloid deposits, which were identified by pathologists, and non-glomerular regions

of tissue sections. Raman spectra of normal tissue samples (NA) were also collected as control cases for comparison. Adjacent sections of each type underwent histopathologic evaluation. Figure 1 illustrates the workflow of this study.

3.1. Amide I and Amide III Bands Reveal Protein Secondary Structures Associated with Amyloidosis

To investigate features of amyloid fibrils, Raman spectra of glomeruli within kidney tissues were obtained (Figure 3). Particularly, we observed peaks within amide I (1600–1700 cm^{-1}) and amide III (1200–1300 cm^{-1}) bands of protein, which are closely related to peptide backbone conformations, the main determinant of protein stability [11,21]. At amide I region, we observed a peak at 1658 cm^{-1} with AA slightly shifted to a higher (1664 cm^{-1}) frequency while AL slightly shifted to a lower (1653 cm^{-1}) frequency, compared to the control case. In amide III spectral region, marked changes in peaks at 1239 and 1278 cm^{-1} were observed, as peaks in AA became more distinguished whereas those in AL appeared more obscure than the NA tissue signal. Such differences are associated with secondary protein structures, particularly β-sheet and α-helix structures, which constitute amyloid fibrils [10,21,29]. The AL spectrum exhibits peaks at 1306 and 1334 cm^{-1}, attributed to sidechain vibrations [11]. In addition, we observed subtle peaks in a higher wavenumber region, associated with changes in lipids. Peaks around 1552 and 1582 cm^{-1} represent aromatic amino acids, such as tryptophan and phenylalanine [21]. The intensities in the observed bands, 1582 cm^{-1} of AL tissue, and 1658 cm^{-1} of AA tissue, vary due to the non-uniform distribution of the amyloid deposits, as marked by the heterogeneity of amyloid-positive samples. In addition, the polymorphism of fibrils may augment the heterogeneity [5]. To assess the changes in protein structures arising from amyloid fibrils, Raman band areas of amide I, amide III, and phenylalanine were evaluated (Figure 3b–d). The amide I band area of AL (Figure 3b) appeared evidently higher than the others, whereas the amide III band area of AA (Figure 3c) showed a clear distinction from the others. In addition, an increase in phenylalanine band area is observed in the AL spectra (Figure 3d), with a statistically significant difference from the band area under the AA or NA tissue spectra. Such an observation indicated that both AA and AL fibrils consist of protein secondary structures with varying contributions of C-N stretching, N-H bending, and C=O stretching vibrations [21].

To further investigate the influence of amyloid fibrils depending on the associated tissue site, we expanded the examination of the Raman spectra of glomeruli, marked in Figure 4a, as well as outside of the glomerulus region. Figure 4b shows distinct spectral profiles for each amyloid type at both glomerular and non-glomerular sites. The corresponding second derivative analysis is shown in Figure 4c. We performed second derivative analysis to objectively identify sharp changes in spectra and locate their vibrational bands, enabling us to further distinguish characteristic spectral features [9,11,44]. Second derivative analysis of amide I, II, and III bands revealed spectral components and peak shifts unnoticed in Raman tissue spectra. Analysis of AA glomerular regions exhibited a split in the 1213 cm^{-1} band, with prominent peaks around 1265, 1305, and 1584 cm^{-1}, associated with the mixture of β-sheet and α-helix structures. The contributions of protein secondary structures in AL fibrils were different from those in AA fibrils, with peaks observed around higher Raman bands, at 1625, 1641, and 1655 cm^{-1}, mainly attributed to C=O stretching vibration. These observations are consistent with previous reports that indicate both AA amyloidosis and AL amyloidosis exhibit protein secondary structures, as the misfolded AA and AL proteins, respectively, aggregate, form amyloid fibrils, and adopt a β-sheet conformation [45]. Second derivative analyses reveal that Raman spectroscopy can molecularly distinguish this common structural feature (β-sheet) across AA and AL amyloidosis, as shown by their distinct Raman bands.

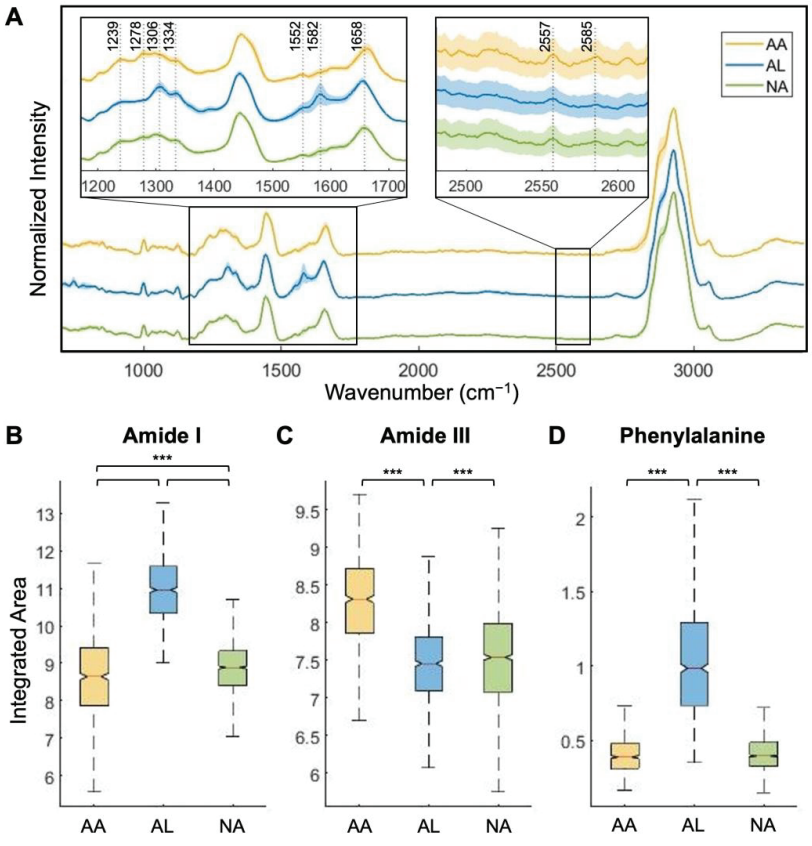

Figure 3. Raman spectroscopy of frozen kidney tissue featuring amyloid deposits. (**A**) Raman spectra of glomeruli within AA, AL, and NA tissues. Each spectrum represents an averaged and normalized spectrum with 1 standard deviation shaded. They are normalized on the spectral region assigned to water (3100–3400 cm^{-1}), assuming an equivalent water content for all samples. Raman band area analyses of (**B**) amide I (1600–1700 cm^{-1}), (**C**) amide III (1200–1300 cm^{-1}), and (**D**) phenylalanine (1582 ± 3 cm^{-1}) of AA, AL, and NA glomeruli. Statistical significance: *** $p < 0.0001$.

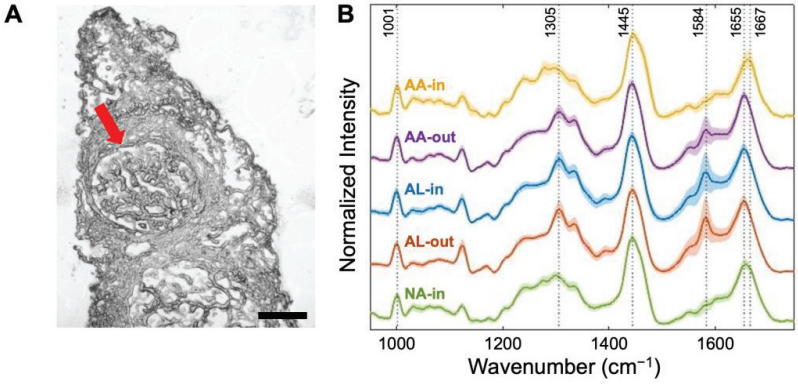

Figure 4. *Cont.*

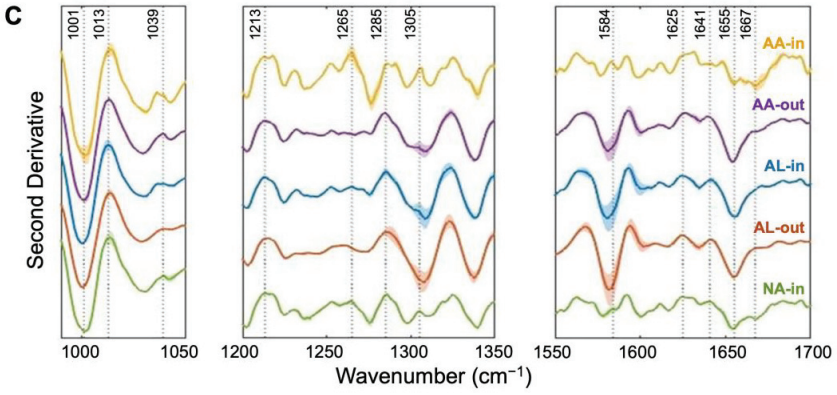

Figure 4. (**A**) Microscopic image of frozen kidney tissue identified with the glomerulus. Scale bar = 100 μm. (**B**) Averaged and normalized Raman spectra collected within and without glomeruli of AA, AL, and NA tissues with 1 standard deviation shaded. (**C**) Second derivative analysis of phenylalanine (1000–1500 cm^{-1}), amide III (1200–1350 cm^{-1}), and amide II-I (1550–1700 cm^{-1}). Each spectrum in (**B**,**C**) is color-coded based on the type and deposition site and plotted in order, from top to bottom: AA-within glomeruli, AA-without glomeruli, AL-within glomeruli, AL-without glomeruli, and NA.

3.2. Machine Learning-Based Raman Spectral Analysis Can Classify Renal Amyloidosis with Respect to Deposition Sites and Types

To distinguish subtle intrinsic spectral differences between amyloid types that were not detected by visual inspection of the tissue spectra, we utilized a multivariate dimension reduction and data exploration technique, t-SNE. Figure 5 shows the t-SNE distribution results of the processed Raman tissue spectra of the biological fingerprint region, ranging between 800 and 1800 cm^{-1}. We subjected a collection of Raman spectra to nonlinear dimensionality reduction and projected them onto a lower dimension, specifically, 2-dimensional space (t-SNE components 1 and 2). The t-SNE map reveals that spectra collected from each amyloid type are clearly separated, as are spectra from glomerular and non-glomerular regions (even those collected from the same tissue sections). Each cluster of identified type is relatively tight without overlap between clusters, indicating that dimensionality reduction of Raman spectra using t-SNE can clearly discriminate between glomeruli constituting amyloid fibrils and normal glomerulus regions, and between AL and AA fibrils. We observed intra-group separation, especially in glomerular AA datapoints; however, the distance between the sub-groups is relatively small compared to the inter-group distances. As inter-group separation is significantly higher than intra-group separation, strong similarity among Raman spectra of the same types and regionality are observed from the t-SNE map. We attribute such clear separation between clusters, not only among different types but also between glomerular and non-glomerular regions, to the function of the glomerulus in the kidney. The glomerulus, a ball-shaped structure identified in Figure 4a, is responsible for filtering waste products and excess fluids from the blood [46]. As amyloidogenic proteins—serum amyloid A (AA) or immunoglobin light chain (AL)—form insoluble fibrils, they fail to pass through the filter; thus, most of these fibrils are deposited and accumulated in the glomeruli. Therefore, the amyloid protein deposits are predominantly found in the glomeruli [34,36]. This concentration of amyloid deposits in the glomeruli of AA and AL tissues is reflected in the Raman fingerprinting of the tissue, leading to clear separation in the t-SNE map.

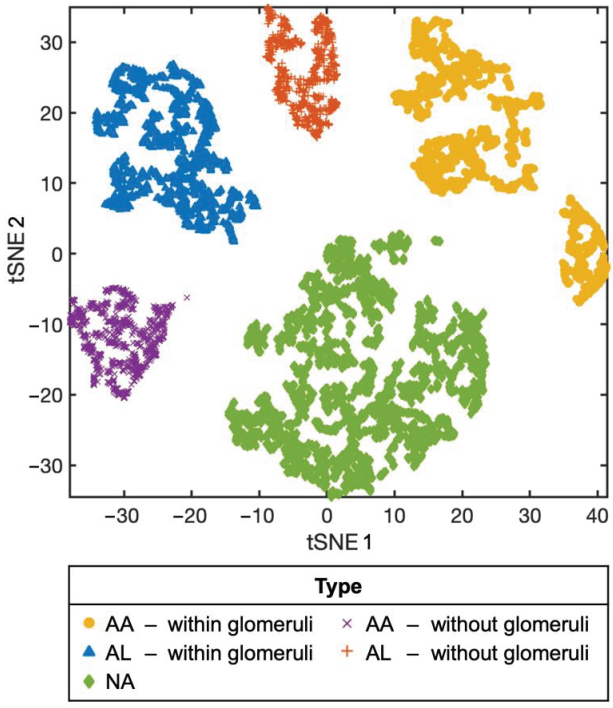

Figure 5. t-SNE map for the distribution of Raman spectra. Spectra were identified with their amyloid types (AA, AL, or NA) and location (within or without glomeruli). Each point represents a Raman spectrum that is positioned based on the similarity probability of the spectra in the dataset. Each group is well separated from other groups, indicating that the Raman spectra of the same group are similar and distinct from those of other groups.

Furthermore, DBSCAN results (Figure 6) obtained using the processed Raman tissue spectra between 800 and 1800 cm^{-1}, show clustering results with distinctive separation among the types and glomeruli. DBSCAN analysis resulted in a total of 12 clusters, of which 5 major clusters represent 96.4% of the entire collection (8360 out of 8672 spectra) with parameters (number of neighbors as 2 within the radius of 1.09). The left panel of Figure 6 summarizes the arrangement of each cluster with respect to amyloid type and deposition site. 96.9% of glomerular AA (Cluster 3), 98.4% of non-glomerular AA (Cluster 6), 96% of glomerular AL (Cluster 1), and 97.2% of non-glomerular AL (Cluster 2) are identified as separate clusters. For the NA tissue, 95.6% of spectra are grouped as an individual cluster (Cluster 8). The remaining spectra are either unidentified or assigned to separate minor clusters. It is worth noting that these minor clusters do not have spectra pertaining to different amyloid types or deposition sites, demonstrating the robustness of the clustering analysis. The average spectra with one standard deviation shaded for the five major cluster groups are presented on the right panel of Figure 6. The spectral profiles demonstrate strong similarities to those of the actual spectra in Figure 4b, indicating that machine learning-based classification indeed enables us to characterize the types of amyloid fibrils and their deposition sites within the tissue.

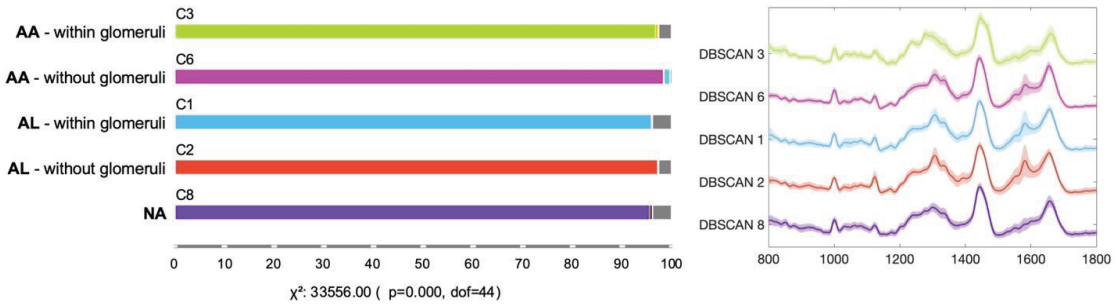

Figure 6. DBSCAN clustering results and representative Raman spectra of each cluster. (**Left**) Out of a total of 12 clusters, 5 dominant clusters were identified. AA glomerular and non-glomerular spectra are primarily grouped as Clusters 3 and 6, respectively. AL glomerular and non-glomerular spectra are primarily grouped as Clusters 1 and 2, respectively. NA tissue is primarily grouped as Cluster 8. The rest of the seven minor clusters are grouped accordingly. Unassigned spectra are marked as gray. (**Right**) Average spectra of the 5 dominant clusters with 1 standard deviation shaded.

In a previous study, we successfully utilized Raman spectroscopy to characterize crystal deposits in kidney biopsies [16], leading us to expand its application to the study of renal amyloid deposits. Spectroscopic techniques, including Raman spectroscopy, have demonstrated promise in detecting and identifying molecular changes in various kidney conditions [47,48]. With the aid of statistical and machine learning algorithms for analysis, these approaches can produce robust results [19,20,49]. Despite the limited sample size in this pilot study, Raman spectroscopy combined with appropriate analysis techniques was able to distinguish between different types of amyloids.

4. Conclusions

In this study, we characterized the Raman spectra of renal amyloid deposits within human tissues affected by systemic AL and AA amyloidosis. This label-free spectroscopic approach made it possible to obtain a biochemical fingerprint of unfixed, unstained specimens, providing intrinsic information on the content and structural profiles of ex vivo amyloid fibrils. Notably, Raman spectroscopy coupled with machine learning approaches exhibits multiple applications: one as a diagnostic tool that detects the presence of amyloid deposits and the other as a characterizing tool that can accurately distinguish AL and AA, two of the most common amyloid types in human kidney tissue. The collected Raman spectra of both glomerular and non-glomerular regions of all three tissue types, combined with t-SNE analysis, were able to identify subtle differences between samples and distinguish between AL, AA, and NA profiles, and even glomerular and non-glomerular regionality. Machine learning analysis equipped with DBSCAN distinguished AL and AA profiles based on their Raman spectra, suggesting the possibility of Raman spectroscopy as a tool for characterizing and subtyping amyloid.

Our label-free, machine learning-assisted spectroscopic analysis presents a new avenue for identifying amyloid within human tissue and promises an objective and reproducible diagnostic tool for systemic amyloidosis with renal involvement. While this study focused on fingerprinting features of AL and AA fibrils in frozen kidney sections, our methods could be extended to other systemic or hereditary amyloidoses in various organs.

Author Contributions: Conceptualization, I.B., C.J.S. and S.M.B.; methodology, investigation, J.H.K. and C.Z.; software, validation, formal analysis, J.H.K.; resources, I.B. and S.M.B.; data curation, J.H.K.; writing—original draft preparation, J.H.K. and S.M.B.; writing—review and editing, J.H.K., C.Z., C.J.S., S.M.B. and I.B.; visualization, J.H.K. and S.M.B.; supervision, project administration, S.M.B. and I.B.; funding acquisition, I.B. All authors have read and agreed to the published version of the manuscript.

Funding: This research was funded by the National Institute of General Medical Sciences (DP2GM128198) and the National Institute of Biomedical Imaging and Bioengineering (2-P41-EB015871-31).

Institutional Review Board Statement: The study was conducted in accordance with the Declaration of Helsinki and approved by the Institutional Review Board of the Johns Hopkins University School of Medicine (IRB00090103 approved on 26 June 2022).

Informed Consent Statement: Not applicable.

Data Availability Statement: Not applicable.

Conflicts of Interest: The authors declare no conflict of interest.

References

1. Merlini, G.; Bellotti, V. Molecular mechanisms of amyloidosis. *N. Engl. J. Med.* **2003**, *349*, 583–596. [CrossRef] [PubMed]
2. Pettersson, T.; Konttinen, Y.T. Amyloidosis—Recent developments. *Semin. Arthritis Rheum.* **2010**, *39*, 356–368. [CrossRef] [PubMed]
3. Dispenzieri, A.; Gertz, M.A.; Buadi, F. What do I need to know about immunoglobulin light chain (AL) amyloidosis? *Blood Rev.* **2012**, *26*, 137–154. [CrossRef] [PubMed]
4. Sanchorawala, V. Light-chain (AL) amyloidosis: Diagnosis and treatment. *Clin. J. Am. Soc. Nephrol.* **2006**, *1*, 1331–1341. [CrossRef] [PubMed]
5. Fändrich, M.; Nyström, S.; Nilsson, K.P.R.; Böckmann, A.; LeVine, H., III; Hammarström, P. Amyloid fibril polymorphism: A challenge for molecular imaging and therapy. *J. Intern. Med.* **2018**, *283*, 218–237. [CrossRef] [PubMed]
6. Nelson, R.; Eisenberg, D. Recent atomic models of amyloid fibril structure. *Curr. Opin. Struct. Biol.* **2006**, *16*, 260–265. [CrossRef]
7. Fändrich, M. On the structural definition of amyloid fibrils and other polypeptide aggregates. *Cell. Mol. Life Sci.* **2007**, *64*, 2066–2078. [CrossRef]
8. Schmidt, A.; Annamalai, K.; Schmidt, M.; Grigorieff, N.; Fändrich, M. Cryo-EM reveals the steric zipper structure of a light chain-derived amyloid fibril. *Proc. Natl. Acad. Sci. USA* **2016**, *113*, 6200–6205. [CrossRef]
9. Flynn, J.D.; McGlinchey, R.P.; Walker, R.L., 3rd; Lee, J.C. Structural features of α-synuclein amyloid fibrils revealed by Raman spectroscopy. *J. Biol. Chem.* **2018**, *293*, 767–776. [CrossRef]
10. Chandra, B.; Korn, A.; Maity, B.K.; Adler, J.; Rawat, A.; Krueger, M.; Huster, D.; Maiti, S. Stereoisomers Probe Steric Zippers in Amyloid-β. *J. Phys. Chem. B* **2017**, *121*, 1835–1842. [CrossRef]
11. Flynn, J.D.; Lee, J.C. Raman fingerprints of amyloid structures. *Chem. Commun.* **2018**, *54*, 6983–6986. [CrossRef] [PubMed]
12. Kurouski, D.; Van Duyne, R.P.; Lednev, I.K. Exploring the structure and formation mechanism of amyloid fibrils by Raman spectroscopy: A review. *Analyst* **2015**, *140*, 4967–4980. [CrossRef]
13. Handen, J.; Lednev, I.K. Chapter 14—Ultraviolet Raman spectroscopy for understanding structure and formation mechanism of amyloid fibrils. In *Vibrational Spectroscopy in Protein Research*; Ozaki, Y., Baranska, M., Eds.; Academic Press: Cambridge, MA, USA, 2020; pp. 415–434.
14. Devitt, G.; Howard, K.; Mudher, A.; Mahajan, S. Raman Spectroscopy: An Emerging Tool in Neurodegenerative Disease Research and Diagnosis. *ACS Chem. Neurosci.* **2018**, *9*, 404–420. [CrossRef] [PubMed]
15. Gulyamov, S.; Shamshiddinova, M.; Bae, W.H.; Park, Y.C.; Kim, H.J.; Cho, W.B.; Lee, Y.M. Identification of biomarkers on kidney failure by Raman spectroscopy. *J. Raman Spectrosc.* **2021**, *52*, 1712–1721. [CrossRef]
16. Sperati, C.J.; Zhang, C.; Delsante, M.; Gupta, R.; Bagnasco, S.; Barman, I. Raman spectroscopy for the diagnosis of intratubular triamterene crystallization. *Kidney Int. Rep.* **2018**, *3*, 997–1003. [CrossRef]
17. Rygula, A.; Majzner, K.; Marzec, K.M.; Kaczor, A.; Pilarczyk, M.; Baranska, M. Raman spectroscopy of proteins: A review. *J. Raman Spectrosc.* **2013**, *44*, 1061–1076. [CrossRef]
18. Talari, A.C.S.; Movasaghi, Z.; Rehman, S.; Rehman, I.U. Raman spectroscopy of biological tissues. *Appl. Spectrosc. Rev.* **2015**, *50*, 46–111. [CrossRef]
19. Lenzi, E.; Dinarelli, S.; Longo, G.; Girasole, M.; Mussi, V. Multivariate analysis of mean Raman spectra of erythrocytes for a fast analysis of the biochemical signature of ageing. *Talanta* **2021**, *221*, 121442. [CrossRef]
20. Durastanti, C.; Cirillo, E.N.M.; De Benedictis, I.; Ledda, M.; Sciortino, A.; Lisi, A.; Convertino, A.; Mussi, V. Statistical Classification for Raman Spectra of Tumoral Genomic DNA. *Micromachines* **2022**, *13*, 1388. [CrossRef]
21. Devitt, G.; Rice, W.; Crisford, A.; Nandhakumar, I.; Mudher, A.; Mahajan, S. Conformational Evolution of Molecular Signatures during Amyloidogenic Protein Aggregation. *ACS Chem. Neurosci.* **2019**, *10*, 4593–4611. [CrossRef]
22. Kurouski, D.; Lednev, I.K. The impact of protein disulfide bonds on the amyloid fibril morphology. *Int. J. Biomed. Nanosci. Nanotechnol.* **2011**, *2*, 167–176. [CrossRef]
23. Ishigaki, M.; Morimoto, K.; Chatani, E.; Ozaki, Y. Exploration of Insulin Amyloid Polymorphism Using Raman Spectroscopy and Imaging. *Biophys. J.* **2020**, *118*, 2997–3007. [CrossRef] [PubMed]
24. Ettema, L.; Lochocki, B.; Hoozemans, J.J.M.; de Boer, J.F.; Ariese, F. Label-free Raman and fluorescence imaging of amyloid plaques in human Alzheimer's disease brain tissue reveal carotenoid accumulations. *J. Opt.* **2022**, *24*, 054005. [CrossRef]

25. Fonseca, E.A.; Lafetá, L.; Cunha, R.; Miranda, H.; Campos, J.; Medeiros, H.G.; Romano-Silva, M.A.; Silva, R.A.; Barbosa, A.S.; Vieira, R.P.; et al. A fingerprint of amyloid plaques in a bitransgenic animal model of Alzheimer's disease obtained by statistical unmixing analysis of hyperspectral Raman data. *Analyst* **2019**, *144*, 7049–7056. [CrossRef]
26. Brauchle, E.; Sevgi, F.; Berrio, D.C.; Schenke-Layland, K.; Casadei, N.; Riess, O.; Salker, M.S.; Singh, Y. Raman imaging of α-synuclein aggregates in a rat model of Parkinson's disease. In Proceedings of the Imaging, Manipulation, and Analysis of Biomolecules, Cells, and Tissues XVII, San Francisco, CA, USA, 4 March 2019.
27. Chen, P.; Shen, A.; Zhao, W.; Baek, S.-J.; Yuan, H.; Hu, J. Raman signature from brain hippocampus could aid Alzheimer's disease diagnosis. *Appl. Opt.* **2009**, *48*, 4743–4748. [CrossRef] [PubMed]
28. Krafft, C.; Sobottka, S.B.; Schackert, G.; Salzer, R. Near infrared Raman spectroscopic mapping of native brain tissue and intracranial tumors. *Analyst* **2005**, *130*, 1070–1077. [CrossRef] [PubMed]
29. Ami, D.; Lavatelli, F.; Rognoni, P.; Palladini, G.; Raimondi, S.; Giorgetti, S.; Monti, L.; Doglia, S.M.; Natalello, A.; Merlini, G. In situ characterization of protein aggregates in human tissues affected by light chain amyloidosis: A FTIR microspectroscopy study. *Sci. Rep.* **2016**, *6*, 29096. [CrossRef]
30. Michael, R.; Lenferink, A.; Vrensen, G.; Gelpi, E.; Barraquer, R.I.; Otto, C. Hyperspectral Raman imaging of neuritic plaques and neurofibrillary tangles in brain tissue from Alzheimer's disease patients. *Sci. Rep.* **2017**, *7*, 15603. [CrossRef] [PubMed]
31. Lochocki, B.; Morrema, T.H.J.; Ariese, F.; Hoozemans, J.J.M.; de Boer, J.F. The search for a unique Raman signature of amyloid-beta plaques in human brain tissue from Alzheimer's disease patients. *Analyst* **2020**, *145*, 1724–1736. [CrossRef]
32. Lochocki, B.; Boon, B.D.C.; Verheul, S.R.; Zada, L.; Hoozemans, J.J.M.; Ariese, F.; de Boer, J.F. Multimodal, label-free fluorescence and Raman imaging of amyloid deposits in snap-frozen Alzheimer's disease human brain tissue. *Commun. Biol.* **2021**, *4*, 474. [CrossRef]
33. Lobanova, E.; Lobanov, S.; Triantafilou, K.; Langbein, W.; Borri, P. Quantitative chemical imaging of amyloid-β plaques with Raman micro-spectroscopy in human Alzheimer's diseased brains. *arXiv* **2018**, arXiv:1803.01201.
34. Said, S.M.; Sethi, S.; Valeri, A.M.; Leung, N.; Cornell, L.D.; Fidler, M.E.; Herrera Hernandez, L.; Vrana, J.A.; Theis, J.D.; Quint, P.S.; et al. Renal Amyloidosis: Origin and Clinicopathologic Correlations of 474 Recent Cases. *Clin. J. Am. Soc. Nephrol.* **2013**, *8*, 1515–1523. [CrossRef] [PubMed]
35. Lu, J.; Yu, Y.; Zhu, I.; Cheng, Y.; Sun, P.D. Structural mechanism of serum amyloid A-mediated inflammatory amyloidosis. *Proc. Natl. Acad. Sci. USA* **2014**, *111*, 5189–5194. [CrossRef] [PubMed]
36. Khalighi, M.A.; Dean Wallace, W.; Palma-Diaz, M.F. Amyloid nephropathy. *Clin. Kidney J.* **2014**, *7*, 97–106. [CrossRef] [PubMed]
37. Sethi, S.; Theis, J.D. Pathology and diagnosis of renal non-AL amyloidosis. *J. Nephrol.* **2018**, *31*, 343–350. [CrossRef] [PubMed]
38. Beier, B.D.; Berger, A.J. Method for automated background subtraction from Raman spectra containing known contaminants. *Analyst* **2009**, *134*, 1198–1202. [CrossRef]
39. Press, W.H.; Teukolsky, S.A. Savitzky-Golay smoothing filters. *Comput. Phys.* **1990**, *4*, 669–672. [CrossRef]
40. Flynn, J.D.; Jiang, Z.; Lee, J.C. Segmental 13C-Labeling and Raman Microspectroscopy of α-Synuclein Amyloid Formation. *Angew. Chem. Int. Ed.* **2018**, *57*, 17069–17072. [CrossRef]
41. Demšar, J.; Curk, T.; Erjavec, A.; Gorup, Č.; Hočevar, T.; Milutinovič, M.; Možina, M.; Polajnar, M.; Toplak, M.; Starič, A. Orange: Data mining toolbox in Python. *J. Mach. Learn. Res.* **2013**, *14*, 2349–2353.
42. Van der Maaten, L.; Hinton, G. Visualizing data using t-SNE. *J. Mach. Learn. Res.* **2008**, *9*, 2579–2605.
43. Sander, J.; Ester, M.; Kriegel, H.-P.; Xu, X. Density-based clustering in spatial databases: The algorithm gdbscan and its applications. *Data Min. Knowl. Discov.* **1998**, *2*, 169–194. [CrossRef]
44. Louros, N.N.; Tsiolaki, P.L.; Baltoumas, F.A.; Chryssikos, G.D.; Gionis, V.; Hamodrakas, S.J.; Iconomidou, V.A. Tracking the amyloidogenic core of IAPP amyloid fibrils: Insights from micro-Raman spectroscopy. *J. Struct. Biol.* **2017**, *199*, 140–152. [CrossRef] [PubMed]
45. Mollee, P.; Renaut, P.; Gottlieb, D.; Goodman, H. How to diagnose amyloidosis. *Intern. Med. J.* **2014**, *44*, 7–17. [CrossRef] [PubMed]
46. Holechek, M.J. Glomerular filtration: An overview. *Nephrol. Nurs. J.* **2003**, *30*, 285–290.
47. Varma, V.K.; Kajdacsy-Balla, A.; Akkina, S.K.; Setty, S.; Walsh, M.J. A label-free approach by infrared spectroscopic imaging for interrogating the biochemistry of diabetic nephropathy progression. *Kidney Int.* **2016**, *89*, 1153–1159. [CrossRef]
48. Varma, V.K.; Kajdacsy-Balla, A.; Akkina, S.; Setty, S.; Walsh, M.J. Predicting Fibrosis Progression in Renal Transplant Recipients Using Laser-Based Infrared Spectroscopic Imaging. *Sci. Rep.* **2018**, *8*, 686. [CrossRef]
49. Guo, S.; Popp, J.; Bocklitz, T. Chemometric analysis in Raman spectroscopy from experimental design to machine learning–based modeling. *Nat. Protoc.* **2021**, *16*, 5426–5459. [CrossRef]

biosensors

MDPI

Article

Robust Detection of Cancer Markers in Human Serums Using All-Dielectric Metasurface Biosensors

Masanobu Iwanaga

National Institute for Materials Science (NIMS), 1-1 Namiki, Tsukuba 305-0044, Japan; iwanaga.masanobu@nims.go.jp

Abstract: One of the most significant characteristics, which biosensors are supposed to satisfy, is robustness against abundant molecules coexisting with target biomolecules. In clinical diagnoses and biosensing, blood, plasma, and serum are used daily as samples. In this study, we conducted a series of experiments to examine the robustness of all-dielectric metasurface biosensors, which comprise pairs of a highly fluorescence-enhancing silicon nanopellet array and a transparent microfluidic chip. The metasurface biosensors were shown to have high performance in detecting various targets from nucleic acids to proteins, such as antigens and antibodies. The present results show almost four-order wide dynamic ranges from 0.16 ng/mL to 1 μg/mL for prostate-specific antigen (PSA) and from 2 pg/mL to 25 ng/mL for carcinoembryonic antigen (CEA). The ranges include clinical criteria for PSA, 4 ng/mL and CEA, 5 ng/mL. To date, a systematic demonstration of robustness has not been reported regarding the metasurface biosensors. In detecting cancer markers of PSA and CEA in human serums, we demonstrate that the metasurface biosensors are robust enough in a wide target concentrations, including the clinical diagnosis criteria.

Keywords: cancer marker; PSA; CEA; sandwich assay; human serum; metasurface; fluorescence detection; robustness

Citation: Iwanaga, M. Robust Detection of Cancer Markers in Humans Serum Using All-Dielectric Metasurface Biosensors. *Biosensors* **2023**, *13*, 377. https://doi.org/10.3390/bios13030377

Received: 27 February 2023
Revised: 9 March 2023
Accepted: 10 March 2023
Published: 13 March 2023

1. Introduction

The detections of biomolecules is a crucial part of clinical diagnosis and health monitoring. To detect target biomolecules in the practical situations, we need not only high sensitivity, but also robustness against other biomolecules present in abundance. It is widely known that human blood usually comprises 55% blood cells, such as red corpuscles and platelets, and 45% plasma, which has proteins, such as immunoglobulin G (IgG) and albumin, other glycerin, and inorganic salts. Normally, concentrations of globulin and albumin in blood are 20–35 and 35–45 g/L, respectively [1]. For medical diagnosis, cancer markers, such as prostate specific antigen (PSA) and carcinoembryonic antigen (CEA), are examined in a range around 5 ng/mL [2]. Thus, biomarker molecules are much rarer than abundant biomolecules; for example, IgG concentration, which is normally 8.61–17.47 mg/mL [2], is 10^6-fold higher than the clinical criteria of PSA and CEA. Therefore, robustness is inevitably a requirement for practical biosensors.

Human serums are most commonly examined for cancer markers in clinical examinations [3–5]. Accordingly, biosensors applicable to cancer markers were often tested for their robustness using human serums [6–17]. All-dielectric metasurface biosensors [18–21] and plasmon–photon hybrid metasurface biosensors [22] were recently reported as efficient fluorescence (FL) biosensors. Figure 1a,b illustrates two situations where sandwich complexes of antibody (Ab)—antigen—Ab are formed. Complexes in the former are in a buffer suitable for proteins, whereas complexes in the latter are in a human serum that contains abundant biomolecules, such as albumin and IgG. For immobilization of the complexes, one of the Abs is labeled with biotin, and for FL detection, the other Ab is labeled with FL molecules. The biotin-labeled Abs serve as capture Abs and the FL-labeled Abs work

as detection Abs in an ordinary immunoassay scheme, e.g., enzyme-linked immunosorbent assay (ELISA). Here, we report a series of proof-of-concept experiments using the all-dielectric metasurface biosensors for the detection of cancer markers that coexist with other actual proteins, such as albumin, IgG, and different cancer markers, thereby clarifying the robustness of metasurface biosensors.

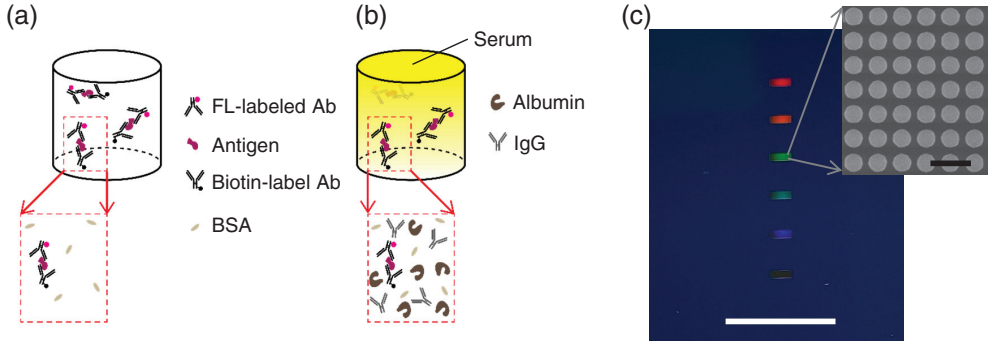

Figure 1. Key concepts of this study. (**a**) Target antigens in a purified condition. (**b**) Targets in a human serum where abundant impeding molecules, exist together with a small number of targets. Antibody (Ab) labeled with fluorescence (FL) molecule (magenta dot), antigen (purple), Ab labeled with biotin (black dot), and bovine serum albumin (BSA, light brown) are shown. Additionally, albumin (brown) and immunoglobulin G (IgG, Y-shaped) are schematically illustrated. (**c**) Photograph (color) of an all-dielectric metasurface substrate and top-view scanning-electron-microscopy image (gray scale), providing a magnified view. The metasurface was a 300-nm periodic array of silicon nanopellets. Six metasurface areas of small rectangular shapes (2.1×0.7 mm^2 each) in the photo were designed to correspond to six microfluidic channels. White and black scale bars indicate 10 mm and 500 nm, respectively.

A color photograph of an all-dielectric metasurface substrate is shown in Figure 1c, where six metasurface areas of small rectangular shapes appear, exhibiting diffraction colors. A white scale bar indicates 10 mm. An scanning-electron-microscopy (SEM) image, which magnifies a metasurface area, is shown on a gray scale. The SEM image was taken in a top-view manner, presenting a periodic array of circular silicon nanopellets of 200 nm height. The periodic length was 300 nm and the diameter of the silicon nanopellets was 224 ± 4 nm. A black scale bar represents 500 nm.

2. Materials and Methods

2.1. All-Dielectric Metasurface Biosensors

The all-dielectric metasurface substrates were fabricated through the nanolithography process for silicon-on-insulator (SOI) substrates. The SOI substrates comprised a top layer of crystalline silicon of 200 nm thickness, a middle layer of buried oxide (or SiO_2) of 375 nm thickness, and a base silicon wafer of 675 μm thickness. Following the nanopatterns written on an electron-beam resist, only the top layer was normally etched down to the middle layer, which resulted in silicon nanopellet arrays (Figure 1c). The top-down nanolithography process has been previously reported in detail [18,23]. Originally, the all-dielectric metasurfaces were conceived with being stimulated from the finding of large FL-enhancing effects in plasmon–photon hybrid metasurfaces [24–26]. We note that the metasurface substrates are reusable after the washdown of the adhered proteins in experiments. The washdown was conducted in two steps: (i) the substrates were first washed for 5 min in a neutral ultrasonic cleaning liquid (7-5337-02, As-One, Osaka, Japan), which was 10-times diluted in advance using purified water, were rinsed four times in the purified water under applying ultrasonic waves (5 min each), and were made dry blowing N_2 gas; (ii) the substrates were immersed in so-called piranha solution, which consists of 96% sulfuric acid

and 30% H_2O_2 liquid (the volume ratio 3:1), for 15 min, and were rinsed with distillated water for 20 min. The validity of the piranha solution to remove organic deposits on silicon nanostructures was previously reported [27]. After the washdown, we did not find any residue emitting FL on the substrates. This reusability has the potential to reduce running costs significantly.

To control the flow of liquid reagents including human serums, we combined the metasurface substrate with a microfluidic (MF) chip and prepared a metasurface biosensor. The MF chip was made of polydimethylsiloxane (PDMS), which was transparent to visible light and was designed to have six MF paths in accordance with the six metasurface areas (Figure 1c). Inlet and outlet holes were introduced at both ends of each MF path to facilitate connecting from the outside; this can be seen in previous reports [20,21]. The PDMS was naturally absorbed on the metasurface substrate, enabling us to flow the liquid reagents.

2.2. Biomolecules and Reagents

Target cancer markers were purchased from companies. We used native human PSA protein (ab78528, Abcam, Cambridge, UK) and CEA (CEA15-N-100, Alpha Diagnostic, San Antonio, TX, USA) as the targets. In diluting the targets to specific concentrations, a sample diluent, NS buffer (ab193972, Abcam), was applied, consisting of phosphate-buffer saline (PBS) and bovine serum albumin. Human serum pool (12181201, Cosmo Bio, Tokyo, Japan), which was a mixture of 10-person serums free from specific diseases, was used for testing the robustness of the metasurface biosensors.

The sandwich complex of Ab—antigen—Ab was designed to have labels, such as biotin-Ab—antigen—Ab-FL. In accordance with this design, a FL label, HiLyte Flour 555 (HL555), was conjugated, in advance, to the Abs using a labeling kit (LK14, Dojindo Laboratories, Kumamoto, Japan). Additionally, biotin was conjugated using a labeling kit (LK03, Dojindo Laboratories). Abs for the PSA and CEA used in this study were mouse monoclonal, being reactive to human PSA and CEA, respectively. Anti-PSA Ab (8A9B8, GenScript, Nanjing, China) and anti-CEA Ab (ab4451, Abcam) were biotin-conjugated, and anti-PSA Ab (MAB6729, Abnova, Taipei, Taiwan) and anti-CEA Ab (10-2370, Fitzgerald Industries, Acton, MA, USA) were HL555-conjugated. After the conjugations, the Abs were collected nominally at 0.5 mg/mL, and then the concentrations of the labeled Abs were tested by light absorption measurement. The HL555-labeling ratios can be evaluated from the light absorbance; we found that HL555 molecules:anti-PSA Ab $\approx$ 4:1 and HL555 molecules:anti-CEA Ab $\approx$ 7:1. For the collection and dilutions of the labeled Abs, PBS at pH 7.4 (164-25511, FujiFilm Wako Pure Chemicals, Osaka, Japan) was used. To immobilize the sandwich complexes on the metasurfaces, Cys-streptavidin (Cys-SA, PRO1005, Click-Biosystems, Richardson, TX, USA) was employed, which can bind to the outermost surface of silicon nanopellets and effectively capture the biotin-labeled sandwich complexes.

2.3. MF Protocols and FL Detection

MF protocol for PSA detection was as follows. PBS was first used to fill the MF paths. Second, the Cys-SA solution, adjusted to 20 μg/mL using the PBS, was flowed at 10–11 μL/min for 10 min on the metasurface areas. In a previous experiment measuring sensorgram for the Cys-SA [22], the immobilized amount reached the maximum at approximately 8 min, so that we set the time to flow the Cys-SA to be 10 min. The Cys-SA was rinsed with the PBS for 7 min; then, a background FL image was captured for 2 s on each channel under illumination by a green LED (M530F2, Thorlab, Newton, NJ, USA). The FL images were acquired using an uncooled CCD camera (Infinity3S-1URC, Teledyne-Lumenera, Ottawa, Canada). Subsequently, the biotin-labeled anti-PSA Abs of 2.0 μg/mL were flowed at 10–11 μL/min for 10 min on the metasurface areas, and then they were rinsed for 7 min with the PBS. The target PSA proteins diluted with the NS buffer or the human serum were flowed at approximately 8 μL/min for 20 min, and then they were rinsed for 7 min with the PBS. Due to the low concentrations, the PSA was flowed at the low flow rate. The HL555-labeled Abs were flowed at 10–11 μL/min for 10 min, and

then the final rinse was conducted at 19–20 μL/min for 8 min with PBS-Tween20 (PBS-T, 163-24361, FujiFilm Wako Pure Chemicals), pH 7.4. Following the MF-flow protocol just above, the green LED light illuminated on each channel, and each FL image was acquired for 2 s exposure time to detect the PSA. A custom-build software was used to control MF flows, liquid reagent changes, and the FL measurements in sequence. The automated setup was as compact as $40 \times 30 \times 60$ cm^3.

MF protocol for CEA detection differed from that for PSA. The sandwich complexes were incubated independently of the MF-flow system because we found that the step flows for the PSA were not suitable for CEA. This difference probably comes from smaller affinity between the CEA and Abs compared to that between PSA and the Abs. The target CEA was adjusted to particular concentrations for each experiment, typically, 0.04–25 ng/mL using the NS buffer or the human serum diluent (serum : NS buffer = 1 : 4 in volume). For the serum, the target CEA was first spiked in the human serum pool and the concentration was 200 μg/mL in the human serum. Afterwards, the target was diluted using the human serum diluent. The anti-CEA Abs were diluted to 10 μg/mL for the serum-diluted CEA and to 2 μg/mL for the NS-buffer diluted CEA using the PBS. Typically, the 50 μL CEA and the two 100 μL anti-CEA Abs were mixed and incubated at 299 K for 40 min at 400 rpm in the dark. After the incubation, the test liquid was flowed at 10–11 μL/min for 23 min on the metasurfaces that was already covered with the Cys-SA; then, the MF paths were rinsed with the PBS-T at 19–20 μL/min for 5 min. Subsequently, FL imaging was conducted on each channel for 3 s exposure time. When the FL images were analyzed, we used a free software, ImageJ [28].

3. Results

3.1. Detections of Individual Cancer Markers

3.1.1. PSA

Figure 2 shows a series of experimental results regarding PSA detection. In Figure 2a, FL images at high PSA concentrations from 40 μg/mL to 0 g/mL are presented from left to right, respectively. The all-dielectric metasurfaces are located near the center of the images; bright horizontal areas are explicitly seen at 40, 4.0, and 0.4 μg/mL; the metasurfaces at the other concentrations are placed similarly though it is not seen brightly. FL intensities were most intense at the center of the excitation LED spots, which take a broad Gaussian shape and can be seen explicitly at 40 and 4.0 μg/mL. The FL intensities were quantified with setting and analyzing a circular region around the center in common with the six MF channels.

The FL intensities in Figure 2a were quantified in the circular regions around the center of excitation spots and plotted in Figure 2b using orange closed circles with error bars on a log-log scale. The error bars were evaluated using Gaussian fitting, being standard deviation σ of the FL-intensity distributions. The detection profile was fitted using Hill equation [29], which is mathematically equivalent to the so-called four-parameter logistic equation:

$$y = y_0 + (S - y_0)\frac{x^n}{x^n + K_D^n} \tag{1}$$

where y denotes the FL intensity, y_0 is the zero level without any target, S is the saturation FL intensity that is regarded as a proportional constant in fitting, x is the concentration of target, n is the degree of cooperative reaction, and K_D is the dissociation constant [30,31]. In the MF paths, stable liquid flow rates are maintained; therefore, the immobilization process on the metasurface is an equilibrium chemical reaction, which is described using the Hill equation (Equation (1)). From the fitted results, it was determined that $S = 36148.3$, $n = 1.18$, $K_D = 195.2$ ng/mL, and $y_0 = 110.0$ in Figure 2b. When the fitted value of n is more than 1, it is suggested that the reaction is cooperative [32]. Therefore, the fitted value n indicates that immobilization of detection Abs with the FL label occurred in a cooperative manner. The value y_0 indicates a zero level in the FL measurement, being approximately six times smaller than the FL intensity at 4.0 ng/mL, which is currently the clinical criterion

value for PSA [2]. Figure 2b shows that even 100-fold higher PSA concentrations can be detected by the metasurface biosensors in a scaled manner. The parameter K_D denotes the dissociation constant and indicates the target concentration at the half height of the Hill curve.

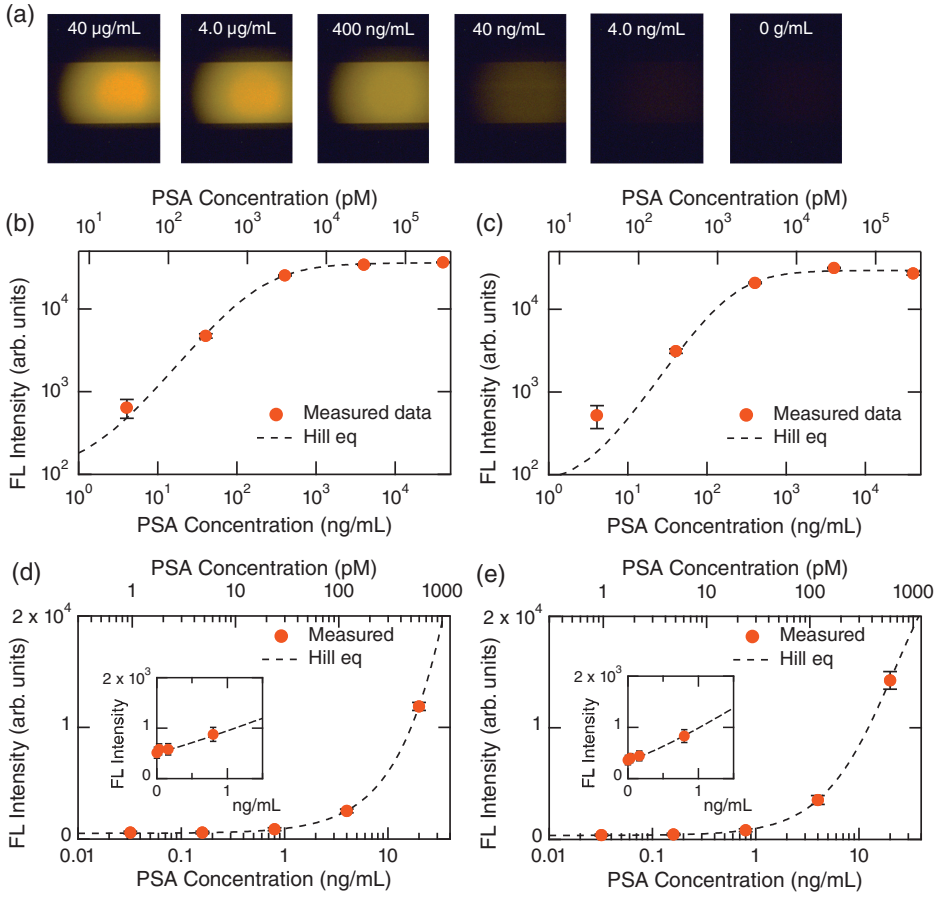

Figure 2. PSA detection. (**a**) FL images at high PSA concentrations from 40 μg/mL to 0 g/mL (from left to right, respectively). The target PSA was diluted using the sample diluent buffer. (**b**) and (**c**) Detection curves of high-concentration PSA diluted with the sample diluent buffer and human serums, respectively. These are presented on a log-log scale. Dashed curves represent fitted curves by the Hill equation (Equation (1)). (**d**,**e**) Detection curves of PSA diluted with the sample diluent buffer and human serums, respectively, presented on a semi-log scale. Dashed curves are fitted curves using the Hill equation. The target concentrations were in a range from 4.0 ng/mL to 0 g/mL. Insets magnify a range near 0 g/mL, presented on a linear scale.

The PSA in a human serum was successfully detected, as shown in Figure 2c. The detection profile is quite similar to that in Figure 2b. This result indicates that PSA detection using the metasurface biosensor is robust, even in human serums. The fitting parameters in Figure 2c were $S = 29620.3$, $n = 1.41$, $K_D = 206.9$ ng/mL, and $y_0 = 72.2$. As a result, the binding reaction is evaluated by n, suggesting that the cooperative reaction is similar to that without human serums. In addition, the interplay of PSA and the Abs is not affected by human serums.

Figure 2d,e shows the FL detection results in a PSA concentration range lower than that in Figure 2b,c, respectively, and is presented on a semi-log scale; insets magnify a range near 0 ng/mL in a linear scale. Orange closed circles with error bars denote measured data, and dashed curves are fitted curves using the Hill equation (Equation (1)). The measured data are well-reproduced using the Hill equation and are scaled. We here define dynamic range, such as a range where we can discriminate measured signals more than 1σ and read out concentrations using a reasonable scale (e.g., linear or the Hill curve). The dynamic range of the PSA detection in the step-flow protocol is found to be 0.16–1000 ng/mL, which is almost four orders of concentrations. In the semi-log plots, it is difficult to see the changes in FL intensity at low concentrations below 1 ng/mL; however, the linear plots in the insets exhibit the scaled responses of the metasurface biosensors, even at the range that is 25-fold smaller than the clinical criterion. We refer to that of the dynamic range, which is mainly limited by the performance of the uncooled CCD camera; indeed, a confocal FL microscopy enabled us to access much lower concentrations when we detected the spike proteins of SARS-CoV-2 [21].

3.1.2. CEA

Figure 3a illustrates a protocol from incubation to immobilization of the CEA-sandwich bodies on the metasurface biosensor composed of a periodic array of silicon nanopellets, though the MF path around the periodic array is not drawn. The binding molecules, Cys-SA, were immobilized in advance on the silicon nanopellets. After the immobilization of the Cys-SA and the rinse of unbound molecules, the CEA-sandwich bodies flowed in the MF paths and effectively bound via the biotin–avidin interplay on the silicon nanopellets. Unbound CEA-sandwich bodies were rinsed with the PBS-T. Afterwards, the FL imaging was conducted from the top of metasurface biosensor; the optical configuration of the biosensor has been described in previous publications [20,21].

A detection curve for CEA in the sample diluent NS buffer is shown in Figure 3b, presented on a semi-log scale. The measured data are shown with orange closed circles associated with error bars. A dashed curve represents a fitted curve using the Hill equation (Equation (1)), which well reproduce the CEA detection data. Thus, the CEA was detected in a scaled manner. A lower concentration range is shown in Appendix (Figure A1a), and the CEA concentration at 0.008 ng/mL was detected in the measurement. From the crossing point of the Hill curve and 3σ level (horizontal bar) in Figure 3b, the limit of detection (LOD) of CEA in this measurement was found to be 0.002 ng/mL (or 11.1 fM). It is to be noted that the detection curve is scaled to the LOD; in other words, the dynamic range covers from 2 pg/mL to 25 ng/mL, exceeding four orders of CEA concentrations. Inset magnifies a concentration range near 0 g/mL on a linear scale.

Figure 3c shows FL signals emitted from the CEA-sandwich bodies in a human serum. The horizontal axis is logarithmic. When we conducted the CEA detection using the serum, the FL-signal level was about five-times lower than that using the NS buffer. It is considered that abundant proteins prevented the CEA and the Abs from forming the sandwich bodies. Accordingly, we conducted a more elaborate FL-signal analysis than that for Figure 3b. In each channel, the FL signal was evaluated in a criterion that intensity more than 3σ from the background level is counted as net signals. This statistical criterion does not output error bar; therefore, the FL signals in Figure 3c are shown only with orange closed circles. A horizontal bar indicates zero-signal level in the measurement. It is to be stressed that the CEA in human serums was detected even at 0.04 ng/mL in a scaled manner; the dynamic range is, at least, 0.04–25 ng/mL. An arrow indicates the clinical diagnosis criterion for CEA, that is, 5 ng/mL [2]. Thus, the metasurface biosensors are capable of detecting CEA in human serums around the diagnosis value.

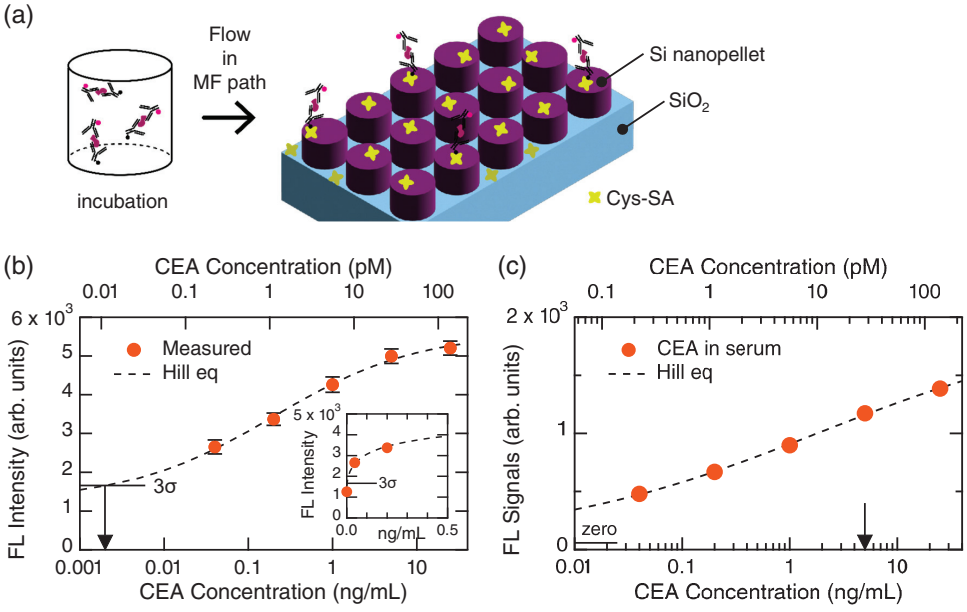

Figure 3. CEA detection. (**a**) Schematic of incubation and immobilization of the CEA sandwich bodies on the metasurface of a periodic array of Si nanopellets. (**b**) Detection of CEA in the sample diluent buffer. Measured FL intensities are shown using orange closed circles with error bars. Dashed curves denote fitted curves by the Hill equation (Equation (1)). 3σ level from the zero level is indicated by a horizontal bar; the crossing point with the Hill curve means the limit of detection, indicating 0.002 ng/mL (arrow). The inset magnifies the detection curve around the zero concentration on a linear scale. (**c**) FL signals from CEA in the human serum. Horizontal bar indicates zero-signal level. Arrow indicates the clinical criterion of 5 ng/mL.

3.2. Coexisting Target Detections

Detection results under conditions that PSA and CEA coexist are shown in Figure 4. Presentation styles in Figure 4 are similar to those in Figure 2,3. We tested two configurations: (i) the target PSA concentrations were 0.8, 4.0, and 20 ng/mL, as shown in Figure 4a, while the CEA concentration was kept at a constant of 5 ng/mL, and (ii) the target CEA concentrations were changed from 0.04 to 25 ng/mL, as shown in Figure 4b, whereas PSA concentration was fixed at 4 ng/mL. In the case (i), CEA was an impeding biomolecule for the target; in (ii), the PSA could impede the detection of target CEA. We note that the clinical criteria for CEA and PSA are 5 and 4 ng/mL, respectively [2].

In both cases, even when the competing cancer markers existed, the target was successfully detected, similarly to the individual detections in Figure 2,3. In detail, the FL intensity in the CEA detection became low (Figure 4b), which suggests that the PSA affects the CEA detection; in contrast, there is no definite signature that the CEA affects the PSA detection because the FL intensity was not reduced in Figure 4a, in comparison with that in Figure 2d. Figure 4a is shown on a linear scale and the three data points around the clinical criterion value, 4 ng/mL, were fitted using a line, being well-reproduced ($R^2 = 0.999$).

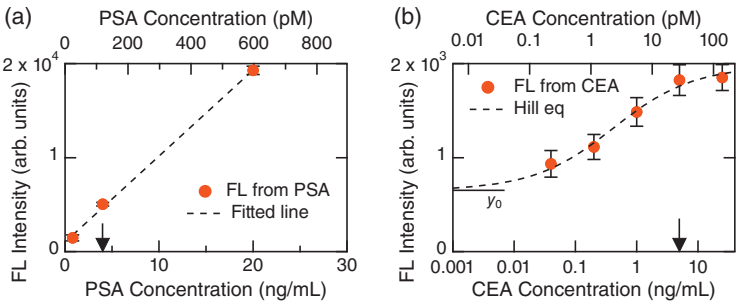

Figure 4. Detection of target cancer markers in coexisting conditions together with other markers. (**a**) PSA detection under a mixture with CEA of 5 ng/mL, presented on a linear scale. FL intensity coming from the PSA is shown using orange circles with error bars. Dashed line: a fitted line. Arrow: the medical criterion value of PSA, 4 ng/mL. (**b**) CEA detection under a mixture with PSA of 4 ng/mL. FL intensity coming from the CEA is shown using orange closed circles with error bars on a semi-log scale. Dashed curve: a fitted curve by the Hill equation (Equation (1)). A black horizontal bar represents the zero level, which is y_0 in the Hill equation. Arrow: the medical criterion value of CEA, 5 ng/mL.

4. Discussion

Practically, cancer markers must be measured precisely in relation to the clinical criterion values. Here, we discuss the detection results for PSA and CEA using human serums from a practical and critical point of view.

Table 1 lists published information on PSA and CEA detections [6–17] and the present results. The dynamic range in Table 1 is defined according to a strict criterion, as is stated in Section 3.1.1. Apart from the claims in the previous reports, the published experimental data were reviewed whether the detection is dynamical, i.e., one concentration is clearly discriminated from the others; for example, if a detected signal at a concentration is overlapped with the other within 1σ, the discrimination is judged to be failure, and the concentration is excluded from the dynamical range in Table 1.

There are mainly two types in the previous reports: one is excessive claims of the dynamical ranges and LODs [7–14,17], and the others are focusing on too low target concentrations in practical senses [6,15]. We here discuss the former cases from a practical viewpoint; the latter does not show any experimental data to support the validity around the clinical criteria. The detections using the electrochemical (EC) methods showed exponential responses, i.e., and most measured data were linearly changed by a factor of 3–5 times and plotted for logarithmic target concentrations, which indicated that narrow signal ranges to the wide target concentrations. Due to such deep sublinear responses, it is generally difficult to discriminate nearest-neighbor concentrations. For example, detection signals at target concentrations of 1 ng/mL and 10 ng/mL cannot be distinguished. This property will be an issue in the practical clinical diagnoses, where definite values should be determined. Thus, it is crucial that signals have a wide dynamic range. It is for this reason that FL detection is considered to be a practically feasible method of detection [33].

For the PSA detections, [8,10,11,13], the dynamic ranges are evaluated to be one or two orders of target concentrations from the strict criterion. In contrast, the present metasurface biosensors provide almost four orders of target concentrations and, furthermore, exhibit robustness for human serums (Figure 2c,e).

The CEA detections based on the EC methods in Table 1 tend to reduce the signals when the target CEA was put in human serums. As an example, the LOD in PBS was claimed to be 0.5 ng/mL, while the CEA detection in human serums was limited to the concentrations at 100 ng/mL and more [6]. A similar reduction in the detection of CEA was reported in an EC method using gold nanoparticles and protein A [34]; the dynamic range was claimed to be from 1 pg/mL to 100 ng/mL; however, the detection range of CEA in rat

serum was substantially reduced to a range of 1–50 ng/mL. In the optical sensing [14,16], such heavy reductions were not observed. In this study, although some FL-signal reduction was observed, the reduction was not substantial. Importantly, the metasurface biosensors offer most precise detection among the related reports [6,9,12,14,16,17] and enable parallel detection, even when PSA coexists (Figure 4). It is referred to that optical nanostructured biosensors, such as metasurface biosensors, are extensively explored [35–38]; so far, better performance and robustness for PSA and CEA than those of the present metasurface biosensors are not found.

Table 1. PSA and CEA detections in human serums. EC and NP stand for electrochemical and nanoparticle, respectively. AD-MSB denotes an all-dielectric metasurface biosensor. PlC denotes plasmonic crystal. NS means the sample diluent NS buffer. The dynamic ranges in this Table are not based on the claims in the references, but on the strict criterion described in the text because the ranges were sometimes overestimated.

Target	Method	Feature	Dynamic Range (ng/mL)	Buffer	Reference
PSA	EC	flow on paper	0.063–0.25	Serum	[7]
PSA	EC	MoS_2-Au	15–110	Serum	[8]
PSA	EC	Ag NP	2–8	Serum	[10]
PSA	EC	polymer brush-Au NP	1–100	Serum	[11]
PSA	microwell	digital FL	0.002–0.2	Serum	[15]
PSA	AD-MSB	resonance shift	1–8	Serum	[13]
PSA	AD-MSB	FL	0.16–1000	Serum	This work
CEA	EC	aptamer	100–140	Serum	[6]
CEA	EC	polyaniline-Au	1–50	Serum	[9]
CEA	EC	aptamer	5–40	Serum	[12]
CEA	gold PlC	resonance shift	3–18	Serum	[14]
CEA	gold PlC	resonance shift	10–87	Serum	[16]
CEA	gold NP	color change	1–30	Serum	[17]
CEA	AD-MSB	FL	0.002–25	Serum	This work
CEA	ELISA	Absorbance	1–50	NS	Figure A1b

5. Conclusions

We have tested the detections of two cancer markers, PSA and CEA, using the metasurface biosensors. In the sample diluent buffer and human serums, the target makers were successfully detected in similar manners. The dynamic ranges were almost four orders of target concentrations of PSA and CEA. Furthermore, the metasurface biosensors were hardly affected by the impeding biomolecules in human serums, demonstrating their robustness. Thus, the all-dielectric metasurface biosensors demonstrated highly sensitive and robust detections of the cancer markers.

6. Patents

Some of the contents in this article were filed in a Japanese patent (JP2022175611).

Funding: This study was partially supported by M-Cube Project and the fourth mid-term project in NIMS.

Institutional Review Board Statement: Not applicable.

Informed Consent Statement: Not applicable.

Acknowledgments: The author thanks Takashi Hironaka for his contribution to the experiment in this study and Naoki Ikeda for the nanofabrication of the metasurfaces.

Conflicts of Interest: The author declares no conflict of interest.

Appendix A

Figure A1 shows further results of FL detection for CEA using a metasurface biosensor and of CEA detection using a commercial ELISA kit (ab264604, Abcam). Figure A1a shows a lower CEA-concentration range than that is Figure 3a, and indicates that CEA was actually detected at the concentrations of 0.008 ng/mL (or 8 pg/mL). The zero level of the FL measurement is shown with an arrow. Thus, it is confirmed that the dynamic range of the metasurface biosensors for CEA covers from ~1 pg/mL to 25 ng/mL.

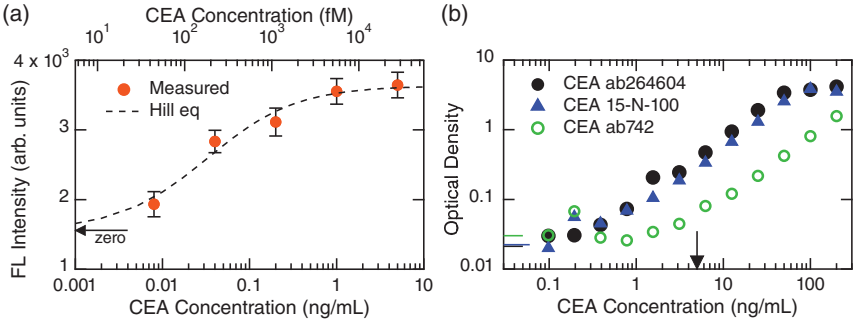

Figure A1. Detection of CEA by the metasurface biosensor and ELISA. (**a**) CEA detection curve in a low concentration range down to 8 pg/mL, measured by the metasurface biosensor. Measured data are shown using orange closed circles with error bars. Dashed curve is a fitted curve by the Hill equation (Equation (1)). (**b**) Detection results for three CEAs (black closed circle: ab264604, Abcam, blue triangle: 15-N-100, Alpha Diagnostic, green open circle: ab742, Abcam) by ELISA, which was conducted using a commercial kit. The vertical axis represents optical density at 450 nm. Three horizontal bars indicate zero levels for the three CEAs; the colors match up the measured data.

Figure A1b shows a set of ELISA results using the commercial kit, which claims high throughput (i.e., 1.5 h running time) and high sensitivity. We used three CEA targets: block closed circles correspond to CEA, ab264604, Abcam, blue triangles to CEA, CEA15-N-100, Alpha Diagnostic, and green open circles to CEA, ab742, Abcam. The detection profiles of the black closed circle and the blue triangle are similar; the dynamic ranges are estimated to be from 0.63 to 50 ng/mL, based on intersection of the two profiles. In contrast, another profile of the green open circle exhibited a lower response than the others, and the dynamic range covers from 1.25 to 200 ng/mL. These results suggest that the enzyme reaction in ELISA can change for detection targets. Practically, we can conclude that the ELISA kit is effective at 1–50 ng/mL for a given CEA, and that the sub-ng/mL ranges are unreliable.

Additionally, we note that the actual running time for the ELISA was approximately 2 h, due to additional procedures (e.g., washing of a microplate) are inevitable; the runtime falls within a short-time category among various ELISA kits. The metasurface biosensors completed the runtime within 2 h and, moreover, exhibited the one-digit pg/mL detection for CEA in a dynamical manner, which is 100-times more effective than the ELISA kit.

References

1. Baynes, J.W.; Dominiczak, M.H. *Medical Biochemistry*, 4th ed.; Elsevier: Amsterdam, The Netherlands, 2014; Chapter 4.
2. Clinical Information. Available online: https://www.ncc.go.jp/jp/ncch/division/clinical_trial/info/clinical_trial/professional/kijunchi_ichiran_2108.pdf (accessed 14 February 2023).
3. Morote, J.; Raventós, C.X.; Lorente, J.A.; Lopez-Pacios, M.A.; Encabo, G.; de Torres, I.; Andreu, J. Measurement of free PSA in the diagnosis and staging of prostate cancer. *Int. J. Cancer* **1997**, *71*, 756–759. [CrossRef]
4. Takehara, K.; Takehara, Y.; Ueyama, S.; Kobayashi, T. A case of stercoral colitis with marked elevation of serum carcinoembryonic antigen. *Clin. Case Rep.* **2020**, *8*, 734–738. [CrossRef] [PubMed]
5. Ushigome, M.; Shimada, H.; Miura, Y.; Yoshida, K.; Kaneko, T.; Koda, T.; Nagashima, Y.; Suzuki, T.; Kagami, S.; Funahashi, K. Changing pattern of tumor markers in recurrent colorectal cancer patients before surgery to recurrence: serum p53 antibodies, CA19-9 and CEA. *Int. J. Clin. Oncol.* **2020**, *25*, 622–632. [CrossRef] [PubMed]

6. Shu, H.; Wen, W.; Xiong, H.; Zhang, X.; Wang, S. Novel electrochemical aptamer biosensor based on gold nanoparticles signal amplification for the detection of carcinoembryonic antigen. *Electrochem. Commun.* **2013**, *37*, 15–19. [CrossRef]
7. Tang, C.K.; Vaze, A.; Rusling, J.F. Paper-based electrochemical immunoassay for rapid, inexpensive cancer biomarker protein detection. *Anal. Methods* **2014**, *6*, 8878–8881. [CrossRef]
8. Wang, X.; Chu, C.; Shen, L.; Deng, W.; Yan, M.; Ge, S.; Yu, J.; Song, X. An ultrasensitive electrochemical immunosensor based on the catalytical activity of MoS_2-Au composite using Ag nanospheres as labels. *Sens. Actuat. B Chem.* **2015**, *206*, 30–36. [CrossRef]
9. Li, X.; Yu, M.; Chen, Z.; Lin, X.; Wu, Q. A sensor for detection of carcinoembryonic antigen based on the polyaniline-Au nanoparticles and gap-based interdigitated electrode. *Sens. Actuat. B Chem.* **2017**, *239*, 874–882. [CrossRef]
10. Miao, P.; Jiang, Y.; Wang, Y.; Yin, J.; Tang, Y. An electrochemical approach capable of prostate specific antigen assay in human serum based on exonuclease-aided target recycling amplification. *Sens. Actuat. B Chem.* **2018**, *257*, 1021–1026. [CrossRef]
11. Wang, J.; Wang, Y.; Chen, H.; Xu, H.; Wang, W.; Bai, L. Sensitive and simultaneous detection of tumor markers assisted by novel functional polymer brush/Au nanoparticles composite. *Sens. Actuat. B Chem.* **2018**, *258*, 998–1007. [CrossRef]
12. Wang, Q.L.; Cui, H.F.; Song, X.; Fan, S.F.; Chen, L.L.; Li, M.M.; Li, Z.Y. A label-free and lectin-based sandwich aptasensor for detection of carcinoembryonic antigen. *Sens. Actuat. B Chem.* **2018**, *260*, 48–54. [CrossRef]
13. Yavas, O.; Svedendahl, M.; Dobosz, P.; Sanz, V.; Quidant, R. On-a-chip Biosensing Based on All-Dielectric Nanoresonators. *Nano Lett.* **2017**, *17*, 4421–4426. [CrossRef] [PubMed]
14. Zhou, J.; Tao, F.; Zhu, J.; Lin, S.; Wang, Z.; Wang, X.; Ou, J.Y.; Li, Y.; Liu, Q.H. Portable tumor biosensing of serum by plasmonic biochips in combination with nanoimprint and microfluid. *Nanophotonics* **2019**, *8*, 307–316. [CrossRef]
15. Akama, K.; Iwanaga, N.; Yamawaki, K.; Okuda, M.; Jain, K.; Ueno, H.; Soga, N.; Minagawa, Y.; Noji, H. Wash- and Amplification-Free Digital Immunoassay Based on Single-Particle Motion Analysis. *ACS Nano* **2019**, *13*, 13116–13126. [CrossRef] [PubMed]
16. Zhu, J.; Wang, Z.; Lin, S.; Jiang, S.; Liu, X.; Guo, S. Low-cost flexible plasmonic nanobump metasurfaces for label-free sensing of serum tumor marker. *Biosens. Bioelectron.* **2020**, *150*, 111905. [CrossRef] [PubMed]
17. Mahmoudi, T.; Pourhassan-Moghaddam, M.; Shirdel, B.; Baradaran, B.; Morales-Narváez, E.; Golmohammadi, H. On-Site Detection of Carcinoembryonic Antigen in Human Serum. *Biosensors* **2021**, *11*, 392. [CrossRef] [PubMed]
18. Iwanaga, M. All-Dielectric Metasurface Fluorescence Biosensors for High-Sensitivity Antibody/Antigen Detection. *ACS Nano* **2020**, *14*, 17458–17467. [CrossRef]
19. Iwanaga, M. High-Sensitivity High-Throughput Detection of Nucleic-Acid Targets on Metasurface Fluorescence Biosensors. *Biosensors* **2021**, *11*, 33. [CrossRef]
20. Iwanaga, M. Rapid Detection of Attomolar SARS-CoV-2 Nucleic Acids in All-Dielectric Metasurface Biosensors. *Biosensors* **2022**, *12*, 987. [CrossRef]
21. Iwanaga, M.; Tangkawsakul, W. Two-Way Detection of COVID-19 Spike Protein and Antibody Using All-Dielectric Metasurface Fluorescence Sensors. *Biosensors* **2022**, *12*, 981. [CrossRef]
22. Iwanaga, M. Highly sensitive wide-range target fluorescence biosensors of high-emittance metasurfaces. *Biosens. Bioelectron.* **2021**, *190*, 113423. [CrossRef]
23. Iwanaga, M. All-Dielectric Metasurfaces with High-Fluorescence-Enhancing Capability. *Appl. Sci.* **2018**, *8*, 1328. [CrossRef]
24. Choi, B.; Iwanaga, M.; Miyazaki, H.T.; Sugimoto, Y.; Ohtake, A.; Sakoda, K. Overcoming metal-induced fluorescence quenching on plasmo-photonic metasurfaces coated by a self-assembled monolayer. *Chem. Commun.* **2015**, *51*, 11470–11473. [CrossRef]
25. Iwanaga, M.; Choi, B.; Miyazaki, H.T.; Sugimoto, Y. The artificial control of enhanced optical processes in fluorescent molecules on high-emittance metasurfaces. *Nanoscale* **2016**, *8*, 11099–11107. [CrossRef]
26. Iwanaga, M. *Plasmonic Resonators: Fundamentals, Advances, and Applications*; Pan Stanford Publishing: Singapore, 2016. [CrossRef]
27. Choi, B.; Iwanaga, M.; Ochiai, T.; Miyazaki, H.T.; Sugimoto, Y.; Sakoda, K. Subnanomolar fluorescent-molecule sensing by guided resonances on nanoimprinted silicon-on-insulator substrates. *Appl. Phys. Lett.* **2014**, *105*, 201106. [CrossRef]
28. ImageJ Official Site. Available online: https://imagej.nih.gov/ij/ (accessed 22 February 2023).
29. Hill, A.V. The possible effects of the aggregation of the molecules of hæmoglobin on its dissociation curves. *Proc. Physiol. Soc.* **1910**, *40*, iv–vii.
30. Neubig, R.R.; Spedding, M.; Kenakin, T.; Christopoulos, A. International Union of Pharmacology Committee on Receptor Nomenclature and Drug Classification. XXXVIII. Update on Terms and Symbols in Quantitative Pharmacology. *Pharmacol. Rev.* **2003**, *55*, 597–606. [CrossRef]
31. Gesztelyi, R.; Zsuga, J.; Kemeny-Beke, A.; Varga, B.; Juhasz, B.; Tosaki, A. The Hill equation and the origin of quantitative pharmacology. *Arch. Hist. Exact Sci.* **2012**, *66*, 427–438. [CrossRef]
32. Irrera, A.; Leonardi, A.A.; Di Franco, C.; Lo Faro, M.J.; Palazzo, G.; D'Andrea, C.; Manoli, K.; Franzò, G.; Musumeci, P.; Fazio, B.; Torsi, L.; Priolo, F. New Generation of Ultrasensitive Label-Free Optical Si Nanowire-Based Biosensors. *ACS Photonics* **2018**, *5*, 471–479. [CrossRef]
33. Giljohann, D.A.; Mirkin, C.A. Drivers of biodiagnostic development. *Nature* **2009**, *462*, 461–464. [CrossRef] [PubMed]
34. Zhou, J.; Du, L.; Zou, L.; Zou, Y.; Hu, N.; Wang, P. An ultrasensitive electrochemical immunosensor for carcinoembryonic antigen detection based on staphylococcal protein A–Au nanoparticle modified gold electrode. *Sens. Actuat. B Chem.* **2014**, *197*, 220–227. [CrossRef]
35. Tseng, M.L.; Jahani, Y.; Leitis, A.; Altug, H. Dielectric Metasurfaces Enabling Advanced Optical Biosensors. *ACS Photonics* **2021**, *8*, 47–60. [CrossRef]

36. Wang, J.; Maier, S.A.; Tittl, A. Trends in Nanophotonics-Enabled Optofluidic Biosensors. *Adv. Opt. Mater.* **2022**, *10*, 2102366. [CrossRef]
37. Qin, J.; Jiang, S.; Wang, Z.; Cheng, X.; Li, B.; Shi, Y.; Tsai, D.P.; Liu, A.Q.; Huang, W.; Zhu, W. Metasurface Micro/Nano-Optical Sensors: Principles and Applications. *ACS Nano* **2022**, *16*, 11598–11618. [CrossRef]
38. Sun, S.; Wu, L.; Geng, Z.; Shum, P.P.; Ma, X.; Wang, J. Refractometric Imaging and Biodetection Empowered by Nanophotonics. *Laser Photon. Rev.* **2023**. [CrossRef]

biosensors

MDPI

Article

Nucleic Acid Quantification by Multi-Frequency Impedance Cytometry and Machine Learning

Mahtab Kokabi [1], Jianye Sui [1], Neeru Gandotra [2], Arastou Pournadali Khamseh [3], Curt Scharfe [2] and Mehdi Javanmard [1,*]

[1] Department of Electrical and Computer Engineering, Rutgers University, Piscataway, NJ 08854, USA
[2] Department of Genetics, Yale University School of Medicine, 333 Cedar Street, New Haven, CT 06520, USA
[3] Department of Mechanical and Aerospace Engineering, Rutgers University, Piscataway, NJ 08854, USA
* Correspondence: mehdi.javanmard@rutgers.edu

Abstract: Determining nucleic acid concentrations in a sample is an important step prior to proceeding with downstream analysis in molecular diagnostics. Given the need for testing DNA amounts and its purity in many samples, including in samples with very small input DNA, there is utility of novel machine learning approaches for accurate and high-throughput DNA quantification. Here, we demonstrated the ability of a neural network to predict DNA amounts coupled to paramagnetic beads. To this end, a custom-made microfluidic chip is applied to detect DNA molecules bound to beads by measuring the impedance peak response (IPR) at multiple frequencies. We leveraged electrical measurements including the frequency and imaginary and real parts of the peak intensity within a microfluidic channel as the input of deep learning models to predict DNA concentration. Specifically, 10 different deep learning architectures are examined. The results of the proposed regression model indicate that an R_Squared of 97% with a slope of 0.68 is achievable. Consequently, machine learning models can be a suitable, fast, and accurate method to measure nucleic acid concentration in a sample. The results presented in this study demonstrate the ability of the proposed neural network to use the information embedded in raw impedance data to predict the amount of DNA concentration.

Keywords: nucleic acid concentration; biosensor; machine learning; regression model; impedance cytometry; microfluidic chip

Citation: Kokabi, M.; Sui, J.; Gandotra, N.; Pournadali Khamseh, A.; Scharfe, C.; Javanmard, M. Nucleic Acid Quantification by Multi-Frequency Impedance Cytometry and Machine Learning. *Biosensors* **2023**, *13*, 316. https://doi.org/10.3390/bios13030316

Received: 11 January 2023
Revised: 15 February 2023
Accepted: 20 February 2023
Published: 24 February 2023

1. Introduction

DNA, the carrier of genetic information, is highly important in the biology and molecular electronics fields [1]. In addition to its biological role, DNA is a topic of significant interest with applications in nanotechnology, self-assembly, and structural flexibility, making it a subject of great interest [2–4]. Moreover, the DNA molecule is a source of rich electrical properties and has the potential to be used as a conducting material in electronic circuits [1]. Due to its electrical properties, we can utilize a multi-frequency lock-in amplifier (Zurich Instruments HF2A, Zurich, Switzerland) to measure the impedance response of beads coupled with different DNA amounts [1]. In this instrument, when a paramagnetic bead or particle passes through the sensing region, it interferes with the AC electric field between two electrodes, and consequently, a momentary increase in impedance can be observed [5]. Nowadays, an impedance-based cytometer can be implemented for the detection of bacteria, DNA amount per bead, cancer cells, and many other biological cells [5–9]. Many studies have shown the importance and application of microfluidic biosensors as a fast, reliable, and rapid platform for early-stage disease detection, as well as many other applications. For example, Mok et al. studied the development of a microfluidic platform to detect proteins [10]. Mahmoodi et al. developed a biosensor platform to detect cortisol in in small volumes of human serum [11]. The goal of this study was to create a cost-effective point-of-care and self-testing platform. Furniturewalla et al. developed a platform to count

the number of blood cells from a pin-prick blood sample pipetted into a standard microfluidic PDMS chip [12]. Xie et al. developed a biomolecular sensing method that utilizes an array of nanoscale wells functionalized with antibodies. The method monitors changes in ionic resistance as the target protein binds inside the wells [13]. On the other hand, the development of microfluidic chips and experimental design often involves extensive investment and time effort, and it is prone to user bias. In this paper, we propose a machine learning (ML)-based model to address this difficulty.

Artificial intelligence (AI) has grown rapidly over the past decade and can be widely used in many aspects of biological information, ranging from drug discovery prediction to cancer prognosis [14–18]. Artificial intelligence employs a variety of statistical methods to detect and extract key features from complex datasets. In addition, AI provides a robust framework for creating feature representations from high-dimensional inputs and generalizing knowledge to new scenarios [19]. In recent years, the integration of machine learning methods with microfluidics has become a popular area of research. The combination of microfluidics, which generates large amounts of data, with machine learning for the analysis of these complex data sets represents a promising development in biotechnology [19–24]. To date, many studies have shown the application of machine learning to impedance cytometry. For example, Caselli et al. demonstrated the ability of neural networks to decipher impedance cytometer signals. They utilized an experimental dataset to predict single cell features, which were then used as inputs for classifier models [25]. Patel et al. applied a designed biosensor for detecting hemoglobin biomolecules with high sensitivity using polynomial regression models [26]. Schütt et al. applied a k-means algorithm for subpopulation clustering of peripheral blood mononuclear cells, based on peak voltage and phase [27]. As another example, Honrado et al. developed an ML-based method of classification of impedance data to distinguish and quantify cellular subpopulations at the early apoptotic versus late apoptotic and necrotic states [28]. Ahuja et al. used a support vector machine (SVM) classifier to discriminate between live and dead breast cancer cells by using the peak impedance magnitude and phase [29]. Feng et al. used fully connected networks to estimate three biophysical parameters based on the peak impedance amplitude at four frequencies, allowing them to classify five cell types [30]. Meanwhile, Sui et al. used a combination of multi-frequency impedance cytometry and supervised machine learning to classify particle barcodes [31].

Given the clinical significance of DNA, here we examine if a machine learning approach could facilitate and expedite the process of identifying the DNA amount per bead. In this analysis, six different concentrations of DNA, with a fixed length of 300 bp (base pairs), are coupled with 2.8 μm paramagnetic beads and passed through a custom-made microfluidic channel. Then, electrical measurements within the microfluidic chip are obtained to construct a machine learning model. The machine learning algorithm learns the relationship between the electrical measurements as an input and the DNA concentration per bead as an output. As a result, the machine learning approach could learn from historical data obtained from experiments to predict new output values [32]. With this technique, a trained model can be generalized to predict the DNA amount per bead for beads with an unknown DNA concentration. The objective of this study is to leverage the electrical measurements obtained from the Zurich Instruments tool, such as the frequency, peak intensity, and phase change of the peak intensity, to predict the DNA concentration. In this work, we proposed a novel regression approach to predict the amount of DNA by using electrical measurement features. To quantify the performance of the specified model, three types of machine learning approaches were constructed: classification, regression, and a hybrid model. In our analysis, we benchmarked 10 different deep learning architectures from simple to complex on four figures of merit (FOMs), namely, accuracy and error for the classification method, R_Squared, and the mean square error (MSE) of the regression model. Furthermore, we combined the best architectures from classification and regression to propose a novel hybrid regression model with an R_Squared value of 97%. The trained

hybrid regression model may provide a general platform to predict the DNA amount per bead from electrical measurements obtained from the Zurich Instruments tool.

2. Materials and Methods

2.1. Experimental Setup

As was described, nucleic acid quantification plays a major role in research and clinical study, ranging from the diagnosis of infectious diseases to food safety assurance and so on. Nucleic acids also have important biomarkers for biological studies and diagnosis [33]. In this experiment, a novel technique to identify DNA fragments is introduced. This technique identifies DNA fragments based on their frequency-dependent dielectric properties. In this experiment, DNA fragments which are coupled on micron-sized particles pass through a microfluidic channel made of polydimethylsiloxane (PDMS). The microfluidic PDMS channel is the first layer of the device. The second layer is a pair of electron beam-deposited reusable coplanar gold electrodes on a fused silica substrate. The microfluidic channel is 30 μm wide and 15 μm high, with a micron-sized electrode. The electrodes are 20 μm in width, and the gap between the two electrodes is 30 μm. We should point out that we experimentally verified that the sensitivity of the microfluidic channel increases as the width of the channel decreases and approaches the size of the bead. However, this increases the risk of clogging in the channel as it becomes too small. We designed the microchannel with the aforementioned configuration, which is large enough to minimize clogging and small enough to obtain sufficient sensitivity during measurements. Figure 1A represents the image of device which is made from PDMS and Figure 1B illustrates the microscopic image of the channel [5].

We compared our method to two commercially available technologies: gel electrophoresis and real-time PCR (also known as quantitative PCR or qPCR). Both of these are commonly used for DNA detection and sizing. The standard detection limit of gel electrophoresis using DNA bound to ethidium bromide is between 0.5 and 5.0 ng/band. However, with optimized gel electrophoresis technology, the Agilent Bioanalyzer can detect PCR products at concentrations as low as 0.1 ng/band and complete the analysis within 30 min. Real-time PCR has a detection limit of several copies of a DNA molecule per microliter or several fg/μL. However, it is relatively slow, with a sample processing time of over an hour, and has limitations in terms of DNA fragment size (e.g., amplicon size should be <200 bp). Furthermore, real-time PCR is costly and complex due to the need for simultaneous thermal cycling and fluorescence detection. It has limited multiplexing capabilities, making it difficult to miniaturize for portable applications. In contrast, our impedance sensor in combination with microfluidic technology has the potential for multiplexing and portability.

In this experiment, six different quantities and concentrations of DNA with a fixed length of 300 bp are integrated with a 2.8 μm paramagnetic bead and pass through a custom-made microfluidic chip. Three different types of magnetic beads (M270, M280, and C1) are tested. Based on the properties and the nature of our sensor, we chose to proceed with the M280 type (2.8 μm paramagnetic bead).

In this study, purified biotinylated DNA of a known quantity was serially diluted to obtain the desired concentrations. This DNA was then mixed with the beads to create DNA bound to the beads. The number of DNA molecules per bead is only an estimated average based on measurements of approximately 500 beads. This estimation was made after testing approximately 2000 beads per sample. The DNA-binding efficiency is determined by the very high binding affinity of the streptavidin–biotin interaction ($K_d = 10^{-15}$). The beads contain streptavidin, and the DNA is biotin-labeled. These beads have a binding capacity of 10 ug ds-DNA per mg of beads. This knowledge was used when combining various DNA amounts with the beads. In this study, the lower limit of detection identified is 0.0039 fmol, and the maximum DNA concentration is 0.19 fmol [5]. For testing the sensitivity of the sensor, we diluted a 1-microliter aliquot of the DNA-coated beads in 60 μL of phosphate-buffered saline (PBS) for detecting small amounts of DNA. PBS, which has a relatively

high salt concentration and high conductivity, has been shown to enhance the sensitivity of impedance measurements. Our sensor is capable of quantifying DNA fragments at high accuracy and precision at the femtomolar level and over a 100-fold dynamic range. Figure 1C represents the streptavidin–biotin linkage between DNA and beads. In this method, the target DNA was generated by using biotinylated DNA oligonucleotides and PCR (polymerase chain reaction) [5]. The procedures are as follows:

1. Biotinylated oligos was synthesized by IDT (Coralville, IA, USA), which is used to amplify different fragment sizes of DNA; in this case the fragment size is 300 bp.
2. The PCR product was purified by using a Qiaquick PCR purification kit to remove any unincorporated biotinylated oligos.
3. The PCR was eluted in water and quantified for immobilization to the streptavidin coated on 2.8 μm (M280) beads.
4. The purified biotinylated DNA was immobilized with beads in room temperature for 15 min using gentle rotation at 2000 rpm.
5. The biotinylated DNA-coated beads were separated on a magnet and washed subsequently.
6. Finally, the washed biotinylated DNA-coated beads were resuspended in 10 μL of water. Different concentrations of DNA were bound to paramagnetic beads (Table 1) [5].

Table 1. Model outputs [5].

DNA Length	DNA Amount per Bead
Bare bead	0
300 bp	1.54×10^{-4}
300 bp	7.69×10^{-5}
300 bp	1.54×10^{-5}
300 bp	1.54×10^{-6}
300 bp	1.54×10^{-7}
300 bp	1.54×10^{-8}

Multi-frequency impedance cytometry techniques have been performed to detect the impedance difference of beads integrated with different amounts of DNA. The impedance response was measured at 8 different frequencies simultaneously by using a multi-frequency lock-in amplifier (Zurich Instruments HF2A, Zurich, Switzerland). When an AC voltage is applied between electrodes, a flowing particle or cell perturbs the AC electric field, which results in a momentary increase in the impedance/decrease in the voltage.

In this experimental setup, the first electrode is excited with combination of 8 frequencies ranging from 100 kHz to 20 MHz, and the second electrode is connected to the transimpedance amplifier. Figure 1E shows representative multi-frequency time series data of bare magnetic beads in voltage. The voltage is normalized for a straightforward comparison. For testing of 300 bp DNA beads, 6 different concentrations of DNA were measured to study the effect of the different amounts of DNA on the frequency. To compare the impedance response from different DNA concentrations, the impedance of bare beads with no DNA was measured in the same experiment. Figure 1F shows representative time series data comparing bare magnetic beads to DNA at the highest concentration (500 kHz frequency). In this figure, as well, the voltage is normalized for better comparison.

Table 1 showed the different concentrations of DNA coupled with paramagnetic beads. To compare the impedance response of different concentrations of DNA integrated with paramagnetic beads, we performed the same experiment with bare beads. In this experiment, 2.8 μm paramagnetic beads with no DNA concentration passed through the microfluidic channel, and the impedance response of a bare bead is obtained.

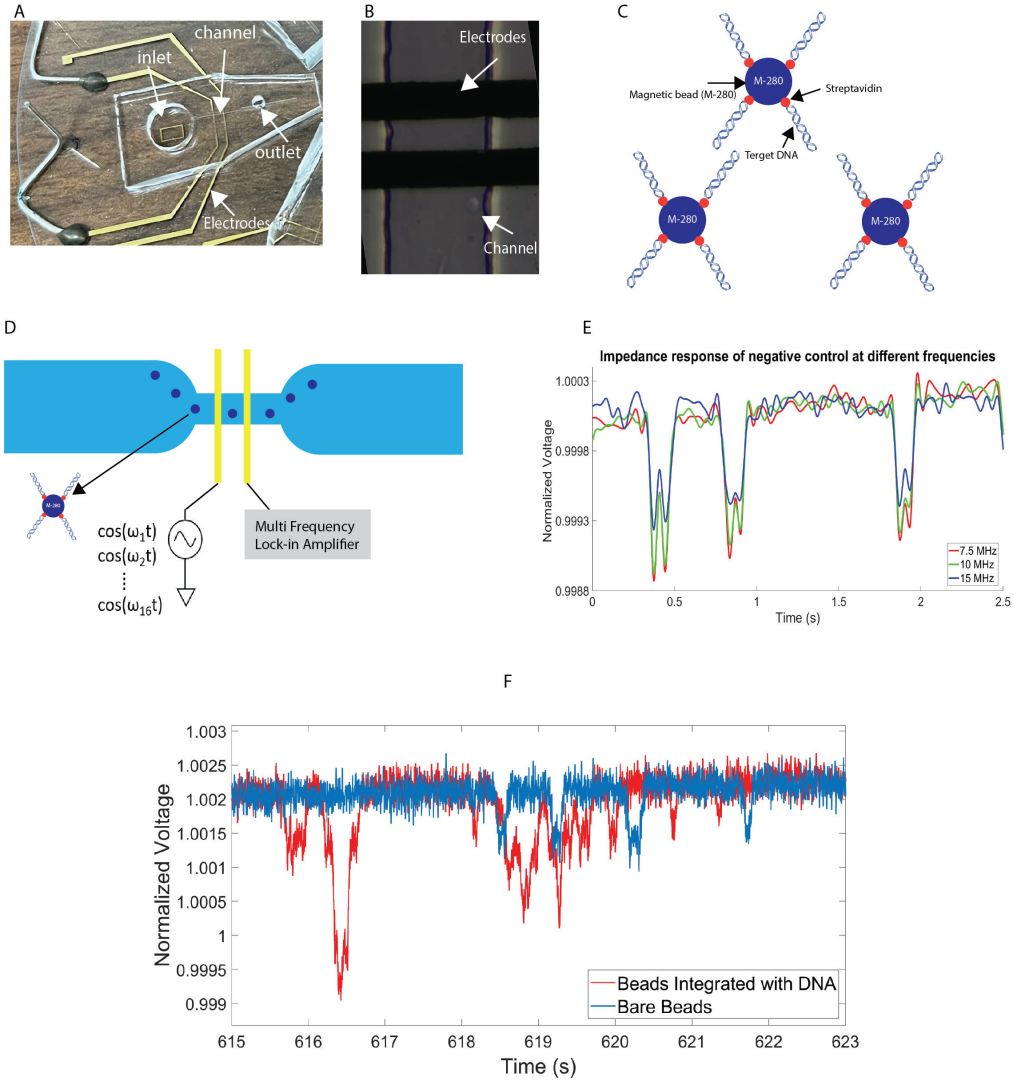

Figure 1. Overview of the process. (**A**) Image of device. (**B**) Microscopic image of channel and electrodes. (**C**) The sample preparation after binding of biotinylated DNA to paramagnetic beads. (**D**) The schematic diagram of detection. (**E**) Representative data of bare paramagnetic beads. (**F**) Representative data of bare paramagnetic beads and beads integrated with most-concentrated DNA.

The results showed that there is positive relationship between DNA amounts per bead and the impedance peak response (IPR). As DNA concentration per bead increases, the IPR increases as well. These findings showed the positive correlation of DNA amounts attached to beads with IPR. In addition, increased DNA amounts resulted in a higher surface potential of the beads, which was associated with a larger impedance difference compared to the control bare bead. The details of the nucleic acid sample preparation and the impedance chip preparation, along with the experimental procedures, are those described in the work by Sui et al. [5].

As we described, in this experiment 6 different DNA concentrations coupled to paramagnetic beads are examined. In addition, it is very difficult to bind very small inputs of

DNA to beads. Given the need for testing small DNA amounts in many samples, there is a utility for novel machine learning approaches for accurate and high-throughput DNA quantification. Furthermore, by proposing a general regression model, we can predict unknown DNA concentrations with a fixed length of 300 bp coupled to a bead. The combination of microfluidics, which generates vast amounts of complex data, with machine learning methods represents an emerging opportunity in biotechnology. On the other hand, the development of microfluidic chips and experimental design is expensive and time-consuming, and the method is prone to bias by the user. In the next section, we propose a novel hybrid regression model to address this difficulty. All the electrical properties obtained from the Zurich Instruments tools (including frequency, imaginary and real part of peak intensity) are leveraged to identify correlations between these properties and the amount of DNA per bead. Machine learning tools are then used to develop a general model and platform for predicting nucleic acid concentration.

2.2. Dataset

This section explains the proposed approach to predicting the DNA amount per bead using experimental data and leveraging deep learning methods. Figure 2 shows an overview of the proposed method. In this study, the dataset was obtained from a custom-based microfluidic chip to detect DNA molecules bound to beads by measuring the impedance peak response (IPR) at multiple frequencies [5]. The proposed machine learning method will be trained on the electrical signals obtained from the biosensor with a specific configuration of the channel and electrode size. It is anticipated that increasing the size of the channel decreases the sensitivity of the biosensor. This means that the passage of beads or particles through the electrodes will result in weaker signals, i.e., smaller peaks in the impedance signals. This makes it more difficult to distinguish the passage of beads with very small amounts of DNA from the signal noise. Consequently, the accuracy of the machine learning method will be negatively affected. In the case of using another configuration, it would be more accurate to retrain the model based on the data obtained from the sensor with the new configuration.

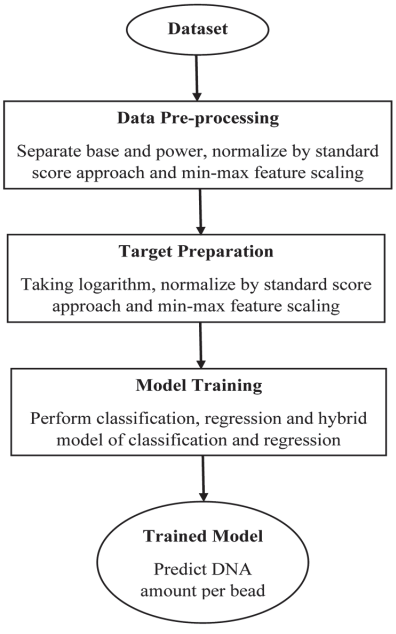

Figure 2. Overview of the proposed framework for prediction of DNA amount per bead.

The impedance response was measured simultaneously at 8 different frequencies ranging from 100 kHz to 20 MHz [5]. This dataset contains 105,104 data points collected on different days. For each piece of data, the frequency; the real, imaginary, and absolute values of the peak intensity; and the phase change of the peak intensity were measured to calculate the DNA amount per bead. All these features are used as input for the neural network model. In this work, our goal is to find a relationship between the aforementioned measurement features and the DNA amount per bead. To accomplish this, we explored three different machine learning approaches: classification, regression, and a hybrid model. The hybrid model is a combination of the best architecture of the classification and regression models.

The proposed model consists of three main steps, which are shown in Figure 2. The frequency; real, imaginary, and absolute values of the peak intensity; and the phase change of the peak intensity were recorded in measurements and will be used as input features. The output is the DNA amount per bead. In total, 7 outputs were examined containing 6 different concentrations of DNA from low to high coupled to paramagnetic beads and one control bead, which is a bare bead (i.e., a bead with no DNA concentration).

2.3. Data Preprocessing

The main goal of data preparation is to guarantee the quality of the data before applying them in any type of machine learning algorithm [34]. Before employing data in any learning algorithms, each input and output feature was normalized. Normalizing data generally prevents any variable from dominating the output values and boosts the accuracy of the model [35]. The most common normalization methods used in machine learning algorithms include min–max scaling, the standard score (z-score), and decimal scaling [36]. In this study, we applied two common normalization methods: the standard score and min–max scaling. First, we applied standard score normalization, and then we normalized the dataset between 0 and 1 (min–max scaling). In the standard score (z-score) normalization, the values for a feature A are normalized based on the mean (i.e., average) and standard deviation of A [34]. A value v_i is normalized to v'_i by computing:

$$v'_i = \frac{v_i - \overline{A}}{\sigma_A} \tag{1}$$

where $\overline{A}$ and σ_A are the mean and standard deviation of attribute A, respectively [26]. Then, we applied min–max scaling normalization to our input features. In this technique, the attribute will be rescaled from its domain to a new range of values. In our case study, the input features are normalized in the (0, 1) range [36], where the following relation is used:

$$\mathrm{f(v)} = \frac{\mathrm{v} - \min(\mathrm{v})}{\max(\mathrm{v}) - \min(\mathrm{v})} \tag{2}$$

Dataset normalization has a great effect on preparing the input data to be suitable for training and improving the accuracy of the output [35]. Many studies have employed more than one normalization method on input data before feeding data to any neural network's algorithms to help comparing two or more datasets with different scales [37–41].

2.4. Target Preparation

Different quantities of DNA with a fixed length of 300 bp were tested in the experiment [5]. The output of our model is the DNA amount per bead for tested beads, including the bare bead and beads bonded with the least-concentrated DNA to those with the most-concentrated DNA, which are exponentially distributed. There is a total number of 7 outputs shown in Table 1. In situations where the data are distributed exponentially, taking a log function is one common way to normalize the data [42]. Therefore, we normalized the output features by using logarithmic transformation. In the next step, the standard score and min–max normalization are applied, which were described in Section 2.3.

2.5. Model Training

After feature extraction and preprocessing of data, 10 different deep learning architecture models are implemented to evaluate the performance of the approach. We employ classification, regression, and a hybrid model. The scikit-learn library is used to build the models in Google Colab using Python [43]. The data are shuffled randomly, and 30% is used for testing, while the rest is used for training. The model training was stopped after 5000 epochs (iterations) for feature selection, which is described in Section 3.1, and after 10,000 epochs for deep learning models both in classification and regression.

Before training the model, the most important task is to determine the combination of best features for DNA amount per bead prediction [40,44]. Moreover, the best number of features is chosen for regression and classification analysis. In each part of the analysis, 10 different models consisting of different numbers of hidden layers and neurons were implemented to examine the performance of different architectures. The best architecture giving the highest test and train accuracy and the lowest error was used as the best model for the classification part.

R_Squared and mean square error (MSE) are statistical parameters used to evaluate the performance of regression models [45]. The best deep learning architecture giving the highest R_Squared and lowest MSE was selected as the best candidate model. The hybrid model (Figure 3) uses the best architecture of the classification and regression models to train the model. The hybrid model is used to enhance the performance of the regression model. The prediction results of the classification model and original features are used as the input to the regression model. In other words, the 7 outputs from the classification method, combined with the 8 original input features, result in a total of 15 features that serve as the input to the candidate regression model. The output of the regression model is the DNA amount per bead.

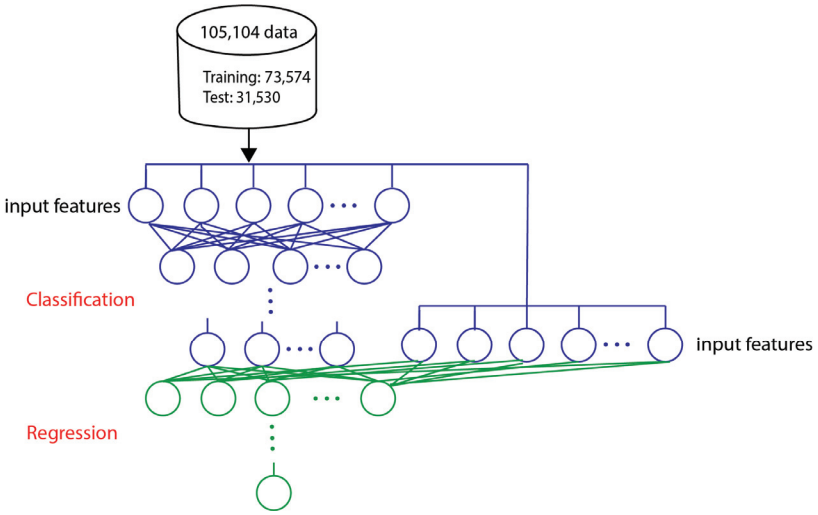

Figure 3. Hybrid model (combining the best architecture of the classification and regression models).

3. Results

3.1. Feature Selection

We first studied the effect of the number of features on the performance of the classification and regression models, benchmarking their performance on four figures of merit (FOMs) in terms of accuracy and error for classification, and R_Squared and MSE for regression analysis. The model training stopped after 5000 epochs. The deep learning model consists of 5 hidden layers with 70, 60, 30, 20, and 10 neurons in each layer. For the

input features, we evaluated two different datasets, including those with five and eight features. In the first dataset for DNA amount per bead prediction, five features consisting of frequency; the real part, imaginary part, and absolute value of the peak intensity; and the phase change of the peak intensity are used. For the second dataset, in addition to the frequency and phase change of the peak intensity, we divided each exponential input feature (real, imaginary, and absolute value of the peak intensity) into two parts: base and power. Figure 4 compares the performance of the classification model trained on the five-feature and eight-feature datasets. The results show that with the second dataset, which includes eight features, can lead to a more than 16% improvement in both training and testing accuracy. Furthermore, the train and test errors markedly decreased.

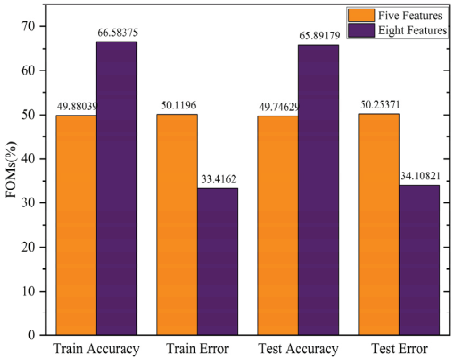

Figure 4. Effect of feature selection on FOMs (%).

The effect of the number of features on the performance of the regression model was evaluated by the R_Squared and mean square error (MSE) values. The results are shown in Figure 5, which indicates that the dataset with eight features yields better results. Specifically, the regression model improved by around a 33% increase in R_Squared and around a 7% decrease in the MSE. Overall, both the classification and regression models performed better on representative FOMs; therefore, the dataset with eight features is chosen as the input for the following analysis.

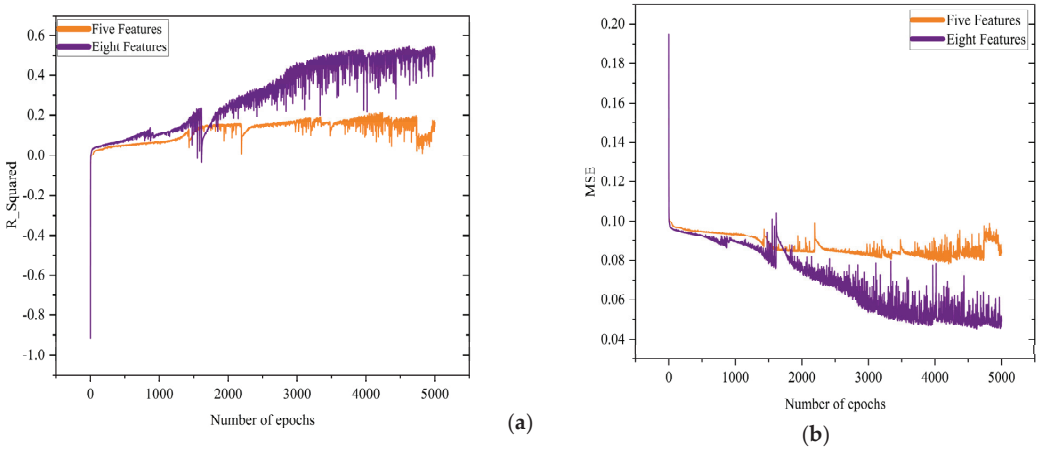

Figure 5. Effect of feature selection on (**a**) R_Squared with respect to number of epochs; (**b**) mean square error (MSE) with respect to number of epochs.

3.2. Classification

To achieve robust network training, reduce the risk of overfitting, and increase the network generalization capabilities, we constructed 10 different deep learning architectures, from simple to complex. The implemented architectures are summarized in Table 2. Determining the optimal number of neurons and hidden layers is a very crucial step in deciding the optimal deep learning architecture [46]. Using too many neurons and hidden layers can result in overfitting by the model. On the other hand, having too few neurons and hidden layers may result in underfitting [46]. There are several methods and approaches to tuning the hyperparameters such as the number of neurons, activation function, number of layers, batch size, and epochs of deep learning algorithms. The possible approaches for finding the optimal parameters are hand or manual tuning, grid search, random search, Bayesian search, and AutoML. Grid search and random search are the most widely used strategies for hyperparameter optimization. In the grid search method, the domain of the hyperparameters is divided into a discrete grid, and the performance of every combination of values will be calculated. The point of the grid that maximizes the average value in cross-validation is the optimal combination of values for the hyperparameters [47]. While grid search evaluates the performance of every possible combination of hyperparameters to find the best model, random search only selects and tests a random combination of hyperparameters. Bergstra et al. [47] demonstrated that the performance of the random search is more efficient for hyperparameter optimization than trials on a grid. The Bayesian method, in contrast to random and grid search, builds a probability model to find the next set of hyperparameters which performs best on a probability function [48]. In other words, Bayesian optimization considers past evaluations when choosing the hyperparameter set to evaluate the next set of parameters [48]. All the aforementioned techniques are dedicated to special cases; as an example, grid search is only reliable for low-dimensional input spaces [47]. On the other hand, it was shown that random search results in better sampling efficiency in high-dimensional search spaces compared to grid search [49]. Bayesian optimization might potentially trap the model at a local optimum. In this analysis, manual tuning has been employed to determine the hyperparameters of the deep learning model to address these difficulties. In addition, manual tuning provides us the behavior of hyperparameters and reduces the runtime of the process. Therefore, we employed 10 architectures and analyzed the effect of the numbers of neurons and hidden layers on FOMs.

Table 2. Deep learning models.

Model Number	Number of Hidden Layers	Number of Neurons in Each Layer
1	2	10,10
2	2	20,20
3	3	20,20,10
4	3	30,20,10
5	4	40,30,20,10
6	5	60,50,30,20,10
7	5	70,50,40,20,10
8	5	80,60,40,30,20
9	6	100,80,60,50,20,10
10	6	100,80,80,60,30,20

The test and train accuracy of each architecture are evaluated. The training procedure was stopped after 10,000 iterations for all models. In addition, the ReLU activation function was used, which is the most commonly used activation function in deep learning models. ReLU stands for rectified linear unit and is an activation function commonly used in neural networks. It is a simple function that outputs the input directly if it is positive and outputs zero if it is negative. Figure 6 represents the train and test accuracy of each architecture.

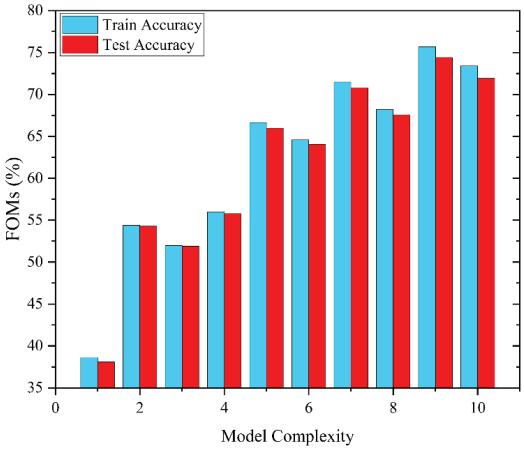

Figure 6. Effect of model complexity on train and test accuracy.

Among all architectures, model number 9 achieved the highest accuracy, which is around 75% on the training data and around 74% on the test data. It is also worth mentioning that the selected model performed well on train and test data. This means that the model generalizes well from observed data (train data) to predict unseen data (test data), and no overfitting occurs [50]. Therefore, we selected model number 9 as the representative model for classification. Table 3 shows the configuration matrix of the representative model. To evaluate the performance of the representative model, the following metrics are used: accuracy (ACC), true positive rate (TPR), true negative rate (TNR), false negative rate (FNR), and false positive rate (FPR). These measures are computed using the following equations:

$$\text{Accuracy (ACC)} = \frac{\text{TP} + \text{TN}}{\text{TN} + \text{TP} + \text{FN} + \text{FP}} \tag{3}$$

$$\text{Sensitivity (TRP)} = \frac{\text{TP}}{\text{TP} + \text{FN}} \tag{4}$$

$$\text{Specificity (TNR)} = \frac{\text{TN}}{\text{TN} + \text{FP}} \tag{5}$$

$$\text{Fallout (FPR)} = \frac{\text{FP}}{\text{TN} + \text{FP}} \tag{6}$$

$$\text{False Negative Rate (FNR)} = \frac{\text{FN}}{\text{TP} + \text{FN}} \tag{7}$$

where TPs (FPs) refer to the number of correct (incorrect) predictions of outcomes in the considered output class, whereas TNs (FNs) refer to the number of correct (incorrect) predictions of outcomes in any other output classes [14]. The below table shows the accuracy (ACC), true positive rate (TPR), true negative rate (TNR), false positive rate (FPR), and false negative rate (FNR) for each individual output (class). For each individual class, we achieved above 88% accuracy.

Table 3. Confusion matrix of representative model.

	1	**2**	**3**	**4**	**5**	**6**	**7**
ACC	0.97	0.91	0.89	0.89	0.88	0.97	0.97
TPR	0.43	0.87	0.80	0.87	0.51	0.8	0.78
TNR	0.99	0.92	0.92	0.89	0.93	0.99	0.99
FPR	0.004	0.07	0.07	0.10	0.06	0.07	0.09
FNR	0.56	0.12	0.19	0.12	0.48	0.99	0.21

3.3. Regression

Similar to classification, we constructed 10 different neural network architectures using the same models previously shown in Table 2. Table 4 displays the R_Squared and MSE of each model. According to the results given in Table 4, it can be concluded that among all architectures, model number 8 achieved the highest R_Squared for both the train and test data. Therefore, model number 8 is selected as the representative architecture for the regression model. Figure 7 shows the results obtained by the representative regression model on the test and train data. In this figure, the average DNA amount per bead prediction for each of our seven outputs is plotted versus its corresponding ground truth. The first point in Figure 7 represents the bare bead prediction, and the next six points represent the beads coupled with DNA concentrations from the lowest to the highest. This figure shows that there is a relationship between electrical measurements and DNA concentrations coupled to paramagnetic beads.

Table 4. Effect of model complexity on R_Squared and MSE.

Model	MSE Train	MSE Test	R^2 Train (%)	R^2 Test (%)
1	0.3077	0.3077	67.61	67.98
2	0.2959	0.2954	57.34	56.83
3	0.2821	0.2873	72.64	71.26
4	0.2796	0.2811	75.39	74.76
5	0.2615	0.2786	90.69	90.6
6	0.2286	0.2481	93.34	93.13
7	0.2281	0.2373	91.89	92.16
8	0.2254	0.232	96.2	96.25
9	0.2117	0.2338	94.01	94.29
10	0.2087	0.2198	95.23	95.07

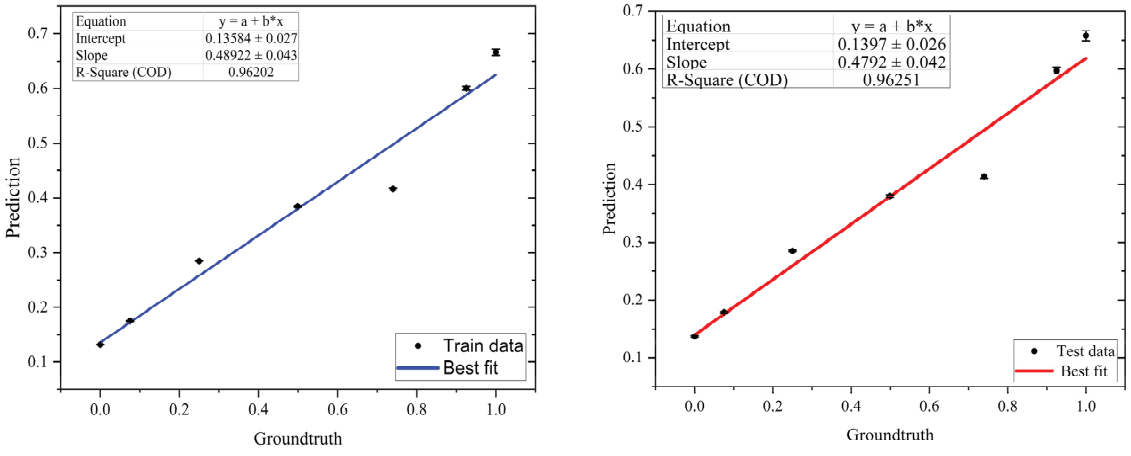

(**a**) (**b**)

Figure 7. Results of representative regression model on (**a**) train and (**b**) test data.

A linear fit was applied to these results, and an R_Squared of around 96% is achieved for both the train and test data, with a maximum standard error of 0.008. For an ideal model, the slope of the trend line should be equal to one, as the prediction should be equal to the ground truth. Here, the slope of trend line is around 0.47 indicating the error between the prediction and ground truth values. This motivated us to design a hybrid model to

improve the performance of the regression model. In the next section, the architecture of the proposed hybrid model will be discussed.

3.4. Hybrid Model

The hybrid model shown in Figure 3 consists of the representative models of classification and regression combined together to increase the accuracy of the regression model. Model number 9 from the classification models (Table 2) is selected to be combined with the representative regression model (model number 8 from Table 2). In the resulting model, the output neurons of the classification model and original features are used as input features for the regression model. In this case, the eight aforementioned features were fed into the representative classification architecture, which resulted in seven categorical outputs. Then, these seven outputs with the eight original features served as the inputs of the candidate regression model. Finally, the regression model output is the DNA amount per bead.

The hybrid model is used to enhance the performance of regression. Figure 8 shows the results of the hybrid model on the train and test data, with an R_Squared of around 97%, a slope of around 0.68, and a maximum standard error of 0.005. Similar to Figure 7, the average DNA amount per bead prediction of each output class is plotted versus its corresponding ground truth. Comparing the hybrid model (Figure 8) and regression model (Figure 7), it can be seen that the slope of the model is improved by around 21%, by knowing the fact that the ideal slope is 1. In addition, the R_Squared value for the train and test data is improved.

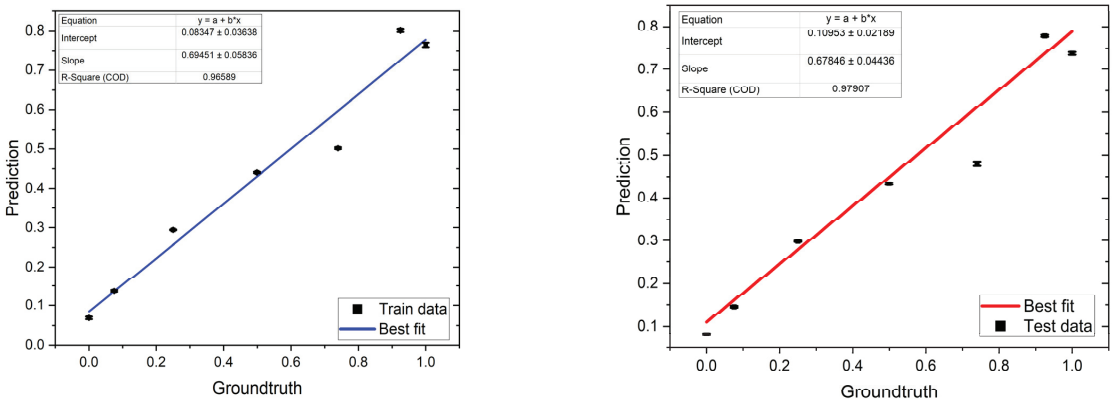

(**a**) (**b**)

Figure 8. Representative hybrid model on (**a**) train and (**b**) test data.

To date, many studies have shown the effectiveness of using a hybrid model to enhance the performance of various systems. For instance, Liaqat et al. [44] proposed a hybrid model approach that combines seven classification algorithms with deep learning models to identify posture detection. In this study, the outputs of the ML classifiers and deep learning models were used as inputs for a convolutional neural network (CNN) architecture. The experimental results demonstrated that the proposed hybrid approach resulted in a better performance compared to traditional machine learning methods [44]. Chieregato et al. [51] also proposed a hybrid model that integrates machine-learning with deep learning methods and is designed to be used as a tool to support clinical decision-making. The proposed hybrid model is capable of predicting COVID-19 outcomes from CT images and clinical data. The reason for combining several state-of-the-art algorithms to build hybrid models is to enhance the accuracy of the model and increase its capability to tolerate significant data incompleteness [52]. However, complexity arises when one or

more deep learning algorithms are combined, so careful consideration needs to be given to the selection of algorithms with different architectures to achieve better performance. Compared to conventional models, the hybrid model may take longer to train or tune.

By employing a hybrid regression model on data from impedance cytometry measurements of DNA, we have observed an 8% improvement in R_Squared compared to the linear regression model reported by Sui et al. [5]. The results presented in this work demonstrate the ability of the proposed neural network to use the information embedded in raw impedance data to predict the amount of DNA concentration coupled to beads. Artificial intelligence (AI) approaches provide a promising new direction to efficiently extract the information embedded in the electrical signals. From an application point of view, machine learning algorithms enable the development of intelligent microfluidic platforms. These platforms are operated by data-driven models and characterized by increased automation [19]. The results presented in this work demonstrate the ability of neural networks to efficiently predict the amount of immobilized DNA that is fixed in 300 bp. In developing our methods, three network types were considered: classification, regression, and a hybrid model. After selecting the best features, we constructed classification and regression models with optimized numbers of hidden layers. In the next step, a hybrid model was presented to improve the R_Squared of the model. The use of AI in analyzing impedance signals could present new challenges and opportunities for next-generation impedance cytometry systems.

4. Conclusions

In this study, we used a machine learning approach to predict the DNA amount per bead by leveraging electrical measurements from a Zurich Instruments tool. Multi-frequency impedance cytometry was performed to measure the electrical impedance responses at 8 different frequencies, ranging from 100 kHz to 20 MHz. In this experiment 6 different DNA concentrations were coupled to paramagnetic beads and passed through the microfluidic channel. To account for device-to-device variation, the response of bare streptavidin-coated paramagnetic beads was studied.

In the next step, we employed data from impedance cytometry measurements of DNA immobilized on paramagnetic beads to develop deep learning methods that can predict the amount of immobilized DNA that is fixed in 300 bp. The dataset used in this study consists of around 105,000 pieces of data with five electrical features. As a first step, we performed feature selection to identify the best combination of features. It was shown that when the base and power for the real, imaginary, and absolute values of the peak intensity were separated, better performance was achieved. Therefore, we continued our analysis using eight features.

In the next step, three different machine learning methods were presented, namely, classification, regression, and a hybrid model, to predict the DNA amount per bead. For classification and regression, underfitting and overfitting were studied by investigating 10 different deep learning architectures. For both classification and regression problems, the architecture with the highest performance was selected as the representative model. We were able to achieve around 75% accuracy for classification and an R_Squared of around 96% for regression. For the regression model, the average prediction values were plotted against ground truth, with a slope of 0.47 for the trend line.

To improve the performance of the regression model, a novel hybrid regression model was presented. In this approach, the best deep learning architectures for classification and regression were combined to predict the DNA amount per bead. The results showed that the proposed hybrid approach achieved a better performance as compared to the previous representative of regression models. In comparison to the regular regression model, the slope of the trend line improved by around 21%. The outcomes presented in this study demonstrate the ability of the proposed neural network to use the information embedded in raw impedance data to predict the DNA concentrations coupled to beads.

In future work, the focus will be on using automotive approaches to tune hyperparameters of deep learning methods, such as grid search, random search, and Bayesian search. The hybrid model has a longer training runtime than traditional machine learning algorithms, so further improvement and optimization are necessary to reduce the time cost. Additionally, testing different configurations of microfluid channels in terms of size and structure will be considered to assess the impact on the model's performance and create a more generalized model.

Author Contributions: Methodology, investigation, software, and writing—original draft preparation, M.K. and A.P.K.; formal analysis, experimental data, conceptualization, resources, and writing—review and editing, J.S., N.G. and C.S.; supervision and project administration, M.J. All authors have read and agreed to the published version of the manuscript.

Funding: This research was funded by the National Science Foundation with Award Nos. 1711165, 1846740, and 2002511, and by a grant from the National Institute of Child Health and Human Development (R01HD102537).

Institutional Review Board Statement: Not applicable.

Informed Consent Statement: Not applicable.

Data Availability Statement: The data presented in this study are available on request from the corresponding author. The data are not publicly available due to ethical constraints.

Acknowledgments: The authors are thankful to their respective institutions/universities for providing valuable support and funding to conduct this research work.

Conflicts of Interest: The authors declare no conflict of interest.

References

1. Roman, K.; Segal, D. Machine Learning Prediction of DNA Charge Transport. *J. Phys. Chem.* **2019**, *123*, 2801–2811.
2. *DNA in Supramolecular Chemistry and Nanotechnology*; Stulz, E., Clever, G.H., Eds.; John Wiley & Sons: Hoboken, NJ, USA, 2015.
3. Drummond, T.G.; Hill, M.G.; Barton, J.K. Barton. Electrochemical DNA sensors. *Nat. Biotechnol.* **2003**, *21*, 1192–1199. [CrossRef]
4. Clausen, C.H.; Dimaki, M.; Bertelsen, C.V.; Skands, G.E.; Rodriguez-Trujillo, R.; Thomsen, J.D.; Svendsen, W.E. Bacteria Detection and Differentiation Using Impedance Flow Cytometry. *Sensors* **2018**, *18*, 3496. [CrossRef]
5. Sui, J.; Gandotra, N.; Xie, P.; Lin, Z.; Scharfe, C.; Javanmard, M. Multi-frequency impedance sensing for detection and sizing of DNA fragments. *Sci. Rep.* **2021**, *11*, 6490. [CrossRef]
6. Lin, Z.; Lin, S.Y.; Xie, P.; Lin, C.Y.; Rather, G.M.; Bertino, J.R.; Javanmard, M. Rapid Assessment of Surface Markers on cancer cells Using immuno-Magnetic Separation and Mul-ti-frequency impedance cytometry for targeted therapy. *Sci. Rep.* **2020**, *10*, 3015. [CrossRef]
7. Schoendube, J.; Wright, D.; Zengerle, R.; Koltay, P. Single-cell printing based on impedance detection. *Biomicrofluidics* **2015**, *9*, 014117. [CrossRef]
8. Jung, T.; Yun, Y.R.; Bae, J.; Yang, S. Rapid bacteria-detection platform based on magnetophoretic concentration, dielectrophoretic separation, and impedimetric detection. *Anal. Chim. Acta* **2021**, *1173*, 338696. [CrossRef]
9. Qu, K.; Wei, L.; Zou, Q. A Review of DNA-binding Proteins Prediction Methods. *Curr. Bioinform.* **2019**, *14*, 246–254. [CrossRef]
10. Mok, J.; Mindrinos, M.N.; Davis, R.W.; Javanmard, M. Digital microfluidic assay for protein detection. *Proc. Natl. Acad. Sci. USA* **2014**, *111*, 2110–2115. [CrossRef]
11. Mahmoodi, S.R.; Xie, P.; Zachs, D.P.; Peterson, E.J.; Graham, R.S.; Kaiser, C.R.W.; Lim, H.H.; Allen, M.G.; Javanmard, M. Single-step label-free nanowell immunoassay accurately quantifies serum stress hormones within minutes. *Sci. Adv.* **2021**, *7*, eabf4401. [CrossRef]
12. Furniturewalla, A.; Chan, M.; Sui, J.; Ahuja, K.; Javanmard, M. Fully integrated wearable impedance cytometry platform on flexible circuit board with online smartphone readout. *Microsyst. Nanoeng.* **2018**, *4*, 20. [CrossRef]
13. Xie, P.; Song, N.; Shen, W.; Allen, M.; Javanmard, M. A ten-minute, single step, label-free, sample-to-answer assay for qualitative detection of cytokines in serum at femtomolar levels. *Biomed. Microdevices* **2020**, *22*, 73. [CrossRef] [PubMed]
14. Kokabi, M.; Donnelly, M.; Xu, G. Benchmarking Small-Dataset Structure-Activity-Relationship Models for Prediction of Wnt Signaling Inhibition. *IEEE Access* **2020**, *8*, 228831–228840. [CrossRef]
15. Cruz, J.A.; Wishart, D.S. Applications of Machine Learning in Cancer Prediction and Prognosis. *Cancer Inform.* **2006**, *2*, 117693510600200030. [CrossRef]
16. Gupta, S.; Tran, T.; Luo, W.; Phung, D.; Kennedy, R.L.; Broad, A.; Campbell, D.; Kipp, D.; Singh, M.; Khasraw, M.; et al. Machine-learning prediction of cancer survival: A retrospective study using electronic administrative records and a cancer registry. *BMJ Open* **2014**, *4*, e004007. [CrossRef]

17. Li, J.; Zhou, Z.; Dong, J.; Fu, Y.; Li, Y.; Luan, Z.; Peng, X. Predicting breast cancer 5-year survival using machine learning: A systematic review. *PLoS ONE* **2021**, *16*, e0250370. [CrossRef]
18. Mccarthy, J.F.; Marx, K.A.; Hoffman, P.E.; Gee, A.G.; O'neil, P.; Ujwal, M.L.; Hotchkiss, J. Applications of machine learning and high-dimensional visualization in cancer detection, diagnosis, and management. *Ann. N. Y. Acad. Sci.* **2004**, *1020*, 239–262. [CrossRef]
19. Galan, E.A.; Zhao, H.; Wang, X.; Dai, Q.; Huck, W.T.; Ma, S. Intelligent Microfluidics: The Convergence of Machine Learning and Microfluidics in Materials Science and Biomedicine. *Matter* **2020**, *3*, 1893–1922. [CrossRef]
20. Raji, H.; Tayyab, M.; Sui, J.; Mahmoodi, S.R.; Javanmard, M. Biosensors and machine learning for enhanced detection, stratification, and classification of cells: A review. *Biomed. Microdevices* **2022**, *24*, 26. [CrossRef]
21. Ashley, B.K.; Sui, J.; Javanmard, M.; Hassan, U. Aluminum Oxide-Coated Particle Differentiation Employing Supervised Machine Learning and Impedance Cytometry. In Proceedings of the 2022 IEEE 17th International Conference on Nano/Micro Engineered and Molecular Systems (NEMS), Taoyuan, Taiwan, 14–17 April 2022.
22. Javanmard, M.; Ahuja, K.; Sui, J.; Bertino, J.R. Use of Multi-Frequency Impedance Cytometry in Conjunction with Machine Learning for Classification of Biological Particles. U.S. Patent Application No. 16/851,580, 2020.
23. Sui, J.; Gandotra, N.; Xie, P.; Lin, Z.; Scharfe, C.; Javanmard, M. Label-free DNA quantification by multi-frequency impedance cytometry and machine learning analysis. In Proceedings of the 21st International Conference on Miniaturized Systems for Chemistry and Life Sciences, MicroTAS 2017, Savannah, GA, USA, 22–26 October 2017; Chemical and Biological Microsystems Society: Basel, Switzerland, 2020.
24. Lin, Z.; Sui, J.; Xie, P.; Ahuja, K.; Javanmard, M. A Two-Minute Assay for Electronic Quantification of Antibodies in Saliva Enabled Through Multi-Frequency Impedance Cytometry and Machine Learning Analysis. In *2018 Solid-State Sensors, Actuators and Microsystems Workshop, Hilton Head 2018*; Transducer Research Foundation: San Diego, CA, USA, 2018.
25. Caselli, F.; Reale, R.; De Ninno, A.; Spencer, D.; Morgan, H.; Bisegna, P. Deciphering impedance cytometry signals with neural networks. *Lab Chip* **2022**, *22*, 1714–1722. [CrossRef]
26. Patel, S.K.; Surve, J.; Parmar, J.; Natesan, A.; Katkar, V. Graphene-Based Metasurface Refractive Index Biosensor For Hemoglobin Detection: Machine Learning Assisted Optimization. *IEEE Trans. NanoBioscience* **2022**, 1. [CrossRef]
27. Schuett, J.; Bojorquez, D.I.S.; Avitabile, E.; Mata, E.S.O.; Milyukov, G.; Colditz, J.; Delogu, L.G.; Rauner, M.; Feldmann, A.; Koristka, S.; et al. Nanocytometer for smart analysis of peripheral blood and acute myeloid leukemia: A pilot study. *Nano Lett.* **2020**, *20*, 6572–6581. [CrossRef] [PubMed]
28. Honrado, C.; Salahi, A.; Adair, S.J.; Moore, J.H.; Bauer, T.W.; Swami, N.S. Automated biophysical classification of apoptotic pancreatic cancer cell subpopulations by using machine learning approaches with impedance cytometry. *Lab Chip* **2022**, *22*, 3708–3720. [CrossRef] [PubMed]
29. Ahuja, K.; Rather, G.M.; Lin, Z.; Sui, J.; Xie, P.; Le, T.; Bertino, J.R.; Javanmard, M. Toward point-of-care assessment of patient response: A portable tool for rapidly assessing cancer drug efficacy using multifrequency impedance cytometry and supervised machine learning. *Microsyst. Nanoeng.* **2019**, *5*, 34. [CrossRef] [PubMed]
30. Feng, Y.; Cheng, Z.; Chai, H.; He, W.; Huang, L.; Wang, W. Neural network-enhanced real-time impedance flow cytometry for single-cell intrinsic characterization. *Lab Chip* **2022**, *22*, 240–249. [CrossRef]
31. Sui, J.; Xie, P.; Lin, Z.; Javanmard, M. Electronic classification of barcoded particles for multiplexed detection using supervised machine learning analysis. *Talanta* **2020**, *215*, 120791. [CrossRef] [PubMed]
32. Nabipour, M.; Nayyeri, P.; Jabani, H.; Shahab, S.; Mosavi, A. Predicting Stock Market Trends Using Machine Learning and Deep Learning Algorithms Via Continuous and Binary Data; A Comparative Analysis. *IEEE Access* **2020**, *8*, 150199–150212. [CrossRef]
33. Zhang, M.; Ye, J.; He, J.-S.; Zhang, F.; Ping, J.; Qian, C.; Wu, J. Visual detection for nucleic acid-based techniques as potential on-site detection methods. A review. *Anal. Chim. Acta* **2020**, *1099*, 1–15. [CrossRef]
34. Nayak, S.C.; Misra, B.B.; Behera, H.S. Impact of data normalization on stock index forecasting. *Int. J. Comput. Inf. Syst. Ind. Manag. Appl.* **2014**, *6*, 257–269.
35. Wong, K.I.; Wong, P.K.; Cheung, C.S.; Vong, C.M. Modeling and optimization of biodiesel engine performance using advanced machine learning methods. *Energy* **2013**, *55*, 519–528. [CrossRef]
36. Eesa, A.S.; Arabo, W.K. A Normalization Methods for Backpropagation: A Comparative Study. *Sci. J. Univ. Zakho* **2017**, *5*, 319–323. [CrossRef]
37. Kumar, S.; Nancy. Efficient K-Mean Clustering Algorithm for Large Datasets using Data Mining Standard Score Normalization. *Int. J. Recent Innov. Trends Comput. Commun.* **2014**, *2*, 3161–3166.
38. Pires, I.M.; Hussain, F.; Garcia, N.M.M.; Lameski, P.; Zdravevski, E. Homogeneous Data Normalization and Deep Learning: A Case Study in Human Activity Classification. *Futur. Internet* **2020**, *12*, 194. [CrossRef]
39. Borkin, D.; Némethová, A.; Michaľčonok, G.; Maiorov, K. Impact of data normalization on classification model accuracy. *Res. Pap. Fac. Mater. Sci. Technol. Slovak Univ. Technol.* **2019**, *27*, 79–84. [CrossRef]
40. Fahami, M.A.; Roshanzamir, M.; Izadi, N.H.; Keyvani, V.; Alizadehsani, R. Detection of effective genes in colon cancer: A machine learning approach. *Inform. Med. Unlocked* **2021**, *24*, 100605. [CrossRef]
41. Kassani, S.H.; Kassani, P.H.; Wesolowski, M.J.; Schneider, K.A.; Deters, R. Classification of Histopathological Biopsy Images Using Ensemble of Deep Learning Networks. *arXiv* **2019**, arXiv:1909.11870.

42. Wong, K.I.; Wong, P.K.; Cheung, C.S.; Vong, C.M. Modelling of diesel engine performance using advanced machine learning methods under scarce and exponential data set. *Appl. Soft Comput.* **2013**, *13*, 4428–4441. [CrossRef]
43. Pedregosa, F.; Varoquaux, G.; Gramfort, A.; Michel, V.; Thirion, B.; Grisel, O.; Blondel, M.; Prettenhofer, P.; Weiss, R.; Dubourg, V.; et al. Scikit-learn: Machine learning in Python. *J. Mach. Learn. Res.* **2011**, *12*, 2825–2830.
44. Liaqat, S.; Dashtipour, K.; Arshad, K.; Assaleh, K.; Ramzan, N. A Hybrid Posture Detection Framework: Integrating Machine Learning and Deep Neural Networks. *IEEE Sens. J.* **2021**, *21*, 9515–9522. [CrossRef]
45. Satu, M.S.; Howlader, K.C.; Mahmud, M.; Kaiser, M.S.; Shariful Islam, S.M.; Quinn, J.M.; Alyamit, S.A.; Moni, M.A. Short-term prediction of COVID-19 cases using machine learning models. *Appl. Sci.* **2021**, *11*, 4266. [CrossRef]
46. Panchal, G.; Ganatra, A.; Kosta, Y.P.; Panchal, D. Behaviour analysis of multilayer perceptrons with multiple hidden neurons and hidden layers. *Int. J. Comput. Theory Eng.* **2011**, *3*, 332–337. [CrossRef]
47. James, B.; Bengio, Y. Random search for hyper-parameter optimization. *J. Mach. Learn. Res.* **2012**, *13*, 281–305.
48. Snoek, J.; Larochelle, H.; Adams, R.P. Practical bayesian optimization of machine learning algorithms. *Adv. Neural Inf. Process. Syst.* **2012**, *2*, 2951–2959.
49. Hasebrook, N.; Morsbach, F.; Kannengießer, N.; Franke, J.; Hutter, F.; Sunyaev, A. Why Do Machine Learning Practitioners Still Use Manual Tuning? A Qualitative Study. *arXiv* **2022**, arXiv:2203.01717.
50. Ying, X. An Overview of Overfitting and its Solutions. *J. Phys. Conf. Ser.* **2019**, *1168*, 022022. [CrossRef]
51. Chieregato, M.; Frangiamore, F.; Morassi, M.; Baresi, C.; Nici, S.; Bassetti, C.; Bnà, C.; Galelli, M. A hybrid machine learning/deep learning COVID-19 severity predictive model from CT images and clinical data. *Sci. Rep.* **2022**, *12*, 4329. [CrossRef] [PubMed]
52. Gavrishchaka, V.; Yang, Z.; Miao, R.; Senyukova, O. Advantages of hybrid deep learning frameworks in applications with limited data. *Int. J. Mach. Learn. Comput.* **2018**, *8*, 549–558.

biosensors

MDPI

Article

Development of Folate-Group Impedimetric Biosensor Based on Polypyrrole Nanotubes Decorated with Gold Nanoparticles

Andrei E. Deller [1], Ana L. Soares [1], Jaqueline Volpe [2], Jean G. A. Ruthes [1], Dênio E. P. Souto [2] and Marcio Vidotti [1,*]

[1] Grupo de Pesquisa em Macromoléculas e Interfaces, Universidade Federal do Paraná (UFPR), Curitiba 81531-980, PR, Brazil
[2] Laboratório de Espectrometria, Sensores e Biossensores, Universidade Federal do Paraná (UFPR), Curitiba 81531-980, PR, Brazil
* Correspondence: mvidotti@ufpr.br

Abstract: In this study, polypyrrole nanotubes (PPy-NT) and gold nanoparticles (AuNPs) were electrochemically synthesized to form a hybrid material and used as an electroactive layer for the attachment of proteins for the construction of a high-performance biosensor. Besides the enhancement of intrinsic conductivity of the PPy-NT, the AuNPs act as an anchor group for the formation of self-assembly monolayers (SAMs) from the gold–sulfur covalent interaction between gold and Mercaptopropionic acid (MPA). This material was used to evaluate the viability and performance of the platform developed for biosensing, and three different biological approaches were tested: first, the Avidin-HRP/Biotin couple and characterizations were made by using cyclic voltammetry (CV) and electrochemical impedance spectroscopy (EIS), wherein we detected Biotin in a linear range of 100–900 fmol L^{-1}. The studies continued with folate group biomolecules, using the folate receptor α (FR-α) as a bioreceptor. Tests with anti-FR antibody detection were performed, and the results obtained indicate a linear range of detection from 0.001 to 6.70 pmol L^{-1}. The same FR-α receptor was used for Folic Acid detection, and the results showed a limit of detection of 0.030 nmol L^{-1} and a limit of quantification of 90 pmol L^{-1}. The results indicate that the proposed biosensor is sensitive and capable of operating in a range of clinical interests.

Keywords: modified electrode; impedimetric biosensor; folate

Citation: Deller, A.E.; Soares, A.L.; Volpe, J.; Ruthes, J.G.A.; Souto, D.E.P.; Vidotti, M. Development of Folate-Group Impedimetric Biosensor Based on Polypyrrole Nanotubes Decorated with Gold Nanoparticles. *Biosensors* **2022**, *12*, 970. https://doi.org/10.3390/bios12110970

Received: 8 October 2022
Accepted: 31 October 2022
Published: 4 November 2022

1. Introduction

The development of electrochemical biosensors has been extensively explored so far. With these devices, the selective detection of low concentrations of different analytes, such as contaminants and biomolecules, is performed in a rapid and straightforward way; in addition, other features are highly desirable, such as low-cost, easy operation, portability, and no need of further analytical steps, as these are key parameters to obtaining an advantageous alternative to the traditional monitoring methods, which are often expensive and also not accessible to the entire population [1,2].

The construction of a high-performance electrochemical biosensor relies on a previous study on the material interface and transduction. Different assemblies of materials and architectures are possible in terms of nanomaterials, metals, and biomolecules to enhance both detection and quantification [3,4]. Special care must be taken on the biomolecule immobilization on the electrode surface, as this experimental step, consisting of the bioreceptor attachment needing to be stable, preserves its conformation and maintains a good orientation to interact with the analyte and provides a reliable signal of recognition [5].

Many different methodologies have been described along the past years [6–8], and in this context, the use of conducting polymers (CPs) and nanoparticles as hybrid synergist materials presents several advantages, not only for biosensors but for any electrochemical-based technology [9–11]. Among CPs, polypyrrole (PPy) plays an important role in electrode modification, as it can be further chemically prepared to attach biomolecules [7,12].

For biosensing, gold nanoparticles (AuNPs) are widely employed, as they present some interesting advantage based on biocompatibility, chemical affinity with sulfur ending molecules, besides the intrinsic metallic conductivity, which represents a rapid and reliable electrochemical transduction signal [13–15]. This last point is a key feature for the development of impedimetric biosensors which presents a remarkable sensitivity of detection; thus, it is possible to obtain trustable results in different stages, even early periods, of any disease [16,17]. Besides that, the impedimetric sensor proposed herein depends greatly on the better accuracy on the measure of the electric resistance of the transducer, so the higher the conductivity, the better will be the analytical parameters.

The folate group molecules have been found to possess different biological functions, such as cellular regulation, DNA synthesis, reparation, and methylation. It is important to adequately maintain the folate levels, as cardiovascular diseases, anemia, embryonic disorders, and various types of cancer are highly related to those levels [18–20]. Mammals do not synthetize folate, so its ingestion as vitamin B9 controls the adequate concentration in organisms [21]. The absorption of folate is performed by three different mediators: the reduced folate carrier (RFC); the proton-coupled folate transporter (PCFT); and the folate-binding proteins (FBPs), e.g., the folate receptor (FR-α) [22,23]. The interaction between FA and FR-α has a high specificity (KD = 10^{-9} mol L^{-1}), so this strong interaction can be explored for the biosensor transduction mechanism. Recent studies indicate that the normal levels of FA in the human serum are around 11.3–34.0 nmol L^{-1}, emphasizing the need for a highly sensitive biosensor [24,25]. In this study, we developed a hybrid nanomaterial formed by polypyrrole nanotubes and gold nanoparticles, electrochemically synthesized in a rapid and straightforward methodology. This modified electrode was employed as a platform to build up the well-known self-assembly monolayer (SAM) based on thiol chemical bonds and the attachment of biomolecules for further detection and quantification, using electrochemical impedance spectroscopy. All steps were properly characterized as well.

2. Materials and Methods

2.1. Reagents and Solutions

All solutions were prepared with ultrapure water (ElgaLab water 18 MΩ cm^{-1}). Pyrrole (PI, Aldrich, San Luis, MO, USA) was distilled before use. Methyl orange (MO, Aldrich), nitric acid (HNO_3, Synth), gold chloride trihydrate (III) ($HAuCl_4.3H_2O$, Aldrich), ethylenediaminetetraacetic acid (EDTA, Aldrich), and potassium chloride (KCl, Aldrich) were used as received, without any further purification step. Mercaptopropionic acid (MPA, Aldrich), N-ethyl-N-(3-dimethylaminopropyl) carbodiimide (EDC, Aldrich), N-hydroxysuccinimide (NHS, Aldrich), and amino acetic acid (Glycine, Aldrich) were kept in a refrigerator at 5 °C. The biological samples, Avidin/Biotin couplings, avidin conjugated with horseradish peroxidase (Avidin-HRP, Abcam, Cambridge, UK), anti-avidin antibody (Biotin, Abcam), recombinant human folate binding protein (FBP, Abcam), and anti-folate binding protein antibody (FBP-Ab, Abcam), were kept in a refrigerator at 5 °C.

2.2. Characterization and Electrochemical Measurements

For the electrochemical experiments, Metrohm DropSens μStat-i 400s potentiostat was employed. The EIS and CV were performed in PBS buffer 0.1 mol L^{-1} at pH 7.4; as the reference electrode, we used $Ag/AgCl/KCl_{sat}$, and platinum wire served as a counter electrode. The working electrode was 316 steel mesh–400 mesh, previously cleaned by immersion in ethanol and ultrapure water. The spectroscopic and microscopic characterizations were performed in UFPR Electronic Microscopy Center (CME-UFPR), with Tescan Vega3 LMU equipment and Transmission Electron Microscopy (MET) with JEOL JEM 1200EX-II equipment with 0.5 nm resolution. All experiments were performed in triplicate to assure homogeneity and reliability of the results.

2.3. Electrode Preparation and Electrochemical Synthesis of PPy/AuNPs

The electrochemical synthesis of PPy nanotubes was performed in aqueous solution containing 100 mmol L^{-1} of pyrrole monomer, methyl orange (MO) 5 mmol L^{-1}, and 8 mmol L^{-1} KNO_3; the pH 3 was adjusted by dropping HNO_3 solution. The electrochemical synthesis was performed over the steel mesh by potentiostatic method, applying 0.8 V over time, controlling the amount of polymer over the mesh with charge control of 0.5 C cm^{-2} [26].

The AuNPs deposition into PPy was performed in a solution of 1.0 mmol L^{-1} $HAuCl_4$, 0.17 mol L^{-1} K_2HPO_4, 0.036 mol L^{-1} Na_2SO_3, and 0.48 mmol L^{-1} EDTA. The chemicals were added in this sequence to avoid the darkening of the solution, due to gold precipitation. The electrodeposition was performed by chronoamperometry, applying −1.1 V vs. $Ag/AgCl/Cl_{-sat}$, with charge control of 300 mC cm^{-2} [27,28].

2.4. Biosensor Construction and Characterization

For biosensor construction, the formation of a favorable environment for the biomolecule immobilization is necessary. Gold has a strong interaction with sulfur, so organic molecules with thiol groups can be easily anchored onto the AuNPs surface by stable covalent bonds [29]. This affinity and stability are explored in SAMs formation, producing an organized and compatible electrode surface for the immobilization of biomolecules.

The methodology for biosensor construction was the same for all the biological systems studied. The modified electrode (PPy/AuNPs) was immersed into MPA 1 mmol L^{-1} aqueous solution for five hours to SAM formation and then was washed in ultrapure water for 15 min. Thus was followed by activation with 100 and 150 mmol L^{-1} EDC:NHS aqueous solution for 20 min. Then it was washed in ultrapure water for 1 min. After activation, the biorecognition element was immobilized by immerging the electrode in a solution of the respective biomolecule for 45 min, followed by a cleansing step in PBS for 15 min. For the complex Avidin/Biotin, both were tested as a bioreceptor in the concentration of 25 μg mL^{-1}. Moreover, in the other two tests evaluated for the folate biomarker, the same bioreceptor was explored: FBP 8 nmol L^{-1}. The next step was blocking unspecific active sites with glycine 100 mmol L^{-1} by submerging the electrode into the glycine solution for 15 min. In Figure 1, the basic steps of the SAM formation are shown.

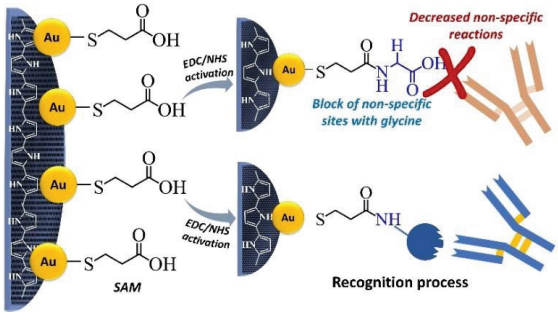

Figure 1. The SAM formation is due to the covalent interaction between gold and sulfur, which makes possible biomolecule immobilization through the carboxylic groups.

The detection of the biomolecule analyte followed the same methodology, where the electrode was immersed in a solution containing the analyte at a known concentration, followed by a washing step in PBS for 5 min before CV and EIS measurements [28,30]. The impedimetric results were modeled by using the proper equivalent circuit and values obtained from NOVA software.

3. Results

3.1. Electrode Modification and Characterizations

The PPy-NT/AuNPs-modified electrodes were characterized by TEM and SEM, as shown in Figure 2. The nanotube morphology is clearly present and fully covered the mesh substrate (Figure 2A,B). The AuNPs can be seen in Figure 2C and in more detail in Figure 2D, using backscattered electron images (Figure 2D); the gold presence was also corroborated by EDS spectrum (Figure A1). The TEM images show individual AuNPs (Figure 2E) with very few nanometers spread along the PPy-NT's surface. Using TEM, it was also possible to verify the filling of the mesh structure with the polymer nanotubes (Figure 2F).

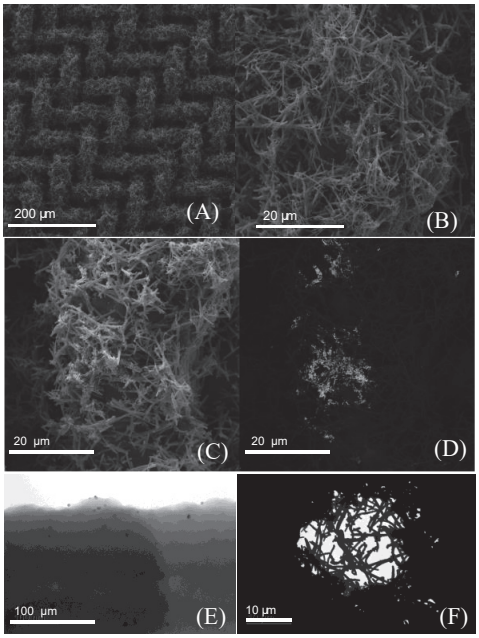

Figure 2. Representative SEM images from the steel mesh coverage: (**A**,**B**) closer approximation of a wire mesh, (**C**) the wire-mesh image of secondary electrons of the hybrid PPy/AuNPs, and (**D**) the SEM with backscattered electrons. (**E**,**F**) TEM representative images from a single nanotube and a small gap in between the steel mash, respectively.

The electrochemical characterization of modified electrodes relies on two fundamental techniques, cyclic voltammetry (CV) and electrochemical impedance spectroscopy (EIS). These two must be studied in consonance to obtain valuable information about the electrode kinetics, adsorption and fouling effects, electron transfer, mass transport effects, steady state conditions, and so on. For EIS studies, it is important to adopt an equivalent circuit model to better understand and quantify different processes at the electrode surface; to date, the Randles modified circuit is very common in the study of conductive-polymer-modified electrodes [31,32]. For the biosensor proposed herein, the main information obtained by the EIS technique is associated with the biomolecule interaction, such as antigen–antibody, a so-called affinity interaction caused by the changes at the interface of the electrochemical active material, in terms of both charge transfer and double-layer effects [1,5,31].

Electrochemical experiments of CV and EIS were performed to characterize and compare the proprieties between PPy-NTs- and PPy-NTs/AuNPs-modified electrodes. Figure 3A shows the CVs for each modified electrode, and it is possible to observe an increment in the current in the presence of AuNPs. It is important to note that no addi-

tional redox processes are observed; there is solely an increment of the capacitive current, indicating an increase of the electroactive surface provoked by the exposure of a large area of the AuNPs. Figure 3B shows the Nyquist plots of the modified electrodes; they show a traditional semicircle response that is characteristic of conducting polymers. Clearly there is a drastic decrease in the semicircle radius in the presence of AuNPs; in general lines, this behavior indicates an increase in the electroactivity of the interface, thus corroborating the presence of a metallic structure on a polymeric matrix. The equivalent circuit used to fit the electrochemical parameters is found in Figure 3C; they can be summarized as follows: the Q_{DL} parameter is related to the energy of the double layer at the interface electrode/electrolyte, the R_{CT} is the resistance of the charge transfer at the electrode surface, R_S is the resistance of the solution, and Q_{LF} deals with the number of interacted ions inserted within the polymeric matrix.

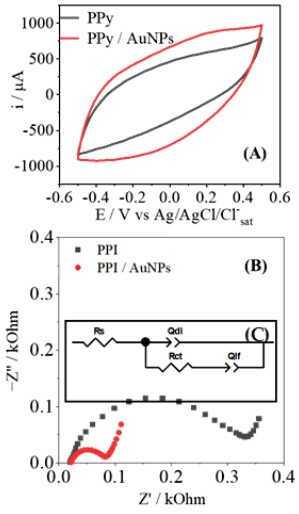

Figure 3. (**A**) CV for the electrodes modified with just PPy (black) and PPy/AuNPs (red). The Nyquist plot is shown in (**B**) from electrodes modified with PPy (black) and with PPy/AuNPs (red). The equivalent circuit used to model the EIS results is also inserted as (**C**).

The experimental results obtained in Figure 3B were modeled according to the equivalent circuit shown in Figure 3C; the results are shown in Table 1. As discussed previously, there is a significant improvement in the charge transfer in the polymer/electrode interface with the AuNPs, as indicated by the lower value of R_{CT}. It is important to add that the presence of a metallic particle itself contributes to the increment of conductivity of the PPy-NTs, and this also facilitates any electron transfer at the surface. Due to the high superficial area of AuNPs, the Q_{DL} value shows an increment of almost 2.5 times, in agreement with the increase that the capacitive current showed in CV. At a low frequency, the Q_{LF} value had no significant variations, indicating that the intercalation of charges in the polymeric matrix is not affected by the presence of AuNPs; this seems reasonable, as the amount of polymer was kept the same, at the same cutoff charge. Regarding the morphology, after the AuNPs' deposition, it was possible to observe a decrease in the n_{DL} and n_{LF} parameters, which represent the escape from ideality of a traditional parallel capacitor, which represents $n = 1$; thus, the further away it is from the unity, the rougher the surface is present at the electrode surface [33,34].

Table 1. Parameters' values obtained by EIS to PPy e PPy/AuNPs, obtained from fitting of EIS results, $R^2 > 0.99$. The equivalent circuit was modeled by the NOVA software.

	$R_S/k\Omega$	Q_{DL} 10^{-5} F s^{n-1}	n_{DL}	$R_{CT}/k\Omega$	Q_{LF} 10^{-3} F s^{n-1}	n_{LF}
PPy-NTs	0.04	1.89	0.82	0.25	3.60	0.83
PPy-NTs/AuNPs	0.03	4.27	0.76	0.05	6.70	0.77

3.2. Functionalized Steel Mesh Electrode (PPy/AuNPs/MPA) for Biosensing Applications

Avidin-HRP/Biotin Complex: A Model System

The steps of the biosensor construction were characterized electrochemically by CV and EIS, as shown in Appendix A Figures A1 and A2, where the blocking of the surface can be easily identified. The availability for the attachment of biomolecules was performed by the Avidin-HRP protein to detect Biotin, as a well-known system, possessing a very strong interaction. Avidin is a basic tetrameric glycoprotein composed of four identical subunits, and each of these subunits can bind to Biotin with high stability and affinity, being one of nature's strongest non-covalent interactions (dissociation constant = 10^{-15} mol L^{-1}). Thus, this interaction can be used to verify the effectiveness of the modified electrode, as shown elsewhere [35,36].

In Figure 4A, it is shown how the concentration of Biotin affects the voltammetric response of the electrode. The voltammogram just after the blocking of glycine is shown for the sake of comparison, as no Biotin is added. Clearly the CVs present a diminishment of the current response, indicating the adsorption of Biotin at the electrode surface, where some active sites are no longer available. This effect is also observed in the Nyquist plots (Figure 4B), with the change of the R_{CT} parameter, as observed in other contributions [28,37]. As the concentration of the insulating Biotin increases, more electroactive sites are being hindering, so there is the increment of the resistance of any potential redox reaction; since this behavior is related to the amount of analyte, a proper analytical curve can be drawn, as shown. The EIS results of Figure 4B were modeled, as mentioned before, and the results are shown in Table 2. Besides the variation of the R_{CT}, the Q_{DL} parameter also changes, indicating that the double layer is also affected by the presence of Biotin, corroborating the strong adsorption at the electrode's surface. The other parameters have shown no drastic changes, and this outcome is in consonance with no redox reactions promoted by the PPy-NT electrodes.

Table 2. Parameters' values obtained by EIS to PPy e PPy/AuNPs after fitting, $R^2 > 0.98$.

	Glycine	**Biotin Concentration (fmol L^{-1})**				
		100	**300**	**500**	**700**	**900**
$R_S/k\Omega$	0.05	0.03	0.06	0.12	0.04	0.06
$Q_{DL}/10^{-5}$F s^{n-1}	2.36	2.96	2.63	3.06	2.37	3.38
n_{DL}	0.87	0.84	0.85	0.80	0.86	0.81
$R_{CT}/k\Omega$	0.16	0.48	1.11	1.31	2.11	2.56
$Q_{LF}/10^{-3}$ F s^{n-1}	4.6	4.6	5.35	4.37	5.17	4.83
n_{LF}	0.80	0.81	0.90	0.84	0.91	0.86

These results obtained with the avidin/biotin biological system indicate the interesting behavior of PPy-NTs/AuNPs-modified electrodes for the construction of biosensors based on electrochemical response, as is later discussed.

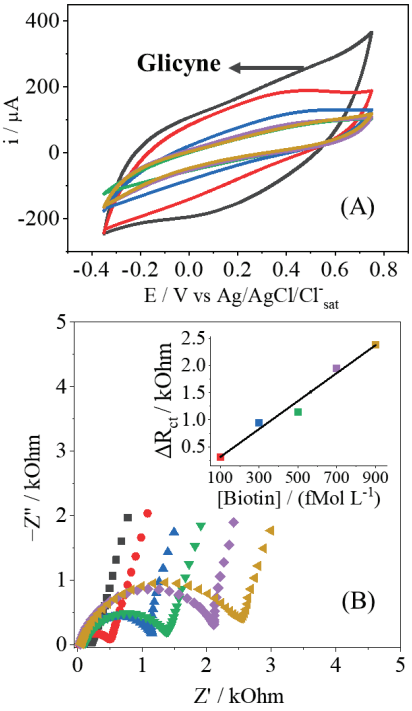

Figure 4. Cyclic voltammetry (**A**) and Nyquist plot (**B**) of the EIS measurement to Biotin detection (100 up to 900 fmol L^{-1}) indicated by colors in both CV and EIS.

3.3. Biosensor for Folate Detection from the Disposable Electrode Modified by PPy/AuNPs/MPA

3.3.1. Biofunctionalization Step: Recombinant Human Folate Binding Protein (FBP, Abcam) as Recognition Element

After the interesting results presented by the PPy-NTs/AuNPs electrodes for the Avidin/Biotin biomolecules, the same platform was used for the construction of FBP-Ab/FBP biosensor. In the same perspective observed in Figure 4, the CV and EIS responses in the presence of FBP-Ab are shown in Figure 5, and a similar behavior was found, indicating that the same effects of strong interaction and adsorption are occurring.

To test the stability of the recognition process, several measurements of EIS were performed for the same antibody concentration, as shown in Figure 5C and Tables A1 and A2. After immersion in FBP-Ab, five measurements in a row were performed, applying analysis of variance (ANOVA) with 95% confidence. The R_{CT} parameter showed no significant difference, maintaining the confidence in the analytical response; this point is related to the strong interaction between the biosensor and analyte, with no desorption of the FBP-Ab from the electrode's surface [38].

We also tested and proved that the glycine blocking step is crucial. It is already known that the adsorption of biomolecules in conductive polymers can cause non-specific interactions on the electrode's surface, interfering with the signal [39]. We performed a test shown in Appendix A Figure A3, where we verified that, without a blocking step, it is possible to have nonspecific antibody adsorption on the polymer matrix, which directly interferes with the signal.

3.3.2. Detection Step: Determination of Femtomolar Concentrations of Folic Acid

Finally, the FBP/Folic Acid biosensor was assembled on the PPy-NT/AuNPs platform, all electrochemical experiments were the same ones descried earlier for the detection of the analyte. Folic Acid has a great affinity for FBP, and the impedimetric response is found

in Figure 6, in the concentration range from 0.02 up to 113.3 nmol L^{-1}, in triplicate. The analytical curve was inserted; the limit of detection (LOD) was calculated as 0.030 nmol L^{-1}, and the limit of quantification (LOQ) was 0.090 nmol L^{-1}, indicating that the proposed biosensor herein can detect and quantify the range of concentration of clinical interest, which is around 11 up to 34 nmol L^{-1} [24,25]. As this biomarker can be found as a group of molecules, many different configurations of biosensors based on folate can be found in the literature, and the simple comparison between analytical parameters is not always easy to study. Nonetheless, in Table 3, different information is presented to better analyze the recent development in this issue.

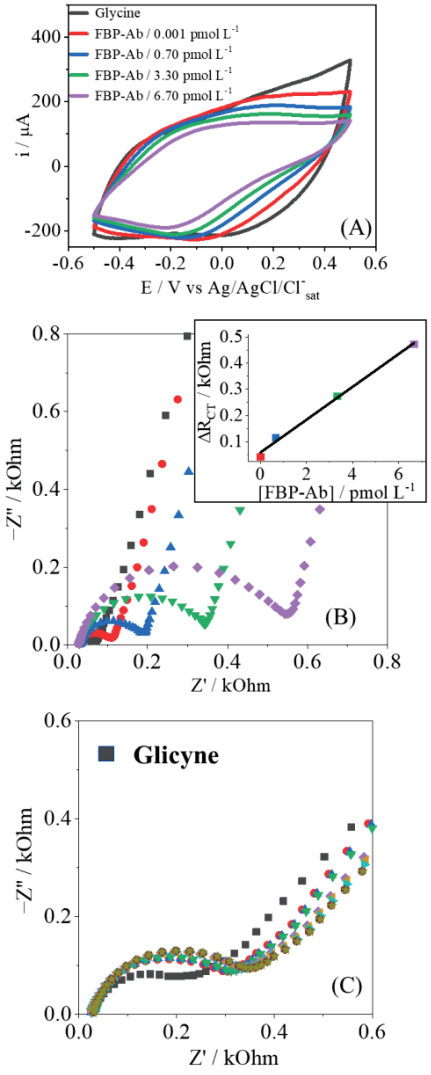

Figure 5. Cyclic voltammetry (**A**) and Nyquist plot (**B**) to FBP-Ab detection (0.001 up to 6.70 pmol L^{-1}); (**C**) the EIS response in stability test to 0.001 pmol L^{-1} of FBP-Ab. The gray measurement was performed in the blank step, while the others correspond to the same antibody concentration.

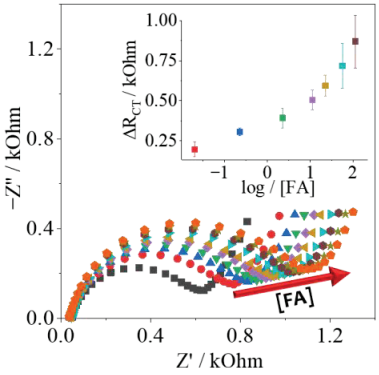

Figure 6. Folic Acid detection (0.02 up to 113.3 nmol L^{-1}) using the PPy/AuNPs-modified electrode.

Table 3. Comparison between experimental conditions and LOD values between different biosensors for FA detection.

Material	Detection Method	Concentration Range (nmol L^{-1})	LOD (nmol L^{-1})	Reference
Steel mesh covered by PPy/AuNPs	EIS	0.02–113.3	0.030	This work
Gold/PPy/POM	Cyclic voltammetry	0.01–1	0.0075	[40]
Gold electrode modified with SAM	Square wave voltammetry	0.008–1	0.004	[41]
Hydroxyapatite NPs/GCE	Differential pulse voltammetry	0.1–350	0.075	[42]
Platinum NPs/MWCNT/GCE	Linear voltammetry	0.2–100	0.05	[43]
MoS_2/rGO/GCE	Differential pulse voltammetry	0.1–100	0.01	[44]
Boron doped diamond electrode	Stripping voltammetry	0.23–45	0.08	[45]
PPy-modified sol–gel carbon ceramic	Differential pulse voltammetry	7–55	1.8	[46]
Chromatographic column	HPLC/UV–Vis	0.3–100	44.14	[42]
SPCE/GO	Amperometry	100–1.6 × 10^6	20	[43]
SPCE/SWCNT	Square wave voltammetry	70–500 × 10^3	800	[46]

4. Conclusions

The electrode modification with PPy-NTs/AuNPs has shown to be rapid, straightforward, and reliable for the construction of biosensors. This hybrid material was used as a platform for SAM layers, followed by the anchoring of different biomolecules, indicating a potential application in different types of biosensors and recognition elements. All characterization experiments corroborated the influence of the nanometric architecture on the electrochemical response for the detection and quantification of different analytes, with the R_{CT} parameter showing the most sensible response for the biological recognition of the biological markers. The nanostructures also are responsible for the possibility of detection in the range of femtomolar to picomolar, corroborating the great sensitivity achieved by the combination of the nanostructures, specific adsorption, and impedance technique.

Author Contributions: Conceptualization, A.E.D., J.V. and A.L.S.; methodology, A.E.D. and J.V.; validation, A.E.D. and A.L.S.; investigation, A.E.D., J.V., D.E.P.S. and M.V.; data curation, A.E.D., J.V. and J.G.A.R.; writing—original draft preparation, A.E.D.; J.V. and D.E.P.S.; writing—review and editing, A.E.D. and M.V.; supervision, D.E.P.S. and M.V.; project administration, D.E.P.S. and M.V.; funding acquisition, D.E.P.S. and M.V. All authors have read and agreed to the published version of the manuscript.

Funding: This research was funded by CAPES (Finance Code 001), FAPESP (grant no. 2014/50867-3), and CNPq (grant no. 465389/2014-7).

Institutional Review Board Statement: Not applicable.

Informed Consent Statement: Not applicable.

Acknowledgments: The authors would like to thank Centro de Microscopia Eletrônica da UFPR for microscopic analysis.

Conflicts of Interest: The funders had no role in the design of the study; in the collection, analyses, or interpretation of data; in the writing of the manuscript; or in the decision to publish the results.

Appendix A

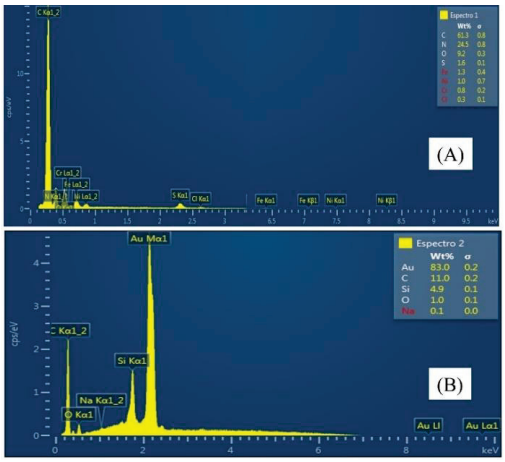

Figure A1. EDS spectra were obtained for the characterization of the electrode modified with PPy (**A**) and the electrode modified with PPy/AuNPs (**B**).

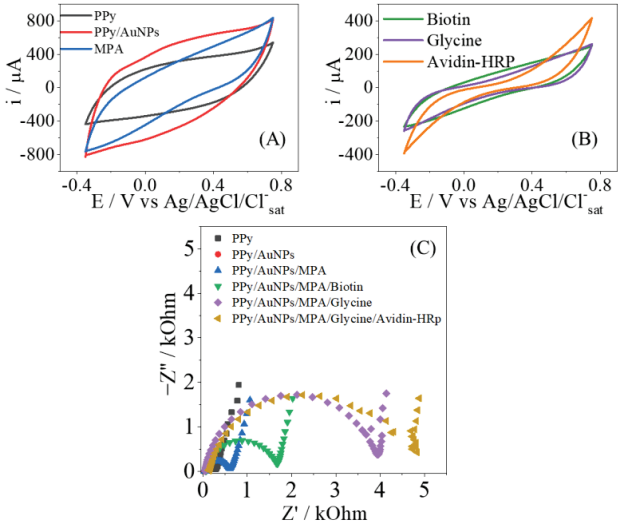

Figure A2. Characterization of the PPy/AuNPs-based biosensor construction steps for the Avidin-HRP/Biotin couple. Cyclic voltammograms (**A**,**B**) show the characterization of different steps in the construction of the platform-based biosensor, and the Nyquist diagram (**C**) is for the same characterization.

Table A1. Parameters' values obtained by EIS to PPy e PPy/AuNPs, in electrode modification steps.

Parameter	MPA	Biotin	Glycine	Avidin-HRP
$R_S/k\Omega$	0.05	0.07	0.05	0.14
$Q_{DL}/10^{-5}F\ s^{n-1}$	1.87	1.88	1.61	2.43
n_{DL}	0.90	0.90	0.91	0.85
$R_{CT}/k\Omega$	0.56	1.62	3.95	4.67
$Q_{LF}/10^{-3}\ F\ s^{n-1}$	5.80	6.70	8.06	8.99
n_{LF}	0.81	0.87	0.96	0.97

Table A2. Parameters' values obtained by EIS to PPy e PPy/AuNPs for stabilization tests using 0.001 pmol L^{-1}.

	Glycine	EIS Measurements to FBP-Ab to 0.001 pmol L^{-1}							
R_{CT} (Ohm)	206.3	283.3	288.2	291.2	312.7	309.3	312.3	315.8	318.2

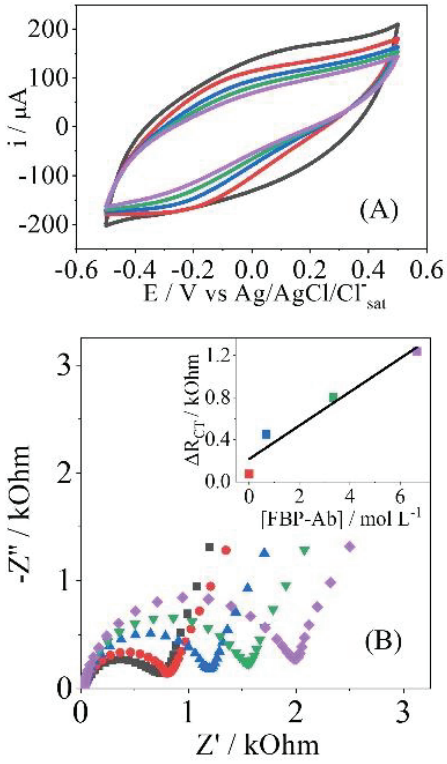

Figure A3. Adsorption test of different antibody concentrations (0.001, 0.67, 3.30, and 6.60 pmol L^{-1}), using a modified electrode only with PPy. Cyclic voltammograms (**A**), Nyquist diagram (**B**).

References

1. Islam, M.N.; Channon, R.B. Electrochemical sensors. In *Bioengineering Innovative Solutions for Cancer*; Ladame, S., Chang, J.Y.H., Eds.; Elsevier: Amsterdam, The Netherlands, 2020; pp. 47–71, ISBN 978-0-12-813886-1.
2. Abdul Ghani, M.A.; Nordin, A.N.; Zulhairee, M.; Che Mohamad Nor, A.; Shihabuddin Ahmad Noorden, M.; Muhamad Atan, M.K.F.; Ab Rahim, R.; Mohd Zain, Z. Portable Electrochemical Biosensors Based on Microcontrollers for Detection of Viruses: A Review. *Biosensors* **2022**, *12*, 666. [CrossRef] [PubMed]
3. Adarakatti, P.S.; Kempahanumakkagari, S.K. Modified electrodes for sensing. In *Electrochemistry*; The Royal Society of Chemistry: London, UK, 2019; pp. 58–95.

4. Baig, N.; Rana, A.; Kawde, A.-N. Modified Electrodes for Selective Voltammetric Detection of Biomolecules. *Electroanalysis* **2018**, *30*, 2551–2574. [CrossRef]
5. Sandhyarani, N. Surface modification methods for electrochemical biosensors. In *Electrochemical Biosensors*; Ensafi, A.A., Ed.; Elsevier: Amsterdam, The Netherlands, 2019; pp. 45–75, ISBN 978-0-12-816491-4.
6. Nemiwal, M.; Zhang, T.C.; Kumar, D. Enzyme Immobilized Nanomaterials as Electrochemical Biosensors for Detection of Biomolecules. *Enzym. Microb Technol.* **2022**, *156*, 110006. [CrossRef] [PubMed]
7. Suni, I.I. Substrate Materials for Biomolecular Immobilization within Electrochemical Biosensors. *Biosensors* **2021**, *11*, 239. [CrossRef]
8. Holzinger, M.; Buzzetti, P.H.M.; Cosnier, S. Polymers and Nano-Objects, a Rational Combination for Developing Health Monitoring Biosensors. *Sens. Actuators B Chem.* **2021**, *348*, 130700. [CrossRef]
9. Wang, Y.; Liu, A.; Han, Y.; Li, T. Sensors Based on Conductive Polymers and Their Composites: A Review. *Polym. Int.* **2020**, *69*, 7–17. [CrossRef]
10. Kaur, G.; Kaur, A.; Kaur, H. Review on Nanomaterials/Conducting Polymer Based Nanocomposites for the Development of Biosensors and Electrochemical Sensors. *Polym.-Plast. Technol. Mater.* **2020**, 1–18. [CrossRef]
11. Kim, J.; Park, M. Recent Progress in Electrochemical Immunosensors. *Biosensors* **2021**, *11*, 360. [CrossRef] [PubMed]
12. Qing, Y.; Yang, Y.; Ouyang, P.; Fang, C.; Fang, H.; Liao, Y.; Li, H.; Wang, Z.; Du, J. Gold Nanoparticle-Based Enzyme-Assisted Cyclic Amplification for the Highly-Sensitive Detection of MiRNA-21. *Biosensors* **2022**, *12*, 724. [CrossRef]
13. Singh, S.; Gill, A.A.S.; Nlooto, M.; Karpoormath, R. Prostate Cancer Biomarkers Detection Using Nanoparticles Based Electrochemical Biosensors. *Biosens. Bioelectron.* **2019**, *137*, 213–221. [CrossRef]
14. Montoro-Leal, P.; Frías, I.A.M.; Vereda Alonso, E.; Errachid, A.; Jaffrezic-Renault, N. A Molecularly Imprinted Polypyrrole/GO@Fe3O4 Nanocomposite Modified Impedimetric Sensor for the Routine Monitoring of Lysozyme. *Biosensors* **2022**, *12*, 727. [CrossRef] [PubMed]
15. O'Connor, C.; Wallace-Povirk, A.; Ning, C.; Frühauf, J.; Tong, N.; Gangjee, A.; Matherly, L.H.; Hou, Z. Folate Transporter Dynamics and Therapy with Classic and Tumor-Targeted Antifolates. *Sci. Rep.* **2021**, *11*, 6389. [CrossRef] [PubMed]
16. Boss, S.D.; Ametamey, S.M. Development of Folate Receptor−Targeted PET Radiopharmaceuticals for Tumor Imaging—A Bench-to-Bedside Journey. *Cancers* **2020**, *12*, 1508. [CrossRef] [PubMed]
17. Bobrowski-Khoury, N.; Ramaekers, V.T.; Sequeira, J.M.; Quadros, E.V. Folate Receptor Alpha Autoantibodies in Autism Spectrum Disorders: Diagnosis, Treatment and Prevention. *J. Pers. Med.* **2021**, *11*, 710. [CrossRef] [PubMed]
18. Miller, J.W. Folic acid. In *Encyclopedia of Human Nutrition*; Elsevier: Amsterdam, The Netherlands, 2013; pp. 262–269.
19. Bailey, L.B.; Caudill, M.A. Folate. In *Present Knowledge in Nutrition*; Wiley: Oxford, UK, 2012; pp. 321–342.
20. Scaranti, M.; Cojocaru, E.; Banerjee, S.; Banerji, U. Exploiting the Folate Receptor α in Oncology. *Nat. Rev. Clin. Oncol.* **2020**, *17*, 349–359. [CrossRef]
21. Müller, C.; Schibli, R. Prospects in Folate Receptor-Targeted Radionuclide Therapy. *Front. Oncol.* **2013**, *3*, 249. [CrossRef]
22. Batra, B.; Narwal, V.; Kalra, V.; Sharma, M.; Rana, J. Folic Acid Biosensors: A Review. *Process Biochem.* **2020**, *92*, 343–354. [CrossRef]
23. Hryniewicz, B.M.; Lima, R.V.; Wolfart, F.; Vidotti, M. Influence of the PH on the Electrochemical Synthesis of Polypyrrole Nanotubes and the Supercapacitive Performance Evaluation. *Electrochim. Acta* **2019**, *293*, 447–457. [CrossRef]
24. Colombo, R.N.P.; Petri, D.F.S.; Córdoba De Torresi, S.I.; Gonçales, V.R. Porous Polymeric Templates on ITO Prepared by Breath Figure Method for Gold Electrodeposition. *Electrochim. Acta* **2015**, *158*, 187–195. [CrossRef]
25. Soares, A.L.; Hryniewicz, B.M.; Deller, A.E.; Volpe, J.; Marchesi, L.F.; Souto, D.E.P.; Vidotti, M. Electrodes Based on PEDOT Nanotubes Decorated with Gold Nanoparticles for Biosensing and Energy Storage. *ACS Appl. Nano. Mater.* **2021**, *4*, 9945–9956. [CrossRef]
26. Singh, M.; Kaur, N.; Comini, E. The Role of Self-Assembled Monolayers in Electronic Devices. *J. Mater. Chem. C Mater.* **2020**, *8*, 3938–3955. [CrossRef]
27. Souto, D.E.P.; Silva, J.V.; Martins, H.R.; Reis, A.B.; Luz, R.C.S.; Kubota, L.T.; Damos, F.S. Development of a Label-Free Immunosensor Based on Surface Plasmon Resonance Technique for the Detection of Anti-Leishmania Infantum Antibodies in Canine Serum. *Biosens. Bioelectron.* **2013**, *46*, 22–29. [CrossRef] [PubMed]
28. Bertok, T.; Lorencova, L.; Chocholova, E.; Jane, E.; Vikartovska, A.; Kasak, P.; Tkac, J. Electrochemical Impedance Spectroscopy Based Biosensors: Mechanistic Principles, Analytical Examples and Challenges towards Commercialization for Assays of Protein Cancer Biomarkers. *ChemElectroChem* **2019**, *6*, 989–1003. [CrossRef]
29. Soares, A.L.; Zamora, M.L.; Marchesi, L.F.; Vidotti, M. Adsorption of Catechol onto PEDOT Films Doped with Gold Nanoparticles: Electrochemical and Spectroscopic Studies. *Electrochim. Acta* **2019**, *322*, 134773. [CrossRef]
30. Gonçalves, R.; Pereira, E.; Marchesi, L. The Overoxidation of Poly(3-Hexylthiophene) (P3HT) Thin Film: CV and EIS Measurements. *Int. J. Electrochem. Sci.* **2017**, *12*, 1983–1991. [CrossRef]
31. Wolfart, F.; Hryniewicz, B.M.; Góes, M.S.; Corrêa, C.M.; Torresi, R.; Minadeo, M.A.O.S.; Córdoba de Torresi, S.I.; Oliveira, R.D.; Marchesi, L.F.; Vidotti, M. Conducting Polymers Revisited: Applications in Energy, Electrochromism and Molecular Recognition. *J. Solid State Electrochem.* **2017**, *21*, 2489–2515. [CrossRef]
32. Samanta, D.; Sarkar, A. Immobilization of Bio-Macromolecules on Self-Assembled Monolayers: Methods and Sensor Applications. *Chem. Soc. Rev.* **2011**, *40*, 2567–2592. [CrossRef]
33. Bănică, F. Affinity-based recognition. In *Chemical Sensors and Biosensors*; John Wiley & Sons: Hoboken, NJ, USA, 2012; pp. 101–117.

34. Bănică, F. Electrical-impedance-based sensors. In *Chemical Sensors and Biosensors*; John Wiley & Sons: Hoboken, NJ, USA, 2012; pp. 367–403.
35. Battistel, A.; Fan, M.; Stojadinović, J.; la Mantia, F. Analysis and Mitigation of the Artefacts in Electrochemical Impedance Spectroscopy Due to Three-Electrode Geometry. *Electrochim. Acta* **2014**, *135*, 133–138. [CrossRef]
36. Teles, F.R.R.; Fonseca, L.P. Applications of Polymers for Biomolecule Immobilization in Electrochemical Biosensors. *Mater. Sci. Eng. C* **2008**, *28*, 1530–1543. [CrossRef]
37. Babakhanian, A.; Kaki, S.; Ahmadi, M.; Ehzari, H.; Pashabadi, A. Development of α-Polyoxometalate–Polypyrrole–Au Nanoparticles Modified Sensor Applied for Detection of Folic Acid. *Biosens. Bioelectron.* **2014**, *60*, 185–190. [CrossRef]
38. Wan, Q.; Yang, N. The Direct Electrochemistry of Folic Acid at a 2-Mercaptobenzothiazole Self-Assembled Gold Electrode. *J. Electroanal. Chem.* **2002**, *527*, 131–136. [CrossRef]
39. Kanchana, P.; Sekar, C. Development of Electrochemical Folic Acid Sensor Based on Hydroxyapatite Nanoparticles. *Spectrochim. Acta A Mol. Biomol. Spectrosc.* **2015**, *137*, 58–65. [CrossRef] [PubMed]
40. Kun, Z.; Ling, Z.; Yi, H.; Ying, C.; Dongmei, T.; Shuliang, Z.; Yuyang, Z. Electrochemical Behavior of Folic Acid in Neutral Solution on the Modified Glassy Carbon Electrode: Platinum Nanoparticles Doped Multi-Walled Carbon Nanotubes with Nafion as Adhesive. *J. Electroanal. Chem.* **2012**, *677–680*, 105–112. [CrossRef]
41. Chekin, F.; Teodorescu, F.; Coffinier, Y.; Pan, G.-H.; Barras, A.; Boukherroub, R.; Szunerits, S. MoS2/Reduced Graphene Oxide as Active Hybrid Material for the Electrochemical Detection of Folic Acid in Human Serum. *Biosens. Bioelectron.* **2016**, *85*, 807–813. [CrossRef]
42. Yardim, Y.; Şentürk, Z. Electrochemical Behavior of Folic Acid at A Boron-Doped Diamond Electrode: Its Adsorptive Stripping Voltammetric Determination in Tablets. *Turk J. Pharm. Sci.* **2012**, *11*, 87–100.
43. Majidi, M.R.; Dastangoo, H.; Hasannejad, M.; Malakouti, J. Voltammetric Determination of Folic Acid with a Overoxidized Polypyrrole Film Modified Sol-Gel Carbon Ceramic Electrode. *Int. J. Polym. Anal. Charact.* **2011**, *16*, 486–495. [CrossRef]
44. Jastrebova, J.; Witthöft, C.; Grahn, A.; Svensson, U.; Jägerstad, M. HPLC Determination of Folates in Raw and Processed Beetroots. *Food Chem.* **2003**, *80*, 579–588. [CrossRef]
45. Mani, V. Highly Sensitive Determination of Folic Acid Using Graphene Oxide Nanoribbon Film Modified Screen Printed Carbon Electrode. *Int. J. Electrochem. Sci.* **2017**, *12*, 475–484. [CrossRef]
46. Karimi-Maleh, H.; Hatami, M.; Moradi, R.; Khalilzadeh, M.A.; Amiri, S.; Sadeghifar, H. Synergic Effect of Pt-Co Nanoparticles and a Dopamine Derivative in a Nanostructured Electrochemical Sensor for Simultaneous Determination of N-Acetylcysteine, Paracetamol and Folic Acid. *Microchim. Acta* **2016**, *183*, 2957–2964. [CrossRef]

biosensors

MDPI

Article

Hyaluronic Acid Methacrylate Hydrogel-Modified Electrochemical Device for Adsorptive Removal of Lead(II)

Nan Wang [1,2,*], Meghali Bora [2], Song Hao [3,*], Kai Tao [4], Jin Wu [5], Liangxing Hu [6], Jianjun Liao [7], Shiwei Lin [8], Michael S. Triantafyllou [2,9] and Xiaogan Li [1]

1 School of Microelectronics, Dalian University of Technology, Dalian 116024, China
2 Center for Environmental Sensing and Modeling (CENSAM) IRG, Singapore-MIT Alliance for Research and Technology (SMART) Centre, Singapore 138602, Singapore
3 School of Optoelectronic Engineering and Instrumentation Science, Dalian University of Technology, Dalian 116024, China
4 Ministry of Education Key Laboratory of Micro and Nano Systems for Aerospace, School of Mechanical Engineering, Northwestern Polytechnical University, Xi'an 710072, China
5 State Key Laboratory of Optoelectronic Materials and Technologies and the Guangdong Province Key Laboratory of Display Material and Technology, School of Electronics and Information Technology, Sun Yat-sen University, Guangzhou 510275, China
6 School of Electrical and Electronic Engineering, Nanyang Technological University, Singapore 639798, Singapore
7 Key Laboratory of Agro-Forestry Environmental Processes and Ecological Regulation of Hainan Province, School of Ecological and Environmental Sciences, Hainan University, Haikou 570228, China
8 School of Materials Science and Engineering, Hainan University, Haikou 570228, China
9 Department of Mechanical Engineering, Massachusetts Institute of Technology, Cambridge, MA 02139, USA
* Correspondence: wang_nan@dlut.edu.cn (N.W.); hao@dlut.edu.cn (S.H.)

Abstract: This paper presents the development of a compact, three-electrode electrochemical device functionalized by a biocompatible layer of hyaluronic acid methacrylate (HAMA) hydrogel for the adsorptive removal of detrimental lead (Pb(II)) ions in aqueous solutions. An adsorption mechanism pertaining to the observed analytical performance of the device is proposed and further experimentally corroborated. It is demonstrated that both the molecular interactions originating from the HAMA hydrogel and electrochemical accumulation originating from the electrode beneath contribute to the adsorption capability of the device. Infrared spectral analysis reveals that the molecular interaction is mainly induced by the amide functional group of the HAMA hydrogel, which is capable of forming the Pb(II)–amide complex. In addition, inductively coupled plasma mass spectrometric (ICP-MS) analysis indicates that the electrochemical accumulation is particularly valuable in facilitating the adsorption rate of the device by maintaining a high ion-concentration gradient between the solution and the hydrogel layer. ICP-MS measurements show that 94.08% of Pb(II) ions present in the test solution can be adsorbed by the device within 30 min. The HAMA hydrogel-modified electrochemical devices exhibit reproducible performance in the aspect of Pb(II) removal from tap water, with a relative standard deviation (RSD) of 1.28% (for $n = 8$). The experimental results suggest that the HAMA hydrogel-modified electrochemical device can potentially be used for the rapid, on-field remediation of Pb(II) contamination.

Keywords: electrochemical device; hyaluronic acid methacrylate hydrogel; metal ion–amide complexation; electrochemical accumulation; lead removal

Citation: Wang, N.; Bora, M.; Hao, S.; Tao, K.; Wu, J.; Hu, L.; Liao, J.; Lin, S.; Triantafyllou, M.S.; Li, X. Hyaluronic Acid Methacrylate Hydrogel-Modified Electrochemical Device for Adsorptive Removal of Lead(II). *Biosensors* **2022**, *12*, 714. https://doi.org/10.3390/bios12090714

Received: 25 July 2022
Accepted: 31 August 2022
Published: 2 September 2022

1. Introduction

Water contamination caused by toxic heavy metals has always been one of the greatest threats to public health due to the aversion of heavy metals to natural degradation. Such non-biodegradable properties enable heavy metals to move along the food chain, which eventually accumulate inside the human body, resulting in severe detrimental effects on

human health. Among the different kinds of heavy metals, lead (Pb(II)) is considered the most hazardous contaminant owing to its strong toxicity. For instance, Pb(II) is capable of restraining the formation of hemoglobin, which is an essential component of red blood cells [1,2]. Other pathological symptoms, such as abdominal pain, arthralgia, anemia, and cognitive deficit, may also occur when exposure rises to a certain limit [3]. More worryingly, the intake of Pb(II) may cause permanent learning and behavioral disorders in infants and children [4–6]. Hence, the development of devices to detect Pb(II) has been of considerable interest to both academia and industry. Over the past decade, many researchers have reported a variety of successfully designed chemical/electrochemical [7–10], fluorescent [11–13], as well as biological devices [14–16] for Pb(II) detection. However, research on developing compact devices for the removal of Pb(II) is still scanty, although the importance of this research area has been reiterated in recent years because of the water crisis [17].

Conventional approaches to achieving the removal of Pb(II) from aqueous solutions include adsorption, chemical precipitation, ion exchange, reverse osmosis, coagulation, and membrane filtration. Among all these approaches, adsorption has proved to be the most practical method due to its simplicity of design and operation, high efficiency, and economical advantage [18–20]. Different kinds of polymer materials, such as poly(pyrrole methane) [21], poly(allylamine-co-methacrylamide-co-acrylic acid) [22], poly(*N*,*N*-dimethylacrylamide-co-2-hydroxyethyl methacrylate) [23], poly(acrylamide-co-itaconic acid) [24], melamine-formaldehyde-diaminohexane [25], poly(*trans*-aconitic acid/2-hydroxyethyl acrylate) [26], polyisoprene-*b*-polystyrene-*b*-poly(*N*,*N*-dimethylacrylamide) [27], nanochitosan/polyurethane/polypropylene glycol [28], etc., have been functionalized or directly utilized as effective adsorbents. Hyaluronic acid (HA), a carbohydrate polymer with repeated disaccharide units of glucuronic acid and N-acetylglucosamine alternatively linked by β-1,3 and β-1,4 glycosidic bonds, is widely present inside the human body (e.g., muscular connective tissues, epithelial tissues, and extracellular matrices). The excellent biocompatible, nontoxic, and biodegradable characteristics of HA permit it to be extensively adopted for clinical, surgical, and biomedical applications, such as (1) the formation of a surgical glue with a higher shear strength for tissue adhesion [29], (2) the development of an implantable macroporous scaffold with degradation regulatability to control tumor microenvironments [30], (3) the manufacture of a pH-triggered nanogel system for tumor-targeted drug delivery [31], and (4) the functionalization of a contact lens surface with improved wettability, water retention, and reduced protein binding [32], to name a few. However, the modification of HA for analytical devices for the adsorptive removal of heavy metal ions is yet to be explored.

In this work, we have developed an electrochemical device that incorporates a layer of methacrylated HA hydrogel for in situ adsorption of Pb(II) in solutions. The electrochemical device is configured to have three electrodes, i.e., one working electrode, one counter electrode, and one reference electrode. The primary polymer is chosen as HA and methacrylic anhydride (MA) is used as the precursor. The adsorption performance of the HAMA hydrogel-modified electrochemical device is theoretically analyzed and further comprehensively investigated through a series of experiments. The practical application of the HAMA hydrogel-modified electrochemical devices for Pb(II) removal from tap water is demonstrated. The use of electrochemical devices for the detection of heavy metal ions has been extensively studied in the past [7–10]. However, the utilization of electrochemical devices for the adsorptive removal of heavy metal ions has rarely been reported. This work paves the way for the development of compact electrochemical devices for in situ removal of heavy metal ions.

2. Materials and Methods

2.1. Chemicals and Reagents

The chemicals and reagents used throughout this study were of analytical grade. Standard Pb(II) and bismuth (Bi(II)) stock solutions (1000 mg/L) were purchased from

Sigma-Aldrich and Merck, respectively. Ultrapure water (18.2 MΩ·cm) collected from a Milli-Q system was used to dilute the stock solutions. Acetate buffer (pH 4.6) was added into diluted Pb(II) solutions as a supporting electrolyte. HA (molecular weight, 1 MDa) was purchased from Samich (HK) Limited, China. Sodium chloride (NaCl), sodium hydroxide (NaOH), MA, and absolute ethanol were used without purification. Nafion 117 solution (5 wt% in a mixture of water and lower alcohols) was diluted by absolute ethanol. Photoinitiator Irgacure I2959 (I2959) was purchased from Ciba Specialty Chemicals, Switzerland.

2.2. Device Fabrication

As illustrated in Figure 1a, the electrochemical devices were fabricated via standard microfabrication techniques [33]. Initially, a liquid crystal polymer (LCP) sheet (ULTRALAM 3850, 100 μm) with copper cladding (18 μm) purchased from Rogers Corporation, USA, was cut into a 4-inch wafer size and used as a substrate for the devices. The cladding layer was removed by dipping the sheet in the copper etchant for 45 min, during which agitation was provided in order to facilitate the etching process. The sheet was then ultrasonically cleaned with acetone and deionized water to remove both organic and inorganic impurities. After drying with nitrogen gas, the sheet was thermally attached to a 4-inch silicon wafer using a photoresist (AZ 9260, 10 μm) as an adhesion layer. Thereafter, another layer of the photoresist (5 μm) was spin-coated on top of the LCP sheet and baked on a hotplate at 110 °C for 4 min. Upon the exposure of the photoresist under ultraviolet (UV, 365 nm, i-line) light followed by developing in the photoresist developer solution (AZ 400K), the patterns of the electrodes, connection lines, and contact pads were formed. After photolithography, a layer of chromium/gold (Cr/Au, 50/300 nm) was deposited using a magnetron sputtering system, in which the Cr layer was used to improve adhesion between the Au layer and the substrate. The remaining photoresist together with the deposited material was completely removed through the lift-off process by dipping the wafer in acetone solution for 12 h. This Au layer served as both the working and counter electrodes for the electrochemical devices. By repeating the photolithography-deposition procedure with a different photomask, the reference electrodes of the electrochemical devices were constructed by a combined layer of silver/silver chloride (Ag/AgCl, 150/250 nm).

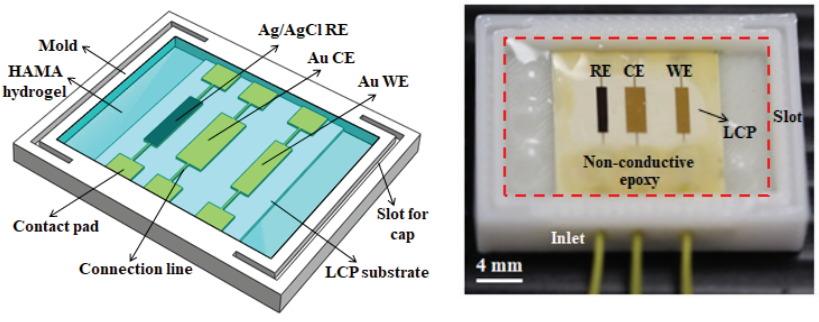

(**a**) (**b**)

Figure 1. (**a**) Schematic drawing to illustrate the structure of the HAMA hydrogel-modified electrochemical device. (**b**) Photograph of the HAMA hydrogel-modified electrochemical device after packaging and modification, in which the cap on two sides of the polycarbonate mold is removed in order to make the swollen hydrogel visible. A transparent HAMA hydrogel layer is successfully formed on top of the electrochemical device inside the mold, which can be seen in the region marked by the dashed red rectangle.

2.3. Device Packaging

The packaging of the electrochemical devices was performed by connecting three wires with one set of contact pads of the working, counter, and reference electrodes, respectively, using EPO-TEK® H20E conductive epoxy (Epoxy Technology, Billerica, MA, USA). After

mixing the resin part A and the hardener part B of the H20E conductive epoxy in a weight ratio of 1:1, the mixture was applied to each contact pad. Each device was then baked inside an oven at 80 °C for 3 h to solidify the conductive epoxy. The resistance of all three electrodes between the other set of contact pads and the wires was measured after the baking process. If the resistance of any electrode was 10% higher than the average value, that device was excluded from subsequent modification and experiment. This is due to the concern that a higher resistance value usually suggests bad connectivity of the Au layer, which can be caused by several factors, such as stripping of the metal connection line, a crack on the electrode or the contact pad, and peeling of the Au layer at certain locations. Thereafter, the EPO-TEK® H70E non-conductive epoxy mixture (resin part A and hardener part B in a weight ratio of 1:1) was drop-casted on the devices to cover all the contact pads (refer to Figure 1b) in order to provide electrical insulation. The non-conductive epoxy was cured by baking inside an oven at 80 °C for 1.5 h. Each packaged device was then placed into a 3D-printed polycarbonate mold for further modification. The detailed dimensions of the mold are presented in Figure S1.

2.4. Device Modification

Hyaluronic acid was modified with methacrylic anhydride and then photocrosslinked to obtain the HAMA hydrogel [34]. Briefly, the HA solution was prepared in ultrapure water and MA (20 mol/L) was added to it. The pH of the solution was adjusted to 8 using 1 M NaOH. After 2 h of reaction (as illustrated in Figure 2), the HAMA solution was incubated at 4 °C for 24 h and dialyzed (Spectra/Por 6 dialysis tubing, 10 kDa molecular weight cutoff) against 0.1 M NaCl solution, 25% (*v*/*v*) ethanol and ultrapure water for 48 h at room temperature. The modified HAMA solution was freeze-dried for 72 h and used to prepare the HAMA hydrogel. An amount of 1% (*w*/*v*) of HAMA was first dissolved in ultrapure water and then 1% (*w*/*w*) of I2959 photoinitiator (prepared in Nafion 117) was added to it and mixed thoroughly. Thereafter, each electrochemical device was contained in the polycarbonate mold, which had inlets for wires and cutout slots to hold a cap on both sides of the mold to keep the swollen hydrogel intact. The HAMA solution was spread uniformly over the device inside the mold without making any air bubbles and then exposed to UV light for 5 min to complete the crosslinking process. The HAMA hydrogel over the device was swollen in ultrapure water for 24 h to form a transparent gel layer, as shown in the dashed red rectangle in Figure 1b.

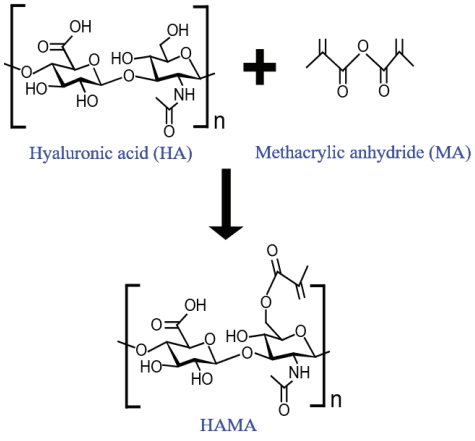

Figure 2. Schematic representation of the synthetic route of HAMA hydrogel.

2.5. Investigation of Morphological and Chemical Structures of the Synthesized HAMA Hydrogel

The HAMA hydrogels were prepared using a similar approach to that mentioned earlier with slight modifications. The hydrogels were formed inside 3D-printed disc-shaped

polycarbonate molds (internal diameter 18 mm, outer diameter 20 mm, and depth 2.5 mm). The HAMA solution together with the photoinitiator was spread uniformly into these molds and exposed to UV light for crosslinking. After crosslinking, the hydrogels were carefully removed from the molds and transferred to Petri dishes for swelling in ultrapure water. For the swelling capacity study, the weights of all the wet hydrogel samples were first recorded. Subsequently, the weights of all the dried hydrogels were measured upon baking the samples inside an oven at 50 °C for 6 h. For scanning electron microscopy (SEM) imaging, the hydrogel samples were quenched in liquid nitrogen for a few seconds and then immediately lyophilized for 72 h. The dried samples were coated with Au and imaged under an SEM microscope (JSM 6360A Jeol, Tokyo, Japan) at a 10 kV acceleration voltage. For Fourier transform infrared spectroscopy (FTIR) analysis, after 24 h of swelling, the ultrapure water was replaced by either a 0.1 M acetate buffer or 100 μg/L Pb(II) solution. Before conducting FTIR analysis, the hydrogel samples were dried inside an oven at 50 °C for 6 h. The FTIR experiments were carried out using a Nicolet iS10 FTIR Spectrometer (Thermo Fisher Scientific, Waltham, MA, USA) in a frequency range between 400 and 4000 cm^{-1}. A total number of 32 scans with a resolution of 2 cm^{-1} were averaged for each spectrum.

2.6. Investigation of Adsorption Performance of the Modified Device

The adsorption performance of the HAMA hydrogel-modified electrochemical devices was evaluated by conducting a series of square-wave anodic stripping voltammetry (SWASV) in the diluted Pb(II) solutions. The output of the devices was recorded on a CHI 600 C electrochemical workstation (CH Instruments, Austin, TX, USA). The SWASV measurements were initiated by applying a deposition potential of −1.0 V to the working electrode for 120 s while the test solution was stirred (800 rpm). This deposition step was aimed at the collection of Pb(II) ions that were available in the vicinity of the working electrode. After an equilibration time of 2 s, the voltammograms were recorded under quiescent conditions in a potential range from −1.2 to 0 V with a frequency of 50 Hz, amplitude of 50 mV, and a step potential of 5 mV. This stripping step was proportionally related to the deposition step, i.e., the higher the stripping current, the more the amount of Pb(II) ions that were collected during the deposition step. Hence, a higher concentration of Pb(II) should be present in the test solution. Prior to the next measurement, a conditioning potential of −0.1 V was provided for 120 s in order to electrochemically clean the working electrode. Herein, all the potentials applied or measured during the SWASV experiments were with respect to the potential of the fabricated Ag/AgCl reference electrode.

2.7. Investigation of Adsorption Efficiency of the Modified Device

The adsorption rate of the HAMA hydrogel-modified electrochemical devices was determined by applying a deposition potential of −1.0 V (with respect to the Ag/AgCl reference electrode) for 5 min to the working electrode in a stirred (800 rpm) solution with 100 μg/L Pb(II). Thereafter, 5 mL of the test solution was transferred to a conical tube. The Pb(II) concentration in the solution was measured using an Agilent 7700 inductively coupled plasma mass spectrometry (ICP-MS) system (Agilent Technologies, Lexington, MA, USA). This series of experiments were repeated 8 times within 40 min, i.e., the Pb(II) concentration in each test solution was separately measured after a period of 5, 10, 15, 20, 25, 30, 35, and 40 min of adsorption. In order to further investigate the influence of electrochemical accumulation on the adsorption performance of the modified devices, another series of experiments were conducted with the same experimental procedure, except for applying the deposition potential, i.e., without the activation of electrochemical accumulation.

The applicability of the HAMA hydrogel-modified electrochemical devices was explored by testing the Pb(II) removal ability of the devices in tap water. Experiments were conducted by keeping the devices in tap water with 400 μg/L Pb(II) for 20 min with the activation of electrochemical accumulation. Thereafter, the Pb(II) concentration in the tap

water was measured using the ICP-MS system. The removal efficiency of each device was calculated based on the concentration difference before and after the adsorption.

3. Results and Discussion

3.1. Characterization of the Synthesized HAMA Hydrogel

First, the swelling capacities of the synthesized HAMA hydrogels were evaluated using a gravimetrical approach. The weights of both the fully swollen and thermally dried hydrogel samples were separately determined. The results obtained are presented in Figure S2, where it can be observed that the average weight before swelling was ~8.17 mg. Once the dried samples had absorbed a sufficient amount of water to reach the equilibrium state of swelling (refer to Figure S3), the average weight dramatically increased to ~1526.23 mg, giving an average swelling ratio of 18,581%. This massive extent of swelling could be due to the superhydrophilic property of the HA. Thereafter, the morphology of the microscopic structure established inside the hydrogel layer was inspected using SEM. Figure 3a depicts the SEM image to illustrate the cross-sectional view of the synthesized HAMA hydrogel. It can be observed that a highly porous structure with an interconnected backbone was formed, in which most pores had either an oval or elongated bubble shape and their size varied from 20 to 200 μm in diameter. Such a high density of the porous structure also proved the considerable swelling capacity exhibited by the HAMA hydrogels.

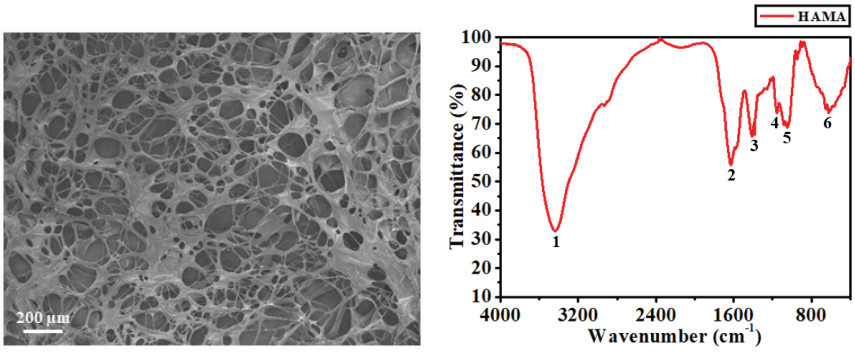

Figure 3. (**a**) Cross-sectional SEM image and (**b**) FTIR spectrum of the synthesized HAMA hydrogel. The numbers in (**b**) denote the prominent peaks detected by the FTIR analysis.

The functional groups associated with the synthesized HAMA hydrogels were identified by FTIR analysis. The FTIR spectrum acquired is presented in Figure 3b, in which numbers (1 to 6) are used to denote the prominent peaks detected. Among all the peaks, peak 1 situated at 3436.34 cm^{-1} was much broader than the others, which could be due to the O-H or N-H stretching, considering that both stretching vibrations occurred at an overlapped frequency band between 3200 and 3600 cm^{-1} [35]. Peak 2 situated at 1628.07 cm^{-1} was likely contributed by the carbonyl (C=O) stretching rather than the N-H bending of the secondary amide group. This is because, for most secondary amides, the weak N-H bending adsorption often appears at the frequency band between 1500 to 1560 cm^{-1} [36]. Peak 3 situated at 1410.64 cm^{-1} corresponded to the vibration of the O-C=O group [37]. Peaks 4 and 5 situated at 1153.41 and 1046.36 cm^{-1} were related to the C-O and C-O-C stretching, respectively. Peak 6 situated at 650.68 cm^{-1} was a fingerprint peak of HA [37], which could have been caused by a combinational manner of bending vibrations.

3.2. Electrochemical Investigation of the HAMA Hydrogel-Modified Device

To evaluate the adsorption performance of the HAMA hydrogel-modified electrochemical devices, a series of SWASV experiments were carried out. The magnitude of each stripping peak obtained in the SWASV experiments was measured with respect to its

baseline. Initially, the response was recorded in a solution with 20 μg/L Pb(II) (blue line in Figure 4a), in which a clear stripping peak was observed close to a potential −0.76 V, with an average peak magnitude of 1.059 μA (refer to Figure 4b). When the Pb(II) concentration was increased to 40 μg/L, the device exhibited a smaller stripping peak (green line in Figure 4a) with a decreased average peak magnitude of 0.848 μA. To investigate whether such a decrease in the stripping peak was caused by the reduced alloying capability of the working electrode, 400 μg/L Bi(II) was added to the test solution. According to the literature [38–40], Bi is capable of forming low-melting-temperature alloys with heavy metals, which significantly facilitates the accumulation of metal ions by the working electrode in the course of the deposition. As shown by the orange line in Figure 4a, adding Bi(II) did not improve the accumulation of Pb(II) ions for the device, which was manifested by an even smaller stripping peak with a further decreased average peak magnitude of 0.496 μA. With 400 μg/L Bi(II) in the test solution, a subsequent increase in the Pb(II) concentration to 60 μg/L (red line in Figure 4a) resulted in an indistinguishable stripping peak with a tiny average peak magnitude of 0.199 μA. The experimental results imply that the developed HAMA hydrogel-modified electrochemical device is capable of adsorbing the Pb(II) ions that are available in the solution.

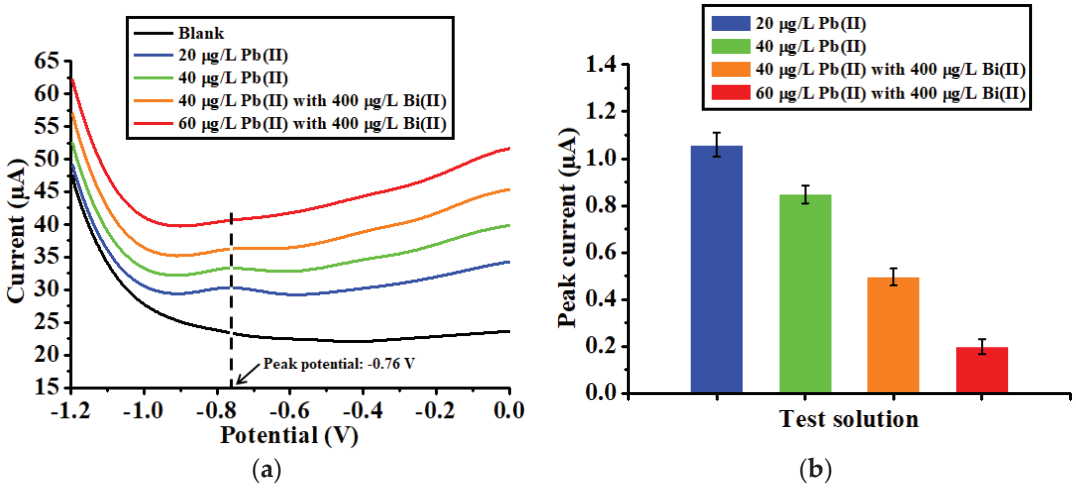

Figure 4. (**a**) Anodic stripping voltammograms and (**b**) the corresponding stripping peak currents recorded for the HAMA hydrogel-modified electrochemical devices in different test solutions.

3.3. Adsorption Mechanism of the HAMA Hydrogel-Modified Device

To explain the observed phenomena, a hypothesis pertaining to the adsorption mechanism of the HAMA hydrogel-modified electrochemical devices is proposed. A schematic model illustrating the mechanism is depicted in Figure 5, in which red circles (with a plus sign or number) represent the dissolved heavy metal ions in the solution. The network denoted by black solid lines above the electrode layer represents the microscopic porous structure of the HAMA hydrogel. First, free-moving metal ions in the solution migrated to the vicinity of the hydrogel under the effect of diffusion due to a high concentration gradient established between the solution and the hydrogel. Thereafter, the metal ions penetrated the hydrogel and interacted with the functional groups of the hydrogel's polymer chain. Some of the metal ions (e.g., No. 1, 2, 3, and 6 in Figure 5) were directly captured by the polymer chain due to the molecular interaction.

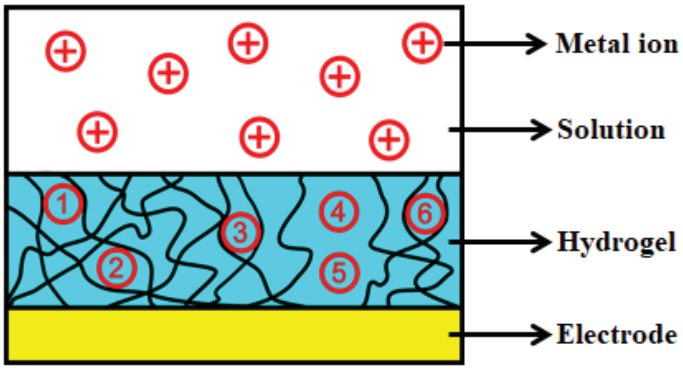

Figure 5. Schematic model to illustrate the adsorption mechanism of the HAMA hydrogel-modified electrochemical device. Red circles (⊕ and ①–⑥) represent heavy metal ions.

On the other hand, some other metal ions (e.g., No. 4 and 5 in Figure 5) reached the surface of the electrode by moving through the holes formed in the porous hydrogel. These ions were further captured by the electrode due to the electrochemical accumulation ($M^+ + e^- \rightarrow M$) triggered by the applied deposition potential. We suspect that most of the metal ions were collected by the hydrogel's polymer chain considering the above electrochemical investigation. If the dominant adsorption was contributed by the electrochemical accumulation, a relatively larger stripping peak should have been observed from the voltammograms when the SWASV experiment was conducted in solutions with a higher concentration. However, without the electrochemically induced adsorption, the collection efficiency of the device should be adversely affected since the high concentration gradient between the solution and the hydrogel could not be continuously maintained. Therefore, we attribute the promising adsorption capability of the HAMA hydrogel-modified device toward the Pb(II) ions to a combined effect of the molecular interaction and electrochemical accumulation.

3.4. Validation of the Molecular Interaction

The proposed hypothesis, specifically the molecular interaction, was validated by analyzing the FTIR spectrum obtained from a HAMA hydrogel sample soaked in a Pb(II) solution, as shown in Figure 6a. A comparison of all of the prominent peak positions in terms of wavenumber (cm^{-1}) between the pure HAMA hydrogel and the Pb(II)-soaked HAMA hydrogel is listed in Table 1. It was found that peaks 1, 3, 4, 5, and 6 in both spectra were situated at similar frequency bands. A new peak 7 emerged at 1237.61 cm^{-1} for the Pb(II)-soaked HAMA hydrogel, which could have been due to either C-O or C-N stretching. In addition, the original peak 2 (corresponding to the carbonyl stretching of the amide group) for the pure HAMA hydrogel separated into two peaks, i.e., peak 2′ situated at 1640.03 cm^{-1} and peak 2″ situated at 1565.72 cm^{-1} for the Pb(II)-soaked HAMA hydrogel, as depicted in Figure 6b. The significant shift of peak 2 implies that the Pb(II) ions mainly interact with the amide group of the HAMA hydrogel. We attribute such a molecular interaction to the effect of the Pb(II)–amide complexation.

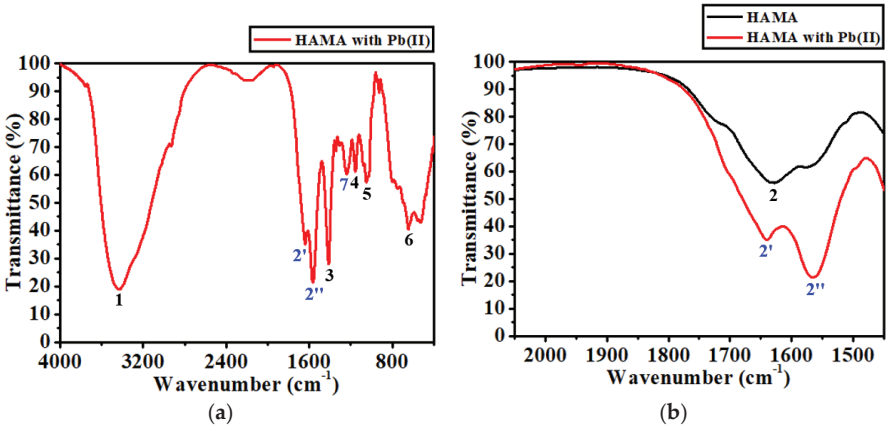

Figure 6. (**a**) FTIR spectrum of the HAMA hydrogel soaked in a solution of 100 μg/L Pb(II), in which the numbers 2′, 2″, 7 (in blue) denote the new peaks. (**b**) Comparison of FTIR spectra in a frequency band from 2050 to 1450 cm^{-1} between the pure HAMA hydrogel and the one soaked in Pb(II) solution.

Table 1. Comparison of peak positions in terms of wavenumber (cm^{-1}) between the pure HAMA hydrogel and the Pb(II)-soaked HAMA hydrogel.

Peak No.	HAMA (cm^{-1})	Assignment	Peak No.	HAMA with Pb(II) (cm^{-1})	Assignment
1	3436.34	O-H or N-H	1	3430.24	O-H or N-H
2	1628.07	C=O	2′	1640.03	Pb(II)-N
			2″	1565.72	Pb(II)-O
3	1410.64	O-C=O	3	1413.62	O-C=O
4	1153.41	C-O	4	1155.69	C-O
5	1046.36	C-O-C	5	1049.44	C-O-C
6	650.68	bending	6	644.68	bending
			7	1237.61	C-O or C-N

The resonance structure of an amide group has two possible configurations [41], which are named type I and type II. For a type I configuration (refer to Figure 7a), the lone pair of electrons on the N atom is not involved in the conjugation with the carbonyl group, making the N atom relatively electronegative. Hence, a positively charged metal ion (here is Pb^{2+}) can coordinate with the N atom of the amide group. Such coordination would result in a positive shift of the carbonyl infrared adsorption to a higher frequency [42]. For a type II configuration (refer to Figure 7b), the lone pair of electrons on the N atom is delocalized into the carbonyl group, making the O atom of the carbonyl group more electronegative. Therefore, a positively charged metal ion can also coordinate with the O atom of the amide group, which would bring about a negative shift of the carbonyl infrared adsorption to a lower frequency [42]. As illustrated in Figure 6b, peak 2′ with a positive shift of ~12 cm^{-1} with respect to peak 2 could be due to the vibration of the Pb(II)-N ligand, which corresponds to the type I complexation. On the other hand, peak 2″ with a negative shift of ~62 cm^{-1} with respect to peak 2 could be due to the vibration of the Pb(II)-O ligand, corresponding to the type II complexation. Based on the experimental observations, it is highly possible that both nitrogen and the carbonyl oxygen of the amide group of the HAMA hydrogel may be simultaneously involved in the formation of the Pb(II)–amide complex.

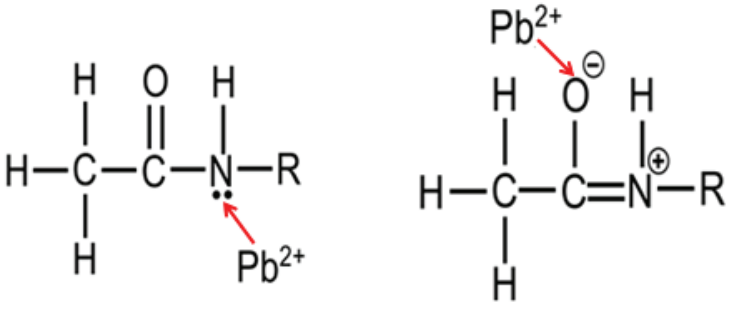

(**a**) (**b**)

Figure 7. Schematic representation of (**a**) type I and (**b**) type II Pb(II)–amide complexations.

Despite the contribution from nitrogen, as well as carbonyl oxygen, in the process of the complex formation, the tendency to form a Pb(II)-O ligand seems much higher than that of a Pb(II)-N ligand if one compares the negative shift with the positive one. The negative shift (~62 cm^{-1}) is 5 times larger than the positive shift (~12 cm^{-1}), suggesting that the carbonyl oxygen of the amide group could play the dominant role in the construction of the Pb(II)–amide complex. This could be explained by the fact that the type II configuration of an amide group is more stable than the type I configuration [41]. Owing to the delocalization, the electron density distributed on the carbonyl oxygen is much greater than that on the nitrogen, making the carbonyl oxygen behave as though it is being completely negatively charged, thereby attracting more Pb(II) ions.

3.5. Validation of the Electrochemical Accumulation

The effect of electrochemical accumulation pertaining to the proposed adsorption mechanism was investigated by quantifying the amount of Pb(II) ions adsorbed by the modified device. Originally, the Pb(II) concentration of each test solution was 100 μg/L. The concentration was subsequently measured by the ICP-MS instrument after every 5 min of adsorption. The results obtained are presented in Figure 8. When the electrochemical accumulation was not activated, i.e., only the HAMA hydrogel was responsible for the adsorption of Pb(II) ions (blue dots in Figure 8), the adsorption rate slowly increased within the first 20 min. Thereafter, there was no significant increase in the adsorption rate. The adsorption behavior of the HAMA hydrogel could be attributed to the diffusion effect. Initially, metal ions moved into the vicinity of the hydrogel driven by the high-ion-concentration gradient established between the solution and the hydrogel. This corresponded to the increase in the adsorption rate observed at 5, 10, 15, and 20 min. Thereafter, the concentration gradient was significantly reduced, which could have resulted in a rapid saturation of adsorption for the HAMA hydrogel, corresponding to the data points observed at 25, 30, 35, and 40 min. It was calculated that only 43.05% of Pb(II) ions were adsorbed by the device if electrochemical accumulation was not triggered.

On the other hand, when the electrochemical accumulation was activated (red dots in Figure 8), the adsorption rate continuously increased up to 30 min. In addition, the slope of the increase was significantly higher than in the case where electrochemical accumulation was not involved. It was found that 94.08% of Pb(II) ions were adsorbed by the device within 30 min once the electrochemical accumulation had been triggered. These experimental results confirm that electrochemical accumulation is particularly beneficial in facilitating the adsorption rate for the device by maintaining a high concentration gradient between the solution and the hydrogel. Considering the above discussion, it is apparent that both intermolecular complexation and electrochemical accumulation make a significant contribution to the adsorption capability of the HAMA hydrogel-modified electrochemical devices. A comparison of the Pb(II) removal efficiency of the HAMA hydrogel-modified

electrochemical device and other polymeric adsorbents is shown in Table 2. Based on the data presented in Table 2, it can be observed that the developed HAMA hydrogel-modified electrochemical device is capable of effectively removing Pb(II) ions with a short adsorption time of 30 min.

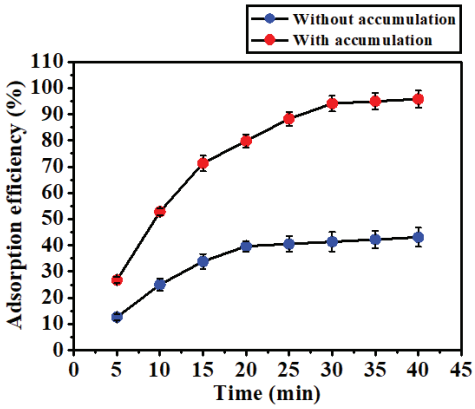

Figure 8. Comparison of adsorption efficiency for the HAMA hydrogel-modified devices without (blue dots) and with (red dots) electrochemical accumulation. Data obtained using three devices.

Table 2. Comparison of Pb(II) removal efficiency of different adsorbents.

Adsorbent	Removal Efficiency (%)	Adsorption Time (min)	Reference
Poly(allylamine-co-methacrylamide-co-acrylic acid) cryogel	83.54	720	Kim et al. [22]
Poly(*N*,*N*-dimethylacrylamide-co-2-hydroxyethyl methacrylate) copolymer	80.00	300	Ramos-Jacques et al. [23]
Melamine-based crosslinked polyamine/CNT composite	98.63	360	Al Hamouz et al. [25]
Polyisoprene-*b*-polystyrene-*b*-poly(*N*,*N*-dimethyl-acrylamide) polymer	94.80	480	Weidman et al. [27]
Nanochitosan/polyurethane/polypropylene glycol	95.00	60	Saranya et al. [28]
Chitosan-aminopropylsilane graphene oxide nanocomposite hydrogel	82.30	60	Amiri et al. [43]
Copolymerized starch-based hydrogel	87.00	60	Aniagor et al. [44]
Thiol-functionalized silica microsphere-loaded polymeric hydrogel	97.00	1440	Singh et al. [45]
HAMA hydrogel-modified electrochemical device	94.08	30	This work

3.6. Applicability of the HAMA Hydrogel-Modified Device

To explore the practical application of the HAMA hydrogel-modified electrochemical device, adsorption experiments were performed in a solution of tap water with 400 μg/L Pb(II). Each device was immersed in the test solution for 20 min, during which the electrochemical accumulation was activated. As shown in Figure 9, all the devices exhibited comparable Pb(II) removal capabilities with an average removal efficiency of 77.2%. The relative standard deviation (RSD) among the eight devices was calculated to be as low as 1.28%, demonstrating good repeatability and reproducibility of the devices. These experimental results reveal that the HAMA hydrogel-functionalized electrochemical device has great potential for deployment at a variety of locations for in situ removal of Pb(II) ions. It is worth mentioning that the water quality conditions (such as pH value, quantity of suspended particulates, other heavy metal ions, etc.) at the locations of interest could affect the adsorption performance of the HAMA hydrogel-modified electrochemical device.

Therefore, it is recommended to conduct some preliminary experiments in some specific areas before the large-scale deployment of the devices.

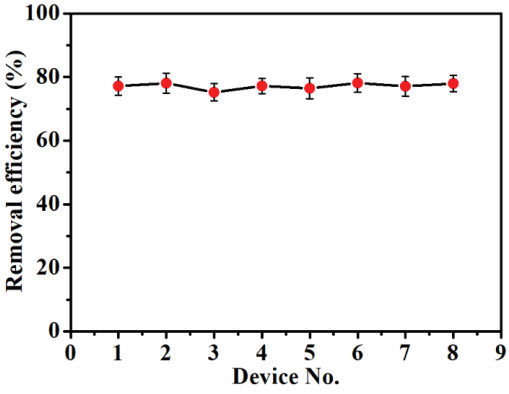

Figure 9. Removal efficiency measured for eight HAMA hydrogel-modified electrochemical devices in a solution of tap water with 400 μg/L Pb(II).

4. Conclusions

In this work, an electrochemical device with a three-electrode configuration covered by a layer of HAMA hydrogel was developed for in situ adsorption of Pb(II) ions in aqueous solutions. The devices were successfully fabricated using microfabrication technology along with a surface modification approach. The material properties of the synthesized HAMA hydrogels in the aspects of the swelling capacity, microscopic structure, as well as molecular composition, were systematically evaluated. Based on the analytical outcomes of the fabricated HAMA hydrogel-modified devices, an adsorption mechanism associated with a combined effect of molecular interaction and electrochemical accumulation, which could explain the observed experimental results, was proposed. By performing FTIR analysis on the Pb(II)-soaked HAMA hydrogel, the molecular interaction was corroborated to be the Pb(II)-amide complexation. We found that both nitrogen and the carbonyl oxygen of the amide group were responsible for the formation of the complex, though the carbonyl oxygen could play a dominant role in the course of intermolecular complexation. The contribution of electrochemical accumulation to the adsorption capability of the HAMA hydrogel-modified devices was also confirmed by activating/deactivating the deposition potential applied to the working electrode of the devices. The experimental investigation shows that 94.08% of Pb(II) ions present in the solution can be adsorbed by the device within 30 min. Application of the HAMA hydrogel-modified devices for removing Pb(II) ions in tap water reveals its potential for use for the rapid remediation of Pb(II) contamination. This study paves the way for the design of compact and portable electrochemical devices for in situ removal of Pb(II) ions. Future work will focus on exploring the HAMA hydrogel-modified devices for the simultaneous adsorption of multiple heavy metal ions and employing other validation methods to further investigate the molecular interaction between HAMA hydrogels and different kinds of heavy metal ions.

Supplementary Materials: The following supporting information can be downloaded at: https://www.mdpi.com/article/10.3390/bios12090714/s1, Figure S1: Schematic drawing to show detailed dimensions of the polycarbonate mold; Figure S2: The weight of the synthesized HAMA hydrogel samples measured before and after swelling in ultrapure water; Figure S3: Photograph of the synthesized HAMA hydrogel samples upon reaching the equilibrium state of swelling.

Author Contributions: Conceptualization, N.W.; formal analysis, N.W., M.B. and S.H.; investigation, N.W. and M.B.; writing—original draft preparation, N.W. and M.B.; writing—review and editing, S.H., K.T., J.W., L.H., J.L. and S.L.; supervision, M.S.T. and X.L.; project administration, N.W., M.S.T. and X.L. All authors have read and agreed to the published version of the manuscript.

Funding: This research was funded by the Fundamental Research Funds for the Central Universities, grant numbers DUT21RC(3)054 and DUT21RC(3)020, and the National Key R&D Program of China, grant number 2021YFB3201302.

Institutional Review Board Statement: Not applicable.

Informed Consent Statement: Not applicable.

Data Availability Statement: Data are available upon reasonable request to Nan Wang (wang_nan@dlut.edu.cn).

Acknowledgments: This research was supported by the Ministry of Education Singapore and the National Research Foundation of Singapore through the Singapore MIT Alliance for Research and Technology's Center for Environmental Sensing and Modeling interdisciplinary research program.

Conflicts of Interest: The authors declare no conflict of interest.

References

1. Counter, S.A.; Buchanan, L.H.; Ortega, F. Association of hemoglobin levels and brainstem auditory evoked responses in lead-exposed children. *Clin. Biochem.* **2012**, *45*, 1197–1201. [CrossRef] [PubMed]
2. Roy, A.; Hu, H.; Bellinger, D.C.; Mukherjee, B.; Modali, R.; Nasaruddin, K.; Schwartz, J.; Wright, R.O.; Ettinger, A.S.; Palaniapan, K.; et al. Hemoglobin, lead exposure, and intelligence quotient: Effect modification by the DRD2 Taq IA polymorphism. *Environ. Health Perspect.* **2011**, *119*, 144–149. [CrossRef]
3. Philip, A.; Marsden, M.D. Increased body lead burden—cause or consequence of chronic renal insufficiency? *N. Engl. J. Med.* **2003**, *348*, 345–347.
4. Bellinger, D.C. Lead. *Pediatrics* **2004**, *113*, 1016–1022. [CrossRef] [PubMed]
5. Kordas, K.; Queirolo, E.I.; Ettinger, A.S.; Wright, R.O.; Stoltzfus, R.J. Prevalence and predictors of exposure to multiple metals in preschool children from Montevideo, Uruguay. *Sci. Total Environ.* **2010**, *408*, 4488–4494. [CrossRef]
6. Roy, A.; Ettinger, A.S.; Hu, H.; Bellinger, D.; Schwartz, J.; Modali, R.; Wright, R.O.; Palaniappan, K.; Balakrishnan, K. Effect modification by *transferrin* C2 polymorphism on lead exposure, hemoglobin levels, and IQ. *Neurotoxicology* **2013**, *38*, 17–22. [CrossRef] [PubMed]
7. Hwang, J.H.; Wang, X.; Zhao, D.; Rex, M.M.; Cho, H.J.; Lee, W.H. A novel nanoporous bismuth electrode sensor for *in situ* heavy metal detection. *Electrochim. Acta* **2019**, *298*, 440–448. [CrossRef]
8. Wang, N.; Kanhere, E.; Miao, J.; Triantafyllou, M.S. Miniaturized chemical sensor with bio-inspired micropillar working electrode array for lead detection. *Sens. Actuators B Chem.* **2016**, *233*, 249–256. [CrossRef]
9. Li, M.; Li, Z.; Liu, C.; Chang, Y.; Wen, J.; Zhao, H.; Cao, H.; Zhang, Y.; Liu, D. Amino-modification and successive electro-chemical reduction of graphene oxide for highly sensitive electrochemical detection of trace Pb^{2+}. *Carbon* **2016**, *109*, 479–486. [CrossRef]
10. Zhou, G.; Chang, J.; Cui, S.; Pu, H.; Wen, Z.; Chen, J. Real-time, selective detection of Pb^{2+} in water using a reduced graphene oxide/gold nanoparticle field-effect transistor device. *ACS Appl. Mater. Interfaces* **2014**, *6*, 19235–19241. [CrossRef]
11. Niu, X.; Zhong, Y.; Chen, R.; Wang, F.; Liu, Y.; Luo, D. A "turn-on" fluorescence sensor for Pb^{2+} detection based on graphene quantum dots and gold nanoparticles. *Sens. Actuators B Chem.* **2018**, *255*, 1577–1581. [CrossRef]
12. Saha, S.K.; Ghosh, K.R.; Gao, J.P.; Wang, Z.Y. Highly sensitive dual-mode fluorescence detection of lead ion in water using aggregation-induced emissive polymers. *Macromol. Rapid Commun.* **2014**, *35*, 1592–1597. [CrossRef] [PubMed]
13. Zhan, S.; Wu, Y.; Liu, L.; Xing, H.; He, L.; Zhan, X.; Luo, Y.; Zhou, P. A simple fluorescent assay for lead(II) detection based on lead(II)-stabilized G-quadruplex formation. *RSC Adv.* **2013**, *3*, 16962–16966. [CrossRef]
14. Skotadis, E.; Tsekenis, G.; Chatzipetrou, M.; Patsiouras, L.; Madianos, L.; Bousoulas, P.; Zergioti, I.; Tsoukalas, D. Heavy metal ion detection using DNAzyme-modified platinum nanoparticle networks. *Sens. Actuators B Chem.* **2017**, *239*, 962–969. [CrossRef]
15. Huang, Y.; Ma, Y.; Chen, Y.; Wu, X.; Fang, L.; Zhu, Z.; Yang, C.J. Target-responsive DNAzyme cross-linked hydrogel for visual quantitative detection of lead. *Anal. Chem.* **2014**, *86*, 11434–11439. [CrossRef]
16. Wang, Y.; Irudayaraj, J. A SERS DNAzyme biosensor for lead ion detection. *Chem. Commun.* **2011**, *47*, 4394–4396. [CrossRef]
17. Renfrew, D. Lead poisoning and the dangers of pragmatism. *Int. J. Environ. Res. Public Health* **2018**, *15*, 1997. [CrossRef] [PubMed]
18. Chowdhury, S.; Mazumder, M.A.J.; Al-Attas, O.; Husain, T. Heavy metals in drinking water: Occurrences, implications, and future needs in developing countries. *Sci. Total Environ.* **2016**, *569–570*, 476–488. [CrossRef]
19. Gupta, V.K.; Agarwal, S.; Saleh, T.A. Synthesis and characterization of alumina-coated carbon nanotubes and their ap-plication for lead removal. *J. Hazard. Mater.* **2011**, *185*, 17–23. [CrossRef]
20. Foo, K.Y.; Hameed, B.H. Insights into the modeling of adsorption isotherm systems. *Chem. Eng. J.* **2010**, *156*, 2–10. [CrossRef]
21. Liu, Y.; Zhang, W.; Zhao, C.; Wang, H.; Chen, J.; Yang, L.; Feng, J.; Yan, W. Study on the synthesis of poly(pyrrole methane)s with the hydroxyl in different substituent position and their selective adsorption for Pb^{2+}. *Chem. Eng. J.* **2019**, *361*, 528–537. [CrossRef]

22. Kim, M.Y.; Lee, T.G. Removal of Pb(II) ions from aqueous solutions using functionalized cryogels. *Chemosphere* **2019**, *217*, 423–429. [CrossRef] [PubMed]
23. Ramos-Jacques, A.L.; Lujan-Montelongo, J.A.; Silva-Cuevas, C.; Cortez-Valadez, M.; Estevez, M.; Hernandez-Martinez, A.R. Lead(II) removal by poly(*N*,*N*-dimethylacrylamide-*co*-2-hydroxyethyl methacrylate). *Eur. Polym. J.* **2018**, *101*, 262–272. [CrossRef]
24. Mohammadinezhad, A.; Marandi, G.B.; Farsadrooh, M.; Ja-vadian, H. Synthesis of poly(acrylamide-co-itaconic ac-id)/MWCNTs superabsorbent hydrogel nanocomposite by ultra-sound-assisted technique: Swelling behavior and Pb(II) adsorption capacity. *Ultrason. Sonochem.* **2018**, *49*, 1–12. [CrossRef]
25. Al Hamouz, O.C.S.; Adelabu, I.O.; Saleh, T.A. Novel cross-linked melamine based polyamine/CNT composites for lead ions removal. *J. Environ. Manag.* **2017**, *192*, 163–170. [CrossRef]
26. Zhang, Y.; Li, Z. Heavy metals removal using hydrogel-supported nanosized hydrous ferric oxide: Synthesis, characterization, and mechanism. *Sci. Total Environ.* **2017**, *580*, 776–786. [CrossRef]
27. Weidman, J.L.; Mulvenna, R.A.; Boudouris, B.W.; Phillip, W.A. Nanoporous block polymer thin films functionalized with bio-inspired ligands for the efficient capture of heavy metal ions from water. *ACS Appl. Mater. Interfaces* **2017**, *9*, 19152–19160. [CrossRef]
28. Saranya, M.; Latha, S.; Reddi, M.R.G.; Gomathi, T.; Sudha, P.N.; Anil, S. Adsorption studies of Lead(II) from aqueous solution onto Nanochitosan /Polyurethane /Polypropylene glycol ternary blends. *Int. J. Biol. Macromol.* **2017**, *104*, 1436–1448.
29. Chandrasekharan, A.; Seong, K.Y.; Yim, S.G.; Kim, S.; Seo, S.; Yoon, J.; Yang, S.Y. In situ photocrosslinkable hyaluronic ac-id-based surgical glue with tunable mechanical properties and high adhesive strength. *J. Polym. Sci. A Polym. Chem.* **2019**, *57*, 522–530. [CrossRef]
30. Ren, L.; Lim, Y.T. Degradation-regulatable architectured implantable macroporous scaffold for the spatiotemporal modulation of immunosuppressive microenvironment and enhanced combination cancer immunotherapy. *Adv. Funct. Mater.* **2018**, *28*, 1804490. [CrossRef]
31. Yang, G.; Fu, S.; Yao, W.; Wang, X.; Zha, Q.; Tang, R. Hyaluronic acid nanogels prepared via ortho ester linkages show pH-triggered behavior, enhanced penetration and antitumor efficacy in 3-D tumor spheroids. *J. Colloid Interface Sci.* **2017**, *504*, 25–38. [CrossRef] [PubMed]
32. Deng, X.; Korogiannaki, M.; Rastegari, B.; Zhang, J.; Chen, M.; Fu, Q.; Sheardown, H.; Filipe, C.D.M.; Hoare, T. "Click" chemistry-tethered hyaluronic acid-based contact lens coatings improve lens wettability and lower protein adsorption. *ACS Appl. Mater. Interfaces* **2016**, *8*, 22064–22073. [CrossRef] [PubMed]
33. Tao, K.; Yi, H.; Yang, Y.; Chang, H.; Wu, J.; Tang, L.; Yang, Z.; Wang, N.; Hu, L.; Fu, Y.; et al. Origami-inspired electret-based triboelectric generator for biomechanical and ocean wave energy harvesting. *Nano Energy* **2020**, *67*, 104197. [CrossRef]
34. Smeds, K.A.; Pfister-Serres, A.; Miki, D.; Dastgheib, K.; In-oue, M.; Hatchell, D.L.; Grinstaff, M.W. Photocrosslinkable polysaccharides for *in situ* hydrogel formation. *J. Biomed. Mater. Res.* **2001**, *54*, 115–121. [CrossRef]
35. Magalhaes, J.; Sousa, R.A.; Mano, J.F.; Reis, R.L.; Blanco, F.J.; Roman, J.S. Synthesis and characterization of sensitive hydrogels based on semi-interpenetrated networks of poly[2-ethyl-(2-pyrrolidone) methacrylate] and hyaluronic acid. *J. Biomed. Mater. Res. Part A* **2013**, *101A*, 157–166. [CrossRef] [PubMed]
36. Anirudhan, T.S.; Nair, S.S.; Nair, A.S. Fabrication of a bioadhesive transdermal device from chitosan and hyaluronic acid for the controlled release of lidocaine. *Carbohydr. Polym.* **2016**, *152*, 687–698. [CrossRef] [PubMed]
37. Reddy, K.J.; Karunakaran, K.T. Purification and characterization of hyaluronic acid produced by *Streptococcus zooepidemicus* strain 3523-7. *J. BioScience Biotechnol.* **2013**, *2*, 173–179.
38. Wang, N.; Kanhere, E.; Miao, J.; Triantafyllou, M.S. Nanoparticles-modified chemical sensor fabricated on a flexible polymer substrate for cadmium(II) detection. *Polymers* **2018**, *10*, 694. [CrossRef]
39. Lee, S.; Park, S.K.; Choi, E.; Piao, Y. Voltammetric determination of trace heavy metals using an electrochemically deposited graphene/bismuth nanocomposite film-modified glassy carbon electrode. *J. Electroanal. Chem.* **2016**, *766*, 120–127. [CrossRef]
40. Serrano, N.; Alberich, A.; Diaz-Cruz, J.M.; Arino, C.; Esteban, M. Coating methods, modifiers and applications of bismuth screen-printed electrodes. *Trends Anal. Chem.* **2013**, *46*, 15–29. [CrossRef]
41. Clayden, J.; Greeves, N.; Warren, S. *Organic Chemistry*, 2nd ed.; Oxford University Press: Oxford, UK, 2012.
42. Feng, Y.; Schmidt, A.; Weiss, R.A. Compatibilization of polymer blends by complexation. 1. spectroscopic characterization of ion-amide interactions in ionomer/polyamide blends. *Macromolecules* **1996**, *29*, 3909–3917. [CrossRef]
43. Amiri, S.; Asghari, A.; Vatanpour, V.; Rajabi, M. Fabrication of chitosan-aminopropylsilane graphene oxide nanocomposite hydrogel embedded PES membrane for improved filtration performance and lead separation. *J. Environ. Manag.* **2021**, *294*, 112918. [CrossRef] [PubMed]
44. Aniagor, C.O.; Afifi, M.A.; Hashem, A. Rapid and efficient uptake of aqueous lead pollutant using starch-based superabsorbent hydrogel. *Polym. Bull.* **2022**, *79*, 6373–6388. [CrossRef]
45. Singh, S.; Basu, H.; Bassan, M.K.T.; Singhal, R.K. Thiol functionalised silica microsphere loaded polymeric hydrogel: Development of a novel hybrid sorbent for removal of lead and cadmium. *Chemosphere* **2022**, *286*, 131659. [CrossRef] [PubMed]

biosensors

MDPI

Article

$La(OH)_3$ Multi-Walled Carbon Nanotube/Carbon Paste-Based Sensing Approach for the Detection of Uric Acid—A Product of Environmentally Stressed Cells

Sara Knežević [1,2], Miloš Ognjanović [3], Vesna Stanković [4], Milena Zlatanova [1], Andrijana Nešić [1], Marija Gavrović-Jankulović [1] and Dalibor Stanković [1,5,*]

[1] Faculty of Chemistry, University of Belgrade, Studentski trg 12-16, 11000 Belgrade, Serbia
[2] University of Bordeaux, CNRS, Bordeaux INP, Institut des Sciences Moléculaires, UMR 5255, 33400 Talence, France
[3] Department of Theoretical Physics and Condensed Matter Physics, "VINČA" Institute of Nuclear Sciences-National Institute of the Republic of Serbia, University of Belgrade, 11000 Belgrade, Serbia
[4] Scientific Institution, Institute of Chemistry, Technology and Metallurgy, National Institute University of Belgrade, 11000 Belgrade, Serbia
[5] Department of Radioisotopes, "VINČA" Institute of Nuclear Sciences-National Institute of the Republic of Serbia, University of Belgrade, 11000 Belgrade, Serbia
* Correspondence: dalibors@chem.bg.ac.rs

Abstract: This paper aims to develop an amperometric, non-enzymatic sensor for detecting and quantifying UA as an alert signal induced by allergens with protease activity in human cell lines (HEK293 and HeLa). Uric acid (UA) has been classified as a damage-associated molecular pattern (DAMP) molecule that serves a physiological purpose inside the cell, while outside the cell it can be an indicator of cell damage. Cell damage or stress can be caused by different health problems or by environmental irritants, such as allergens. We can act and prevent the events that generate stress by determining the extent to which cells are under stress. Amperometric calibration measurements were performed with a carbon paste electrode modified with $La(OH)_3$@MWCNT, at the potential of 0.3 V. The calibration curve was constructed in a linear operating range from 0.67 μM to 121 μM UA. The proposed sensor displayed good reproducibility with an RSD of 3.65% calculated for five subsequent measurements, and a low detection limit of 64.28 nM, determined using the 3 S/m method. Interference studies and the real sample analysis of allergen-treated cell lines proved that the proposed sensing platform possesses excellent sensitivity, reproducibility, and stability. Therefore, it can potentially be used to evaluate stress factors in medical research and clinical practice.

Keywords: $La(OH)_3$@MWCNT; electrochemical sensor; uric acid; DAMP molecule; cell damage; stress

Citation: Knežević, S.; Ognjanović, M.; Stanković, V.; Zlatanova, M.; Nešić, A.; Gavrović-Jankulović, M.; Stanković, D. $La(OH)_3$ Multi-Walled Carbon Nanotube/Carbon Paste-Based Sensing Approach for the Detection of Uric Acid—A Product of Environmentally Stressed Cells. *Biosensors* **2022**, *12*, 705. https://doi.org/10.3390/bios12090705

Received: 25 July 2022
Accepted: 24 August 2022
Published: 1 September 2022

1. Introduction

Various events can strain the human body, putting stress on the cells and tissues. Oxidative stress, heat shock, hypersensitivity, autoimmune diseases and other disorders can cause cell dysfunction and lead to apoptosis [1]. Besides passive release, dying cells produce an increased amount of uric acid (UA), which can indicate both the environmental and medical conditions that induce cell damage [2]. DAMPs are molecules that have a physiological role inside the cell but acquire additional functions when released from the cells: they alert the body about danger, stimulate an inflammatory response, and promote the regeneration process [3]. Apart from their passive release by dead cells, some DAMPs can be secreted or exposed by living cells undergoing life-threatening stress.

Uric acid, being a final product of purine metabolism, has a high impact on human health. It is produced in the liver, intestines, kidneys, vascular endothelium, and muscles by the metabolism of purine [2].

Both high and low human plasma UA concentrations can indicate a pathological state. On the one hand, UA acts as a scavenger of peroxyl radicals, hydroxyl radicals, and singlet oxygen, thus exhibiting antioxidative features. It is a specific inhibitor of radicals generated by the decomposition of peroxynitrite, preventing cell injuries and nitration of tyrosine residues in proteins. Furthermore, it can protect against oxidative damage by chelating metal ions such as iron and copper, lowering their catalytic activity in free-radical reactions [4]. UA also shows neuroprotective properties and reduces the risk of multiple sclerosis, Parkinson's disease, Alzheimer's disease, and optic neuritis [5].

UA also acts as an initiator and amplifier of allergic inflammation and can cause hypertension and cardiovascular diseases via the induction of growth factors, hormones, cytokines, and autacoids. UA penetrates vascular smooth muscle fibers and activates signal transduction, increasing the expression of inflammatory mediators. Furthermore, urate crystals can deposit in the connective tissues of the joints, tendons, kidneys, and rarely in heart valves and the pericardium. Consequently, UA is a risk factor for renal disorders (kidney injuries and kidney stones), acute and chronic inflammatory arthritis, gout, myocardial infarction, and stroke [2,5]. Elevated serum uric acid levels are associated with insulin resistance and diabetes mellitus [2].

The important UA feature is that it is produced in higher concentrations when the cells suffer from stress. Both live and dying cells degrade their nucleic acids in deamination and dephosphorylation processes. Purine nucleoside phosphorylase converts the relevant degradation products, inosine and guanosine, to the purine bases, hypoxanthine and guanine, which further metabolize to xanthine. Oxidation of xanthine via xanthine oxidase leads to the formation of UA. Therefore, although uric acid is regularly present in cells, it increases in concentration when the cells are damaged [2]. The UA's release from dying cells can serve as an indicator of unfavorable environmental factors or pathological states.

Considering its importance and abundance in the human body, it is no wonder that numerous methods have been developed for UA detection and determination. The separation and detection methods commonly involve chromatography or electrophoresis coupled with UV/VIS [6–10] spectroscopy or electrochemical detection (voltammetry [11–16], ECL [17–20], and amperometry [21–25]), including both enzymatic and nonenzymatic approaches [26]. Recently, attention has shifted toward electrochemical sensors and biosensors because they enable the fast, direct, and precise determination of the analyte in the complex biological matrix.

Enzyme-based UA biosensors use uricase as an enzyme for the oxidation of uric acid [27,28]. The enzyme-based approach is expensive, and the obtained sensor is sensitive to environmental conditions, lacks reproducibility, and requires complicated immobilization of the enzyme. Non-expensive and robust non-enzymatic sensors perform direct oxidation of UA on the surface of the electrode material [29,30]. Various materials, such as covalent organic and metal incorporated conductive polymers [13,16,19,23], metal oxides [30–32], carbon-based materials, and their composites [11,12,33], have been tested for UA detection [5,26]. These nanomaterials have been recognized as promising materials for the development of analytical methods for the detection not only of UA but also of numerous other biologically active compounds [34–37].

The use of La [32,38,39]-based electrode materials has been reported in the literature with the main applications in fuel cells [40–42] and sensing devices [43–46], while Wang et al. [47] used $LaFeO_3$ for the simultaneous determination of dopamine, uric acid and ascorbic acid, thus proving the materials' compatibility with these analytes. La doping can affect lattice structures and phase transformations of compounds due to its larger atomic radius and unique electron structure, thus enhancing the catalytic and electrochemical properties of La-doped materials [32]. Furthermore, Guo et al. [48] suggested that the alkaline properties of $La(OH)_3$ contribute to the acidic analytes' bonding. To improve the conductivity and increase the active surface and electron transfer of the electrode, lanthanum hydroxide was incorporated into the composite with multi-walled

carbon nanotubes (MWCNTs), which possess exceptional mechanical and physicochemical properties [38,49].

This study aims to develop an electrochemical sensor for the fast, accurate, and precise measurement of UA released from damaged cells, or rather for monitoring the dependence between environmental factors and the stress they cause to the cells/tissues (Scheme 1). An electrochemical sensor was developed using a glassy carbon paste electrode modified with newly synthesized nanomaterial consisting of MWCNTs decorated with $La(OH)_3$. The obtained sensor was used for the amperometric detection of uric acid under optimal experimental conditions. Furthermore, the influence of common interfering substances on UA determination was examined, as well as the reproducibility, repeatability, and stability of the proposed sensor. We showed that the proposed method could be used to evaluate stress factors in medical research and clinical practice.

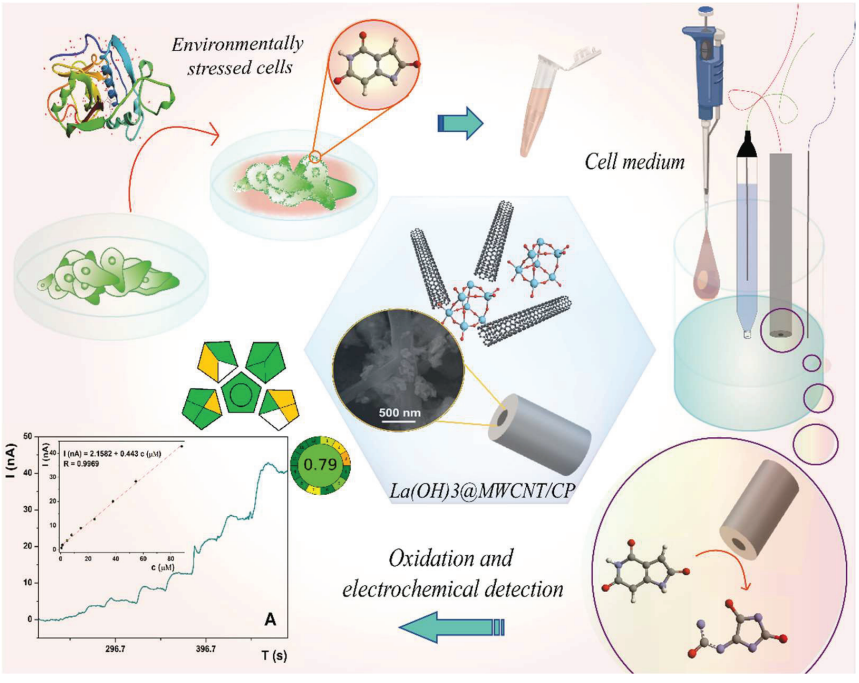

Scheme 1. Idea of the work.

2. Materials and Methods

2.1. Cell Cultures

Cell lines cultivated for the allergen treatment included HEK293 and HeLa. HEK293 cells were cultivated in Dulbecco's modified Eagle medium (DMEM, Sigma-Aldrich, St. Louis, MO, USA) supplemented with 10% heat-inactivated fetal bovine serum (FBS), 1% pen/strep (penicillin 10,000 U/mL; streptomycin 10 mg/mL) and 200 mM L-glutamine (Sigma-Aldrich, St. Louis, MO, USA), and HeLa cells were cultivated in Eagle's minimum essential medium (EMEM, Lonza, Basel, Switzerland) supplemented with 20% FBS, 1% pen/strep (penicillin 10,000 U/mL; streptomycin 10 mg/mL) and 1% (*v*/*v*) 200 mM L-glutamine. Cell lines were grown in a humidified atmosphere of 95% air and 6% CO_2 at 37 °C, in T-25 flasks (Thermo Scientific, Waltham, MA, USA) until confluence and then were trypsinized (0.25% Trypsin-0.53 mM EDTA). HEK293 (250,000 cells per mL) and HeLa (300,000 cells per mL) cells were seeded at a volume of 1 mL in 12-well plates (Sarstedt, Nümbrecht, Germany) and grown to confluence before allergen treatment.

2.2. Cysteine Protease Treatment

Two proteolytic enzymes, papain from Carica papaya and actinidin from Actinidia deliciosa, were employed for the induction of acute cellular response in the HEK293 and HeLa cell lines. Commercial papain from papaya was purchased from Sigma–Aldrich (P 4762, Sigma–Aldrich, St. Louis, MO, USA), while actinidin was isolated from kiwifruit (Actinidia deliciosa) according to the previously published procedure [50]. Before the treatment, actinidin (0.9 mg/mL) was incubated for 1 h at 37 °C in DMEM (enzyme activation) or DMEM with an equimolar amount of E64 inhibitor (enzyme inactivation). Before the treatment, papain (0.4 mg/mL) was dissolved in the medium without or with an equimolar amount of E-64 cysteine protease inhibitor. Confluent HEK293 and HeLa cell monolayers were treated with papain, inactivated papain, activated actinidin, inactivated actinidin, or DMEM/EMEM without FBS at 37 °C for 0 (1 h before the treatment), 3, 6, or 12 h, respectively. The leakage of UA from HEK293 and HeLa cells into the medium was measured using the electrochemical sensor $La(OH)_3$@MWCNT/CP.

2.3. Reagents and Apparatus

The crystal structure of $La(OH)_3$@MWCNT nanocomposite was examined using powder X-ray diffraction (XRD) data collected using a high-resolution SmartLab® X-ray diffractometer (Rigaku, Japan) with a Cu Kα radiation source. The operating current and voltage were 30 mA and 40 kV, respectively. For the experiments, the dried powders were flattened with a zero-background silicon plate. Diffraction data were collected in the range of 10–60° 2θ with a step of 0.03° and recording speed of 2°/min. The average crystallite size was estimated by applying Scherrer's equation on the most intensive diffraction peaks (Ls = κλ/βscos(θB. The morphology and surface properties of nanocomposite used for electrode modification were investigated using a field emission-scanning electron microscope FE-SEM MIRA3 (Tescan, Czech Republic) operating at 20 keV. The magnification of the composites was in the range of 10–100,000 times. The samples were prepared by fixating the conductive tape on a holder, vacuum drying, and spray-coating with gold using a Sputter coater.

All electrochemical measurements were carried out using a CH Instruments analyzer (Austin, TX, USA) driven by voltammetric software CHI (Version 4.03). A three-electrode system was employed, with a modified carbon paste (CP) working electrode (WE), a Calomel reference electrode (RE), and a Pt wire as the counter electrode (CE). The measurements were conducted in 10 mL of 0.1 phosphate buffer (PB) at pH 6. Electrochemical characterization of working electrodes was conducted using electrochemical impedance spectroscopy (EIS) and cyclic voltammetry (CV) in 5 mM $K_3[Fe(CN)_6]/K_4[Fe(CN)_6]$ (1:1) in 0.1 M KCl solution. EIS measurements were conducted in the frequency range from 10 kHz to 10 mHz, at 0.3 V. The used experimental parameters for CV measurements were: potential range from −0.5 V to 1 V and the scan rate of 50 mV/s. The CV measurements were also performed in the 0.1 M PB (pH 6) solution containing 10 μM UA Chronoamperometry (CA) was the detection and quantification method of choice. Measurements were taken in 0.1 M PB at pH 6, with the potential set on 0.3 V while adding an increasing quantity of UA during the period of 600 s. High-performance liquid chromatography (HPLC) for uric acid analysis was conducted (Dionex Ultimate 3000, Thermo Fisher, Waltham, Massachusetts, USA) with photodiode array detection on a Hypersil Gold aQ C18 analytical column (150 mm × 3 mm, 3 μm).

2.4. Material Preparation

2.4.1. Synthesis of $La(OH)_3$@MWCNT Nanocomposite

$La(OH)_3$@MWCNT powder was prepared by means of the method reported in the literature [51], after some modifications. At the very beginning, a 1 M solution of $LaCl_3$ was prepared by dissolving the proper amount of corresponding salt in ultra-pure water. A volume (5 mL) of the starting solution was treated with vigorous and constant stirring. Then, the same volume of 2 M K_2CO_3 solution (5 mL) was rapidly introduced into this

mixture, with the addition of a few drops of 1 M NaOH solution to initiate precipitation. After the precipitation was complete, the precipitate was filtered and washed with distilled water several times until the washed water became neutral (pH = 7). Furthermore, the obtained product was washed three times with ethanol and then dried at 100 °C for 6 h.

2.4.2. Electrode Preparation

An unmodified glassy carbon paste electrode was prepared by mixing 80% of glassy carbon powder and 20% of paraffin oil in a mortar to form the homogeneous carbon paste. Modified glassy carbon paste electrodes were made by mixing 1.6 weight percent of $La(OH)_3$, 0.4% of MWCNTs and 2, 5, and 10% of $La(OH)_3$@MWCNTs (with the $La(OH)_3$ to MWCNT balance being 4:1) in the unmodified paste. Subsequently, the working electrode was filled with the paste, and the electrode surface was polished with paper, washed with DI water, and directly used for measurements.

3. Results and Discussion

3.1. Characterization

The XRD patterns of synthesized $La(OH)_3$@MWCNT are shown in Figure 1A. It is clear that the sample is highly crystalline and the diffraction peaks at 15.6°, 26.3°, 27.9°, 31.5°, 36.0°, 39.5°, 47.1°, 48.7°, 49.9°, and 55.3° match well with the crystal planes of (100), (110), (101), (200), (111), (201), (002), (211), (102), (112). All of the reflections can be assigned to lanthanum hydroxide having a hexagonal symmetry and P63/m space group (JCPDS #36-148128) [52]. The average crystallite size of $La(OH)_3$ nanoparticles is (26 ± 4) nm, calculated by Scherrer's equation. The peaks from other phases occurring at 19.6° and 42.3° can be assigned to (002) and (110) reflections of graphitic MWCNT [53]. This can be proof of successful composite formation.

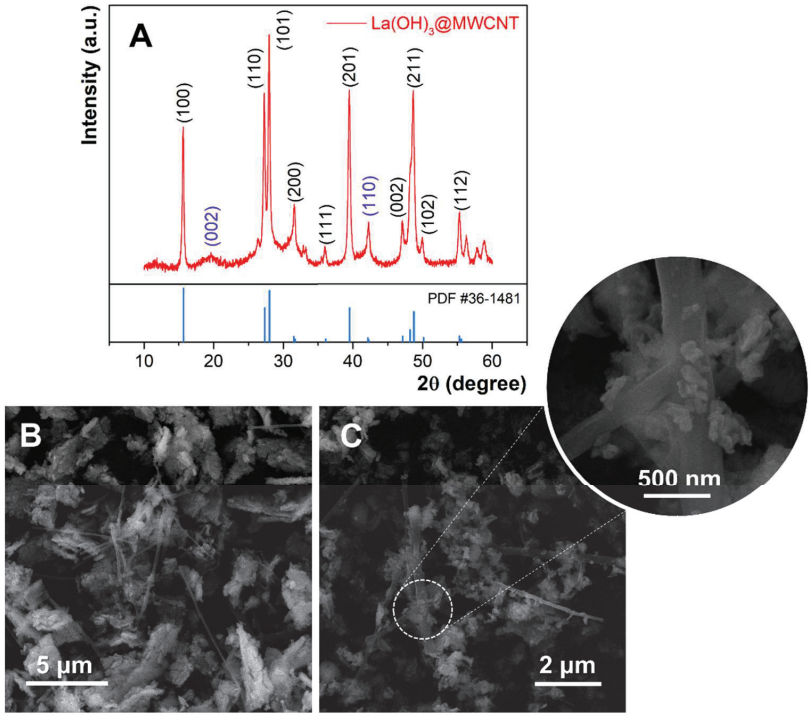

Figure 1. (**A**) XRD pattern of prepared $La(OH)_3$@MWCNT composite, (**B**,**C**) SEM micrographs of $La(OH)_3$@MWCNT at different magnifications.

The morphology and the shape of prepared $La(OH)_3$, as well as the $La(OH)_3$@MWCNT composite, are analyzed by FE-SEM. Different magnifications of the composite are displayed in Figure 1B,C. The $La(OH)_3$ nanoparticles are scattered over long multi-walled carbon nanotubes. This makes the surface of the nanotubes significantly larger, which can potentially affect the electrochemical properties of the composite. The rice-like lanthanum hydroxide nanoparticles are partially agglomerated, with an average diameter between 100 and 200 nm, and a width ranging from 30 to 60 nm (inset of Figure 1C).

3.2. Treatment of HEK293 and HeLa Cells with Cysteine Proteases

Many allergens have biological activities, including enzymatic ones. Exposure to proteases via the respiratory tract can induce the release of UA into the airway lumen, and promote type 2 immune response [53]. In this study, two allergens with cysteine protease activity, papain and actinidin, were employed as stressor agents for the induction of UA release as an endogenous danger signal molecule. Papain is a potent proteolytic enzyme [54] (EC 3.4.22.2) and allergen from papaya. Actinidin is a major allergen from kiwifruit (Actinidia deliciosa), which was purified under native conditions. The purified enzyme preserved cysteine protease activity [54] and was employed for cell treatment. Detection of UA was performed in the respective cell culture medium after the treatment of HEK293 cells as well as HeLa cells with papain and actinidin after 0, 6, 12, and 24 h, respectively. Papain was a potent inducer of UA release from both cell lines in a time-dependent manner, while actinidin did not induce detectable amounts of the UA molecule. Although the molecular mechanisms for UA release upon allergen treatment are not clarified in detail, papain exhibits five times higher proteolytic (caseinolytic) activity than actinidin [54].

3.3. Electrocatalytic Properties of the Electrode Materials

Characterization of the electrodes' surfaces during the optimization of the final electrode modification was performed using CV and EIS. CV was employed to determine the interfacial properties of electrode materials and examine electron transfer kinetics between the electrode surface and the electrolyte. Firstly, the unmodified carbon paste electrode was compared to $La(OH)_3$-, MWCNT-, and $La(OH)_3$@MWCNT-modified CP electrodes to define the optimal nanomaterial composition to use for electrode modification. CVs were performed in PB at pH 6 in the 5 mM redox probe $K_3[Fe(CN)_6]/K_4[Fe(CN)_6]$ and 0.1 M KCl support electrolyte, at the scan rate of 50 mV/s (Figure S1). The oxidation and reduction peaks that originate from the $Fe^{2+/3+}$ redox pair are visible on every voltammogram obtained using unmodified and modified CP electrodes (Figure S1A). The oxidation peak currents, for 2% (weight percent) of individual modifiers in the paste amount 16.73 μA, 12.39 μA, 16.87 μA and 18.21 μA for CP, $La(OH)_3$/CP, MWCNTs/CP and $La(OH)_3$@MWCNTs/CP, respectively. Consequently, $La(OH)_3$@MWCNTs/CP was determined to have the best electrocatalytic properties and was chosen for further examination. The next step in the electrode's surface optimization was varying the modifier percentage in CP. The resulting voltammograms (Figure S1A) show a steady rise in oxidation peak current with the increase in the share of the modifier in CP. The peak current values equaled 18.13 μA for 2%, 23.47 μA for 5%, and 30.81 μA for 10% of $La(OH)_3$@MWCNTs in the CP. Furthermore, with the increase in the modifier content in CP from 2% to 10%, the oxidation peak potential shifted from 0.46 V to 0.32 V, with peak-to-peak separations (ΔE) = 0.69 V, 0.47 V and 0.36 V and oxidation/reduction current ratios (Ia/Ic) = 1.02, 1.01 and 1.04 for 2%, 5% and 10% $La(OH)_3$@MWCNTs/CP, respectively. Higher values for the peak-to-peak separation in this system, in comparison with the theoretical value of 59 mV, is a common phenomenon and it is the product of the heterogeneity of the hand-made carbon paste electrodes. The reported decrease in the ΔE value, as a result of the increase in the amount of the modifier, indicate excellent properties of the selected composite regarding the diffusion properties of the electrode surface. Since oxidation occurs on lower potentials and the other parameters point out that the electrode reaction is reversible when

using 10% $La(OH)_3$@MWCNTs/CP, this electrode material is assumed to have the best electrocatalytic properties.

To further support the abovementioned assumptions, effective surface areas were estimated for each electrode. Calculations were performed using the Randles–Sevcik Equation and the specific surface areas of the electrodes were 2.02 mm^2, 1.50 mm^2, 2.04 mm^2, 2.20 mm^2, 2.83 mm^2 and 3.72 mm^2 for CP, $La(OH)_3$/CP, MWCNT/CP, 2% $La(OH)_3$@MWCNT/CP, 5% $La(OH)_3$@MWCNT/CP and 10% $La(OH)_3$@MWCNT/CP, respectively. This proves, once again, that composite material formation is a crucial part of the modification process. Not only does it enhance the material's electrocatalytic properties, but also leads to an increase in the effective surface area.

In addition to estimating the electron transfer resistance of the chosen electrode and comparing its values to those obtained using different materials, EIS gives information on other conductivity/resistance-related properties of the electrode system, such as double-layer capacitance or diffusion rate. EIS spectra consist of a semicircle (high frequency) and a linear (low frequency) region. The semicircle radius is electron transport resistance-dependent and is defined by its Rct value, while the linear part is diffusion-dependent. The measurements were conducted in PB pH 6, in the 5 mM redox probe containing $Fe^{2+/3+}$ redox pair from cyano complexes and 0.1 M KCl support electrolyte. Rct values of CP, $La(OH)_3$/CP, MWCNTs/CP and $La(OH)_3$@MWCNTs/CP (Figure S2A) were 40,480 Ω, 29,956 Ω, 48,345 Ω and 35,160 Ω, respectively.

Contrary to our beliefs, these values indicate that MWCNTs have the poorest electrocatalytic features. However, $La(OH)_3$ encourages the electron shuttle and thus has the lowest Rct value, while the composite material exhibits improved properties when compared to the unmodified paste and MWCNTs alone. Moreover, as previously discussed, this material shows the best current response in the cyclic voltammetry measurements, which confirms that $La(OH)_3$@MWCNTs exhibits the optimal electrocatalytic activity. Furthermore, the increase in the $La(OH)_3$@MWCNTs amount in the paste leads to the reduction in Rct and thus the improvement of the overall electrochemical performance, which is evident from the experimental data (Figure S2B). The obtained Rct values are 35,015 Ω, 29,889 Ω, and 19,559 Ω for the 2%, 5%, and 10% $La(OH)_3$@MWCNTs/CP, respectively. In short, better CV response and the decrease in the Rct values with the increase in the modifier content prove the positive impact of the composite formation and the synergetic effect of its components on the electron transfer kinetics enhancement.

3.4. The Material Behavior in the Presence of UA

To further examine electrodes' compatibility with the chosen analyte, their electrochemical response was measured in the presence of UA. The measurements were conducted in 10 mM uric acid solution in 0.1 M PB pH 6, in the potential range from 0.2 V to 1 V and at the scan rate of 50 mV/s. Cyclic voltammograms of CP, $La(OH)_3$/CP, MWCNTs/CP, and $La(OH)_3$@MWCNTs/CP electrodes show the oxidation peak current values 0.31 μA, 0.28 μA, 0.27 μA, and 0.27 μA, respectively (Figure S3A). Considering only anode peak height, we could assume that electrode modification does not significantly influence the electrodes' performance in the presence of UA. We could also incorrectly conclude that the unmodified CP electrode shows the best properties. However, reflecting on the complete potential area, it is obvious this is not the case. We can see that with the electrode modification, the resolution of the peak improves and residual current decreases. This leads to better peak to peak separation and to a lowering of the detection limit. Furthermore, while the oxidation of the analyte occurs on the same potential on every voltammogram, the electrolysis of the supporting electrolyte shifts to higher potentials as we proceed with the electrode modification, from 0.49 V for CP to 0.67 V for $La(OH)_3$@MWCNTs/CP. This additionally lowers capacitive current, improves peak shape, and enables a stable and reproductive environment for detecting low analyte concentrations.

When compared to an unmodified CP electrode, modified electrodes (MWCNTs/CP, $La(OH)_3$/CP, and $La(OH)_3$@MWCNT/CP) provide a significantly improved voltammetric

peak and higher currents (I) toward UA detection. The CV signals of UA using these modified electrodes were similar, so for the selection of the optimal electrode for further experiments, we used the data obtained from the electrochemical characterization of all electrodes, as previously described. The $La(OH)_3$/CP electrode had the poorest CV response based on these measurements, most likely due to a decrease in electrode active surface area. MWCNTs promoted electron transfer and decreased the interfacial resistance, and better CV response was achieved when MWCNTs/CP were used. The $La(OH)_3$ likely makes the entire complex of MWCNTs and $La(OH)_3$ more porous, which can help improve the response of the modified electrode. All of this led to the conclusion that the synergistic effect of MWCNTs and $La(OH)_3$ improved the modified electrode's electrochemical properties, which will contribute to the sensor's analytical performance for uric acid detection. The electrochemical behavior of $La(OH)_3$@MWCNTs/CP electrodes, with different weight percent of the modifier (from 2% to 10%) was compared using CV (Figure S3B). It is evident from the graph that the material manifests a catalytic effect on the electron shuttle, with the oxidation peak currents being 0.27 μA, 0.36 μA, and 0.45 μA for the electrodes containing 2%, 5%, and 10% of the modifier. Furthermore, the increase in the material contained in the paste was followed by oxidation peak potential shift to lower values, from 0.39 V for 2% to 0.33 V for 10% of the composite material in CP, in addition to a further decrease in the capacitive current. Therefore, the material containing 10% of the composite was determined to be the most suitable for further development of the sensing platform for UA detection in human cells. Additionally, we recorded the CV of three different concentrations of UA, using the electrode with 10% of the composite material in CP (Figure S3C).

3.5. Optimization of pH of the Supporting Electrolyte. Study of the Reaction Kinetics-Influence of Varying Scan Rates on the Material

For optimization of the pH of the supporting electrolyte, CV measurements were performed with $La(OH)_3$@MWCNTs/CP electrode containing 10% of the modifier mixed in the carbon paste. Measurements were taken in 0.1 M PB, in the pH range from 2 to 9, at the scan rate of 50 mV/s, and they confirm that the reaction is pH-sensitive. The more alkaline the solution becomes, the oxidation peak potential shifts to lower values, from 0.56 V at pH 2 to 0.24 V at pH 9 (Figure 2A). On the contrary, peak current values increase with the rise in pH, only to gradually drop afterwards, reaching the maximum of 0.45 μA at pH 6. Furthermore, peak resolution is fairly good on lower pH values, ending with pH 6 where the peak is well defined and narrow, unlike the broad peaks at higher pH. The obtained results correlate well with UA's pKa [55] values and electrocatalytic oxidation mechanism (Scheme 2) [55].

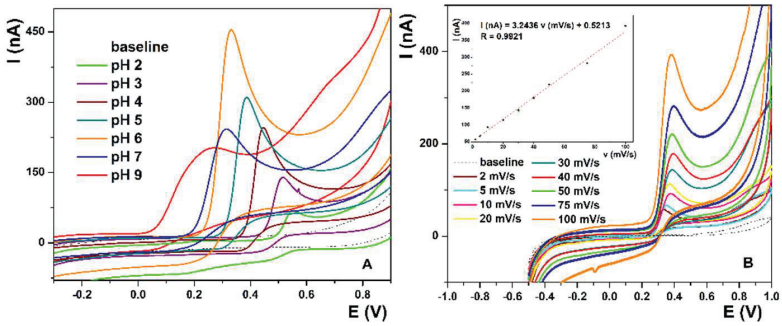

Figure 2. (**A**) Optimization of pH of the 0.1 M PB supporting electrolyte from pH 2 to pH 9. (**B**) CV in 0.1 M PB pH 6 in the potential range from −0.5 V to 1 V at the scan rates from 2 mV/s to 100 mV/s. (inset B) Linear plot of oxidation peak current vs. scan rate.

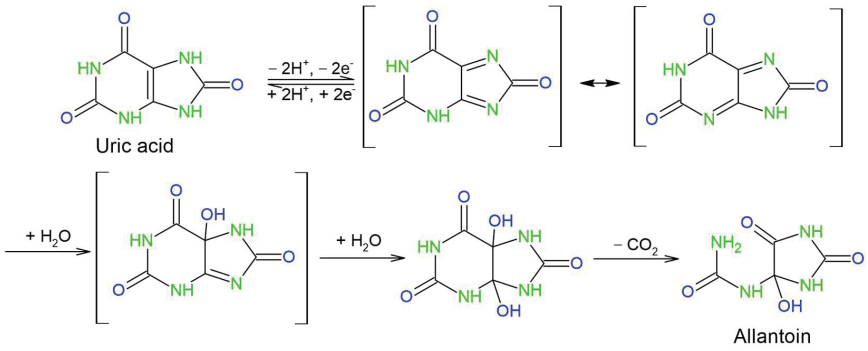

Scheme 2. Mechanism of electrooxidation of UA.

The reported mechanism can be divided into three main steps—2e-/$2H^+$ deprotonation and the oxidation of uric acid, the hydration of the intermediate diimine and its subsequent decomposition into allantoin and CO_2. While this mechanism infers that the reaction is pH-dependent and that alkaline conditions allow the initial deprotonation to proceed, it is less obvious as to why the pH values higher than pH 6 are less favorable. Since pKa values for uric acid are 5.4 and 9.8, we can assume that the elevation of pH above pH 6 leads to further deprotonation of urate or diimine, thus introducing new intermediate species and broadening the oxidation peak, lowering its resolution and decreasing the maximal peak current.

The best performance of the electrochemical system at pH 6, and its similarity with the physiological conditions are the reasons why this pH is used for all further measurements.

The CV measurements in PB pH 6 were conducted with optimized electrode surface parameters at various scan rates (from 2 mV/s to 100 mV/s) to determine the reaction kinetics. The oxidation peak potential and ΔE are constant for all scan rates in the measured range (Figure 2B), while the peak current values (inset Figure 2B) increase linearly with the increase in the scan rate, which is described by the equation I(nA) = 3.2436 v (mV/s) + 0.5213, with the linear regression coefficient R = 0.9921. This means that the UA solution is stable, the electron transfer processes are fast, and the electrode reaction is an adsorption-controlled process. From the equation $i\_p = (n^2 F^2)/4RT\ vA\Gamma^*$, we can calculate the surface coverage of the adsorbed species (Γ*) [56]. The surface coverage values for the scan rates from 2 mV/s to 100 mV/s are 0.11 μmol/cm^2, 44.08 nmol/cm^2, 22.04 nmol/cm^2, 11.02 nmol/cm^2, 7.35 nmol/cm^2, 5.51 nmol/cm^2, 4.41 nmol/cm^2, 2.94 nmol/cm^2 and 2.20 nmol/cm^2. These values indicate that, although the adsorption of the UA on the electrode surface decreases with the increase in the scan rate, it is not negligible and can influence the accuracy of the measurements. To prevent introducing a systematic error in the measurements, the surface of the electrode was renewed before each measurement (the excess paste was squeezed out of the electrode, polished with a clean piece of paper and washed with deionized water). The simple and reproducible restoration of the clean electrode surface was one of the major advantages of using the carbon paste electrode in this study.

Even though the anodic peak does not show potential shift and its current linearly increases with the scan rate, the reduction peak is almost absent in all voltammograms, while the cathodic capacitive current increases with the increase in the scan rate. This indicates that the electrode reaction is characterized by a reversible electron transfer followed by an irreversible chemical reaction [56]. In this case, the irreversible chemical reaction is allantoin formation, and it is incorporated in the electrochemical step.

3.6. Uric Acid Detection

Amperometric determination was used for UA quantification due to its low detection limit, rapidness, wide linear range, easy signal processing, and the possibility of following the real-time concentration changes in flow systems. The amperometric response of the

$La(OH)_3$@MWCNTs/CP electrode, containing 10% of nanomaterial mixed in the CP, toward different standard solutions of the UA, was recorded in 0.1 M PB pH 6, at the fixed potential at 0.3 V (Figure 3A). Successive UA addition to the solution was accompanied by a corresponding current increase and the calibration plot I (nA) against c (μM) was constructed (Figure 3B). The linear response was in the range from 0.67 μM to 121 μM UA with the detection limit, calculated from the plot as 3 S/m (where S is the standard deviation of the blanc and m is the slope of the calibration plot), 64.28 nM, and the analogously calculated limit of quantification (10 S/m) was 0.22 μM. The calibration curve follows the trend expressed by the linear regression equation I (nA) = 2,1582 + 0.4430 c (μM), with the linear regression coefficient R = 0.9969.

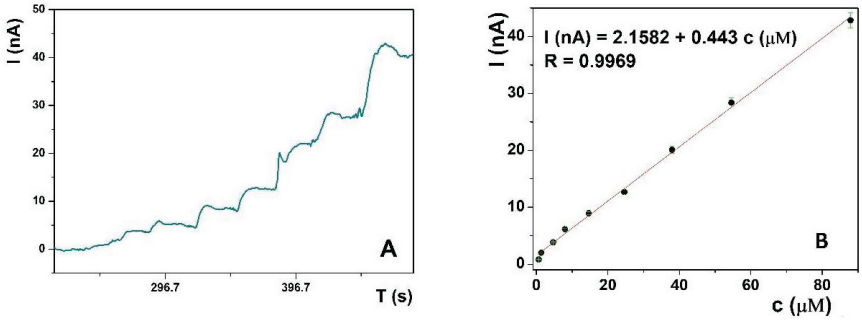

Figure 3. (**A**) Amperometric response of the $La(OH)_3$@MWCNT modified CP electrode in 0.1 M PB pH 6 towards successive addition of UA standard solution. (**B**) Calibration curve of amperometric current depending on the concentration of UA in the analyte solution, in the range from 0.67 μM to 121 μM.

Five successive measurements of 2 μM UA standard solution were performed, to test the repeatability of the proposed sensing platform for UA determination and monitoring, and the obtained current values were 6.01 nA, 5.71 nA, 5.70 nA, 5.71 nA and 5.42 nA, giving an RSD of 3.65% (Figure S4). The reproducibility was estimated with five different electrodes, which were constructed independently using the proposed procedure (Figure S4). The RSD is 4.13% for the peak current measured in 2 μM UA in PBS (pH 6.0), which demonstrates the reliability of the fabrication procedure. The stability of the modified electrode was also studied using CV. When the electrode was cyclically swept for 30 cycles, the decrease in the initial responses of the modified electrode was 3.6%.

Furthermore, we conducted an extensive literature overview and compared the linear working range, LOD and RSD of our method to the best methods documented in the literature (Table 1). The results suggest that the proposed sensing platform is comparable, if not better than those previously reported. Several UA detection methods using only carbon nanotubes as the electrode material have been reported [21,57]. Although these sensors have adequate linear ranges, they generally have slightly higher detection limits compared to electrode utilizing modified materials, or require complex purification techniques prior analysis. By using MWCNTs decorated with $La(OH)_3$ nanoparticles to modify the CP electrode, a very good sensitivity of the UA detection method was achieved. This is probably due to the joint action of the modifier—the alkaline properties of $La(OH)_3$, which facilitate the binding of UA, as well as the increase in the active surface area and electron transfer efficiency by MWCNTs.

Table 1. An overview of recently reported nanomaterial-based electrochemical methods for the determination of UA.

Materials Used	LOD	Linear Working Range (μM)	RSD (%)	Detection Method	Ref. No.
$La(OH)_3$@MWCNT/CP	64.28 nM	0.67–121	3.65	CA	This work
SWCNTs array-GCE	0.82 μM	10–200	/	SWV	[57]
MoS_2/rGO	0.46 μM	25–2745	3.23	DPV	[58]
$LaFeO_3$	30 nM	0.15–800	3.47	DPV	[47]
NiO/GO	0.14 μM	2.0–120	/	DPV	[11]
$TmPO_4$/GO	3.73 μM	10–100	3.20	DPV	[12]
PEDOT/PANI	0.24 μM	0.7–100	3.10	DPV	[13]
Fe_2O_3–NG/GCE	75 nM	10–100	3.09	DPV	[14]
Au-MoS_2	18.2 nM	0.033–10	1.29	DPV	[15]
TiO_2/TiCT/NUF	0.18 nM	0.001–60	0.42	DPV	[16]
NiTSPc/ITO	8 μM	60–600	3.80	ECL	[19]
Pt	20 nM	2.0–100	2.90	ECL	[20]
CNT	60 nM	1–500	1.20	BIA-MPA	[21]
Pd-Pt/OMC/SPCE	0.25 μM	0.25–800	2.40	FIA	[22]

3.7. Interference Studies

One of the essential features of the sensor is its selectivity. CV measurements of a 10 μM UA solution in 0.1 M PB at pH 6 were conducted in the presence of common interferents found in biological matrices. Both organic and inorganic interfering species which exist in the lysed cell culture were taken into account. The measurements are performed in the potential range from −0.5 V to 1 V, at the scan rate of 50 mV/s, with the ratio of UA and potential organic interferents 1:1. The chemical behavior of UA in the presence of ascorbic acid (AA), citric acid (CA), dopamine (DOPA), gallic acid (GA) and glucose (GLU) is shown in the Supplementary Data (Figure S5A). While CA and GLU do not influence UA detection, the other interferents lead to signal elevation. However, the peak originating from UA remains visible and measurable in the presence of DOPA, AA and GA (Figure S5A). Although considerable interferences originating from the substances commonly present in the biological matrix present the major drawback of the proposed method, they can be overcome by careful experiment planning and execution and/or the use of chemometric methods. We proved this by measuring only the height of the peak originating from UA oxidation, which remains nearly the same in all samples, with the highest deviation for the ascorbic acid (histogram on Figure S5B).

Considering the fact that high concentrations of salts can be present in the sample, the influence of 0.1 M KCl, NaCl, $CaCl_2$, MgOAc and NaOAc in 0.1 M PB at pH 6 on detection of 10 mM UA was studied. The results show that none of the mentioned salts in a 1000:1 ratio to UA influence UA detection. The interference study proves that the proposed sensing platform shows satisfying selectivity towards UA in the presence of common organic and inorganic interferents.

The practicability estimation of the developed method after the cell stress.

To analyse the applicability of the proposed sensing platform in biological samples, measurements were conducted in a real sample matrix. CV measurements were performed in the potential range from −0.5 V to 1 V at the scan rate of 50 mV/s in the presence and absence of UA to scan for potential interferents (Figure S6A). The baseline in the biological matrix gives a high current response, originating from the oxidation of electrochemically active species contained in the matrix. However, this does not influence the UA amperometric detection, because, at 0.3 V, where uric acid oxidation occurs, no matrix interferences are present. To prove this, a calibration curve is constructed once again in the biological sample matrix (DMEM). The obtained results are displayed by the amperometric curve (Figure S5B) and corresponding plot (inset Figure S6B). The amperometric current response changes linearly with the UA concentration in the range from 1 μM to 38 μM, which is described by the equation I (nA) = 4.1455 + 0.4326c μM, with the linear regression coefficient R = 0.9910.

After the calibration, real sample analysis was conducted. The samples were obtained by treating the human HEK293 and HeLa cell cultures with the papain, and the actinidin allergen, respectively, during a time frame of 12 h. Ten microliters of the sample was added to 5 mL of 0.1 PB at pH 6, and the change in the amperometric current at 0.3 V was measured. However, the UA concentration in the sample was found to be lower than the limit of quantification. Therefore, the sample was spiked with UA standard solution, so the final concentration of UA (spiked) was 100 μM. The measurements were repeated five times with the spiked sample, and the mean value of the rise in the amperometric signal corresponded to the 0.2010 mM UA concentration in the 5 mL of PB, which agrees with the total UA concentration in the sample of 100.5 μM. That proves that the proposed method is applicable in real sample analysis. However, it requires either more concentrated samples, larger quantities of samples, or spiking the samples with a known amount of UA.

To further support this claim, a series of HeLa and Hek293 cell cultures were treated with papain and EG4 inhibited papain for prolonged periods. The cell cultures were prepared in duplicate with each of the abovementioned allergens independently and the amperometric response at 0.3 V was recorded immediately after the addition of allergens, and after incubation periods of 3 h, 6 h and 12 h. The obtained results are given as mean values of the measurements in Table 2. The control groups of cells, without the added allergens, were also analyzed to compare the UA release from the treated and the untreated cells.

Table 2. The concentrations of UA obtained using the developed amperometric method (sensor) and HPLC as the reference method after the incubation of HeLa and HEK293 cells with papain.

Human Cell Lines	Incubation Period	Papain		Standard Deviation		E64 Inhibited Papain		Control	
		Sensor	HPLC	Sensor	HPLC	Sensor	HPLC	Sensor	HPLC
HeLa	0	/	/	/	/	/	/	/	/
	3	/	/	/	/	/	/	/	/
	6	1.03	1.00	0.0919	0.10	/	/	/	/
	12	1.96	1.89	0.0981	0.11	/	/	/	/
Hek 293	0	/	/	/	/	/	/	/	/
	3	/	/	/	/	/	/	/	/
	6	0.78	0.81	0.1626	0.16	/	/	/	/
	12	2.56	2.55	0.0283	0.03	/	/	/	/

The acquired values indicate that the stress on the cells after the adequately long (6 h and 12 h) exposure to papain is sufficient to release considerable amounts of UA. Furthermore, the quantity of UA released is directly proportional to the incubation period, proving that the developed method is suitable for real-time detection or monitoring of cell damage or stress.

For method validation, the same real samples were analyzed by using HPLC as a standard method. The obtained results display good agreement with those achieved in the developed electrochemical method. The recoveries of the determination are 94.3–103.0%, indicating good accuracy of the developed method in real sample analysis.

3.8. Environmental Impact of the Analysis

While developing an analytical procedure, attention is being shifted more and more to its ecological acceptability. Several methods can assess the green aspects of an analytical procedure in which the green analytical procedure index (GAPI) (Scheme 3A) and Analytical GREEnness metric approach and software (AGREE) (Scheme 3B) are used. While GPAI is the most comprehensive and has the advantages of graphically describing all relevant factors-quantification; sample collection, preservation, transport and storage; sample preparation; reagents and compounds used and instrumentation, AGREE enables straightforward interpretation, since the level of greenness is expressed numerically on a scale from

0 to 1, with 1 being the greenest. Furthermore, AGREE contains all the relevant data about the analytical procedure and is easy to generate thanks to a free software downloadable from https://mostwiedzy.pl/AGREE (accessed on 7 June 2022) [59]. For GAPI, each aspect is presented with a pentagon further divided into segments that stand for specific demands that make a procedure green (amounts of solutions used, purification, energy consumption, generated waste, etc.). The colors of the segments depict the low, medium or high impact of the method on the environment, moving from green through yellow to red, and each of them has to fulfil certain conditions to be considered green [60].

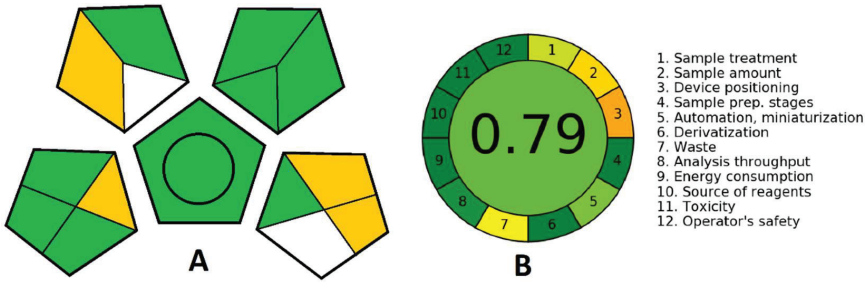

Scheme 3. (**A**) GAPI and (**B**) AGREE pictograms for the estimation of the greenness of the analytical procedure.

In Scheme 3, we can see that the analysis performed with the proposed sensing platform is quantitative and can be performed at-line. Thus, no sample preservation, transport or storage is needed. Furthermore, the cell culture matrix can be used directly or dissolved in water or biological buffer without any prior purification or sample preparation. This minimizes the energy consumption and the amount of generated waste, while the minimum volume needed for the analysis is 5 mL. Overall, this analytical procedure can be considered green, direct and robust and it can easily be further miniaturized for commercial application.

4. Conclusions

This paper developed and tested a sensing platform for UA determination in the biological sample. Knowing that the electrode surface modifications are the key enabler for next-generation chemistries based on the interface reactions, we offered a sensing platform based on the novel composite material, optimized to have the best electrochemical performance. Their compatibility with the UA as the analyte was tested and the calibration was performed in the optimal conditions, showing remarkable sensitivity and a wide dynamic working range. Reproducibility and repeatability tests have shown excellent accuracy and precision of the method as a limiting and key factor for practical application. The disadvantage of this method is its limited selectivity in the presence of the common interfering species in the biological matrix. However, this drawback can be bypassed by good experiment planning and/or the use of chemometrics. In the end, the proposed sensing platform was tested in the human cell cultures exposed to the allergens. In the first series of samples (stressed with the papain, and actinidin allergen), concentrations of UA were too low to perform the direct measurement, so the samples had to be spiked. In spite of that, we were able to determine the UA concentration and to repeat the measurements with the unspiked samples stressed with papain. In this way, we not only proved that the stress induced in the cells can be measured by this method, but clearly distinguished the levels of stress induced in HeLa and Hek 293 cell cultures by the use of three different allergens (papain, and actinidin). Since UA is released when cells suffer from stress, sensing devices that can measure a change in the UA concentration can provide us with plenty of information on both the environmental factors and pathological states that cause stress to the human organism. Furthermore, the simplicity of this method and the device itself

opens up opportunities for its commercial use. Hence, we think that this sensing device, as it is, can potentially find applications in medical research and clinical practice.

Supplementary Materials: The following supporting information can be downloaded at: https://www.mdpi.com/article/10.3390/bios12090705/s1. Figure S1. Cyclic voltammograms in 5 mM $Fe^{2+}/^{3+}$ in 0.1 M KCl and 0.1 M PB pH 6, in the potential range from −0.5 V to 1 V at the 50 mV/s scan rate of (A) unmodified CP electrode and electrodes modified with 2% of $La(OH)_3$, MWCNT and $La(OH)_3$@MWCNT B) electrodes modified with 2%, 5% and 10% of $La(OH)_3$@MWCNT. Figure S2. EIS spectra in 5 mM $Fe^{2+}/^{3+}$ in 0.1 M KCl and 0.1 M PB pH 6 on 0.3 V and in the frequency range from 10 kHz to 10 mHz of (A) unmodified CP electrode and electrodes modified with 2% of $La(OH)_3$, MWCNT and $La(OH)_3$@MWCNT (B) electrodes modified with 2%, 5% and 10% of $La(OH)_3$@MWCNT. Figure S3. (A) CV in 0.1 M PB pH 6 in the presence of 10 μM UA—unmodified CP electrode and electrodes modified with 2% of $La(OH)_3$, MWCNT and $La(OH)_3$@MWCNT (B) CV in 0.1 M PB pH 6 in the presence of 10 μM UA—electrodes modified with 2%, 5% and 10% of $La(OH)_3$@MWCNT (C) CV in 0.1 M PB pH 6 in the presence of 7.5; 10 and 100 μM UA using electrode modified with 10% of $La(OH)_3$@MWCNT. Figure S4. Repeatability and reproducibility studies for proposed sensor. Figure S5. Studying the impact of potential interferents on UA detection (A) CV in 0.1 M PB pH 6, at the potential range from −0.05 V to 1 V at the scan rate 50 mV/s, (B) Histogram—percent of the anodic peak current which arose from the oxidation of UA. Figure S6. (A) CV in the potential range from 0.5 V to 1 V at the scan rate of 50 mV/s in the biological matrix in the presence and absence of UA (B) Amperometric curve of UA in the real sample matrix (inset B) Calibration curve of UA standard solutions in the biological matrix.

Author Contributions: Conceptualization, S.K., M.O., M.Z. and V.S.; formal analysis, A.N.; investigation, S.K. and M.O.; writing—original draft preparation, S.K., M.O., M.G.-J. and D.S.; writing—review and editing, S.K., M.O., M.G.-J. and D.S.; supervision, M.G.-J. and D.S. All authors have read and agreed to the published version of the manuscript.

Funding: This work was supported by Ministry of Education, Science and Technological Development of Republic of Serbia Contract number: 451-03-68/2022-14/200168, and the research was funded by Ministry of Science and Higher Education of the Russian Federation (agreement No. 075-15-2022-1135) and South Ural State University.

Institutional Review Board Statement: Not applicable.

Informed Consent Statement: Not applicable.

Data Availability Statement: The study did not report any data.

Conflicts of Interest: The authors declare that they have no known competing financial interests or personal relationships that could have appeared to influence the work reported in this paper.

References

1. Hu, R.; Walker, E.; Huang, C.; Xu, Y.; Weng, C.; Erickson, G.E.; Coldren, A.; Yang, X.; Brissova, M.; Kaverina, I.; et al. Myt Transcription Factors Prevent Stress-Response Gene Overactivation to Enable Postnatal Pancreatic β Cell Proliferation, Function, and Survival. *Dev. Cell* **2020**, *53*, 390–405.e10. [CrossRef]
2. El Ridi, R.; Tallima, H. Physiological Functions and Pathogenic Potential of Uric Acid: A Review. *J. Adv. Res.* **2017**, *8*, 487–493. [CrossRef] [PubMed]
3. Vénéreau, E.; Ceriotti, C.; Bianchi, M.E. DAMPs from Cell Death to New Life. *Front. Immunol.* **2015**, *6*, 422. [CrossRef] [PubMed]
4. Glantzounis, G.; Tsimoyiannis, E.; Kappas, A.; Galaris, D. Uric Acid and Oxidative Stress. *CPD* **2005**, *11*, 4145–4151. [CrossRef] [PubMed]
5. Lakshmi, D.; Whitcombe, M.J.; Davis, F.; Sharma, P.S.; Prasad, B.B. Electrochemical Detection of Uric Acid in Mixed and Clinical Samples: A Review. *Electroanalysis* **2011**, *23*, 305–320. [CrossRef]
6. Hou, S.; Yang, C.; Wang, H.; Tanaka, K.; Ding, M. Determination of Uric Acid in Human Urine by Ion-Exclusion Chromatography with UV Detection Using Pure Water as Mobile Phase. *Chin. J. Chem.* **2012**, *30*, 1102–1104. [CrossRef]
7. Kand'ár, R.; Drábková, P.; Hampl, R. The Determination of Ascorbic Acid and Uric Acid in Human Seminal Plasma Using an HPLC with UV Detection. *J. Chromatogr. B* **2011**, *879*, 2834–2839. [CrossRef]
8. Norazmi, N.; Rasad, Z.R.A.; Mohamad, M.; Manap, H. Uric Acid Detection Using Uv-Vis Spectrometer. In *IOP Conference Series: Materials Science and Engineering*; IOP Publishing: Bristol, UK, 2017; Volume 257, p. 012031. [CrossRef]

9. Li, X.-L.; Li, G.; Jiang, Y.-Z.; Kang, D.; Jin, C.H.; Shi, Q.; Jin, T.; Inoue, K.; Todoroki, K.; Toyo'oka, T.; et al. Human Nails Metabolite Analysis: A Rapid and Simple Method for Quantification of Uric Acid in Human Fingernail by High-Performance Liquid Chromatography with UV-Detection. *J. Chromatogr. B* **2015**, *1002*, 394–398. [CrossRef]
10. Zinellu, A.; Sotgia, S.; Deiana, L.; Carru, C. Field-Amplified Sample Injection Combined with Pressure-Assisted Capillary Electrophoresis UV Detection for the Simultaneous Analysis of Allantoin, Uric Acid, and Malondialdehyde in Human Plasma. *Anal. Bioanal. Chem.* **2011**, *399*, 2855–2861. [CrossRef]
11. Gao, J.; He, P.; Yang, T.; Zhou, L.; Wang, X.; Chen, S.; Lei, H.; Zhang, H.; Jia, B.; Liu, J. Electrodeposited NiO/Graphene Oxide Nanocomposite: An Enhanced Voltammetric Sensing Platform for Highly Sensitive Detection of Uric Acid, Dopamine and Ascorbic Acid. *J. Electroanal. Chem.* **2019**, *852*, 113516. [CrossRef]
12. Huang, H.; Yue, Y.; Chen, Z.; Chen, Y.; Wu, S.; Liao, J.; Liu, S.; Wen, H. Electrochemical Sensor Based on a Nanocomposite Prepared from $TmPO_4$ and Graphene Oxide for Simultaneous Voltammetric Detection of Ascorbic Acid, Dopamine and Uric Acid. *Microchim. Acta* **2019**, *186*, 189. [CrossRef] [PubMed]
13. Wang, Q.; Sun, H.; Liu, Q.; Li, L.; Kong, J. Electrodeposition of Three-Dimensional Network Nanostructure PEDOT/PANI for Simultaneous Voltammetric Detection of Ascorbic Acid, Dopamine and Uric Acid. *ChemistrySelect* **2020**, *5*, 1288–1293. [CrossRef]
14. Liu, H.; Xiong, R.; Zhong, P.; Li, G.; Liu, J.; Wu, J.; Liu, Y.; He, Q. Nanohybrids of Shuttle-like α-Fe_2O_3 Nanoparticles and Nitrogen-Doped Graphene for Simultaneous Voltammetric Detection of Dopamine and Uric Acid. *New J. Chem.* **2020**, *44*, 20797–20805. [CrossRef]
15. Selvam, S.P.; Hansa, M.; Yun, K. Simultaneous Differential Pulse Voltammetric Detection of Uric Acid and Melatonin Based on a Self-Assembled Au Nanoparticle–MoS2 Nanoflake Sensing Platform. *Sens. Actuators B Chem.* **2020**, *307*, 127683. [CrossRef]
16. Lu, X.; Li, S.; Guo, W.; Zhang, F.; Qu, F. A Covalent Organic Polymer–TiO_2/Ti_3C_2 Heterostructure as Nonenzymatic Biosensor for Voltammetric Detection of Dopamine and Uric Acid. *Microchim. Acta* **2021**, *188*, 95. [CrossRef]
17. Jiang, M.; Chen, J.S. A Lable-Free ECL Biosensor for The Detection of Uric Acid Based on Au NRs@TiO_2 Nanocomposite. *Int. J. Electrochem. Sci.* **2019**, *14*, 2333–2344. [CrossRef]
18. Ballesta-Claver, J.; Rodríguez-Gómez, R.; Capitán-Vallvey, L.F. Disposable Biosensor Based on Cathodic Electrochemiluminescence of Tris(2,2-Bipyridine)Ruthenium(II) for Uric Acid Determination. *Anal. Chim. Acta* **2013**, *770*, 153–160. [CrossRef]
19. Lin, Z.; Chen, Z.; Liu, Y.; Wang, J.; Chen, G. An Electrochemiluminescent Biosensor for Uric Acid Based on the Electrochemiluminescence of Bis-[3,4,6-Trichloro-2-(Pentyloxycarbonyl)-Phenyl] Oxalate on an ITO Electrode Modified by an Electropolymerized Nickel Phthalocyanine Film. *Analyst* **2008**, *133*, 797–801. [CrossRef]
20. Tao, Y.; Zhang, X.; Wang, J.; Wang, X.; Yang, N. Simultaneous Determination of Cysteine, Ascorbic Acid and Uric Acid by Capillary Electrophoresis with Electrochemiluminescence. *J. Electroanal. Chem.* **2012**, *674*, 65–70. [CrossRef]
21. Caetano, L.P.; Lima, A.P.; Tormin, T.F.; Richter, E.M.; Espindola, F.S.; Botelho, F.V.; Munoz, R.A.A. Carbon-Nanotube Modified Screen-Printed Electrode for the Simultaneous Determination of Nitrite and Uric Acid in Biological Fluids Using Batch-Injection Amperometric Detection. *Electroanalysis* **2018**, *30*, 1870–1879. [CrossRef]
22. Khumngern, S.; Choosang, J.; Thavarungkul, P.; Kanatharana, P.; Numnuam, A. Flow Injection Enzyme-Free Amperometric Uric Acid Sensor Consisting of Ordered Mesoporous Carbon Decorated with 3D Pd-Pt Alloy Nanodendrite Modified Screen-Printed Carbon Electrode. *Microchem. J.* **2020**, *157*, 104923. [CrossRef]
23. Manna, B. Reduced Graphene Oxide-Based Covalent Hybrid Film Electrode Self-Assembled with Gold Nanoparticles for the Enzyme-Free Amperometric Sensing of Serum Uric Acid. *Anal. Sci.* **2020**, *36*, 121–126. [CrossRef] [PubMed]
24. Shaidarova, L.G.; Chelnokova, I.A.; Gafiatova, I.A.; Gedmina, A.V.; Budnikov, H.C. Sequential-Injection Amperometric Determination of Glucose, Insulin, Cholesterol, and Uric Acid on Electrodes Modified by Nickel and Cobalt Particles. *J. Anal. Chem.* **2020**, *75*, 1218–1226. [CrossRef]
25. Manriquez, J.; Banda-Alemán, J.A.; Sotomayor-Villezcas, V.; de Larrea, G.Z.-L.; Bustos, E.; Sepúlveda, S.; Sánchez-Fernández, L.; Sosa-Ferreyra, C.F. Amperometric Detector of Uric Acid in Human Serum Based on Glassy Carbon Electrodes Modified By Gold Nanoparticles and Poly(Amidoamine) Dendrimers and Its Application to the Early Diagnosis of Preeclampsia. *Meet. Abstr.* **2020**, *MA2020-01*, 2485. [CrossRef]
26. Wang, Q.; Wen, X.; Kong, J. Recent Progress on Uric Acid Detection: A Review. *Crit. Rev. Anal. Chem.* **2020**, *50*, 359–375. [CrossRef]
27. Shi, W.; Li, J.; Wu, J.; Wei, Q.; Chen, C.; Bao, N.; Yu, C.; Gu, H. An Electrochemical Biosensor Based on Multi-Wall Carbon Nanotube–Modified Screen-Printed Electrode Immobilized by Uricase for the Detection of Salivary Uric Acid. *Anal. Bioanal. Chem.* **2020**, *412*, 7275–7283. [CrossRef]
28. Yan, Q.; Zhi, N.; Yang, L.; Xu, G.; Feng, Q.; Zhang, Q.; Sun, S. A Highly Sensitive Uric Acid Electrochemical Biosensor Based on a Nano-Cube Cuprous Oxide/Ferrocene/Uricase Modified Glassy Carbon Electrode. *Sci. Rep.* **2020**, *10*, 10607. [CrossRef] [PubMed]
29. Gupta, J.; Arya, S.; Verma, S.; Singh, A.; Sharma, A.; Singh, B.; Prerna; Sharma, R. Performance of Template-Assisted Electrodeposited Copper/Cobalt Bilayered Nanowires as an Efficient Glucose and Uric Acid Senor. *Mater. Chem. Phys.* **2019**, *238*, 121969. [CrossRef]
30. Sattar Chang, A.; Tahira, A.; Chang, F.; Naeem Memon, N.; Nafady, A.; Kasry, A.; Hussain Ibupoto, Z. Silky Co_3O_4 Nanostructures for the Selective and Sensitive Enzyme Free Sensing of Uric Acid. *RSC Adv.* **2021**, *11*, 5156–5162. [CrossRef]
31. Alam, M.M.; Asiri, A.M.; Uddin, M.T.; Islam, M.A.; Awual, M.R.; Rahman, M.M. Detection of Uric Acid Based on Doped ZnO/Ag_2 O/Co_3O_4 Nanoparticle Loaded Glassy Carbon Electrode. *New J. Chem.* **2019**, *43*, 8651–8659. [CrossRef]

32. Zhou, Y.; Yang, L.; Zhu, M.; Dang, Y.; Peng, Z. Hydrothermal Method Prepared La-Doped $ZnWO_4$ Nanospheres as Electrocatalytic Sensing Materials for Selective and Sensitive Determination of Dopamine and Uric Acid. *J. Electrochem. Soc.* **2016**, *163*, B737. [CrossRef]
33. Manjula, N.; Vinothkumar, V.; Chen, S.-M.; Sangili, A. Simultaneous and Sensitive Detection of Dopamine and Uric Acid Based on Cobalt Oxide-Decorated Graphene Oxide Composite. *J. Mater. Sci. Mater. Electron.* **2020**, *31*, 12595–12607. [CrossRef]
34. Sehit, E.; Altintas, Z. Significance of nanomaterials in electrochemical glucose sensors: An updated review (2016–2020). *Biosens. Bioelectron.* **2020**, *159*, 112165. [CrossRef]
35. Bonanni, A.; del Valle, M. Use of nanomaterials for impedimetric DNA sensors: A review. *Anal. Chim. Acta* **2010**, *678*, 7–17. [CrossRef]
36. Fang, L.; Cai, Y.; Huang, B.; Cao, Q.; Zhu, Q.; Tu, T.; Ye, X.; Liang, B. A highly sensitive nonenzymatic glucose sensor based on Cu/Cu_2O composite nanoparticles decorated single carbon fiber. *J. Electroanal. Chem.* **2021**, *880*, 114888. [CrossRef]
37. Adhikari, B.-R.; Govindhan, M.; Chen, A. Carbon Nanomaterials Based Electrochemical Sensors/Biosensors for the Sensitive Detection of Pharmaceutical and Biological Compounds. *Sensors* **2015**, *15*, 22490–22508. [CrossRef]
38. Zhang, Y.; Yuan, R.; Chai, Y.; Zhong, X.; Zhong, H. Carbon Nanotubes Incorporated with Sol–Gel Derived $La(OH)_3$ Nanorods as Platform to Simultaneously Determine Ascorbic Acid, Dopamine, Uric Acid and Nitrite. *Colloids Surf. B Biointerfaces* **2012**, *100*, 185–189. [CrossRef]
39. Kumar, Y.; Pradhan, S.; Pramanik, S.; Bandyopadhyay, R.; Das, D.K.; Pramanik, P. Efficient Electrochemical Detection of Guanine, Uric Acid and Their Mixture by Composite of Nano-Particles of Lanthanides Ortho-Ferrite $XFeO_3$ (X = La, Gd, Pr, Dy, Sm, Ce and Tb). *J. Electroanal. Chem.* **2018**, *830–831*, 95–105. [CrossRef]
40. Zhang, J.; Kang, Q.; Yang, Z.; Dai, H.; Zhuang, D.; Wang, P. A Cost-Effective NiMoB–$La(OH)_3$ Catalyst for Hydrogen Generation from Decomposition of Alkaline Hydrous Hydrazine Solution. *J. Mater. Chem. A* **2013**, *1*, 11623–11628. [CrossRef]
41. Wang, K.; Yao, Q.; Qing, S.; Lu, Z.-H. $La(OH)_3$ Nanosheet-Supported CoPt Nanoparticles: A Highly Efficient and Magnetically Recyclable Catalyst for Hydrogen Production from Hydrazine in Aqueous Solution. *J. Mater. Chem. A* **2019**, *7*, 9903–9911. [CrossRef]
42. Zou, H.; Guo, F.; Luo, M.; Yao, Q.; Lu, Z.-H. $La(OH)_3$-Decorated NiFe Nanoparticles as Efficient Catalyst for Hydrogen Evolution from Hydrous Hydrazine and Hydrazine Borane. *Int. J. Hydrog. Energy* **2020**, *45*, 11641–11650. [CrossRef]
43. Yang, S.; Li, G.; Xia, N.; Liu, P.; Wang, Y.; Qu, L. High Performance Electrochemical L-Cysteine Sensor Based on Hierarchical 3D Straw-Bundle-like Mn-La Oxides/Reduced Graphene Oxide Composite. *J. Electroanal. Chem.* **2020**, *877*, 114654. [CrossRef]
44. Nilabh, A.; Sen, S.; Narjinary, M.; Kundu, S. A Novel Ppm Level Ethanol Sensor Based on La Loaded ITO Impregnated with Pd and Sb Additives. *Microchem. J.* **2020**, *158*, 105146. [CrossRef]
45. Rzaij, J.M.; Habubi, N.F. Room Temperature Gas Sensor Based on La_2O_3 Doped CuO Thin Films. *Appl. Phys. A* **2020**, *126*, 560. [CrossRef]
46. Zhang, Y.; Ma, C.; Yang, X.; Song, Y.; Liang, X.; Zhao, X.; Wang, Y.; Gao, Y.; Liu, F.; Liu, F.; et al. NASICON-Based Gas Sensor Utilizing $MMnO_3$ (M: Gd, Sm, La) Sensing Electrode for Triethylamine Detection. *Sens. Actuators B Chem.* **2019**, *295*, 56–64. [CrossRef]
47. Wang, G.; Sun, J.; Zhang, W.; Jiao, S.; Fang, B. Simultaneous Determination of Dopamine, Uric Acid and Ascorbic Acid with $LaFeO_3$ Nanoparticles Modified Electrode. *Microchim. Acta* **2009**, *164*, 357–362. [CrossRef]
48. Guo, J.; Xu, G.; Shen, F.; Fu, Y.; Zhang, Y.; Guo, Q. Catalytic Conversion of Jatropha Oil to Alkanes under Mild Conditions with a $Ru/La(OH)_3$ Catalyst. *Green Chem.* **2015**, *17*, 2888–2895. [CrossRef]
49. Liu, X.-M.; Huang, Z.-D.; Oh, S.-W.; Zhang, B.; Ma, P.-C.; Yuen, M.M.F.; Kim, J.-K. Carbon Nanotube (CNT)-Based Composites as Electrode Material for Rechargeable Li-Ion Batteries: A Review. *Compos. Sci. Technol.* **2012**, *72*, 121–144. [CrossRef]
50. Nešić, A.; Čavić, M.; Popović, M.; Gavrović-Jankulović, M. A New Approach for Activation of the Kiwifruit Cysteine Protease for Usage in In-Vitro Testing. *Mol. Biol. Rep.* **2021**, *48*, 4065–4072. [CrossRef]
51. Haron, W.; Wisitsoraat, A.; Wongnawa, S. Nanostructured Perovskite Oxides–$LaMO_3$ (M=Al, Co, Fe) Prepared by Co-Precipitation Method and Their Ethanol-Sensing Characteristics. *Ceram. Int.* **2017**, *43*, 5032–5040. [CrossRef]
52. Yousaf, A.B.; Imran, M.; Farooq, M.; Kasak, P. Interfacial Phenomenon and Nanostructural Enhancements in Palladium Loaded Lanthanum Hydroxide Nanorods for Heterogeneous Catalytic Applications. *Sci. Rep.* **2018**, *8*, 4354. [CrossRef] [PubMed]
53. Fallah-Shojaei, A.; Tabatabaeian, K.; Shirini, F.; Hejazi, S.Z. Multi-Walled Carbon Nanotube Supported Fe_3O_4NPs: An Efficient and Reusable Catalyst for the One-Pot Synthesis of 4H-Pyran Derivatives. *RSC Adv.* **2014**, *4*, 9509. [CrossRef]
54. Čavić, M.; Grozdanović, M.; Bajić, A.; Srdić-Rajić, T.; Anđjus, P.R.; Gavrović-Jankulović, M. Actinidin, a Protease from Kiwifruit, Induces Changes in Morphology and Adhesion of T84 Intestinal Epithelial Cells. *Phytochemistry* **2012**, *77*, 46–52. [CrossRef] [PubMed]
55. Crosnier de Lassichere, C.; Latapie, L.; Evrard, D.; Gros, P. New Insight into the EC' Mechanism of Uric Acid Regeneration in the Presence of Ascorbic Acid on a Poly(3,4-Ethylenedioxithiophene) Modified Gold Electrode. *Electroanalysis* **2018**, *30*, 1653–1658. [CrossRef]
56. Elgrishi, N.; Rountree, K.J.; McCarthy, B.D.; Rountree, E.S.; Eisenhart, T.T.; Dempsey, J.L. A Practical Beginner's Guide to Cyclic Voltammetry. *J. Chem. Educ.* **2018**, *95*, 197–206. [CrossRef]
57. Yang, Y.; Li, M.; Zhu, Z. A novel electrochemical sensor based on carbon nanotubes array for selective detection of dopamine or uric acid. *Talanta* **2019**, *201*, 295–300. [CrossRef]

58. Xing, L.; Ma, Z. A Glassy Carbon Electrode Modified with a Nanocomposite Consisting of MoS_2 and Reduced Graphene Oxide for Electrochemical Simultaneous Determination of Ascorbic Acid, Dopamine, and Uric Acid. *Microchim. Acta* **2016**, *183*, 257–263. [CrossRef]
59. Pena-Pereira, F.; Wojnowski, W.; Tobiszewski, M. AGREE—Analytical GREEnness Metric Approach and Software. *Anal. Chem.* **2020**, *92*, 10076–10082. [CrossRef]
60. Płotka-Wasylka, J. A New Tool for the Evaluation of the Analytical Procedure: Green Analytical Procedure Index. *Talanta* **2018**, *181*, 204–209. [CrossRef]

biosensors

MDPI

Review

Advancing Healthcare: Synergizing Biosensors and Machine Learning for Early Cancer Diagnosis

Mahtab Kokabi, Muhammad Nabeel Tahir, Darshan Singh and Mehdi Javanmard *

Department of Electrical and Computer Engineering, Rutgers the State University of New Jersey, Piscataway, NJ 08854, USA; mk1903@scarletmail.rutgers.edu (M.K.); nabeel.tahir@rutgers.edu (M.N.T.); ds1464@scarletmail.rutgers.edu (D.S.)
* Correspondence: mehdi.javanmard@rutgers.edu

Abstract: Cancer is a fatal disease and a significant cause of millions of deaths. Traditional methods for cancer detection often have limitations in identifying the disease in its early stages, and they can be expensive and time-consuming. Since cancer typically lacks symptoms and is often only detected at advanced stages, it is crucial to use affordable technologies that can provide quick results at the point of care for early diagnosis. Biosensors that target specific biomarkers associated with different types of cancer offer an alternative diagnostic approach at the point of care. Recent advancements in manufacturing and design technologies have enabled the miniaturization and cost reduction of point-of-care devices, making them practical for diagnosing various cancer diseases. Furthermore, machine learning (ML) algorithms have been employed to analyze sensor data and extract valuable information through the use of statistical techniques. In this review paper, we provide details on how various machine learning algorithms contribute to the ongoing development of advanced data processing techniques for biosensors, which are continually emerging. We also provide information on the various technologies used in point-of-care cancer diagnostic biosensors, along with a comparison of the performance of different ML algorithms and sensing modalities in terms of classification accuracy.

Keywords: biosensors; impedance cytometry; lab-on-a-chip; cancer detection; machine learning; microfluidic chips

Citation: Kokabi, M.; Tahir, M.N.; Singh, D.; Javanmard, M. Advancing Healthcare: Synergizing Biosensors and Machine Learning for Early Cancer Diagnosis. *Biosensors* **2023**, *13*, 884. https://doi.org/10.3390/bios13090884

Received: 21 August 2023
Revised: 8 September 2023
Accepted: 9 September 2023
Published: 13 September 2023

1. Introduction

Cancer is a major cause of death worldwide, and the incidence of cancer continues to rise, making early detection and diagnosis essential. In 2020, nearly 10 million people died of cancer, according to the World Health Organization [1]. Cancer is a genetic disease caused by changes in the DNA sequence of cells due to DNA damage, harmful substances, or errors in cell division [2]. Lung and breast cancers are prevalent types of cancer that affect men and women. Carcinoma, lymphoma, leukemia, sarcoma, and melanoma are frequently encountered cancer classifications that can emerge in various organs of the human body. Aging, prolonged exposure to sunlight, smoking, radiation exposure, viral infections, the use of hormonal medications, and exposure to certain chemicals are among the known factors contributing to the development of cancer [3].

Cancer involves the abnormal growth of cells that are clones of each other, and these cancerous cells can divide and spread beyond the neighboring cells, generating tumors. Tumors can be benign or malignant [4]. Benign tumors stay in their primary stage and may grow in size without spreading into neighboring tissues or organs. In contrast, malignant tumors consist of cancer cells that grow uncontrollably and spread into neighboring cells, tissues, or organs. Cancer cells can spread to other parts of the body via the lymphatic node system or through the bloodstream. From benign tumors to malignant, cancer passes through four stages, where the fourth stage is called metastatic, and the chances of survival

are very low [5]. Unfortunately, there are no advanced methods to diagnose cancer at the earliest stages.

Typical cancer detection processes involve physical exams, lab tests that use expensive and harmful equipment based on electromagnetic radiation, or a surgical diagnosis called a biopsy [6]. These lab tests use biological samples, such as blood, urine, saliva, or sweat, to detect specific biomarkers. Imaging-based tests include magnetic resonance imaging (MRI), computed tomography (CT), positron emission tomography (PET), ultrasound, and X-rays [7–10]. Although these imaging tests are non-invasive, they require expensive equipment and experienced pathologists. Biopsies are useful for determining the type of tumor, but they are invasive, painful, time-consuming, and expensive [11–13]. These issues with the current cancer diagnostic and detection methods make them unsuitable for point-of-care testing (POCT) and early cancer diagnosis [14–19]. Therefore, there is an urgent need to develop biosensing platforms for early cancer diagnosis that are low-cost, non-invasive, accurate, less time-consuming, and can be used at the point of care.

Biosensors can fill the void of point-of-care testing by providing low-cost, non-invasive, high-speed, and on-site testing of bio samples. A biosensor is a specialized type of sensor designed to detect and capture biological signals or molecules within a given sample or environment. These biological signals can include various entities, such as specific proteins, enzymes, DNA sequences, antibodies, or even whole cells. Biosensors are particularly significant in the field of medical and healthcare applications due to their ability to provide valuable information about biological processes, disease diagnosis, and patient monitoring [20]. Various point-of-care devices and lab-on-chip technologies have been employed to detect and diagnose various biomarkers from bio samples, such as pregnancy tests, blood glucose, or tuberculosis. Biosensors search for a specific biomarker in the bio sample and use either electrical or optical sensing modalities to detect biomarkers [19,21–26] associated with a cancer type. Additionally, researchers have conducted significant research on biosensors that use sweat or exhaled air as a potential sensing mode and have tried to associate the concentrations of volatile organic compounds with the presence of cancer or some other disease [25,27].

Biosensors can generate large amounts of data at the time of diagnosis and may require complex processing algorithms to generate the results. To effectively analyze the vast amounts of data obtained from biosensors and extract valuable information, researchers have harnessed the power of machine learning (ML) techniques. These methods include but are not limited to support vector machines (SVM), k-nearest neighbor (KNN), decision trees (DT), artificial neural networks (ANN), and convolutional neural networks (CNN) [28,29]. This paper is a review of the research projects that develop biosensors for early cancer detection and diagnosis and employ ML algorithms to enhance data analysis. In this regard, a review of ML algorithms is presented, along with the fundamental working principles of different biosensing techniques. The papers in this review study are divided into two main categories: electrical detection and optical detection biosensors. To facilitate a reader's understanding of how ML models are advancing biosensors in diagnosing different types of cancer, sub-categories have been created based on the type of cancer detected using specific biomarkers or cells.

2. Overview of Machine Learning Algorithms

Machine learning (ML) has grown rapidly over the past few decades and has widely used applications not only limited to healthcare problems, such as predicting drug discoveries and diagnosing diseases, but also in other fields, such as mechanics, robotics, and image recognition [30–34]. In simple words, ML is a rapidly developing field of computational algorithms that aims to replicate human intelligence by adapting to their surroundings and learning from them [35]. There are two main types of machine learning algorithms: supervised and unsupervised learning [36]. The difference between these two main classes is the existence of labels in the training data subset, which will be discussed in the following sections.

2.1. Supervised Machine Learning

Supervised algorithms are a subset of machine learning models which generate a function that maps inputs to desired outputs [37]. Supervised learning is characterized by the usage of labeled datasets to train algorithms for accurate classification or outcome prediction. The model adjusts its weights as input data is fed into it, achieving proper fitting during the cross-validation process [38]. During the model training process, the predicted output is compared to the actual output, and modifications are made to decrease the overall error between the two. Supervised machine learning algorithms have a broad range of applications in biosensors and healthcare, including tasks such as distinguishing cancer from non-cancer cells, detecting circulating tumor cells (CTCs), and predicting DNA quantities [31,38,39]. In the following sections, the most well-known and commonly supervised algorithms will be discussed.

2.1.1. Support Vector Machines (SVMs)

The support vector machine algorithm is a popular supervised algorithm used both in classification and regression models [40]. In classification, the SVM aims to identify a hyperplane in an N-dimensional feature space, which effectively separates the data points into distinct classes (Figure 1A), while, in regression models, the SVM aims to find a line that best fits the data [41]. The kernel-based SVM algorithm uses kernel functions to transform the input data into a higher dimensional feature space when the data cannot be separated linearly. The performance of the SVM model depends on two hyperparameters: kernel parameters and kernel types. The selection of the kernel type is determined based on the characteristics of the input data [29].

2.1.2. K-Nearest Neighbor (KNN)

The k-nearest neighbor (KNN) algorithm is a type of supervised machine learning algorithm that classifies objects based on the classes of their nearest neighbors [42]. It is typically used for classification but can also be applied to regression problems. The algorithm predicts the class or value of a new data point based on the k-closest data points in the training dataset. To identify the nearest neighbors, the algorithm calculates the distance between the new data point and all other data points in the dataset. For example, in Figure 1B, the green unknown data point belongs to the red dataset. For classification, the algorithm assigns the new data point to the most common class among its k-nearest neighbors, while for regression analysis, it calculates the average value of the k-nearest neighbors and assigns it to the new data point [42]. The value of k is usually determined through cross-validation or other optimization techniques, and it impacts the bias-variance trade-off of the model. Despite its simplicity, KNN is a highly effective algorithm and is widely used in many fields, including image recognition, natural language processing, and healthcare problems [43–45].

2.1.3. Decision Tree (DT)

The decision tree algorithm is a popular supervised machine learning algorithm used for classification and regression tasks. It works by constructing a tree-like model of decisions and their possible consequences based on the data [46]. The decision tree algorithm works by dividing the feature space of the training set recursively. Its goal is to identify a collection of decision rules that can partition the feature space in a way that produces a reliable and informative hierarchical classification model. In this algorithm, each node represents an attribute or feature, and each branch represents an outcome. The root node represents the entire dataset, and at each internal node, the algorithm divides the data based on a specific attribute's value. The schematic of the DT algorithm is shown in Figure 1C. This process is repeated recursively until a stopping condition is met, such as achieving a specified level of purity or reaching a predetermined depth [46].

2.1.4. Gaussian Naïve Bayes (GNB)

The Gaussian naïve Bayes (GNB) algorithm is a classification technique used in machine learning that leverages a probabilistic approach and the Gaussian distribution to make predictions of input data. GNB treats each attribute variable as independent, enabling it to be trained efficiently in supervised learning and used in complex real-world scenarios. GNB is particularly effective when dealing with high-dimensional data since it assumes independence between features, making it less susceptible to the curse of dimensionality [47].

2.1.5. Logistic Regression (LR)

Logistic regression is a supervised machine learning algorithm designed to solve classification problems where the target variable is categorical. The primary objective of logistic regression is to establish a mapping function from the dataset's features to the target. This allows the algorithm to predict the probability of a new data point belonging to a particular class [48]. As shown in Figure 1D, the input space is divided into two regions, which are separated by a boundary. Logistic regression is a widely used algorithm in many fields, such as marketing, healthcare, and finance, as it can help identify patterns and relationships between variables that can assist in making accurate predictions and decisions [49].

2.1.6. Random Forest (RF)

Random forest is a supervised machine learning algorithm that builds on the concept of tree classifiers. It generates a large number of classification trees and uses them to classify new feature vectors. Each tree in the forest classifies the input vector, and the tree's classification is counted as a "vote" for that class. The forest then chooses the classification with the highest number of votes across all the trees in the forest as the final prediction. RF is a highly effective algorithm for handling complex, high-dimensional datasets. It uses ensemble learning to reduce overfitting and improve the model's accuracy by combining the outputs of multiple decision trees [50].

2.1.7. Artificial Neural Network (ANN)

Artificial neural networks (ANNs) are computer programs designed to mimic the way the human brain processes information. They derive their inspiration from biological neural networks and adopt a similar structure of interconnected neurons to perform complex tasks. ANNs acquire knowledge through experience by identifying patterns and relationships in data instead of relying on explicit programming to accomplish the task.

An ANN typically consists of many processing elements (PE), also known as artificial neurons, which are connected by weights. These weights constitute the neural structure of the network and are organized into layers. The structure of an ANN is shown in Figure 1E. Through a process of training, the network learns to adjust the weights between the neurons to produce the desired output given a specific input. ANNs can be used for a variety of tasks, such as image and speech recognition, natural language processing, predictive analytics, and healthcare [51]. Figure 1 represents common supervised ML algorithms.

2.2. Unsupervised Machine Learning

Unsupervised learning is a subfield of machine learning where the data provided to the machine learning algorithm is unlabeled, and it is up to the algorithm to make sense of the data on its own. In unsupervised learning, the algorithm looks for patterns and structures in the data and tries to group similar data points together based on their similarities or differences. One of the key advantages of unsupervised learning is that it can reveal insights and relationships that may not be immediately apparent to human observers. By discovering patterns and similarities in the data, unsupervised learning can help uncover the hidden relationships that can be useful for making decisions or solving problems. For example, unsupervised machine learning can be used to identify customer

segments in a marketing dataset or to find anomalies or outliers in a dataset that may indicate fraudulent activity [41].

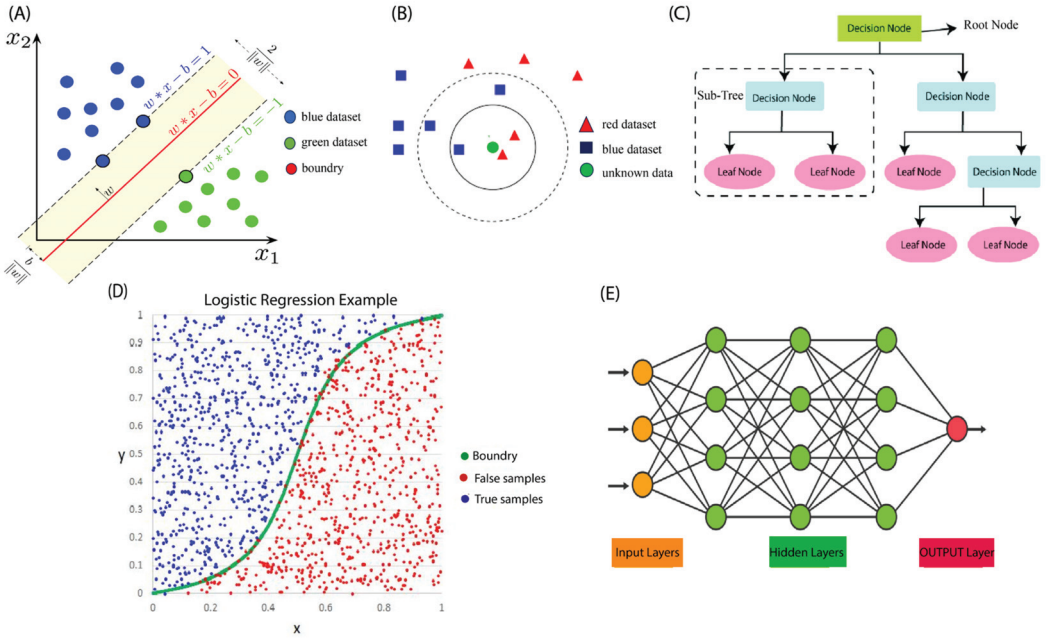

Figure 1. Schematic illustrations of supervised machine learning algorithms. (**A**) SVM model. Reprinted from [52]. (**B**) KNN model Reprinted from [53]. (**C**) DT model. Reprinted from [54]. (**D**) LR model Reprinted from [55]. (**E**) ANN model. Reprinted from [56].

2.3. Machine Learning Figures of Merits

To evaluate the performance of the representative model, the following metrics are used: accuracy (ACC), true positive rate (TPR), true negative rate (TNR), false negative rate (FNR), and false positive rate (FPR). These measures are computed using the following forms:

$$\text{Accuracy(ACC)} = \frac{\text{TP} + \text{TN}}{\text{TN} + \text{TP} + \text{FN} + \text{FP}} \tag{1}$$

$$\text{Sensitivity(TRP)} = \frac{\text{TP}}{\text{TP} + \text{FN}} \tag{2}$$

$$\text{Specificity(TNR)} = \frac{\text{TN}}{\text{TN} + \text{FP}} \tag{3}$$

$$\text{Fallout(FPR)} = \frac{\text{FP}}{\text{TN} + \text{FP}} \tag{4}$$

$$\text{False Negative Rate(FNR)} = \frac{\text{FN}}{\text{TP} + \text{FN}} \tag{5}$$

where the TP's and FPs refer to the number of correct and incorrect predictions of outcomes to be in the considered output class, whereas the TN's and FNs refer to the number of correct and incorrect predictions of outcomes to be in any other output classes respectively [30].

The ROC (receiver operating characteristic) curve is a graphical representation of the performance of a binary classification model. It is a graph that shows the trade-off between the true positive rate and the false positive rate. A diagonal line in the ROC curve indicates

that the test has no discriminatory ability, while an ROC curve above the diagonal line indicates a test with better-than-chance discrimination ability. The area under the ROC curve (AUC) is a measure of the overall ability of the test to discriminate between the presence or absence of a condition. An AUC of 1.0 indicates perfect discrimination, and an AUC of 0.5 indicates no discriminatory ability [57].

3. Lab-on-a-Chip in Cancer Detection

This section provides a brief overview of the various types of sensors, including optical and electrical sensors, such as image-based, fluorescence, and impedance sensors, that can be used to detect cancer cells. Additionally, the results of machine learning algorithms to analyze data collected from these sensors have been discussed.

3.1. Optical Detection

Optical detection of cells implies the use of optical techniques and instruments for the detection, classification, and stratification of cells [41]. Various types of optical-based biosensors have been developed and utilized for diverse biological and clinical applications, such as surface plasmon resonance (SPR), optical waveguides, optical resonators, and fluorescence [3,58,59]. Optical biosensors have several advantages, including their high sensitivity, real-time detection, label-free analysis, small form factor, and low cost [41]. These characteristics make optical biosensors an appealing option for integration into lab-on-a-chip devices, which seek to carry out sample preparation, research, and detection in a miniaturized and automated format [59]. In the next section, we will review the latest developments of optical-based biosensor devices in the identification and clinical diagnosis of various types of cancers, as well as data analysis with machine learning techniques.

3.1.1. Breast Cancer

Based on the World Health Organization (WHO), breast cancer is the most frequent cancer among women, affecting over 1.5 million women each year, and is responsible for the most significant cancer-related deaths among women. In 2015, 570,000 women died from breast cancer [60]. This highlights the potential of biosensors for the early detection of cancer cells. Biosensors are promising and selective detection devices which hold immense potential as point-of-care (POC) tools [61]. Several studies have shown the application of optical-based biosensors to detect breast cancer cells, demonstrating the promising potential of biosensors for early-stage detection of breast cancer cells.

The surface plasmon resonance (SPR) sensor is an optical sensor employing a unique mode of electromagnetic field called the surface plasmon, which propagates at the interface of a metal and a dielectric. The SPR sensor utilizes the evanescent field generated by the surface plasmon to detect alterations in the refractive index of the dielectric material near the interface [62]. Numerous studies have suggested the effectiveness of SPR sensors in the early detection of cancers [63]. Kumar et al. [64] described a photonic crystal fiber-based surface plasmon resonance (SPR) sensor for detecting breast cancer cells based on their refractive index (Figure 2A). They used simulations and numerical analysis to measure the wavelength sensitivity and resolution of the sensors for normal and cancerous cells, achieving a high sensitivity and low resolution. The refractive index of normal and cancerous cells was estimated using a multi-layer perceptron, and the machine learning algorithm was used to optimize the structural parameters. The proposed sensor shows promising results and could be a potential alternative sensing device for early-stage breast cancer diagnosis. In another study, Verma et al. [65] developed a machine learning approach for breast cancer cell detection using a surface plasmon resonance (SPR) based on a photonic crystal fiber sensor, which is shown in Figure 2B. The sensor operates by detecting changes in the refractive index of the fiber when breast cancer cells are present. The machine learning algorithm is trained on a dataset of SPR spectra obtained from both breast cancer and non-cancerous cells and is used to classify new samples as either cancerous or non-cancerous based on their spectral patterns.

Another type of optical sensor is the fluorescence sensor, widely used to identify and measure biomolecules or metal ions. The advantages of this type of sensor include its sensitivity, specificity, resistance to light scattering, and ease of use [66]. In a study reported by Jin et al. [67], they developed a breast cancer liquid biopsy system that integrates a fluorescence sensor array with a deep learning model. The sensor array uses fluorescent probes to gather diverse information about cells and exosomes. The deep learning model employs a CNN-based architecture to distinguish between normal and cancerous cells. The system has demonstrated successful discrimination between normal and different cancerous cells and achieved a 100% accurate classification of different breast cancer cells. In addition, Pala et al. [68] constructed and tested a digital in-line holographic microscope for imaging breast cancer cells using holography, which is shown in Figure 2C. The microscope was constructed using a white LED for illumination, a pinhole to make the light semi-coherent, and a CMOS sensor to record images of the plane above it. Holograms were captured and numerically reconstructed, and the amplitude of individual cells was collected. Using machine learning, these images were transformed into a fractal dimension and rotated to calculate the identifying features of each cell. Upon testing the accuracy of this system, the team achieved an accuracy of 99.65%.

3.1.2. Lung Cancer

Lung cancer is a primary cancer that poses a significant threat to human life globally, having the highest mortality rate. Early detection of lung cancer is crucial for a timely diagnosis and subsequent treatment. However, conventional methods for lung cancer detection have limitations, such as their low sensitivity, high costs, and invasive procedures, which restrict their practicality [69]. In this section, we will review the optical biosensors for detecting lung cancer and explore how machine learning can aid in analyzing data and improving their application.

Image-based detection implies the use of images or videos of cells. These images or videos need to be processed to identify and quantify cells [41]. To demonstrate, Hashemzadeh et al. [70] developed a microfluidic chip for lung cancer detection that employs image-based analysis. Images were obtained using an inverted Olympus fluorescence microscope and were analyzed by a deep learning model. The researchers achieved an accuracy of 98.37% in classifying images of lung cancer cell lines and normal cell lines. The overview of the combined microfluidic deep learning approach has been shown in Figure 3A. As another example, Sui et al. [71] described the development of a microfluidic imaging flow cytometer that can detect lung cancer using complex-field imaging and fluorescence detection subsystems. The system can analyze millions of cells and provide a hierarchical analysis of the intrinsic morphological descriptors of single-cell optical and mass density, as well as fluorescently labeled biochemical markers. The data collected from the system were used to train deep learning-based models, which achieved a classification accuracy ranging from 91% to 95% for lung cancer detection.

Volatile organic compounds (VOCs) are potential biomarkers for lung cancer detection. In the study reported by Nguyen et al. [72], a controllable gap plasmonic color film biosensor was developed for the detection and quantification of VOCs. The goal of the study was to diagnose lung cancer based on VOC gas detection from exhaled breath samples. The color changes in the sensor arrays when exposed to humidity and VOCs were recorded using a camera, and a CNN model was trained to classify them into different VOCs (Figure 3B). They collected the data from 70 healthy and 50 lung cancer patients and trained the ML models, reporting a training classification accuracy of 90% and 92.8% for lung cancer and healthy patients, respectively. They achieved a classification accuracy of 89% on the test data.

A label-free classification of lung cancer cell lines was developed by Wei et al. [73] by using a two-dimensional (2D) light-scattering static cytometric technique. In this study, a method for the automatic classification of small cell lung cancer (SCLC) and poorly differentiated lung adenocarcinoma (PD-LUAD) cells was introduced by using 2D light-

scattering static cytometry and machine learning (Figure 3C). A laser was used to detect the cells by means of a two-dimensional light-scattering static cytometric technique, where measurements of forward and side scattered light enabled the differentiation of overlapping SCLC and PD-LUAD cells. By employing a support vector machine (SVM) classifier, the team achieved the classification of these cells with an accuracy greater than 99.78%.

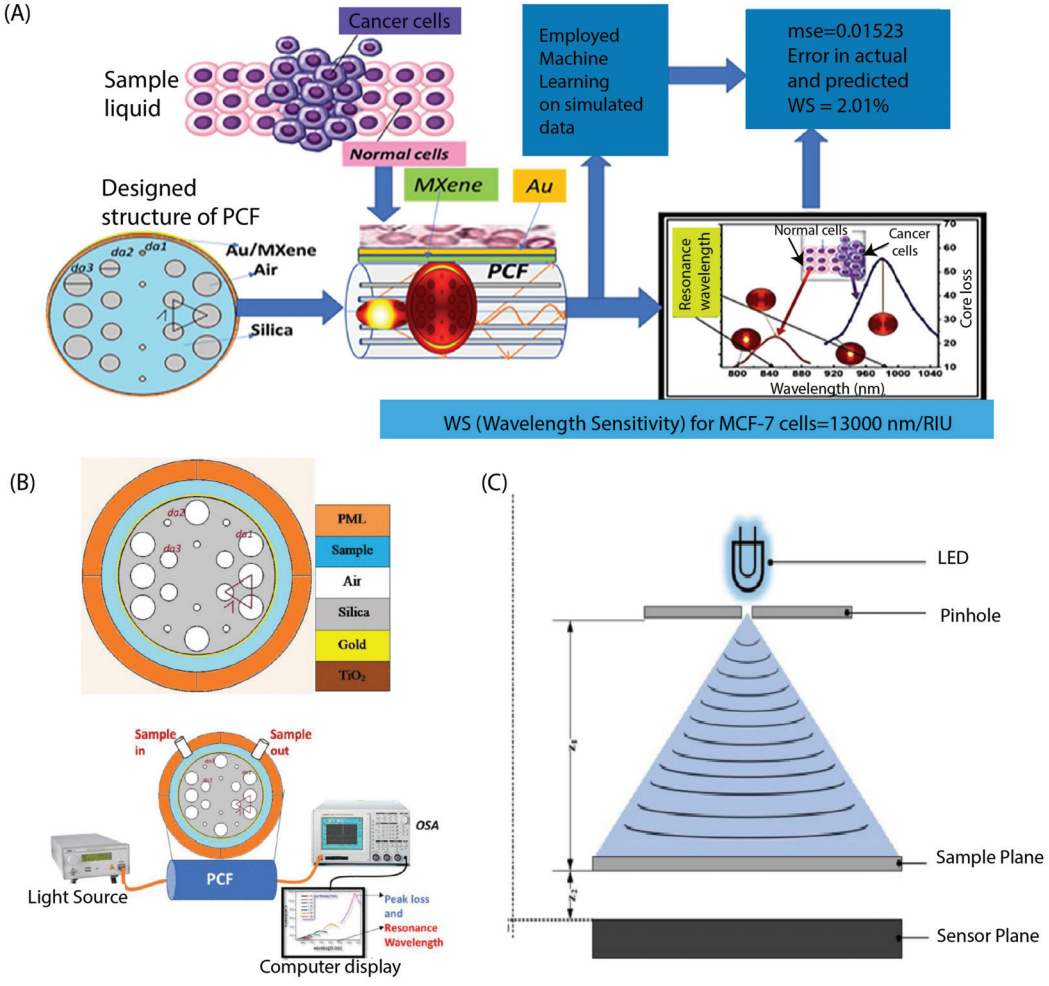

Figure 2. (**A**) Cross-sectional view of the proposed SPR sensor with the experimental setup. Reprinted with permission from [64]. Copyright 2023 Elsevier. (**B**) Colored entities of the designed sensor with a cross-sectional view with the experimental setup. Reprinted with permission from [65]. Copyright 2023 IEEE. (**C**) Schemes of the digital in-line holographic microscope (DIHM). Reprinted with permission from [68]. Copyright 2023 Springer Nature.

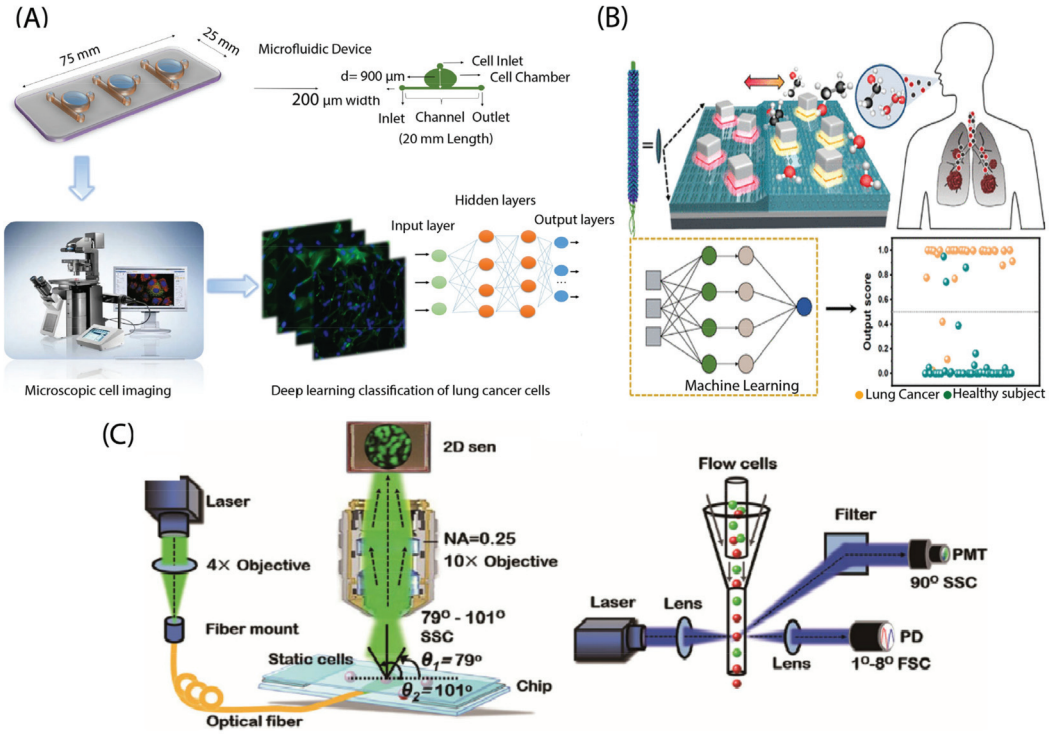

Figure 3. (**A**) Overview of the combined microscopic cell imaging and deep learning approach. Reprinted from [70]. Copyright 2021 Springer Nature. (**B**) Schematic of the biosensor with the combination of machine learning methods to detect lung cancers. Reprinted from [72]. (**C**) Schematic of the experimental setups. Reprinted with permission from [73]. Copyright 2018 John Wiley and Sons.

Feature extraction plays a vital role in machine learning when dealing with large amounts of data. It helps to identify and extract the most relevant and informative aspects or characteristics from the data, enabling a more effective and efficient analysis [74]. For example, Ahmad et al. [75] presented a microfluidic platform and light-sheet fluorescence microscopy based on a single-cell classification system to classify human mammary epithelial cells, primary tumor cells, and lung metastasis-derived cells. They used an optofluidic device to deliver single cells to the fluorescent microscope and simulated 3D point clouds of the fluorescent markers. They applied feature extraction techniques along with custom CNN models to classify the images. The authors achieved high accuracy on both the simulated and actual datasets and studied the effects of varying flow rates on accuracy. They reported an accuracy of 99.4% on the actual dataset.

Surface-enhanced Raman scattering (SERS) is a powerful method for identifying chemical information at a single molecular scale [76]. Lin et al. [76] developed a new biosensing platform that can identify and differentiate exosomes derived from cancerous and non-cancerous sources. The platform uses a porous-plasmonic SERS chip with CP05 polypeptide to capture and distinguish exosomes without the need for labeling or purification. By combining biological analysis with Raman spectra and machine learning methods, the team accurately differentiated between lung and colon cancer cell–derived exosomes and normal exosomes at the single vesicle level, achieving an 85.72% accuracy. This protocol is fast, reliable, and easy to operate, making it a promising tool for early tumor detection and prognosis. As another example, Park et al. [77] used SERS and statistical pattern analysis

to identify lung cancer cells (Figure 4). Instead of looking at specific peak positions and amplitudes in the spectrum, they analyzed the whole SERS spectra of exosomes using principal component analysis (PCA). Using this approach, they were able to distinguish the exosomes derived from lung cancer cells from those derived from normal cells, with a 95.3% sensitivity and 97.3% specificity.

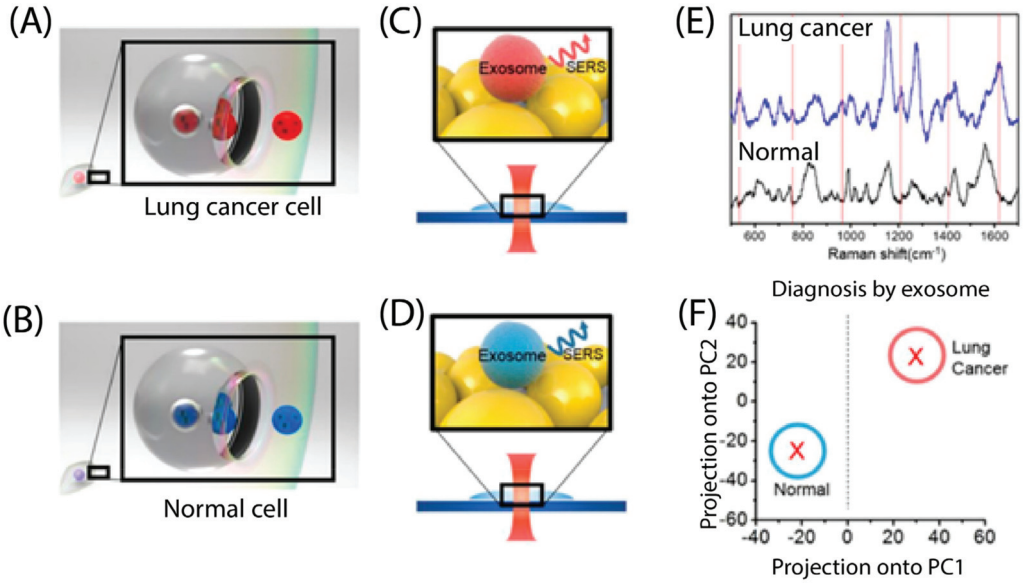

Figure 4. Schematic diagram of lung cancer diagnosis by SERS classification of the exosome. (**A**,**B**) Lung cancer cells and normal cells release exosomes to the extracellular environment, having their own profiles by fusing multivesicular endosomes to the plasma membrane, respectively. (**C**,**D**) Raman spectra of lung cancer cells and normal cell-derived exosomes were achieved by SERS, respectively. (**E**) SERS spectra, achieved by methods of panels (**C**,**D**), are shown. Red lines indicate specific peaks of lung cancer-derived exosomes. (**F**) Exosome classification is obtained by PCA of SERS spectra. Reprinted with permission from [77]. Copyright 2017 American Chemical Society.

3.1.3. Gastrointestinal Cancer

In this section, we will review the application of optical-based biosensors in combination with machine learning to analyze the data collected from sensors for the detection of gastrointestinal cancers, such as pancreatic and liver cancers.

Nowadays, many studies detect pancreatic cancer cells using exosomes, which are small vesicles secreted by cancer cells, as biomarkers for detection. To demonstrate, Ko et al. [78] developed a multichannel nanofluidic system to analyze crude clinical samples. They used exosomes as biomarkers for detecting pancreatic cancer. The exosomes were isolated and analyzed using a microfluidic chip with a nanoporous membrane that allowed the capture of exosomes based on their size. The captured exosomes were then analyzed using machine learning algorithms to classify them as either cancerous or non-cancerous. The results showed that the approach had a high accuracy with an area under curve (AUC) of 0.81 in diagnosing pancreatic cancer, indicating its potential for use in clinical settings as a non-invasive diagnostic tool. As another example, Li et al. [79] developed a new method for detecting colorectal cancer using exosomes as a specific protein biomarker. They created a microfluidic chip with a 3D porous sponge structure and functionalized it with CD9 antibodies to capture exosomes flowing through the microfluidic channel. The authors then used an anti-SORL1 antibody modified with Si-QD silicon quantum dots to label the captured exosomes and obtain fluorescence images. They extracted three features

(luminance, mean, and variance) and trained an RF algorithm to classify the exosomes. The authors report that they achieved a high classification accuracy of 91.14%. Last but not least, Cheng et al. [80] described a nano biosensing chip that utilizes SERS to detect cancer without the need for antibodies. This study showcased a simple and intelligent detection method for efficiently screening liver cancer, achieving a sensitivity of 90% and specificity of 92% in identifying 50 serum SERS spectra from HCC patients compared to 50 serum SERS spectra from healthy individuals.

D'Orazio et al. [81] introduced the concept of machine learning phenomics (MLP), which combines deep learning with time-lapse microscopy to monitor drug responses in colorectal cancer cells. This study aims to evaluate the effectiveness of this approach by comparing it with the conventional methods used to analyze drug responses in these cells. The results demonstrate that MLP can accurately predict drug responses in colorectal adenocarcinoma cells based on their gene expression patterns, and it outperforms the conventional methods in terms of accuracy and efficiency.

Quantum dot immunobionsensors are powerful optical sensors used to detect cancer cells, which were introduced by Saren et al. [82] to detect and quantify gastrointestinal tumor biomarkers. They developed quantum dot (QD)-labeled biofilms to detect four biomarkers: CEA, CA125, CA19-9, and AFP, indicating the presence of gastrointestinal tumors. The antibody conjugates of the QD were analyzed using fluorescence and ultraviolet absorption spectroscopy. The PCA technique was applied to the images obtained from the data collected. The approach was tested on standard samples rather than clinical samples, achieving a classification precision of 99.52% and 99.03% and classification accuracy of 94.86% and 94.2% for colon tumors and gastric tumors, respectively.

Pyruvate kinase disease (PKD) is an inherited disorder that affects red blood cell metabolism and may have an increased risk of developing liver cancer and some types of colon and kidney cancer [83,84]. Mencattini et al. [85] described a machine learning microfluidic-based platform that integrates lab-on-chip devices and data analysis algorithms to evaluate the plasticity of red blood cells in PKD monitoring. The platform uses microfluidic channels to measure the deformability of red blood cells, which is a critical indicator of the disease. The data collected from the microfluidic device are then analyzed using machine learning algorithms to determine the severity of the disease. The blood cells were recorded through a 'forest of pillars', and the video was saved for offline analysis. The efficacy of three networks, AlexNet, ResNet-101, and NasNetLarge, pre-trained deep learning architectures, was tested on actual samples. On the live samples, the performance of AlexNet was 88%, ResNet-101 was 82%, and NasNetLarge was 85%.

3.1.4. Gynecological Cancer

The most common types of gynecological cancers are cervical, ovarian, and endometrial (uterine) cancers. Late diagnosis and chemoresistance present significant obstacles to the successful treatment of gynecological cancers. Therefore, there is a pressing need to develop new markers to detect gynecological cancers at an early stage. In this regard, biosensors that are low-cost and non-invasive hold great potential for predicting these types of cancers at an early stage [86]. Moreover, with the emergence of biosensors that generate large amounts of data, the application of machine learning to analyze this data has become increasingly important.

High-content VFC (video flow cytometry) utilizes a 2D light-scattering technique to project optical signals from cells onto an image sensor without optical focusing. This allows for high-content patterns to be obtained and combined with machine learning algorithms, enabling automated, high-throughput analysis of single cells. The VFC technique developed by Liu et al. [87] achieves a measurement rate of around 1000 unlabeled cells per minute and demonstrates high accuracy in classifying cervical carcinoma cell lines, including Caski, HeLa, and C33-A cells. An accuracy of 91.5%, 90.5%, and 90.5% for these cell lines by using a deep learning model has been reported. This study provides high-quality

cell images, automatic digital filtering, and label-free cell classification, offering potential clinical applications. The illustration of our high-content VFC is shown in Figure 5.

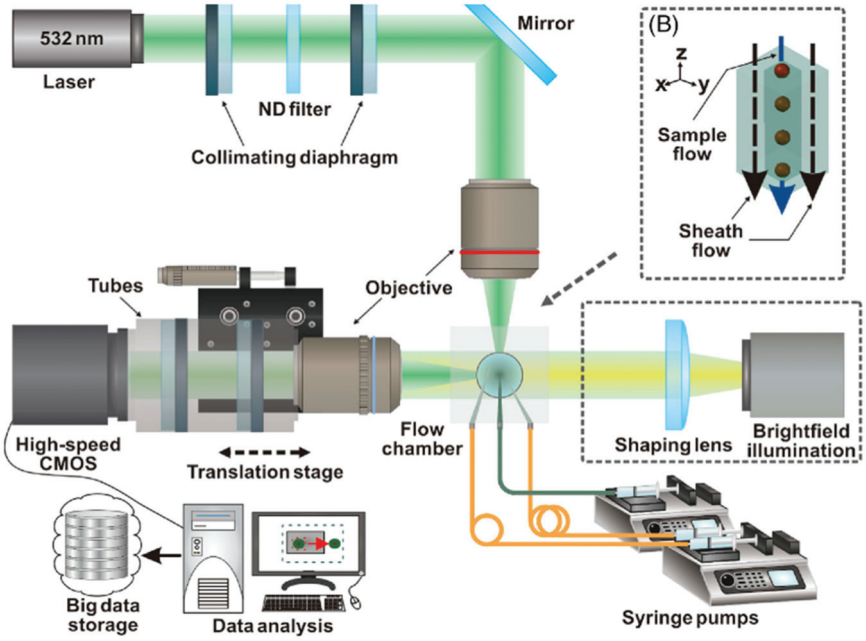

Figure 5. The schematic diagram of high-content VFC and the 3D schematic diagram of the sheath flow in the flow chamber. Reprinted with permission from [87]. Copyright 2022 John Wiley and Sons.

Serum biomarkers are frequently utilized due to their sensitivity and specificity, which makes them valuable for cancer screening or diagnostic testing purposes. To demonstrate, Kim et al. [88] developed a nanosensor array and a computational model that resulted in the perception-based detection of ovarian cancer from patient serum samples. The researchers aimed to develop a novel approach for diagnosing ovarian cancer based on the unique spectral characteristics of carbon nanotubes modified with quantum defects. They utilized machine learning algorithms to analyze the spectral data obtained from the serum samples. They trained and validated several machine learning classifiers with 269 serum samples to distinguish patients from those with other diseases and healthy individuals. Their results showed that the SVM algorithm yielded the best F-scores among the five machine learning algorithms tested, with an accuracy of 95%.

In another study reported by Pirone et al. [89], a digital holography to model cells in 3D space instead of 2D space was developed. This method provides a better characterization of endometrial cancer cells. They extracted 67 features, such as morphology and histogram, as inputs of machine learning algorithms. In order to test the classification performance with the 3D and 2D features, several common machine-learning methods have been trained and tested on the feature data. The results show that 3D features achieve a better classification performance, and the LDA classifier achieves the best score.

3.1.5. Prostate Cancer

Prostate cancer (PCa) is a widespread health concern, affecting 1.3 million men globally in 2018 [90]. Detecting prostate cancer (Pca) in its early stages is vital for effective treatment, and the utilization of biosensors can assist in the early detection of Pca. Furthermore, by utilizing machine learning to analyze the vast amounts of data generated by biosensors, we can achieve highly accurate predictions, ultimately leading to better patient outcomes.

Prostate cancer gene 3 (PCA3) is specifically expressed in the prostate and is strongly associated with prostate cancer. It shows promise as a potential biomarker for detecting prostate cancer. The PCA3 gene has been detected in 95% of prostate cancer samples, making it highly associated with the disease. Even small amounts of PCA3 can indicate a significant likelihood that a patient either has or will develop prostate cancer [91]. As an example, Rodrigues et al. [91] developed a genosensor with carbon-printed electrodes and a layer of a complementary DNA sequence (PCA3 probe). They investigated the ability of electrochemical and optical detection methods, along with machine learning algorithms, to diagnose prostate cancer using images of the genosensors. The study demonstrated that the meta-classifier machine learning algorithms, including SVM and LDA, could accurately classify scanning electron microscopy images with 99.9% accuracy.

Differences in the metabolite components between patient urine and normal urine have been reported, indicating the need for a rapid, easy-to-use, and label-free technique to analyze urine metabolites. Such a technique is crucial for developing on-site urine diagnostic platforms and identifying unknown metabolite biomarkers for cancer detection. In a study conducted by Ling et al. [92], the researchers applied an integrated on-site detection system based on SERS sensor technology and deep learning models to diagnose prostate and pancreatic cancer. The sensor is based on a 3D plasmonic coral nanoarchitecture (3D-PCN) synthesized on a paper substrate, which was integrated with a handheld Raman spectrometer to create an on-site diagnostic platform. Human urine samples are directly absorbed into the paper-based 3D-PCN, and the SERS signals of complicated urine components are obtained without any pretreatment. The RNN and CNN models are employed for the supervised classification of SERS spectra, and the platform achieved high sensitivity and specificity for detecting cancer. The system demonstrates the potential for use as a diagnostic platform in various human biofluid analyses in the future.

The bio-nanochip platform shows promising potential as a versatile and efficient biosensor system for various applications, including medical diagnostics and environmental monitoring. For instance, McRae et al. [93] designed a programmable bio-nanochip (p-BNC) system, a biosensor platform with the capacity for learning. In this system, small quantities of patient samples generate an immunofluorescent signal on agarose bead sensors that are optically extracted and converted to antigen concentrations. This biochip sensor has the potential to detect prostate cancer and ovarian cancer with single-use disposable cartridges. They applied machine learning methods to analyze the dataset.

3.1.6. Brain Cancer

In this section, we will review the application of optical-based biosensors and machine learning for brain cancer detection.

A supervised machine learning approach is commonly used for the identification and classification of cancer cell gestures, enabling early diagnosis. Hasan et al. [94] developed a system that captures time-lapse images of cancer cells and analyzes their morphological changes over time using image-processing techniques (Figure 6). The system also incorporates machine learning algorithms for the automated classification of cancer cells based on their dynamic morphology. As a proof of concept, the morphologies of human glioblastoma (hGBM), which causes brain tumors [95,96], and astrocyte cells were used. The cells were captured and imaged with an optical microscope. Three different classifier models, the SVM, RF, and naïve Bayes classifier (NBC), were trained with the known dataset using machine learning algorithms. All the classifier models detected the cancer cells with an average accuracy of at least 82%.

In another study, Hossain et al. [97] employed a sensor-based portable microwave brain imaging (SMBI) system to obtain the reconstructed microwave (RMW) brain images. The proposed method consists of a segmentation model called MicrowaveSegNet (MsegNet) and a classifier called BrainImageNet (BINet). A dataset of 300 RMW brain image samples was used to create an original dataset, which was then augmented to make 6000 training images for a five-fold cross-validation. The performance of MsegNet and BINet was

compared to state-of-the-art segmentation and classification models, and the proposed models achieved impressive results. The proposed cascaded model has the potential to be used in sensor-based SMBI systems to investigate the progression of brain cancer disease.

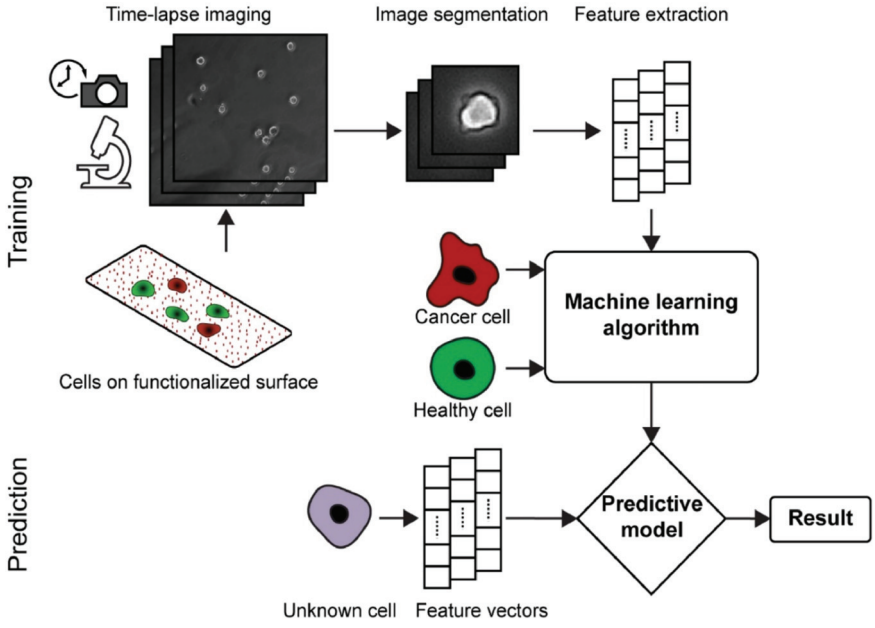

Figure 6. The schematic shows an overview of the dynamic morphological analysis of cell gestures. Reprinted with permission from [94]. Copyright 2018 Elsevier.

3.1.7. Hematological Cancer

Leukemic diseases are a diverse group of neoplasms that result from genetic disorders affecting hematopoietic precursor cells, and they represent one of the most common forms of hematologic cancer globally. Accurate diagnosis of these disorders requires specialized expertise and often involves using multiple techniques [98]. In this section, we presented the use of optical biosensors in conjunction with machine learning for detecting hematological cancer.

DNA methylation is a process in which a methyl group is attached to the fifth carbon atom of a cytosine (C) residue, resulting in the formation of 5-methylcytosine (5-mC). The methylation patterns in cancer genomes exhibit unique characteristics, known as the methyl cape, and can serve as a potential universal biomarker for cancer detection [99]. For example, Koowattanasuchat et al. [99] presented the development of a methyl cape sensing platform for leukemia screening using cysteamine-decorated gold nanoparticles (Cyst/AuNPs). The platform is based on methylation-dependent DNA solvation, and normal and cancerous DNAs have distinct methylation profiles. The authors report 95.3% accuracy in leukemia screening using an optical spectrophotometer and 90% accuracy when a smartphone system is used.

Minimal residual disease (MRD) testing is used mostly for blood cancers, such as lymphoma and leukemia [100,101]. Uslu et al. [102] investigated the signal readout mechanism of a biochip designed to detect MRD, which refers to highly resistant cancer cells that can cause relapse in cancer survivors after treatment. To improve the capture, isolation, and counting of these tumor cells, the team combined previously explored methods with the use of immunomagnetic beads. These beads are coated with receptors that bind to and capture target molecules, allowing them to be manipulated using magnetic fields. Once the unbound beads were filtered out of the microfluidic channel, the remaining beads were

imaged at 20× and 40× magnifications using a CCD camera and processed using computer vision. The authors demonstrated the accuracy and reproducibility of the method through various experiments and comparisons with manual counting. They also discussed the potential applications of the automated method in research and clinical settings for the detection and monitoring of leukemia and other diseases. Machine learning algorithms to analyze the images obtained were utilized. Among the algorithms tested, the RF algorithm achieved the highest accuracy of 87.4%.

Tremendous progress has been made in the field of cancer treatment through the utilization of high-affinity T-cell receptors and chimeric antigen receptor (CAR)-modified T cells. These innovative approaches have recently obtained approval from the Food and Drug Administration (FDA) for treating certain hematologic malignancies [103]. To demonstrate, Sarkar et al. [103] implemented the droplet microfluidics-based cytotoxicity imaging approach to isolate individual natural killer cells. They measured their ability to kill cancer cells in the presence of different types of antibodies. Machine learning algorithms for analyzing the resulting data were used, and they predicted which types of antibodies were most effective in activating the natural killer cells.

Last but not least, Li et al. [104] presented a novel approach to improving the accuracy of blood cancer cells and biomarker identification in label-free flow cytometry using parallel quantitative phase imaging. Such technology holds promise for the early detection of primary cancer or metastasis. The team used this imaging technique to assess additional parameters, such as cell protein concentration, allowing for increased accuracy in categorizing unlabeled cells. Additionally, they developed a CNN that directly operated on the measurement signals of this setup to detect cancer cells more efficiently. They demonstrated the applicability of the new method in the classification of white blood cells and epithelial cancer cells with more than 95% accuracy in a label-free fashion. Table 1 provides a summary of the cancer cell types that were detected using optical biosensors, along with the outcomes of the machine learning algorithms applied to the data.

Table 1. Comparison of different optical-based biosensors with ML analysis for cancer cell detection.

Authors	Cancer Cell Type	Biosensor Type	ML Algorithm	Results (%)
Kumar et al. [64]	Breast Cancer	(Surface plasmon resonance) SPR sensor	ANN	MSE = 0.01525 percentage error of 2%
Verma et al. [65]	Breast Cancer	SPR sensor	ANN	MSE = 0.116
Jin et al. [67]	Breast Cancer	Fluorescence sensor	ANN	ACC = 100
Pala et al. [68]	Breast Cancer	CMOS imaging sensor	ANN	ACC = 99.65
Hashemzadeh et al. [70]	Lung Cancer	Olympus fluorescence microscope	ANN	ACC = 98.37
Sui et al. [71]	Lung Cancer	Fluorescence sensor	CNN	ACC = 91–95
Nguyen et al. [72]	Lung Cancer	Gap plasmonic color sensors	Convolutional neural network (CNN)	ACC = 89
Wei et al. [73]	Lung Cancer	Two-dimensional (2D) light-scattering	SVM	ACC = 99.87
Ahmad et al. [75]	hTERT-immortalized human mammary epithelial cells (IMEC WT) Xenograft-derived primary tumor cells (XD) Lung metastasis-derived cells (MD)	Fluorescence microscopy Image-based sensor	CNN	ACC = 99.4
Lin et al. [76]	Lung and Colon Cancer	Localized plasmonic sensor	SVM	ACC = 85.72

Table 1. *Cont.*

Authors	Cancer Cell Type	Biosensor Type	ML Algorithm	Results (%)
Park et al. [77]	Lung Cancer	Surface-enhanced Raman spectroscopy (SERS)	Principal component analysis (PCA)	Sensitivity = 95.3
Ko et al. [78]	Pancreatic Cancer	Image-based multichannel nanofluidic system	LDA	AUC = 0.81
Li et al. [79]	Colorectal Cancer	Image-based 3D porous microfluidic chip	RF	ACC = 91.4
Cheng et al. [80]	Liver Cancer	SERS sensor	ANN	ACC = 91
D'Orazio et al. [81]	Colorectal Cancer	image-based time-lapse microscopy	ANN	ACC = 86.77
Saren et al. [82]	Gastrointestinal Cancer	Quantum dot (QD)-labeled biofilms	Principal component analysis (PCA)	ACC = 94
Mencattini et al. [85]	PKD, which may cause Liver, Colon, and Kidney Cancer	Image-based time-lapse microscopy	ANN	ACC = 88
Liu et al. [87]	Cervical Cancer	Image-based high-content VFC (video flow cytometry)	CNN + SVM	ACC = 90.8
Kim et al. [88]	Ovarian Cancer	Nanosensor array	SVM	ACC = 95
Pirone et al. [89]	Endometrial cancer	Holographic flow cytometry (DHFC)	LDA	ACC = 96
Rodrigues et al. [91]	Prostate Cancer	Genosensors	SVM and LDA	ACC = 99.9
Linh et al. [92]	Prostate and Pancreatic Cancers	SERS sensor	ANN	ACC = 99.4
McRae et al. [93]	Prostate and Ovarian Cancer	Bio-nanochip sensor	ANN	AUC = 0.94
Hasan et al. [94]	Brain Cancer	Image-based time-lapse images	SVM + RF + NBC	ACC > 82
Hossain et al. [97]	Brain Cancer	Sensor-based microwave brain imaging (SMBI)	CNN	ACC = ~90
Koowattanasuchat et al. [99]	Leukemia Cancer	Colorimetric biosensors	RF + SVM	ACC = 90
Uslu et al. [102]	Lymphoma and Leukemia Cancer	Microscope images	RF	ACC = 87.4
Sarkar et al. [103]	Hematological Cancer	Droplet microfluidics-based cytotoxicity imaging approach	ANN	ACC = 94
Li et al. [104]	Epithelial Cancer	Image-based microfluidic channel	CNN	ACC > 95

3.2. Electrical Detection

The use of electrical circuits to gather data in the form of electrical signals is known as electrical detection. These signals can take the form of impedance, voltage, current, or any other electrical signal [41]. Among these, impedance is the most commonly used parameter for identifying and quantifying cells. As a cell or particle passes through the electrodes in a microfluidic channel, it causes a change in impedance, and the output signal is determined by the cell's properties, such as size, conductivity, and permittivity. Compared to traditional optical detection, the electrical detection of cells has several advantages, including a smaller footprint and lower cost due to the absence of bulky optical equipment [41]. In the following paragraphs, we will discuss the biosensors that utilize machine learning techniques for the electrical detection of various cancer cells. A schematic diagram of an electrical impedance cytometer with ANN for data analysis is shown in Figure 7.

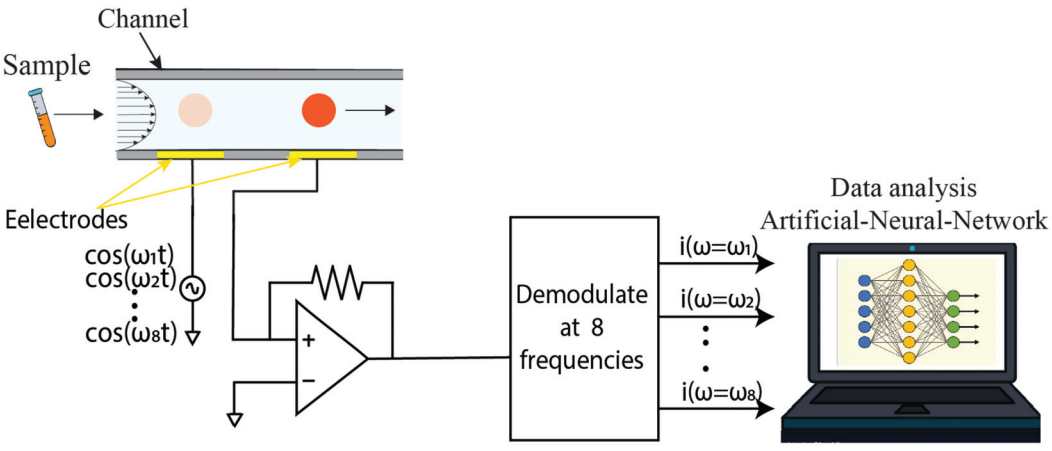

Figure 7. Schematic diagram of an electrical impedance cytometer. As cells flow through microfluidic chips, the change in impedance is measured by a lock-in amplifier. The lock-in amplifier can apply signals in different frequencies at a time. The data is then recorded and analyzed using the ANN algorithm.

Within the preceding section, we provided an overview of the optical biosensors, which, in conjunction with machine learning, are utilized to analyze the data acquired from the sensors. Additionally, we emphasized the utility of an affordable and non-invasive biosensor in the detection of cancer cells. This section will focus on the employment of electrical-based biosensors in combination with machine learning for the detection of cancer.

3.2.1. Breast Cancer

Electrical impedance spectroscopy/cytometry is a technique that allows the measurement of AC electrical properties of particles in a liquid suspension. This method provides information about the frequency-dependent dielectric parameters of the particles. The main advantage of impedance cytometry is its label-free nature, allowing analysis to be conducted at the individual cell level [41]. To demonstrate, a study by Ahuja et al. [105] presented a microfluidic device that utilizes multifrequency impedance spectroscopy and supervised machine learning, which is shown in Figure 8A, to rapidly evaluate the tumor cell's sensitivity to drugs. In this experiment, T47D cancer cells, which are a type of breast cancer cell, were passed through a microfluidic chip and their impedance and phase features were recorded. The goal of this experiment was to classify T47D cancer cells treated with the target drug and T47D dead cancer cells. The resulting classifier exhibited an accuracy of 95.9% using amplitude change and phase change as features for the SVM classifier.

A surface acoustic wave (SAW) biosensor is an electrical biosensor. It operates based on the generation and detection of surface acoustic waves on a piezoelectric substrate, which are electrical signals. Sountharrajan et al. [106] developed a SAW biosensor for the label-free detection of HER-2/neu, a biomarker associated with breast cancer cells. The biosensor output, along with data from the Wisconsin dataset (the name of the breast cancer dataset), was inputted into a proposed system for data mining classification algorithms. The proposed model was improved by ranking the attributes using the Ranker algorithm, resulting in an accuracy of 79.25% using an SVM classifier. Overall, the study demonstrated the potential of SAW biosensors for the efficient detection of HER-2/neu, offering a promising avenue for early breast cancer diagnosis.

Breast cancer causes metabolic alteration, and volatile metabolites in the breath of patients may be used to diagnose breast cancer [107]. As a proof of concept, Yang et al. [107] developed a new breath test for breast cancer by analyzing the volatile metabolites in

exhaled breath (Figure 8B). They collected air samples from breast cancer patients and non-cancer controls and used an electronic nose made of 32 carbon nanotube sensors to analyze the volatile metabolites. Machine learning techniques were employed to create predictive models for breast cancer. Using a RF algorithm, they achieved a 91% accuracy in predicting breast cancer in the test set.

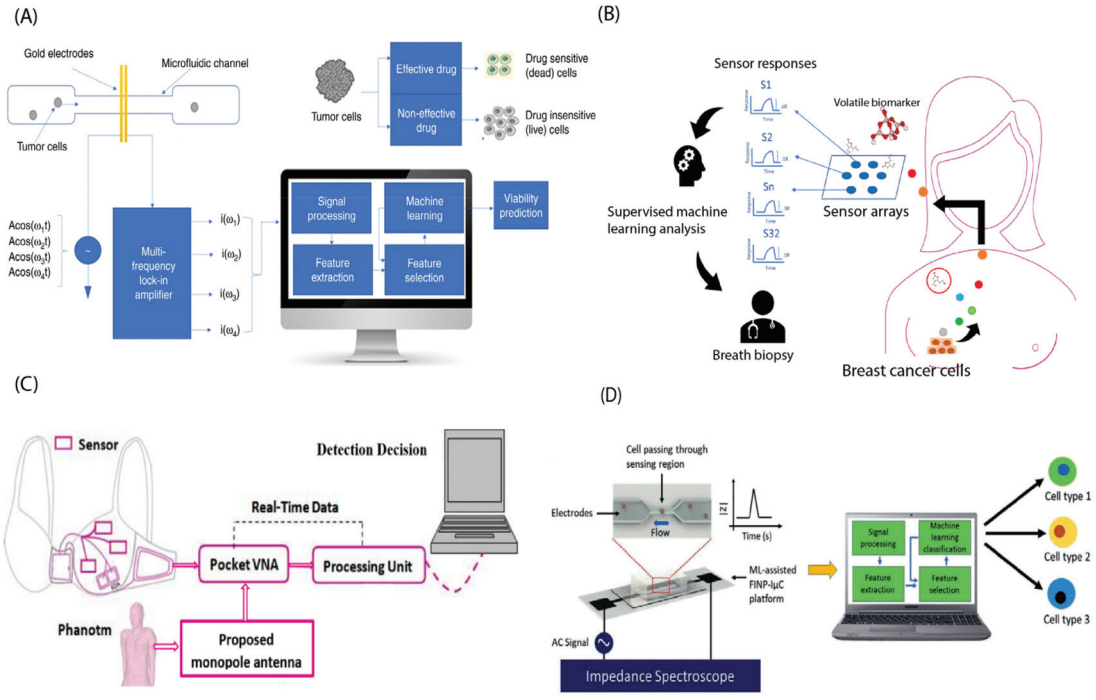

Figure 8. (**A**) Multifrequency impedance cytometry measures the response across a broad range of frequencies to assess cellular responses to a target drug. Machine learning algorithms are utilized to predict the viability of both live and dead cells. Reprinted with permission from [105]. Copyright 2021 Springer Nature. (**B**) Graphical representation illustrating the concept of breath biopsy. Breast cancer cells produce volatile metabolites that travel to the lungs and are exhaled. By using a sensor array to analyze these biomarkers in the breath, we can identify the molecular subtype of breast cancer at an early stage. Reprinted from [107]. (**C**) The proposed breast cancer detection system is a Smart Bra. Reprinted with permission from [108]. Copyright 2020 John Wiley and Sons. (**D**) The ML-assisted biochip performs single-cell classification in a label-free manner. The machine learning algorithm is used to perform both cell health classification (cancerous vs. non-cancerous) and cancer subtype cell discrimination at the single cell level. Reprinted with the permission from [109]. Copyright 2020 John Wiley and Sons.

One innovative way to detect breast cancer is through the use of a wearable system designed for detecting breast tumors. For instance, Elsheakh et al. [108] presented a breast cancer detection and monitoring system that utilizes microwave textile-based antenna sensors. The system consists of a wearable device that integrates the microwave antenna sensors and a portable measurement unit that wirelessly communicates with the device to collect and analyze the sensor data, as seen in Figure 8C. The proposed system aims to provide a low-cost, non-invasive, and reliable solution for the early detection and monitoring of breast cancer. The proposed system was tested on a dataset of 110 breast tissue samples, and it achieved an accuracy of 100% for breast cancer detection and classification.

As we discussed earlier, the most commonly used parameter for identifying and quantifying cells is impedance. Joshi et al. [109] demonstrated the effectiveness of single-cell impedance spectroscopy in distinguishing different types of breast cancer cells when used in conjunction with a machine learning classifier (Figure 8D). To evaluate the effectiveness of the method, the researchers pumped two types of cells through a microfluidic channel while constantly measuring the channel's impedance throughout the entire test. The impedance measurements were then fed into a quadratic discriminant analysis (QDA) classifier, which was able to distinguish between the two types of cells with an accuracy of greater than 95% using single-feature classification. As another example, Bondancia et al. [110] developed an immunosensor to detect the cancer biomarker p53 in MCF7 breast cancer cells using electrical impedance spectroscopy. In this sensor, interdigitated electrodes were printed on bacterial nanocellulose substrates using a screen-printing technique. These electrodes were then coated with a layer-by-layer matrix of chitosan and chondroitin sulfate. On top of this matrix, a layer of anti-p53 antibodies was applied by adsorption. They also applied the DT algorithm and achieved 90% accuracy.

To enhance the detection of cancer cells, it is more logical to integrate the electrical and optical methods together. For example, Liang et al. [111] introduced a novel imaging and impedance-based single-cell analysis system called IM2Cell that enables multi-stress level mechanical phenotyping. The system is capable of simultaneously measuring both the mechanical and electrical properties of cells, providing high-dimensional information on cell structures and functions. The authors validated the imaging and impedance-based analyses separately and then combined the techniques to obtain high accuracy in predicting the characteristics of fixed and living MDA-MB-231 breast cancer cells. The authors also demonstrated IM2Cell's ability to classify a mixture of unlabeled MCF-10A, MCF-7, and MDA-MB-231 cell lines with high accuracy. Next, IM2Cell demonstrates a 91.2% classification accuracy in a mixture of unlabeled MCF-10A, MCF-7, and MDA-MB-231 cell lines.

3.2.2. Lung Cancer

In this section, we will explain two examples of different electrical sensors to detect lung cancer cells. The first example is Zhang et al. [112] developing a new biosensing strategy called SHARK (Synthetic Enzyme Shift RNA Signal Amplifier Related Cas13a Knockdown Reaction) for lung cancer detection. SHARK has broad compatibility and can be used as a portable SARS-CoV-2 biosensor with high sensitivity and selectivity, consistent with qRT-PCR results. They combined the output from the biosensors with SVM machine-learning algorithms to predict target miRNAs for (non-small cell lung cancer) NSCLC diagnosis with an accuracy of 82.81%. As another example, Van de Goor et al. [113] utilized five e-nose devices to collect breath samples from lung cancer patients and healthy controls. A total of 60 lung cancer patients and 107 healthy individuals exhaled through the e-nose for five minutes, with the participants assigned to either a training or a blinded control group. The results showed that the e-nose had a diagnostic accuracy of 83%, with a sensitivity of 83%, for discriminating between lung cancer patients and healthy controls. This study provides evidence for the feasibility and effectiveness of using a portable e-nose for accurately detecting lung cancer.

3.2.3. Liver Cancer

Volatile organic compounds (VOCs) in breath are increasingly being recognized as favorable biomarkers, particularly for cancers, due to their ease of sample retrieval and specific association with early metabolic changes [114]. In the article by Nazir and Abbas [114], the use of an e-nose biosensor to detect phenol 2,2-methylene bis, 6 [1,1-D] in breath samples of hepatocellular carcinoma (HCC), which is a type of primary liver cancer, is described. Figure 9 represents an overview of the proposed model.

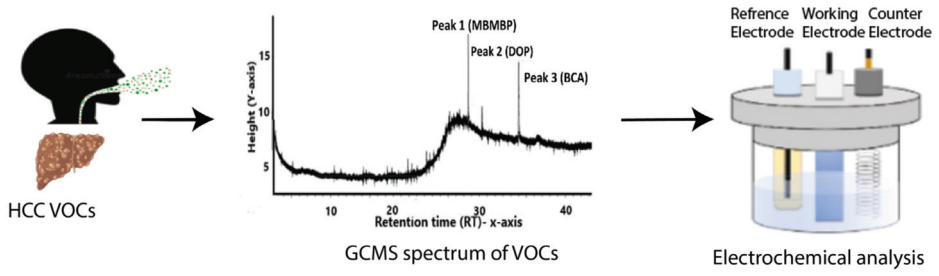

Figure 9. Overview of e-nose biosensor for liver cancer detection from VOCs in breath. Reprinted with permission from [114]. Copyright 2023 Elsevier.

They conducted a screening of breath samples from patients with HCC to identify volatile organic compounds (VOCs) using gas chromatography-mass spectrometry (GC-MS). They applied unsupervised machine learning models to validate their findings. The accuracy of the developed sensor was found to be 86%, demonstrating the promising potential of this approach.

3.2.4. Pancreatic Cancer

Multifrequency single-cell impedance cytometry provides multiparametric biophysical information. To demonstrate, Salahi et al. [115] developed a label-free approach to distinguish pancreatic cancer cells from their associated fibroblasts based on their biophysical properties using impedance cytometry data and machine learning algorithms. The authors demonstrate that gemcitabine treatment changes the biophysical properties of cancer cells and fibroblasts in different ways, resulting in distinguishable patterns in the impedance measurements. The approach has potential applications in cancer diagnosis, treatment monitoring, and drug development.

Combining various types of machine learning techniques has the potential to improve the accuracy of classification. By integrating different approaches, we can leverage the strengths of each method and mitigate their individual limitations, resulting in more precise and reliable classification outcomes. For instance, Honrado et al. [116] improved the classification of cancerous pancreatic cells by combining unsupervised clustering with KNN classification to detect the state of cell death experienced by the cancerous cell. The researchers collected impedance data from flow cytometry and fed it into an unsupervised clustering algorithm that operated at a hyper-dimensional level to autonomously cluster the data. The resulting metrics were then used to quantify the drug-sensitive phenotypes of cancer cells across their progression from viable to early apoptotic, late apoptotic, and necrotic subpopulations. To validate their findings, the team compared the results to those obtained through staining and found that their model was 98.4% accurate in detecting the correct phase of apoptosis in pancreatic cancer cells.

3.2.5. Hematological Cancer

Recently, impedance spectrometers have been shown to generate all-inclusive lab-on-a-chip platforms to detect nucleus abnormalities. The paper, presented by Ferguson et al. [117], is a proof-of-concept study on the classification of cancerous cells using a biosensor that employs impedance-based spectroscopy to identify the type of cells based on the size of their nucleus. The biosensor consists of a microfluidic channel attached to a quartz substrate containing an ultra-wideband waveguide. The cells passing through the PDMS channel are electrically trapped using a dielectrophoretic signal, and electrical signals are collected using microwave spectroscopy. The authors used statistical elimination and feature selection techniques along with SVMs and RF algorithms to achieve a 96% accuracy on multi-class classification. The study demonstrates the potential of using machine learning in combination with microwave impedance spectroscopy for single-cell classification

based on the population nucleus size, which could have significant implications for cancer diagnosis and treatment.

3.2.6. Head and Neck Cancer

Currently, there is a lack of well-established effective biomarkers and convenient detection methods for predicting radioresistance. In the study by Wu et al. [118], surface-enhanced Raman spectroscopy combined with proteomics was employed to initially profile the distinct spectral patterns of the exosomes released by self-established nasopharyngeal cancer cells (NPC). They identified specific variations in protein expression during the formation of radioresistance, including collagen alpha-2 (COL1A2), which is negatively associated with DNA repair. The researchers used bioinformatics analysis and a deep learning model to accurately identify the exosomes from the radioresistance group, achieving an accuracy of 92.4%. Overall, the study provides a promising approach for identifying radioresistance-associated biomarkers in NPC.

Diagnosing cancer and other diseases using data from non-specific sensors, like electronic tongues (e-tongues), poses challenges due to the lack of selectivity and the variability of biological samples [119]. Braz et al. [119] presented an e-tongue biosensor based on microfluidic impedance flow cytometry for mouth cancer detection. Saliva samples from 27 individuals were analyzed using multidimensional projection techniques and machine learning algorithms, including the SVM with a radial basis function kernel and RF algorithms. The authors achieved an accuracy of over 80% for the binary classification of cancer vs. healthy individuals. The study suggests that the impedance data obtained with the e-tongue in saliva samples can be used for cancer diagnosis in the mouth, and the approach presented here is promising for computer-assisted diagnoses. The accuracy tended to increase when clinical information, such as alcohol consumption, was used in conjunction with the e-tongue data.

3.2.7. Gynecological Cancer

A microfluidic chip for single-cell cultures utilizes self-assembled graphene oxide quantum dots (GOQDs) to facilitate high-activity single-cell cultures. This chip enables the maintenance of normal biomarker secretion in single cells and allows for efficient single cell separation at high throughputs. Consequently, it provides an ample amount of statistical data necessary for machine learning applications [120]. As a proof of concept, Wang et al. [120] developed a novel method for profiling single cells in real time using microfluidic chip technology and machine learning algorithms. They used this method to classify tumor cells based on the secreted biomarkers they produce. The microfluidic chip is designed to allow for the high-throughput analysis of single cells, enabling the measurement of multiple secreted biomarkers in real time. Then, machine learning algorithms were employed to analyze the data and classify the cells based on their biomarker profiles. The K-means strategy with machine learning was combined to analyze thousands of single tumor cell secretion data, resulting in the ability to classify tumor cells with a recognition accuracy of 95.0%.

As another example, Feng et al. [121] proposed the use of neural network-enhanced impedance flow cytometry (IFC) for the real-time, label-free, and non-invasive characterization of single cells based on intrinsic biophysical metrics. The method can obtain three intrinsic parameters (radius, cytoplasm conductivity, and specific membrane capacitance) online and in real time, achieving a significant improvement in the calculation speed. The experiments involved four cancer cell types and demonstrated a 91.5% classification accuracy. The paper suggests that this method could provide a new platform for high-throughput, real-time, and online cell intrinsic electrical characterization. Table 2 summarizes the electrical-based biosensors in conjunction with machine learning for cancer detection.

Table 2. Comparison of different electrical-based biosensors with ML analysis for cancer cell detection.

Authors	Cancer Cell Type	Biosensor Type	ML Algorithm	Result (%)
Ahuja et al. [105]	T47D cancer cells (Type of Breast cancer)	Microfluidic device impedance cytometry	SVM	ACC = 95.9
Sountharrajan et al. [106]	Breast Cancer	Surface acoustic wave (SAW) biosensor	SVM	ACC = 79.25
Yang et al. [107]	Breast Cancer	Nanotube sensors	Random forest (RF)	ACC = 91
Elsheakh et al. [108]	Breast Cancer	Microwave textile-based antenna sensors	CatBoost (Type of gradient boosting)	ACC = 100
Joshi et al. [109]	Breast Cancer	Microfluidic channel sensor	Quadratic discriminant analysis (QDA)	ACC > 95.3
Bondancia et al. [110]	Breast Cancer	Immunosensor	DT	ACC = 90
Liang et al. [111]	Breast Cancer Combination of electrical and optical-based sensors	Impedance-based sensor	(Linear discriminant analysis) LDA + SVM	ACC = 91.2
Zhang et al. [112]	Lung Cancer	SHARK (Synthetic Enzyme Shift RNA Signal Amplifier Related Cas13a Knockdown Reaction)	SVM	ACC = 82.81
Van de Goor et al. [113]	Lung Cancer	E-nose biosensor	ANN	ACC = 93
Nazir and Abbas [114]	Liver Cancer	E-nose biosensor	Unsupervised ML	ACC = 86
Salahi et al. [115]	Pancreatic Cancer	Microfluidic device impedance cytometry	SVM	ACC = 93.7
Honrado et al. [116]	Pancreatic Cancer	Microfluidic device impedance cytometry	KNN	ACC = 98.4
Ferguson et al. [117]	Jurkat Cells (Type of Leukemia Cancer)	Microfluidic device	RF + SVM	ACC = 96
Wu et al. [118]	Nasopharyngeal Cancer	Surface-enhanced Raman spectroscopy	ANN	ACC = 92.4
Braz et al. [119]	Oral Cancer	E-tongue biosensor	RF + SVM	ACC = 80
Wang et al. [120]	Ovarian, Kidney, Breast, Lymph Cancer	Microfluidic chip	K-means	ACC = 95
Feng et al. [121]	Breast, Cervical, Lung, Leukemia Cancer	Impedance flow cytometry (IFC)	ANN	ACC = 91.5

4. Conclusions

The pressing need to identify cancer in its earliest stages while avoiding invasive treatments has spurred the integration of innovative sensory techniques with cutting-edge machine learning algorithms. This fusion holds the potential to create a future where individuals can conveniently and promptly detect cancer within the confines of their homes. With advancements in detection technology and machine learning algorithms, our aim is to detect cancer at its early stage. Several studies have achieved highly accurate results in excess of 90% with optical biosensors, regardless of the type of cancer cell being detected or the ML algorithm used in the study. Among all the research papers analyzed for this study, most teams utilized ANNs for the machine learning aspect of their optical detection setups. On the other hand, some studies using electrical biosensors achieved slightly lower, yet consistently high, results when compared to the teams that employed optical biosensors. Slightly more than half of these teams recorded an accuracy greater than 90%, while the remaining teams had accuracies that were slightly lower. Most of these teams used SVMs to incorporate machine learning into their research, with ANNs being used to a lesser extent than in the optical detection teams. With further progress and advancements in these methodologies, we can hope for continuous improvements in the results and eventually strive towards a cancer-free future.

Biosensors are analytical devices that combine biological components, known as bioreceptors, with transducers to detect specific biological or chemical analytes. Despite the significant advancements, biosensors still face challenges related to the bioreceptor immobi-

lization matrices, immobilization efficiency, and predicting responses in complex matrices. Machine learning (ML) can play a vital role in addressing these issues. For instance, ML models can assist in selecting the most suitable immobilization matrix for a specific bioreceptor by considering factors such as the bioreceptor type, analyte characteristics, and environmental conditions. This predictive capability helps researchers optimize the immobilization process and anticipate and correct deviations in sensor responses. Additionally, ML can aid in sensor calibration and data fusion, enhancing the accuracy and reliability of biosensor readings by continuously monitoring and adjusting the sensor responses based on historical data and real-time measurements.

In summary, biosensors are essential analytical tools with some inherent limitations. ML can offer valuable solutions by assisting in the selection of immobilization matrices for bioreceptors and improving sensor calibration and data fusion processes. These ML-driven interventions enhance the overall performance and reliability of biosensors, making them more effective in applications such as cancer cell detection and other complex analytical tasks.

Author Contributions: Conceptualization, M.K. and M.N.T.; methodology, M.K., D.S. and M.N.T.; validation, M.K., M.N.T. and D.S.; writing—original draft preparation, M.K.; writing—review and editing, M.N.T., D.S. and M.K.; supervision, M.J.; project administration, M.J.; funding acquisition, M.J. All authors have read and agreed to the published version of the manuscript.

Funding: This research was funded by the National Science Foundation grant numbers 1846740, and 2002511.

Institutional Review Board Statement: Not applicable.

Informed Consent Statement: Not applicable.

Data Availability Statement: The data presented in this study are available on request from the corresponding author. The data are not publicly available due to ethical constraints.

Acknowledgments: The authors are thankful to their respective institutions/universities for providing valuable support and funding to conduct this research work.

Conflicts of Interest: The authors have no conflict of interest.

References

1. Available online: https://www.who.int/news-room/fact-sheets/detail/cancer (accessed on 6 May 2023).
2. Stratton, M.R.; Campbell, P.J.; Futreal, P.A. The cancer genome. *Nature* **2009**, *458*, 719–724. [CrossRef] [PubMed]
3. Kaur, B.; Kumar, S.; Kaushik, B.K. Recent advancements in optical biosensors for cancer detection. *Biosens. Bioelectron.* **2022**, *197*, 113805. [CrossRef] [PubMed]
4. Sinha, T. Tumors: Benign and malignant. *Cancer Ther. Oncol. Int. J.* **2018**, *10*, 52–54. [CrossRef]
5. Weinberg, R.A. How cancer arises. *Sci. Am.* **1996**, *275*, 62–70. [CrossRef] [PubMed]
6. Vaidyanathan, R.; Soon, R.H.; Zhang, P.; Jiang, K.; Lim, C.T. Cancer diagnosis: From tumor to liquid biopsy and beyond. *Lab Chip* **2019**, *19*, 11–34. [CrossRef]
7. Crulhas, B.P.; Basso, C.R.; Castro, G.R.; Pedrosa, V.A. Recent advances based on a sensor for cancer biomarker detection. *ECS J. Solid State Sci. Technol.* **2021**, *10*, 047004. [CrossRef]
8. Alharthi, S.D.; Bijukumar, D.; Prasad, S.; Khan, A.M.; Mathew, M.T. Evolution in biosensors for cancers biomarkers detection: A review. *J. Bio-Tribo-Corros.* **2021**, *7*, 42. [CrossRef]
9. Khanmohammadi, A.; Aghaie, A.; Vahedi, E.; Qazvini, A.; Ghanei, M.; Afkhami, A.; Hajian, A.; Bagheri, H. Electrochemical biosensors for the detection of lung cancer biomarkers: A review. *Talanta* **2020**, *206*, 120251. [CrossRef]
10. Zhang, Y.; Li, M.; Gao, X.; Chen, Y.; Liu, T. Nanotechnology in cancer diagnosis: Progress, challenges and opportunities. *J. Hematol. Oncol.* **2019**, *12*, 137. [CrossRef]
11. Shahbazi, N.; Zare-Dorabei, R.; Naghib, S.M. Design of a ratiometric plasmonic biosensor for herceptin detection in HER2-positive breast cancer. *ACS Biomater. Sci. Eng.* **2022**, *8*, 871–879. [CrossRef]
12. Mwesige, B.; Yeo, S.-G.; Yoo, B.C. Circulating tumor cells: Liquid biopsy for early detection of cancer. *Soonchunhyang Med. Sci.* **2019**, *25*, 1–9. [CrossRef]
13. de Vries, M.; Jager, P.; Suurmeijer, A.; Plukker, J.; van Ginkel, R.; Hoekstra, H. Sentinel lymph node biopsy for melanoma: Prognostic value and disadvantages in 300 patients. *Ned. Tijdschr. Geneeskd.* **2005**, *149*, 1845–1851.

14. Yeasmin, S.; Ammanath, G.; Ali, Y.; Boehm, B.O.; Yildiz, U.H.; Palaniappan, A.; Liedberg, B. Colorimetric urinalysis for on-site detection of metabolic biomarkers. *ACS Appl. Mater. Interfaces* **2020**, *12*, 31270–31281. [CrossRef] [PubMed]
15. Zhang, Z.; Liu, J.; Cheng, Y.; Chen, J.; Zhao, H.; Ren, X. Urine analysis has a very broad prospect in the future. *Front. Anal. Sci.* **2022**, *1*, 13. [CrossRef]
16. Wang, L. Screening and biosensor-based approaches for lung cancer detection. *Sensors* **2017**, *17*, 2420. [CrossRef]
17. Altintas, Z.; Tothill, I. Biomarkers and biosensors for the early diagnosis of lung cancer. *Sens. Actuators B Chem.* **2013**, *188*, 988–998. [CrossRef]
18. Zhang, X.; Yao, B.; Hu, Q.; Hong, Y.; Wallace, A.; Reynolds, K.; Ramsey, C.; Maeder, A.; Reed, R.; Tang, Y.; et al. Detection of biomarkers in body fluids using bioprobes based on aggregation-induced emission fluorogens. *Mater. Chem. Front.* **2020**, *4*, 2548–2570. [CrossRef]
19. Singh, A.; Sharma, A.; Ahmed, A.; Sundramoorthy, A.K.; Furukawa, H.; Arya, S.; Khosla, A. Recent advances in electrochemical biosensors: Applications, challenges, and future scope. *Biosensors* **2021**, *11*, 336. [CrossRef]
20. Zhang, K.; Wang, J.; Liu, T.; Luo, Y.; Loh, X.J.; Chen, X. Machine learning-reinforced noninvasive biosensors for healthcare. *Adv. Healthc. Mater.* **2021**, *10*, 2100734. [CrossRef]
21. Bax, C.; Taverna, G.; Eusebio, L.; Sironi, S.; Grizzi, F.; Guazzoni, G.; Capelli, L. Innovative diagnostic methods for early prostate cancer detection through urine analysis: A review. *Cancers* **2018**, *10*, 123. [CrossRef]
22. Azab, M.Y.; Hameed, M.F.O.; Obayya, S.S. Overview of Optical Biosensors for Early Cancer Detection: Fundamentals, Applications and Future Perspectives. *Biology* **2023**, *12*, 232. [CrossRef] [PubMed]
23. Roberts, A.; Gandhi, S. A concise review on potential cancer biomarkers and advanced manufacturing of smart platform-based biosensors for early-stage cancer diagnost ics. *Biosens. Bioelectron. X* **2022**, *11*, 100178.
24. Tothill, I.E. Biosensors for cancer markers diagnosis. In *Seminars in Cell & Developmental Biology*; Elsevier: Amsterdam, The Netherlands, 2009; Volume 20, pp. 55–62.
25. Queralto, N.; Berliner, A.N.; Goldsmith, B.; Martino, R.; Rhodes, P.; Lim, S.H. Detecting cancer by breath volatile organic compound analysis: A review of array-based sensors. *J. Breath Res.* **2014**, *8*, 027112. [CrossRef] [PubMed]
26. Ortiz-Casas, B.; Galdámez-Martínez, A.; Gutiérrez-Flores, J.; Ibañez, A.B.; Panda, P.K.; Santana, G.; de la Vega, H.A.; Suar, M.; Rodelo, C.G.; Kaushik, A.; et al. Bio-acceptable 0D and 1D ZnO nanostructures for cancer diagnostics and treatment. *Mater. Today* **2021**, *50*, 533–569. [CrossRef]
27. Gao, Q.; Lee, W.-Y. Urinary metabolites for urological cancer detection: A review on the application of volatile organic compounds for cancers. *Am. J. Clin. Exp. Urol.* **2019**, *7*, 232.
28. Amethiya, Y.; Pipariya, P.; Patel, S.; Shah, M. Comparative analysis of breast cancer detection using machine learning and biosensors. *Intell. Med.* **2022**, *2*, 69–81. [CrossRef]
29. Cui, F.; Yue, Y.; Zhang, Y.; Zhang, Z.; Zhou, H.S. Advancing biosensors with machine learning. *ACS Sens.* **2020**, *5*, 3346–3364. [CrossRef]
30. Kokabi, M.; Donnelly, M.; Xu, G. Benchmarking Small-Dataset Structure-Activity-Relationship Models for Prediction of Wnt Signaling Inhibition. *IEEE Access* **2020**, *8*, 228831–228840. [CrossRef]
31. Kokabi, M.; Sui, J.; Gandotra, N.; Khamseh, A.P.; Scharfe, C.; Javanmard, M. Nucleic Acid Quantification by Multi-Frequency Impedance Cytometry and Machine Learning. *Biosensors* **2023**, *13*, 316. [CrossRef]
32. Kokabi, H.; Najafi, M.; Jazayeri, S.A.; Jahanian, O. Performance optimization of RCCI engines running on landfill gas, propane and hydrogen through the deep neural network and genetic algorithm. *Sustain. Energy Technol. Assess.* **2023**, *56*, 103045. [CrossRef]
33. Fujiyoshi, H.; Hirakawa, T.; Yamashita, T. Deep learning-based image recognition for autonomous driving. *IATSS Res.* **2019**, *43*, 244–252. [CrossRef]
34. Varkonyi, A.; Mosavi, A. Learning in Robotics. *Int. J. Comput. Appl.* **2017**, *157*, 8–11. [CrossRef]
35. El Naqa, I.; Murphy, M.J. *What Is Machine Learning?* Springer: Berlin/Heidelberg, Germany, 2015.
36. Alloghani, M.; Al-Jumeily, D.; Mustafina, J.; Hussain, A.; Aljaaf, A.J. A systematic review on supervised and unsupervised machine learning algorithms for data science. In *Supervised and Unsupervised Learning for Data Science*; Springer: Berlin/Heidelberg, Germany, 2020; pp. 3–21.
37. Nasteski, V. An overview of the supervised machine learning methods. *Horizons B* **2017**, *4*, 51–62. [CrossRef]
38. Berry, M.W.; Mohamed, A.; Yap, B.W. *Supervised and Unsupervised Learning for Data Science*; Springer: Berlin/Heidelberg, Germany, 2019.
39. Poellmann, M.J.; Bu, J.; Liu, S.; Wang, A.Z.; Seyedin, S.N.; Chandrasekharan, C.; Hong, H.; Kim, Y.; Caster, J.M.; Hong, S. Nanotechnology and machine learning enable circulating tumor cells as a reliable biomarker for radiotherapy responses of gastrointestinal cancer patients. *Biosens. Bioelectron.* **2023**, *226*, 115117. [CrossRef] [PubMed]
40. Noble, W.S. What is a support vector machine? *Nat. Biotechnol.* **2006**, *24*, 1565–1567. [CrossRef] [PubMed]
41. Raji, H.; Tayyab, M.; Sui, J.; Mahmoodi, S.R.; Javanmard, M. Biosensors and machine learning for enhanced detection, stratification, and classification of cells: A review. *Biomed. Microdevices* **2022**, *24*, 26. [CrossRef]
42. Sun, S.; Huang, R. An adaptive k-nearest neighbor algorithm. In Proceedings of the 2010 Seventh International Conference on Fuzzy Systems and Knowledge Discovery, Yantai, China, 10–12 August 2010; IEEE: Piscataway, NJ, USA, 2010; Volume 1, pp. 91–94.

43. Laaksonen, J.; Oja, E. Classification with learning k-nearest neighbors. In Proceedings of the International Conference on Neural Networks (ICNN'96), Washington, DC, USA, 3–6 June 1996; IEEE: Piscataway, NJ, USA, 1996; Volume 3, pp. 1480–1483.
44. Ozaki, K.; Shimbo, M.; Komachi, M.; Matsumoto, Y. Using the mutual k-nearest neighbor graphs for semi-supervised classification on natural language data. In Proceedings of the Fifteenth Conference on Computational Natural Language Learning, Portland, OR, USA, 23–24 June 2011; pp. 154–162.
45. Khateeb, N.; Usman, M. Efficient heart disease prediction system using K-nearest neighbor classification technique. In Proceedings of the International Conference on Big Data and Internet of Thing, London, UK, 20–22 December 2017; pp. 21–26.
46. Myles, A.J.; Feudale, R.N.; Liu, Y.; Woody, N.A.; Brown, S.D. An introduction to decision tree modeling. *J. Chemom.* **2004**, *18*, 275–285. [CrossRef]
47. Jahromi, A.H.; Taheri, M. A non-parametric mixture of Gaussian naive Bayes classifiers based on local independent features. In Proceedings of the 2017 Artificial Intelligence and Signal Processing Conference (AISP), Shiraz, Iran, 25–27 October 2017; IEEE: Piscataway, NJ, USA, 2017; pp. 209–212.
48. Bisong, E.; Bisong, E. Logistic regression. In *Building Machine Learning and Deep Learning Models on Google Cloud Platform: A Comprehensive Guide for Beginners*; Springer: Berlin/Heidelberg, Germany, 2019; pp. 243–250.
49. Goswami, M.; Sebastian, N.J. Performance Analysis of Logistic Regression, KNN, SVM, Naïve Bayes Classifier for Healthcare Application during COVID-19. In *Innovative Data Communication Technologies and Application: Proceedings of ICIDCA 2021*; Springer: Singapore, 2022; pp. 645–658.
50. Kulkarni, A.D.; Lowe, B. Random Forest Algorithm for Land Cover Classification. 2016. Available online: https://scholarworks.uttyler.edu/compsci_fac/1/ (accessed on 6 May 2023).
51. Agatonovic-Kustrin, S.; Beresford, R. Basic concepts of artificial neural network (ANN) modeling and its application in pharmaceutical research. *J. Pharm. Biomed. Anal.* **2000**, *22*, 717–727. [CrossRef]
52. Available online: https://en.wikipedia.org/wiki/Support_vector_machine (accessed on 6 May 2023).
53. KNN. Available online: https://en.wikipedia.org/wiki/K-nearest_neighbors_algorithm (accessed on 6 May 2023).
54. DT Algorithm. Available online: https://www.javatpoint.com/machine-learning-decision-tree-classification-algorithm (accessed on 6 May 2023).
55. LR. Available online: https://machine-learning.paperspace.com/wiki/logistic-regression (accessed on 6 May 2023).
56. ANN. Available online: https://www.tibco.com/reference-center/what-is-a-neural-network (accessed on 6 May 2023).
57. Hoo, Z.H.; Candlish, J.; Teare, D. What is an ROC curve? *Emerg. Med. J.* **2017**, *34*, 357–359. [CrossRef]
58. Chen, C.; Wang, J. Optical biosensors: An exhaustive and comprehensive review. *Analyst* **2020**, *145*, 1605–1628. [CrossRef]
59. García-Hernández, L.A.; Martínez-Martínez, E.; Pazos-Solís, D.; Aguado-Preciado, J.; Dutt, A.; Chávez-Ramírez, A.U.; Korgel, B.; Sharma, A.; Oza, G. Optical Detection of Cancer Cells Using Lab-on-a-Chip. *Biosensors* **2023**, *13*, 439. [CrossRef] [PubMed]
60. Salahandish, R.; Ghaffarinejad, A.; Naghib, S.M.; Majidzadeh-A, K.; Zargartalebi, H.; Sanati-Nezhad, A. Nano-biosensor for highly sensitive detection of HER2 positive breast cancer. *Biosens. Bioelectron.* **2018**, *117*, 104–111. [CrossRef] [PubMed]
61. Mittal, S.; Kaur, H.; Gautam, N.; Mantha, A.K. Biosensors for breast cancer diagnosis: A review of bioreceptors, biotransducers and signal amplification strategies. *Biosens. Bioelectron.* **2017**, *88*, 217–231. [CrossRef] [PubMed]
62. Piliarik, M.; Homola, J. Surface plasmon resonance (SPR) sensors: Approaching their limits? *Opt. Express* **2009**, *17*, 16505–16517. [CrossRef] [PubMed]
63. Gade, A.; Sharma, A.; Srivastava, N.; Flora, S. Surface plasmon resonance: A promising approach for label-free early cancer diagnosis. *Clin. Chim. Acta* **2022**, *527*, 79–88. [CrossRef]
64. Kumar, A.; Verma, P.; Jindal, P. Surface plasmon resonance sensor based on MXene coated PCF for detecting the cancer cells with machine learning approach. *Microelectron. Eng.* **2023**, *267*, 111897. [CrossRef]
65. Verma, P.; Kumar, A.; Jindal, P. Machine Learning Approach for SPR based Photonic Crystal Fiber Sensor for Breast Cancer Cells Detection. In Proceedings of the 2022 IEEE 7th Forum on Research and Technologies for Society and Industry Innovation (RTSI), Paris, France, 24–26 August 2022; IEEE: Piscataway, NJ, USA, 2022; pp. 7–12.
66. Li, H.; Jiang, B.; Li, J. Recent advances in dopamine-based materials constructed via one-pot co-assembly strategy. *Adv. Colloid Interface Sci.* **2021**, *295*, 102489. [CrossRef]
67. Jin, Y.; Du, N.; Huang, Y.; Shen, W.; Tan, Y.; Chen, Y.Z.; Dou, W.T.; He, X.P.; Yang, Z.; Xu, N.; et al. Fluorescence analysis of circulating exosomes for breast cancer diagnosis using a sensor array and deep learning. *ACS Sens.* **2022**, *7*, 1524–1532. [CrossRef]
68. Pala, M.A.; Çimen, M.E.; Akgül, A.; Yıldız, M.Z.; Boz, A.F. Fractal dimension-based viability analysis of cancer cell lines in lens-free holographic microscopy via machine learning. *Eur. Phys. J. Spec. Top.* **2022**, *231*, 1023–1034. [CrossRef]
69. Yang, G.; Xiao, Z.; Tang, C.; Deng, Y.; Huang, H.; He, Z. Recent advances in biosensor for detection of lung cancer biomarkers. *Biosens. Bioelectron.* **2019**, *141*, 111416. [CrossRef]
70. Hashemzadeh, H.; Shojaeilangari, S.; Allahverdi, A.; Rothbauer, M.; Ertl, P.; Naderi-Manesh, H. A combined microfluidic deep learning approach for lung cancer cell high throughput screening toward automatic cancer screening applications. *Sci. Rep.* **2021**, *11*, 9804. [CrossRef] [PubMed]
71. Siu, D.M.; Lee, K.C.M.; Lo, M.C.K.; Stassen, S.V.; Wang, M.; Zhang, I.Z.Q.; So, H.K.H.; Chan, G.C.F.; Cheah, K.S.E.; Wong, K.K.Y.; et al. Deep-learning-assisted biophysical imaging cytometry at massive throughput delineates cell population heterogeneity. *Lab Chip* **2020**, *20*, 3696–3708. [CrossRef] [PubMed]

72. Nguyen, T.M.; Chung, J.H.; Bak, G.H.; Kim, Y.H.; Kim, M.; Kim, Y.J.; Kwon, R.J.; Choi, E.J.; Kim, K.H.; Kim, Y.S.; et al. Multiarray Biosensor for Diagnosing Lung Cancer Based on Gap Plasmonic Color Films. *ACS Sens.* **2022**, *8*, 167–175. [CrossRef]
73. Wei, H.; Xie, L.; Liu, Q.; Shao, C.; Wang, X.; Su, X. Automatic Classification of Label-Free Cells from Small Cell Lung Cancer and Poorly Differentiated Lung Adenocarcinoma with 2D Light Scattering Static Cytometry and Machine Learning. *Cytom. Part A* **2018**, *95*, 302–308. [CrossRef] [PubMed]
74. Khalid, S.; Khalil, T.; Nasreen, S. A survey of feature selection and feature extraction techniques in machine learning. In Proceedings of the 2014 Science and Information Conference, London, UK, 27–29 August 2014; IEEE: Piscataway, NJ, USA, 2014; pp. 372–378.
75. Ahmad, A.; Sala, F.; Paiè, P.; Candeo, A.; D'Annunzio, S.; Zippo, A.; Frindel, C.; Osellame, R.; Bragheri, F.; Bassi, A.; et al. On the robustness of machine learning algorithms toward microfluidic distortions for cell classification via on-chip fluorescence microscopy. *Lab Chip* **2022**, *22*, 3453–3463. [CrossRef]
76. Lin, C.; Liang, S.; Li, Y.; Peng, Y.; Huang, Z.; Li, Z.; Yang, Y.; Luo, X. Localized plasmonic sensor for direct identifying lung and colon cancer from the blood. *Biosens. Bioelectron.* **2022**, *211*, 114372. [CrossRef]
77. Park, J.; Hwang, M.; Choi, B.; Jeong, H.; Jung, J.H.; Kim, H.K.; Hong, S.; Park, J.H.; Choi, Y. Exosome classification by pattern analysis of surface-enhanced Raman spectroscopy data for lung cancer diagnosis. *Anal. Chem.* **2017**, *89*, 6695–6701. [CrossRef]
78. Ko, J.; Bhagwat, N.; Yee, S.S.; Ortiz, N.; Sahmoud, A.; Black, T.; Aiello, N.M.; McKenzie, L.; O'Hara, M.; Redlinger, C.; et al. Combining machine learning and nanofluidic technology to diagnose pancreatic cancer using exosomes. *ACS Nano* **2017**, *11*, 11182–11193. [CrossRef]
79. Li, P.; Chen, J.; Chen, Y.; Song, S.; Huang, X.; Yang, Y.; Li, Y.; Tong, Y.; Xie, Y.; Li, J.; et al. Construction of Exosome SORL1 Detection Platform Based on 3D Porous Microfluidic Chip and its Application in Early Diagnosis of Colorectal Cancer. *Small* **2023**, *19*, 2207381. [CrossRef]
80. Cheng, N.; Fu, J.; Chen, D.; Chen, S.; Wang, H. An antibody-free liver cancer screening approach based on nanoplasmonics biosensing chips via spectrum-based deep learning. *NanoImpact* **2021**, *21*, 100296. [CrossRef]
81. D'Orazio, M.; Murdocca, M.; Mencattini, A.; Casti, P.; Filippi, J.; Antonelli, G.; Di, G.D.; Comes, M.C.; Di, N.C.; Sangiuolo, F.; et al. Machine learning phenomics (MLP) combining deep learning with time-lapse-microscopy for monitoring colorectal adenocarcinoma cells gene expression and drug-response. *Sci. Rep.* **2022**, *12*, 8545. [CrossRef] [PubMed]
82. Saren, G.; Zhu, L.; Han, Y. Quantitative Detection of Gastrointestinal Tumor Markers Using a Machine Learning Algorithm and Multicolor Quantum Dot Biosensor. *Comput. Intell. Neurosci.* **2022**, *2022*, 9022821. [CrossRef] [PubMed]
83. Yu, T.-M.; Chuang, Y.W.; Yu, M.C.; Chen, C.H.; Yang, C.K.; Huang, S.T.; Lin, C.L.; Shu, K.H.; Kao, C.H. Risk of cancer in patients with polycystic kidney disease: A propensity-score matched analysis of a nationwide, population-based cohort study. *Lancet Oncol.* **2016**, *17*, 1419–1425. [CrossRef] [PubMed]
84. Cachat, F.; Renella, R. Risk of cancer in patients with polycystic kidney disease. *Lancet Oncol.* **2016**, *17*, e474. [CrossRef]
85. Mencattini, A.; Rizzuto, V.; Antonelli, G.; Di Giuseppe, D.; D'Orazio, M.; Filippi, J.; Comes, M.C.; Casti, P.; Vives Corrons, J.L.; Garcia-Bravo, M.; et al. Machine Learning Microfluidic based platform: Integration of Lab-on-Chip devices and data analysis algorithms for Red Blood Cell plasticity evaluation in Pyruvate Kinase Disease monitoring. *Sens. Actuators A Phys.* **2023**, *351*, 114187. [CrossRef]
86. Asare-Werehene, M.; Hunter, R.A.; Gerber, E.; Reunov, A.; Brine, I.; Chang, C.Y.; Chang, C.C.; Shieh, D.B.; Burger, D.; Anis, H.; et al. The application of an extracellular vesicle-based biosensor in early diagnosis and prediction of chemoresponsiveness in ovarian cancer. *Cancers* **2023**, *15*, 2566. [CrossRef]
87. Liu, C.; Wang, Z.; Jia, J.; Liu, Q.; Su, X. High-content video flow cytometry with digital cell filtering for label-free cell classification by machine learning. *Cytom. Part A* **2022**, *103*, 325–334. [CrossRef]
88. Kim, M.; Chen, C.; Wang, P.; Mulvey, J.J.; Yang, Y.; Wun, C.; Antman-Passig, M.; Luo, H.B.; Cho, S.; Long-Roche, K.; et al. Detection of ovarian cancer via the spectral fingerprinting of quantum-defect-modified carbon nanotubes in serum by machine learning. *Nat. Biomed. Eng.* **2022**, *6*, 267–275. [CrossRef]
89. Pirone, D.; Xin, L.; Bianco, V.; Miccio, L.; Xiao, W.; Che, L.; Li, X.; Memmolo, P.; Pan, F.; Ferraro, P. Identification of drug-resistant cancer cells in flow cytometry combining 3D holographic tomography with machine learning. *Sens. Actuators B Chem.* **2023**, *375*, 132963. [CrossRef]
90. Kim, H.; Park, S.; Jeong, I.G.; Song, S.H.; Jeong, Y.; Kim, C.S.; Lee, K.H. Noninvasive precision screening of prostate cancer by urinary multimarker sensor and artificial intelligence analysis. *ACS Nano* **2020**, *15*, 4054–4065. [CrossRef]
91. Rodrigues, V.C.; Juliana, C.S.; Andrey, C.S.; Daniel, C.B.; Matias, E.M.; Lucas, C.R.; Leonardo, F.S.S.; Odemir, M.B.; Andre, L.C.; Rui, M.R.; et al. Electrochemical and optical detection and machine learning applied to images of genosensors for diagnosis of prostate cancer with the biomarker PCA3. *Talanta* **2021**, *222*, 121444. [CrossRef]
92. Linh, V.T.N.; Lee, M.-Y.; Mun, J.; Kim, Y.; Kim, H.; Han, I.W.; Park, S.-G.; Choi, S.; Kim, D.-H.; Rho, J.; et al. 3D plasmonic coral nanoarchitecture paper for label-free human urine sensing and deep learning-assisted cancer screening. *Biosens. Bioelectron.* **2023**, *224*, 115076. [CrossRef] [PubMed]
93. McRae, M.P.; Simmons, G.; Wong, J.; McDevitt, J.T. Programmable bio-nanochip platform: A point-of-care biosensor system with the capacity to learn. *Acc. Chem. Res.* **2016**, *49*, 1359–1368. [CrossRef] [PubMed]
94. Hasan, M.R.; Hassan, N.; Khan, R.; Kim, Y.-T.; Iqbal, S.M. Classification of cancer cells using computational analysis of dynamic morphology. *Comput. Methods Programs Biomed.* **2018**, *156*, 105–112. [CrossRef]

95. Weindel, K.; Moringlane, J.R.; Marmé, D.; Weich, H.A. Detection and quantification of vascular endothelial growth factor/vascular permeability factor in brain tumor tissue and cyst fluid: The key to angiogenesis? *Neurosurgery* **1994**, *35*, 439–449. [CrossRef]
96. Behnan, J.; Isakson, P.; Joel, M.; Cilio, C.; Langmoen, I.A.; Vik-Mo, E.O.; Badn, W. Recruited brain tumor-derived mesenchymal stem cells contribute to brain tumor progression. *Stem Cells* **2014**, *32*, 1110–1123. [CrossRef] [PubMed]
97. Hossain, A.; Islam, M.T.; Rahman, T.; Chowdhury, M.E.H.; Tahir, A.; Kiranyaz, S.; Mat, K.; Beng, G.K.; Soliman, M.S. Brain Tumor Segmentation and Classification from Sensor-Based Portable Microwave Brain Imaging System Using Lightweight Deep Learning Models. *Biosensors* **2023**, *13*, 302. [CrossRef]
98. Avelino, K.Y.; Oliveira, L.S.; Santos, M.R.; Lucena-Silva, N.; Andrade, C.A.; Oliveira, M.D. Electrochemical DNA Biosensor for Chronic Myelocytic Leukemia Based on Hybrid Nanostructure. *Bioelectrochemistry* **2022**, *147*, 108176. Available online: https://www.sciencedirect.com/science/article/abs/pii/S156753942200127X?via%3Dihub (accessed on 6 May 2023). [CrossRef]
99. Koowattanasuchat, S.; Ngernpimai, S.; Matulakul, P.; Thonghlueng, J.; Phanchai, W.; Chompoosor, A.; Panitanarak, U.; Wanna, Y.; Intharah, T.; Chootawiriyasakul, K.; et al. Rapid detection of cancer DNA in human blood using cysteamine-capped AuNPs and a machine learning-enabled smartphone. *RSC Adv.* **2023**, *13*, 1301–1311. [CrossRef]
100. Soumerai, J.D.; Mato, A.R.; Dogan, A.; Seshan, V.E.; Joffe, E.; Flaherty, K.; Carter, J.; Hochberg, E.; Barnes, J.A.; Hamilton, A.M.; et al. Zanubrutinib, obinutuzumab, and venetoclax with minimal residual disease-driven discontinuation in previously untreated patients with chronic lymphocytic leukaemia or small lymphocytic lymphoma: A multicentre, single-arm, phase 2 trial. *Lancet Haematol.* **2021**, *8*, e879–e890. [CrossRef]
101. Alten, J.; Klapper, W.; Leuschner, I.; Eckert, C.; Beier, R.; Vallo, E.; Krause, M.; Claviez, A.; Vieth, S.; Bleckmann, K.; et al. Secondary histiocytic sarcoma may cause apparent persistence or recurrence of minimal residual disease in childhood acute lymphoblastic leukemia. *Pediatr. Blood Cancer* **2015**, *62*, 1656–1660. [CrossRef] [PubMed]
102. Uslu, F.; Icoz, K.; Tasdemir, K.; Yilmaz, B. Automated quantification of immunomagnetic beads and leukemia cells from optical microscope images. *Biomed. Signal Process. Control.* **2019**, *49*, 473–482. [CrossRef]
103. Sarkar, S.; Kang, W.; Jiang, S.; Li, K.; Ray, S.; Luther, E.; Ivanov, A.R.; Fu, Y.; Konry, T. Machine learning-aided quantification of antibody-based cancer immunotherapy by natural killer cells in microfluidic droplets. *Lab Chip* **2020**, *20*, 2317–2327. [CrossRef] [PubMed]
104. Li, Y.; Mahjoubfar, A.; Chen, C.L.; Niazi, K.R.; Pei, L.; Jalali, B. Deep cytometry: Deep learning with real-time inference in cell sorting and flow cytometry. *Sci. Rep.* **2019**, *9*, 11088. [CrossRef] [PubMed]
105. Ahuja, K.; Rather, G.M.; Lin, Z.; Sui, J.; Xie, P.; Le, T.; Bertino, J.R.; Javanmard, M. Toward point-of-care assessment of patient response: A portable tool for rapidly assessing cancer drug efficacy using multifrequency impedance cytometry and supervised machine learning. *Microsyst. Nanoeng.* **2019**, *5*, 34. [CrossRef]
106. Sountharrajan, S.; Karthiga, M.; Suganya, E.; Rajan, C. Automatic classification on bio medical prognosisof invasive breast cancer. *Asian Pac. J. Cancer Prev. APJCP* **2017**, *18*, 2541.
107. Yang, H.-Y.; Wang, Y.-C.; Peng, H.-Y.; Huang, C.-H. Breath biopsy of breast cancer using sensor array signals and machine learning analysis. *Sci. Rep.* **2021**, *11*, 103. [CrossRef]
108. Elsheakh, D.N.; Mohamed, R.A.; Fahmy, O.M.; Ezzat, K.; Eldamak, A.R. Complete Breast Cancer Detection and Monitoring System by Using Microwave Textile Based Antenna Sensors. *Biosensors* **2023**, *13*, 87. [CrossRef]
109. Joshi, K.; Joshi, K.; Javani, A.; Park, J.; Velasco, V.; Xu, B.; Razorenova, O.; Esfandyarpour, R. A machine learning-assisted nanoparticle-printed biochip for real-time single cancer cell analysis. *Adv. Biosyst.* **2020**, *4*, 2000160. [CrossRef]
110. Bondancia, T.J.; Soares, A.C.; Popolin-Neto, M.; Gomes, N.O.; Raymundo, P.P.A.; Barud, H.S.; Machado, S.A.S.; Ribeiro, S.J.L.; Melendez, M.E.; Carvalho, A.L.; et al. Low-cost bacterial nanocellulose-based interdigitated biosensor to detect the p53 cancer biomarker. *Biomater. Adv.* **2022**, *134*, 112676. [CrossRef]
111. Liang, M.; Tang, Q.; Zhong, J.; Ai, Y. Machine learning empowered multi-stress level electromechanical phenotyping for high-dimensional single cell analysis. *Biosens. Bioelectron.* **2023**, *225*, 115086. [CrossRef] [PubMed]
112. Zhang, C.; Zhang, P.; Ren, H.; Jia, P.; Ji, J.; Cao, L.; Yang, P.; Li, Y.; Liu, J.; Li, Z.; et al. Synthetic biology-powered biosensors based on CRISPR/Cas mediated cascade signal amplification for precise RNA detection. *Chem. Eng. J.* **2022**, *446*, 136864. [CrossRef]
113. Van de Goor, R.; van Hooren, M.; Dingemans, A.-M.; Kremer, B.; Kross, K. Training and validating a portable electronic nose for lung cancer screening. *J. Thorac. Oncol.* **2018**, *13*, 676–681. [CrossRef] [PubMed]
114. Nazir, N.U.; Abbas, S.R. Identification of phenol 2,2-methylene bis, 6 [1,1-D] as breath biomarker of hepatocellular carcinoma (HCC) patients and its electrochemical sensing: E-nose biosensor for HCC. *Anal. Chim. Acta* **2023**, *1242*, 340752. [CrossRef]
115. Salahi, A.; Honrado, C.; Moore, J.; Adair, S.; Bauer, T.W.; Swami, N.S. Supervised learning on impedance cytometry data for label-free biophysical distinction of pancreatic cancer cells versus their associated fibroblasts under gemcitabine treatment. *Biosens. Bioelectron.* **2023**, *231*, 115262. [CrossRef]
116. Honrado, C.; Salahi, A.; Adair, S.J.; Moore, J.H.; Bauer, T.W.; Swami, N.S. Automated biophysical classification of apoptotic pancreatic cancer cell subpopulations by using machine learning approaches with impedance cytometry. *Lab Chip* **2022**, *22*, 3708–3720. [CrossRef]
117. Ferguson, C.A.; Hwang, J.C.; Zhang, Y.; Cheng, X. Single-Cell Classification Based on Population Nucleus Size Combining Microwave Impedance Spectroscopy and Machine Learning. *Sensors* **2023**, *23*, 1001. [CrossRef] [PubMed]

118. Wu, Q.; Ding, Q.; Lin, W.; Weng, Y.; Feng, S.; Chen, R.; Chen, C.; Qiu, S.; Lin, D. Profiling of Tumor Cell-Delivered Exosome by Surface Enhanced Raman Spectroscopy-Based Biosensor for Evaluation of Nasopharyngeal Cancer Radioresistance. *Adv. Healthc. Mater.* **2023**, *12*, 2202482. [CrossRef]
119. Braz, D.C.; Neto, M.P.; Shimizu, F.M.; Sá, A.C.; Lima, R.S.; Gobbi, A.L.; Melendez, M.E.; Arantes, L.M.R.B.; Carvalho, A.L.; Paulovich, F.V.; et al. Using machine learning and an electronic tongue for discriminating saliva samples from oral cavity cancer patients and healthy individuals. *Talanta* **2022**, *243*, 123327. [CrossRef]
120. Wang, C.; Wang, C.; Wu, Y.; Gao, J.; Han, Y.; Chu, Y.; Qiang, L.; Qiu, J.; Gao, Y.; Wang, Y.; et al. High-Throughput, Living Single-Cell, Multiple Secreted Biomarker Profiling Using Microfluidic Chip and Machine Learning for Tumor Cell Classification. *Adv. Healthc. Mater.* **2022**, *11*, 2102800. [CrossRef]
121. Feng, Y.; Cheng, Z.; Chai, H.; He, W.; Huang, L.; Wang, W. Neural network-enhanced real-time impedance flow cytometry for single-cell intrinsic characterization. *Lab Chip* **2022**, *22*, 240–249. [CrossRef] [PubMed]

biosensors

MDPI

Review

Progress in Nano-Biosensors for Non-Invasive Monitoring of Stem Cell Differentiation

Min-Ji Kang, Yeon-Woo Cho and Tae-Hyung Kim *

School of Integrative Engineering, Chung-Ang University, 84 Heukseuk-ro, Dongjak-gu, Seoul 06974, Republic of Korea
* Correspondence: thkim0512@cau.ac.kr

Abstract: Non-invasive, non-destructive, and label-free sensing techniques are required to monitor real-time stem cell differentiation. However, conventional analysis methods, such as immunocytochemistry, polymerase chain reaction, and Western blot, involve invasive processes and are complicated and time-consuming. Unlike traditional cellular sensing methods, electrochemical and optical sensing techniques allow non-invasive qualitative identification of cellular phenotypes and quantitative analysis of stem cell differentiation. In addition, various nano- and micromaterials with cell-friendly properties can greatly improve the performance of existing sensors. This review focuses on nano- and micromaterials that have been reported to improve sensing capabilities, including sensitivity and selectivity, of biosensors towards target analytes associated with specific stem cell differentiation. The information presented aims to motivate further research into nano-and micromaterials with advantageous properties for developing or improving existing nano-biosensors to achieve the practical evaluation of stem cell differentiation and efficient stem cell-based therapies.

Keywords: stem cell differentiation; biosensing; nano- and micromaterials

1. Introduction

Stem cells can differentiate into specific cell subtypes, which has resulted in the development of tissue engineering and regenerative medicine [1,2]. Due to stem cells' ability to produce cells in vitro that are associated with the physiological functions of specific tissues, stem cell therapy has emerged as a potential solution for many diseases that are difficult to treat with conventional chemotherapy over the past few decades [3–6]. There have been 40,183 research papers about stem cell therapy published between 1971 and 2021; many of these studies demonstrated its clinical potential. However, the only stem cell therapy approved by the United States Food and Drug Administration to date is haematopoietic (or blood) stem cell transplantation [7–10].

There are many challenges in the development of stem cell therapy, including low differentiation efficiency, differentiation into undesired cell subtypes, carcinogenesis, and post-transplant inflammatory response [11,12]. Therefore, many stem cell differentiation studies have been conducted to (i) understand the developmental stages of stem cell differentiation, (ii) control stem cell behaviour in vitro, and (iii) enhance stem cell differentiation efficiency [13–16]. Consequently, a need for measuring stem cell differentiation using a variety of analytical methods has arisen. These techniques include polymerase chain reaction (PCR), immunocytochemistry, flow cytometry and Western blot (WB), which have been widely used with biomarkers, such as proteins, ribonucleic acid (RNA) and deoxyribonucleic acid (DNA) [17–20]. However, these techniques are destructive, laborious, and costly; therefore, they are inappropriate for the quantitative and qualitative analysis of differentiated cells prearranged in therapeutic transplantation [21]. Hence, non-destructive and real-time monitoring of cell differentiation is necessary for efficient stem cell therapy. Many biosensing and nanotechnology methods have been proposed for the

Citation: Kang, M.-J.; Cho, Y.-W.; Kim, T.-H. Progress in Nano-Biosensors for Non-Invasive Monitoring of Stem Cell Differentiation. *Biosensors* **2023**, *13*, 501. https://doi.org/10.3390/bios13050501

Received: 23 February 2023
Revised: 20 April 2023
Accepted: 22 April 2023
Published: 26 April 2023

non-invasive monitoring of stem cell differentiation, such as impedance and Raman spectroscopy, deep learning-based approaches, electrochemical immunoassay biosensors, and electroluminescence [22–33]. In particular, electrochemistry-based sensing methods, such as impedance spectroscopy and electroluminescence, have been demonstrated as analytical techniques that selectively detect target materials through electrical signals generated from the redox reaction of analytes. These techniques have the following advantages: (i) facile, (ii) inexpensive, (iii) simple, portable analytical devices, and (iv) non-invasive [34–38]. Similarly, optical sensing methods, such as fluorescence, near-infrared (NIR), and Raman spectroscopy, can selectively detect the optical properties or signals of target materials. These methods have the following advantageous features: (i) high selectivity, (ii) flexibility, and (iii) non-invasive [39–44].

The medium for in vitro stem cell cultivation contains cells with many organelles, but also several types of proteins, small molecules, and other chemicals; this means that the analytical conditions for cell-based sensing are highly complex [41,45]. Therefore, improving sensing performance, including sensitivity and selectivity towards target analytes, is essential for the accurate and sensitive label-free monitoring of stem cell differentiation with electrochemical or optical-based sensors. More specifically, a highly sensitive sensing capability for differentiation-associated targets is required to quantitatively analyse how much differentiation was induced from the stem cells in real-time. In addition, to qualitatively analyse whether specific differentiation into desired cell subtypes has been induced during stem cell differentiation, selectivity for the analytes is a key indicator.

Various nano- and micromaterials have been used to modify sensor surfaces to improve performance, including sensitivity, selectivity, and reliability [44,46]. For instance, highly conductive metal nanomaterials, such as gold nanoparticles (AuNPs) and silver nanoparticles (AgNPs), and carbon-based conductive materials, such as graphene oxide (GO), have excellent electrical or electrochemical properties and are widely used in electrochemical sensors [47,48]. In addition, three-dimensional (3D) micromaterials, such as microelectrode assays and microfluidics, have been used to improve electrochemical sensors' performance by increasing the active surface area [49–51]. In the case of Raman spectroscopy-based sensors, two-dimensional (2D) or 3D combinations of metal nanoparticles with good optical properties and carbon-based conductive materials have been used to improve the sensitivity [52,53]. However, each electrochemical and optical-based sensor's sensing mechanism is different; therefore, the strategies for improving the sensing performance and capabilities and the techniques for sensor surface modification are different.

This review highlights and compares recent studies on non-invasive and real-time monitoring of stem cell differentiation, including neurogenesis, cardiomyogenesis, osteogenesis, and adipogenesis (Figure 1). In addition, various biosensors fused with specific analysis technology, such as electrochemistry and optical sensing, and various nano- and micro materials, such as AuNPs, AgNPs, upconversion nanoparticles (UCNPs), autofluorescence probes, nucleic acids, microfluidic systems, and microelectrode arrays, are reviewed and compared (Table 1).

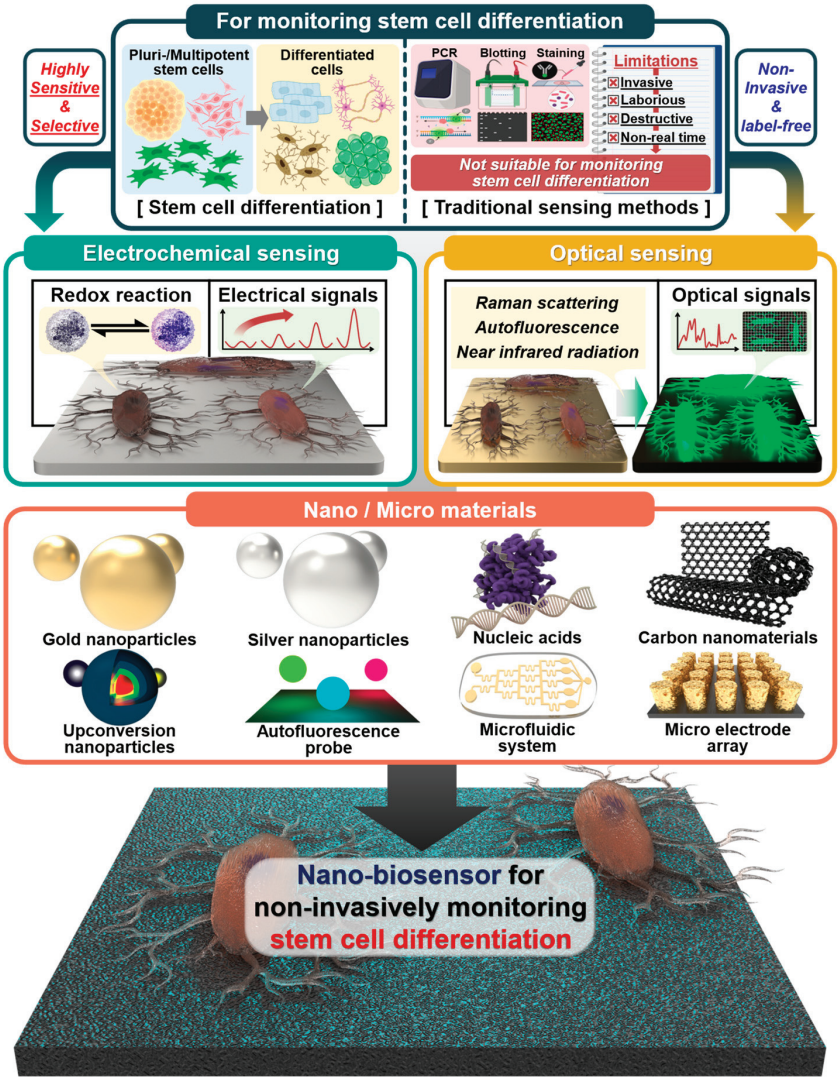

Figure 1. Schematic illustration of traditional sensing and nano- and micromaterial-based methods for monitoring stem cell differentiation. Created with BioRender.com.

2. Electrochemical Sensors

2.1. Gold Nanoparticle-Based Electrochemical Sensors

Gold's conductivity is 4.11×10^7 S/m, which is highly favourable for electrochemical sensors [54]. Moreover, gold is colloidal in AuNPs, which has various advantageous features for electrochemical sensors [55–63]. For example, AuNPs are easy to synthesise and can be conjugated with multiple biomolecules, such as protein ligands, nucleic acids, and antibodies, which can enforce the intrinsic properties of the AuNPs [64–66]. Moreover, it has been reported that AuNPs are non-cytotoxic, cell-friendly materials with great potential for sensing biomolecules in a cell-based environment and for cell cultivation platforms [67–72]. Therefore, AuNPs have been widely used to develop electrochemical sensors with new nanostructures or modify existing electrochemical electrode surfaces at the nanoscale.

Many studies have described AuNP-based electrochemical sensors capable of sensing stem cell differentiation. For example, Suhito et al. developed an electrochemical AuNP-based electrochemical nano-biosensor to identify the differentiation of embryonic stem cells (ESCs) [59]. To fabricate this sensor, AuNPs were densely deposited on a transparent indium–tin oxide-coated glass electrode through electrochemical deposition. The study's cell detection results using differential pulse voltammetry (DPV) showed that the undifferentiated ESCs generated relatively strong electrochemical signals compared with differentiated ESCs-derived endothelial cells. Interestingly, this sensor could sensitively measure ESCs based on the high electrical conductivity of gold, detecting at least 12,500 cells on one platform. Moreover, it was shown that this sensor could ensure ESCs' adhesion and long-term cell growth, suggesting its application as an ESCs' cultivation platform and a platform for electrochemically monitoring various stem cell differentiation.

In another study, Lee et al. described a AuNP-based nano-biosensor for non-invasive, real-time monitoring of the osteogenesis of mesenchymal stem cells (MSCs) [73]. Specifically, this sensor comprised a 3D AuNP-based nanoarray; the surface of the gold nanoarray was modified with GO. This nanostructure efficiently increased gold's electrical conductivity and electron transfer rate through GO modification, allowing the detection of p-aminophenol (PAP) produced by the enzymatic reaction occurring in MSCs' osteogenesis. Furthermore, this study observed that this nanoarray provided physicochemical cues beneficial to cellular adhesion and osteogenic differentiation. As a result, this gold-based electrochemical sensing platform detected the anodic signals of PAP using cyclic voltammetry (CV), quantitatively monitoring differentiation during 3 weeks of osteogenesis.

In 2021, a AuNP-based sensing platform was developed that monitored the differentiation of stem cells and controlled their cell differentiation by regulating cellular adhesion (Figure 2a,b) [74]. This sensor was based on a nanoassembly in which AuNPs and Arg-Gly-Asp peptide (RGD) ligands were conjugated on the surface of magnetic iron (II, III) oxide (Fe_3O_4) nanoparticles. Specifically, the magnetite mediated the control of falling and rising ligand movements via linker compression and stretching, thereby regulating MSCs' integrin expression pattern, cellular adhesion, and consequent osteogenic differentiation. Additionally, due to the high electrical conductivity of the AuNP nanoassembly-based sensor, osteogenic differentiation could be monitored by sensitively measuring PAP's redox using CV.

In 2022, a AuNP-based electrochemical nano-biosensor capable of sensing the generation process and maturity of kidney organoids produced through the differentiation of induced pluripotent stem cells (iPSCs) was developed (Figure 2c,d) [75]. Moreover, the variations of organoids led to the need for a non-destructive evaluation of their maturity [76–78]. Therefore, this sensor was developed to assess the iPSCs differentiation into kidney organoid by sensitively detecting the electrochemical signals originating from the organoids through a gold film structure on which there was electrochemically deposited AuNPs. Interestingly, while monitoring the kidney organoid generation on this sensor, two peaks were detected in the DPV results. Specifically, it was confirmed that the first peak corresponded to cell outgrowth, while the second peak differed depending on the maturity of kidney organoids. A strong second peak was observed for organoids with distinct tubular structures. These results demonstrate that this electrochemical sensor could detect the successful production of kidney organoids in a label-free, non-destructive manner.

In general, studies have shown that AuNPs can be applied to develop electrochemical sensors that sensitively detect the target analytes involved in stem cell differentiation because of AuNPs' excellent electrical conductivity, versatility, and ease of synthetic manipulation with various biomolecules and nanomaterials.

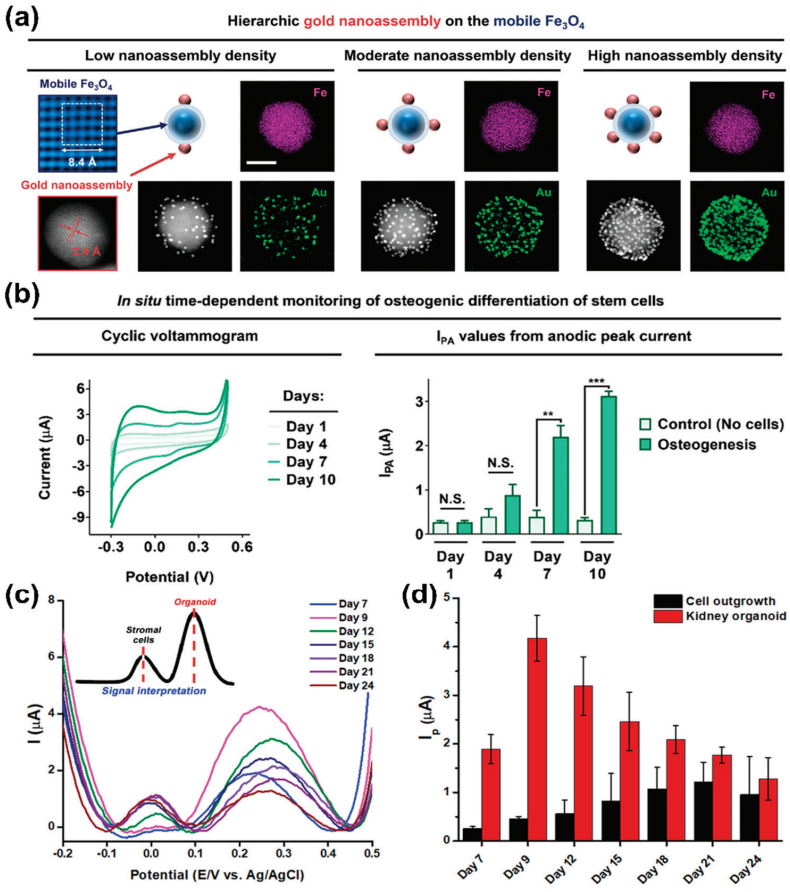

Figure 2. Gold nanoparticle-based electrochemical sensors. (**a**) Characterisation of gold nanoassembly and magnetic nanoparticles. (**b**) Time-dependent monitoring of osteogenesis using the gold nanoassembly-based electrochemical sensors. (**c**,**d**) DPV results of iPSCs differentiation and organoid generation on gold-based electrochemical electrode. Reprinted with permission from [74]. Copyright 2021, Wiley Online Library; Reprinted with permission from [75]. Copyright 2022, Wiley Online Library. AuNPs, gold nanoparticles; DPV, differential pulse voltammetry; Fe_3O_4, iron (II, III) oxide; iPSCs, induced pluripotent stem cells. N.S. indicates "not significant." ** $p < 0.01$, and *** $p < 0.001$.

2.2. Nucleic Acid-Based Electrochemical Sensors

Nucleic acids, including DNA and RNA, are biopolymers composed of nucleotide units [79]. Nucleic acid molecules have specific nucleotide sequences, which comprise of the bases of adenine, thymine, cytosine, and guanine, that can bind strongly with complementary base-pair sequences. The intrinsic properties of nucleic acids have the potential as nanomaterials for biosensors [74,80–83], as they impart high selectivity in terms of the capability to detect target molecules selectively. In addition, nucleic acid-based aptamers can be developed as ligands for target materials through the systematic evolution of ligands by exponential enrichment technology [84,85]. These aptamers can be developed faster and cheaper than antibodies. Moreover, aptamers have unique 3D structures (e.g., loop, stem, quadruplex, bulge, hairpin, and pseudoknot) through the nucleotide sequence alignment of the nucleic acids; this allows the aptamers to bind more strongly and selectively to the target [86–88]. In addition, nucleic acid materials can be

chemically conjugated to fluorescent or electrochemical probes, giving a stronger signal and higher affinity toward analytes.

Park et al. [89] described a microelectrode based on carboxylated polypyrrole nanotubes conjugated with aptamers capable of evaluating the neuronal maturation of neurons. These authors showed that the aptamer-based sensor could sensitively and selectively measure dopamine (DA) exocytosis as a neuronal function. To improve the sensor's performance, the DA sensitivity according to the carboxylated polypyrrole nanotube diameter was first analysed. Then, the optimised aptamer-based sensor was evaluated for DA-sensing performance using amperometry, which showed an excellent limit of detection (LOD) of 100 pM. Furthermore, the sensor could electrochemically distinguish DA in the presence of other neurotransmitters, such as norepinephrine, serotonin, and phenethylamine. This study demonstrated that the developed sensor could electrochemically detect exocytotic DA released from neuronal cells due to DA's high sensitivity and selectivity. The study's results suggested the possibility of aptamer-based electrochemical sensors to monitor the neural differentiation process of stem cells.

A nucleic acid-based electrochemical sensor capable of monitoring cardiomyocyte differentiation was reported in 2021 [90]. This nucleic acid-based sensor contained hybrid materials, including short DNA domains and peptide motifs that bind complementarily to cardiomyocyte-specific regulatory proteins. Notably, this sensor showed a low level of LOD of 0.42 pg/mL. In addition, the sensor selectively detected electrochemical signals from cardiac troponin (cTnl) as a target molecule in the presence of other proteins, including human serum albumin and human brain natriuretic peptide. Due to the sensor's high affinity and sensitivity to cTnl, it was possible to determine the cTnl expression level through electrochemical signals measured from cardiomyocytes differentiated from MSCs. In addition, the electrochemical signal for cTnl obtained while monitoring the cardiomyocyte differentiation process was consistent with the result of flow cytometry, validating the high reliability of this sensor.

In another study, an aptamer-based electrochemical sensor was developed to evaluate the neuronal function at the single cell level [91]. This sensor comprised micro-wells, DA aptamers, and co-reactant-embedded polymer dots (Pdots). The sensor's embedded Pdots provided electrochemical luminescence signals, which served to visualise the electrochemical DA signal (Figure 3a,b). The hybrid structure of this sensor allowed it to capture a single or a small number of differentiated cells inside a micro-well, which then selectively detected the DA released from the captured neurons using the DA aptamer. This sensor exhibited stable cell viability as a cell cultivation and differentiation platform with low cell toxicity. In addition, this sensor demonstrated a low LOD of 53 pM DA (Figure 3c,d) and was capable of evaluating the amount of DA exocytosis.

Nakatsuka et al. reported a DNA aptamer-based nanopipette capable of monitoring the differentiation process of iPSCs into serotonin neurons [92]. This sensor was used to electrochemically detect 5-hydroxytryptamine (5-HT) release from serotonin neurons as differentiated cells. In addition, the nanopipette form of the sensor allowed size exclusion of non-specific proteins in complex culture medium environments, further enhancing the sensor's 5-HT selectivity. Specifically, this sensor was able to detect 5-HT of less than 3 nM using fast scan CV, which is an excellent sensing capability for DA, similar to the sensing capability of enzyme-linked immunosorbent assay (ELISA). Above all, this sensor was able to detect 5-HT released at the cellular level through the introduction of an aptamer capable of binding specifically to 5-HT.

These studies support that nucleic acid materials can greatly improve electrochemical sensing ability, especially target selectivity, through their specific binding sites. In addition, nucleic acid materials can be combined with other types of biomolecules or sensing probes through chemical conjugation to provide various 3D ligands, which can improve electrochemical sensors' capabilities.

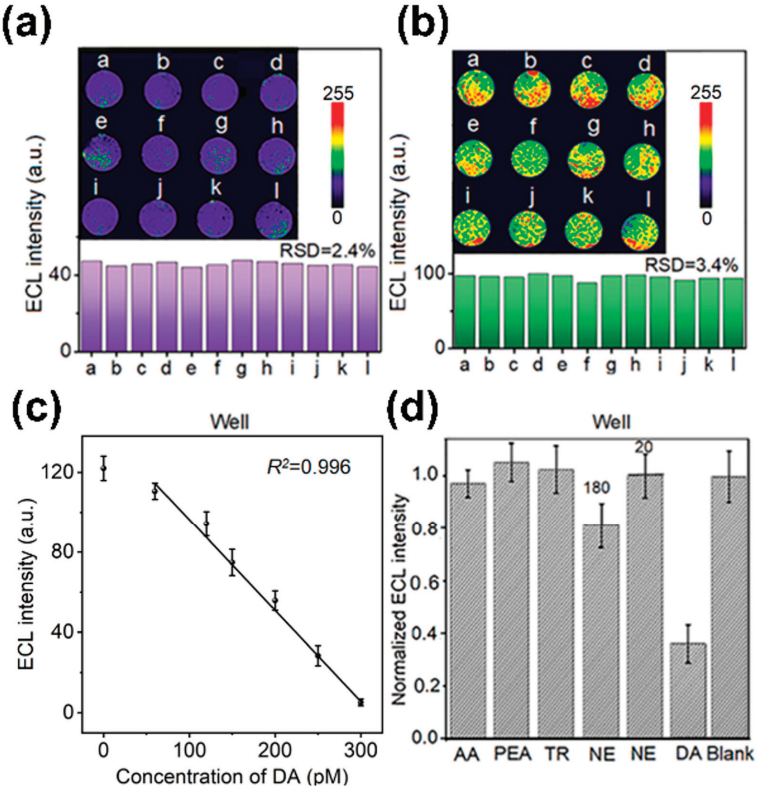

Figure 3. Aptamer-based electrochemical sensors. (**a**,**b**) ECL images of neurons injected in the micro-well and DA aptamer-based electrochemical sensor. (**c**,**d**) Analysis of DA sensing capability of micro-well and DA aptamer-based electrochemical sensor. Reprinted with permission from [91]. 5-HT, 5-hydroxytryptamine; Ag, silver; AgCl silver chloride; Au, gold; DA, dopamine; ECL, electrochemical luminescence; RSD, relative standard deviation.

2.3. Carbon Nanomaterial-Based Electrochemical Sensors

Carbon nanomaterials (CNPs), such as graphene and its derivatives, fullerene and carbon nanotubes (CNTs), and nanofibres are composed of chemical structures in which carbon atoms are combined through sp^2 hybridisation, resulting in the delocalisation of electrons [93]. The intrinsic properties of CNPs depend on their configuration and include good thermal stability, mechanical properties and chemical resistance. Furthermore, due to their structural characteristics, they have good electrical properties, including electron mobility and electrical conductivity. Moreover, CNPs can be synthesised into specific 3D structures, such as CNTs, and sheet forms, such as graphene. In addition, CNPs are biocompatible and can improve cellular functions, for example, cell adhesion and proliferation, making them suitable for stem cell cultivation platforms [94–103].

In a 2021 article, Castagnola et al. describe a graphene-based electrochemical nanosensor to evaluate neuronal function [104]. This sensor comprised graphene flakes with a 3D arrangement via photolithographic processes. This sensor showed high electrochemically active area enhancement. Specifically, the electrochemically active area of the sensor was about 88 times higher than that of conventional carbon fibre electrodes. The sensor sensitively and selectively detected DA as a target analyte using fast scan CV to evaluate neuronal function; the LOD for DA was calculated to be approximately 364.44 nM. Furthermore, the sensor was demonstrated to discriminate between serotonin and DA. Overall, this sensor's enhanced electrochemical properties for sensitive and selective sensing of DA

suggested that neurogenesis could be monitored in real-time by sensing DA released from neurons in vitro.

Vasudevan et al. [105] developed a nanosensor based on CNPs (Figure 4a). Specifically, this sensor was composed of carbon fibre, which detected DA released from neural stem cell-derived dopaminergic neurons and promoted neurogenesis in vivo based on optogenetics as an optical fibre. To improve the electrochemically active surface area of the sensor, a 15 μm thick polyimide buffer layer was coated onto the surface of a silica-based optical fibre; then, this layer was processed to form of 8 μm thick pyrolytic carbon fibre surrounded by cladding. Subsequently, human neural stem cells (hNSCs) were cultured on the sensor surface and differentiated into dopaminergic neurons to detect DA exocytosis electrochemically using an amperometric method. According to the amperometric results, the electrochemical signal towards DA was not confirmed from undifferentiated cells on the sensor surface. However, a clear electrochemical current peak towards DA was confirmed from the differentiated cells (Figure 4b,c). Moreover, as a result of monitoring the DA signals on the sensor surface during the 10-day differentiation period, it was observed that the DA signal gradually improved according to dopaminergic differentiation. These results suggested that the sensor could monitor dopaminergic differentiation non-invasively.

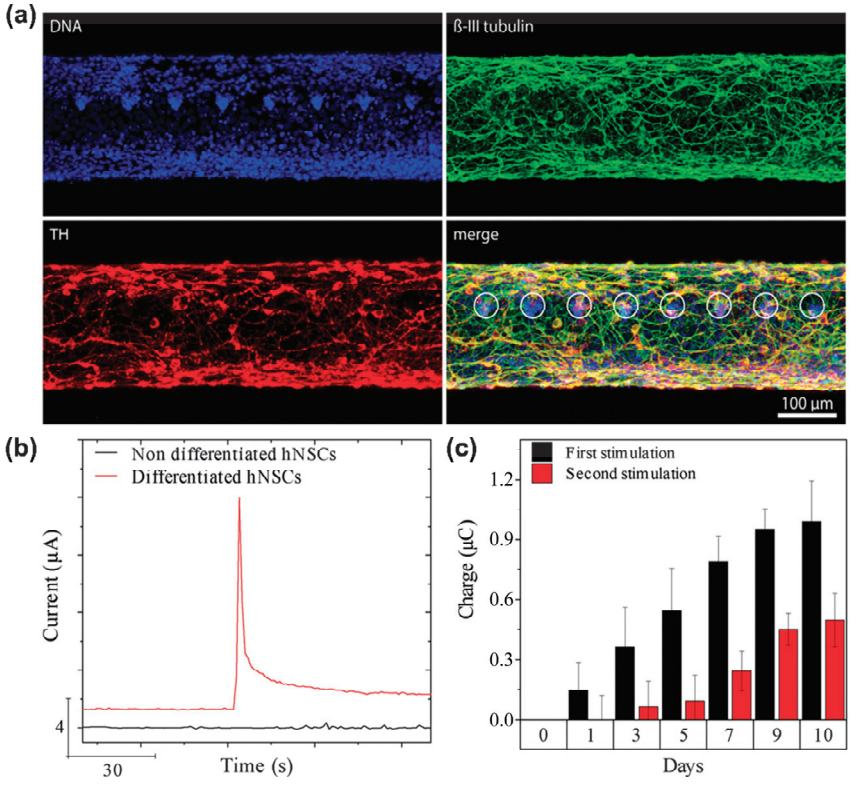

Figure 4. A carbon fibre-based electrochemical sensor for monitoring in vitro neurogenesis. (**a**) Immunocytochemistry images of hNSCs-derived dopaminergic neurons cultured on the sensor. (**b**) Amperometry graph of non-differentiated and differentiated cells after stimulating DA exocytosis. (**c**) Electrochemical current peaks toward DA for time-dependent monitoring of the dopaminergic differentiation on the sensor. Reprinted with permission from [105]. Copyright 2019, Wiley Online Library. DA, dopamine; DNA, deoxyribonucleic acid; hNSCs, human neural stem cells; TH, tyrosine hydroxylase.

Similarly, Pham Ba et al. constructed a CNT-based nanosensor to monitor neuronal differentiation [106]. This sensor's Nafion®-radical layer was composed of CNT transistors

and was demonstrated to selectively detect DA in the presence of the interfering molecules acetylcholine and glutamine. In addition, it was confirmed that neuronal cells could be normally attached and cultured on the sensor surface. Moreover, an amperometric response to DA was observed immediately after potassium chloride (KCl) stimulation from neurons cultured on the sensor surface. Furthermore, the sensor obtained different amperometric responses to DA by adding different concentrations of KCl, suggesting that the sensor could discriminate between different degrees of DA exocytosis.

The previously mentioned studies support that carbon nanomaterials, including graphene, carbon fibre, and CNT, can be actively utilised to construct excellent sensing platforms with high electrical properties. In particular, nanosensors based on the graphene family have been demonstrated to monitor neuronal differentiation by sensitively and selectively sensing DA through π-π stacking. Moreover, CNPs' biocompatibility and high sensing capability make them suitable for stem cell cultivation platforms and non-invasive monitoring of various types of stem cells, such as ESCs and MSCs.

2.4. Microfluidic System-Based Electrochemical Sensors

Microfluidic systems refer to systems in which fluid can flow through micro-scale channels fabricated on a substrate [107]. The microfluidic system has the advantage that it can be performed on a single chip under various conditions in a short time using only a small volume of reagents. Due to these structural features, microfluidic systems have been actively applied as biosensors [108–110]. Furthermore, given that the microchannel in microfluidic systems enables electrochemical species in the analytes to be confined near the electrochemical electrodes, they are advantageous to electrochemical sensing with high performance [111]. Above all, microfluidic systems can mimic the cellular microenvironment, which can be applied as a stem cell cultivation platform [112].

An example of an electrochemical sensor based on a droplet microfluidic system capable of sensing osteogenic differentiation was described by Fan et al. in 2019 [113]. This sensor could detect the impedance of a single cell; therefore, it was possible to analyse the differentiation of stem cells non-invasively without a label. The sensor detected a difference between the impedance of undifferentiated and differentiated cells. As osteogenic differentiation progressed, the variation in cell impedance decreased. In addition, the average impedance decreased as the differentiation progressed. Conversely, the capacity of the cells analysed on the sensor gradually increased with differentiation. These results were consistent with the fact that calcium ion channels were gradually formed on the cell membrane following osteogenic differentiation.

In 2020, a brain-on-a-chip device based on a microfluidic system capable of analysing neural differentiation was developed [114]. This platform's design structure included three isolated compartments, suggesting that this structure was suitable for pharmacological manipulations, and a plastic lid and a specific gas supply chamber to build a gas supply system. It was validated that neurons could be cultured and maintained for up to 98 days on the platform. In addition, it was confirmed that neurons were differentiated normally on the device with positive expression of axonal and dendritic markers and that their neuronal networks were formed normally. Furthermore, the spike train tiling coefficient was successfully measured from the neuronal network of neurons differentiated on the platform.

Another study by Lee et al. described a microfluidic system-based sensing and cultivation platform capable of electrochemically analysing the cellular function of cardiomyocytes differentiated from iPSCs [115] (Figure 5a). Interestingly, the platform developed contained an aptamer and a gold-based microfluidic system. The functionality of cardiomyocytes could be electrochemically monitored by selectively sensing markers, such as troponin T, creatine kinase, and human epidermal growth factor receptor 2; these markers are related to the functionality of cardiomyocytes (Figure 5b). In addition, to investigate the interaction between cardiac and heart cancer tissues cultured on the platform, troponin secreted from each cell was detected after single or dual interaction with the platform on which each

tissue was cultured (Figure 5c). Results showed that troponin released from healthy cardiac tissues increased in the single and dual platforms. In contrast, troponin released from healthy tissues on the dual platform was lower than from cells that did not interact with heart cancer tissues. In addition, cell functionality was evaluated electrochemically by measuring biomarkers released from healthy cardiomyocytes and heart cancer cells on the aptamer and microfluidic system-based platforms. The results obtained on the platform were consistent with ELISA results.

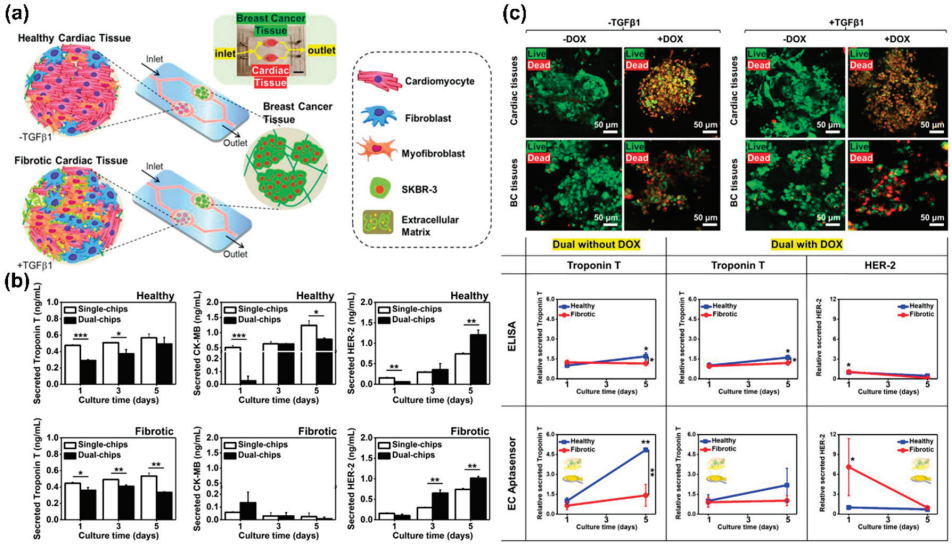

Figure 5. A microfluidic system-based electrochemical sensor for monitoring cardiomyocyte differentiation. (**a**) A schematic illustration showing an aptamer and microfluidic system-based electrochemical sensor. (**b**) Analysis of the important role of interaction between cardiac and heart cancer tissues through biomarkers sensing. (**c**) Monitoring of cardiotoxicity-associated biomarkers using the aptamer and microfluidic system-based electrochemical sensor. Reprinted with permission from [115]. Copyright 2020, Wiley Online Library. DOX, doxorubicin; HER2, human epidermal growth factor receptor 2; TGFβ1, transforming growth factor beta 1.* $p < 0.05$, ** $p < 0.01$, and *** $p < 0.001$.

Therefore, it can be concluded that microfluidic systems are effective micromaterials for constructing sensing platforms for the non-invasive and label-free monitoring of stem cell differentiation. In particular, microfluidic systems are suitable for application as a stem cell culture platform and can considerably improve the performance of existing electrochemical sensors.

2.5. Microelectrode Array-Based Electrochemical Sensors

Microelectrode arrays refer to micromaterials in which multiple micro-scale electrodes are arranged on a single substrate [116]. Microelectrode arrays are based on a 3D structure that improves and increases the electrochemically active area in which analytes participate in the redox reaction, providing a high sensing performance [117]. In addition, considering that a plurality of electrodes is spatially arranged in a microelectrode array, it is possible to analyse signals of cells by position on a single substrate and to analyse single cells and spheroids electrochemically [118].

The literature reports that microelectrode array-based electrochemical sensors that can non-invasively monitor stem cell differentiation have been developed. For example, a microelectrode array that electrochemically monitors cardiomyocyte differentiation has been described [119]. This platform was designed to culture iPSCs for an extended period and to perform qualitative and quantitative analyses of the differentiated cells' maturity for

efficient cardiomyocyte differentiation. The platform was used to monitor the cardiomyocyte differentiation of iPSCs for 119 days using electrochemical impedance spectroscopy. In addition, the effect of 2D and 3D culture environments on cardiomyocyte differentiation was evaluated non-invasively by analysing the differentiated cells' impedance. The results confirmed that more mature cardiomyocytes were produced in a 3D environment.

Gao et al. [120] decribed a microelectrode array-based sensing platform that monitors neuronal differentiation by electrochemically detecting neurotransmitters released from olfactory bulb neurons. The olfactory bulb neurons were cultured in a microelectrode array located on the corresponding platform; cells were stimulated using glutamate and gamma-aminobutyric acid (GABA) to detect electrochemical signals from the cells. As a result of detecting cells at various concentrations of glutamate and GABA, it was confirmed that cell signals depended on the concentration of the stimulant and that neurotoxicity occurred at high concentrations. The sensing ability of the platform to detect neurotransmitters through GABA stimulation can be used to detect neural differentiation of stem cells non-invasively and label-free.

Similarly, a sensing platform capable of electrochemically analysing DA exocytosis in dopaminergic neurons differentiated from human ESCs was developed in 2020 [121]. The microelectrode array in the platform was composed of reduced GO and poly(3,4-ethylene dioxythiophene):polystyrene sulfonate (PEDOT:PSS) nanocomposites. Due to the nanocomposites' excellent electrochemical properties, the device's LOD for DA was calculated to be 2 nM. Moreover, it could detect DA released from neurons in a location-by-amperometric manner thanks to the intrinsic advantage of the microelectrode array (Figure 6). The platform's superior dopaminergic sensing ability allowed dopaminergic differentiation to be detected in real-time.

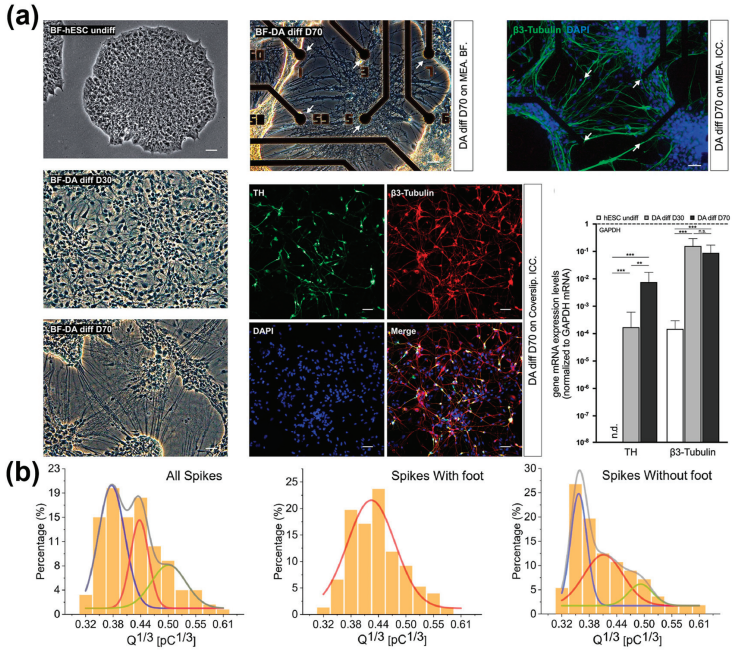

Figure 6. A microelectrode array-based electrochemical sensor. (**a**) Analysis of dopaminergic differentiation of hESCs cultured on the platform. (**b**) Detection of DA exocytosis on the platform. Reprinted with permission from [121]. Copyright 2022, Elsevier. DA, dopamine; DAPI, 4′,6-diamidino-2-phenylindole; GAPDH, glyceraldehyde 3-phosphate dehydrogenase; hESCs, human embryonic stem cells; mRNA, messenger ribonucleic acid; TH, tyrosine hydroxylase. "n.d.", indicates non-detected; "n.s.", indicates non-significant; ** $p < 0.01$, *** $p < 0.001$.

A review of the current literature supports that microelectrode arrays have several advantages as electrochemical sensors. First, the 3D regularly arranged electrodes could considerably improve existing electrodes' electrochemical sensing ability by increasing the electrochemically active area. Second, the microelectrode array can be used as a stem cell cultivation platform to analyse cells on a single substrate by location. In addition, single cells and spheroids can be effectively detected.

3. Optical Sensors

3.1. Gold and Silver Nanoparticle-Based Optical Sensors

Nanomaterials, such as AuNPs and AgNPs, have excellent optical properties [122], which are unique depending on their particle size [123,124]. In addition, AuNPs can be modified through chemical conjugation with various other nanomaterials and probes to form new types of hybrid nanomaterials; this allows sensors with higher selectivity and sensitivity to target analytes to be developed [125,126]. In particular, AuNPs can greatly enhance the surface plasmon effect because they are mainly applied to optical sensing Raman spectroscopy methods [127].

Various AuNP-based optical sensors capable of monitoring stem cell differentiation non-invasively and in real-time have been reported. For example, Cao et al. report a gold-based surface-enhanced Raman spectroscopy (SERS) sensor for monitoring osteogenic differentiation [128]. This sensor had a hybrid structure based on AuNPs and nucleic acids and sensitively detectable micro-RNAs (miRs), such as miR-144-3p, associated with osteogenesis. The DNA nucleic acid binds site-specific targets via its complementary interaction. Therefore, hybrid nanostructures in which a specific DNA strand is conjugated on the surface of AuNPs are highly selective. Furthermore, the gold-based nanostructures selectively detected the Raman signals from the target miR. In addition, the probe showed high optical properties and enhanced Raman signals. These advantageous features allowed the sensor to be used in stem cell cultivation and long-term monitoring of their osteogenic differentiation.

In another study, Sun et al. developed a smart gold nanoprobe for detecting alkaline phosphatase (ALP) activity during bone marrow MSCs' osteogenic differentiation [129]. The smart nanoprobe was designed by decorating the surface of AuNPs with 5-bromo-4-chloro-3-indolyl phosphate (Au@BCIP), which is suitable for use as a SERS nanoprobe. This probe allowed non-invasive and living-cell permeable monitoring of ALP activity with high sensitivity and selectivity. Moreover, this probe could detect a single cell without cell deformation, and the preparation process was simple, so time and effort could be saved compared to conventional methods. Therefore, the non-invasive detection of ALP activity associated with bone disease in vivo models and osteogenic differentiation of bone marrow MSCs can be more fully understood from the perspective of ALP activity.

A 2021 article by Hua et al. describes the development of an imaging probe consisting of gold nanostars (AuStar) and silver sulphide quantum dots for labelling and accurately tracking MSCs in a hypodermic and myocardial infarction model with deep tissue penetration [130] (Figure 7). The probe's AuStar-disseminated tumour cell cluster section enabled high-resolution Raman imaging, effectively delineating stem cells in surrounding normal tissues at a single-cell resolution scale. In addition, the labelling agents were biocompatible and did not alter the MSCs' biological properties, compensating for existing invasive monitoring methods used for tracking stem cells' shortcomings.

Lee et al. [131] fabricated magneto-plasmonic nanorods that detected the expression level of miRNA-124 and characterised the neurogenesis of human-iPSC-derived hNSCs in a non-destructive and efficient way. The plasmonic (gold) parts of the nanorod selectively and sensitively recognised target exosomal miRNAs using a molecular beacon (MB), which was on the gold component. The MB and miRNA hybridised to form an MB–miRNA complex with an increased fluorescence signal, increasing the signal-to-noise ratio through the metal-enhanced fluorescence effect. This system was non-destructive and could possibly advance the transplantation of differentiated stem cells.

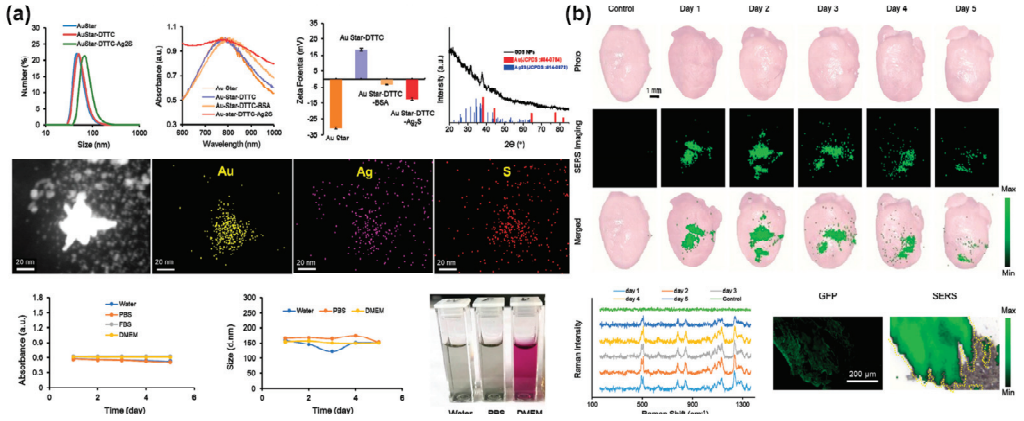

Figure 7. A gold-based NIR sensor for monitoring of chondrogenic differentiation. (**a**) Characterisation of the AuStar-DTTC-Ag_2S (GDS) nanoparticles. (**b**) Ex vivo Raman imaging of GDS-MSCs in a myocardial infarction model. Reprinted with permission from [130]. Copyright 2020, Wiley Online Library. Ag, silver; Ag_2S, silver sulphide; Au, gold; AuStar, gold nanostar; BSA, bovine serum albumen; DMEM, Dulbecco's modified eagle medium; DTTC, 3.3′-diethylthiatricarbocyanine iodide; GFP, green fluorescent protein; MSCs, mesenchymal stem cells; NIR, near-infrared; PBS, phosphate-buffered saline; S, sulphur; SERS, surface-enhanced Raman spectroscopy.

An ultrasensitive nanosensor consisting of a Au-coated nanopore thin film was reported by Yang et al. in 2021 [132]. This nanosensor was developed for the detection of N27 cells' Glial cell-derived neurotrophic factor (GDNF) secretion [132]. The GDNF is a small protein that strongly promotes the survival of dopaminergic and motor neurons, and the evaluation of its magnetic stimulation is valuable. Due to the characteristics of gold, the nanosensor's conversion signal appeared as an optical signal (optical interference fringes) reflected from the nanopore thin film. The optical signal shift occurred because of changes in the effective optical thickness when the GDNF bound to its antibody. The nanostructure helped coat more gold, greatly increasing the sensor's sensitivity; this was demonstrated by a significantly improved GDNF LOD (2 pg/mL) compared with the rat ELISA kit assay (32 pg/mL). In addition, it was inexpensive, easy to use, and suitable for measuring GDNF secretion with ultra-high sensitivity. Furthermore, it can potentially be used for other highly secreted substances.

In a study on AgNP-based optical sensors, Koh et al. [133] developed a 3D cell culture scaffold and SERS-based biosensor to detect multiple differentiated markers from adipose-derived MSCs. Scaffolds were composed of electrospun nanofibres with hydrogel patterns. Moreover, the sensing scaffolds were coated with AgNPs, which can be conjugated with specific antibodies for SERS analysis. This type of scaffold culture platform successfully supported adipose-derived MSCs' proliferation and differentiation in osteogenic differentiation media. In addition, the SERS-capture substrate detected various differentiation markers with SERS tags made of Au-Ag alloy nanoboxes. The time-dependent release of three different osteogenic differentiation markers (ALP, osteocalcin, and fibronectin) were detected up to the pg/mL levels without interference or crosstalk for three weeks. Therefore, the platform was sufficiently sensitive to monitor markers during osteogenic differentiation. This platform was suggested to overcome the limitations of existing stem cell differentiation monitoring methods, as it did not require cell pre-processing, enabled continuous analysis with a single platform, and the multi-sensing scaffold could detect various biomarkers.

Similarly, Li et al. [134] developed a SERS sensor for accurate and quantitative detection of DA in blood. The sensor consisted of zipper-like ortho-nanodimers and AgNPs with a uniform 1 nm gap. The AgNPs were electrostatically self-assembled onto a glass slide;

then, the complementary DNA of the DA aptamer was bound to the surface of the AgNPs. The SERS probe was synthesised by decorating AgNPs with DA aptamers and the Raman reporter 5,5′-dithiobis-(2-nitrobenzoic acid). When these SERS probes were added to a substrate, they combined with the complementary DNA forming zipper-like ortho nanodimers with a 1 nm gap between the probe and AgNPs on the substrate in a state of equilibrium between electrostatic repulsive force and hybridisation contractility. The uniform gap allowed the SERS sensors to detect DA with ultra-high sensitivity (LOD = 10 aM) while maintaining signal uniformity (relative standard deviation < 5%). Even in a complex serum environment, the sensor maintained excellent validity and stability from 1 pM to 10 nM, which was about two times lower than conventional methods. In addition, monitoring the DA of cells released from living neurons was performed for the first time. This was achieved by introducing a single microfluidic chip containing a 3D cell culture device. The DA quantification in human blood samples showed recoveries ranging from 87.5% to 123.7%. Given the difficulty of DA quantification in complex physiological samples, this SERS sensor may provide a powerful tool for the in vitro investigation of neurological processes and clinical examination of dopaminergic disorders.

Based on the literature reviewed, gold- and silver nanomaterials have excellent optical properties and the advantage of being easily transformable into various 3D nanostructures. In addition, AuNPs can be widely applied to optical sensing methods because of their easy surface modification with other nanomaterials.

3.2. Upconversion Nanoparticle-Based Optical Sensors

Upconversion refers to a phenomenon in which external energy is changed into higher energy through a phosphor [135]. Considering that UCNPs show unique optical properties different from conventional phosphors, they have been applied to bioimaging and the optical applications of conventional phosphors. Specifically, UCNPs do not quench and are chemically stable. Furthermore, unlike conventional quantum dots, the maximum emission wavelength does not depend on particle size. In addition, UCNPs can easily emit multi-colour emissions by changing doping materials. In particular, UCNPs doped with lanthanum elements are excited by long wavelengths and have very low cytotoxicity; therefore, they are very useful for use in cell-based sensors [136]. To date, various UCNP-based sensors capable of monitoring stem cell differentiation have been reported in the literature.

For example, Wang et al. [137] developed a multifunctional UCNP capable of real-time detection and control of osteogenic differentiation in MSCs using NIR. The researchers synthesised thulium/erbium-doped core-shell UCNPs coated with mesoporous silica for drug loading and to install photomechanical azobenzene that acted as an agitator. Then, the RGD peptide and matrix metalloproteinase 13 (MMP13) sensitive peptide-black hole quencher-3 group were conjugated to the UCNP surface responsible for cell targeting and detecting differentiation. Finally, icariin, a drug that can induce MSCs' osteogenic differentiation, was loaded onto the UCNPs to form a nanocomplex. The drug was released from the fabricated UCNP nanocomplexes using NIR light in a controlled way, which was based on trans-azobenzene being converted to a cis isomer under UV and visible light. According to the results of reverse transcription (RT)-PCR, WB, and autonomously replicating sequence (ARS), the UCNP nanocomplex efficiently induced osteogenic differentiation of MSCs under NIR light at a wavelength of 980 nm and successfully detected MMP13 produced by osteogenesis. Therefore, this developed multifunctional UCNP could control the osteogenesis of MSCs and detect cell differentiation in real time, making it a potential tool for progressing regenerative medicine.

Similarly, Yan et al. [138] reported on the controlled osteogenic differentiation of MSCs with a light-responsive nanoplatform to treat osteoporosis (OP). The nanoplatform was a modification of that of Wang et al. described previously. Like Wang et al.'s method, the UCNPs were first doped with thulium/erbium and coated with mesoporous silica. Then photocaged linker 4-(hydroxymethyl)-3-nitrobenzoic acid and polyethylene glycol linker were linked to the surface to conjugate to the cap β-cyclodextrin and the RGD-targeted

peptide/MMP13-sensitive peptide-black hole quencher, creating a drug loading nanoplatform. According to the RT-PCR, WB, ALP/ARS/immunofluorescence staining, and ALP activity results, the release of icariin by NIR light at 980 nm induced controlled osteogenic differentiation of MSCs for OP treatment. In addition, MMP13 produced by the MSCs' osteogenic differentiation cleaved the MMP13-sensitive peptide, removing the peptide-black hole quencher and allowing the UCNPs to fluoresce; this allowed real-time detection of osteogenic differentiation. The results of haematoxylin and eosin, Masson's trichrome, immunohistochemical, tartrate-resistant acid phosphatase, and toluidine blue staining of a femoral terminal section showed that significant bone remodelling had occurred in the OP rat model. This study's results suggested that the synthesised UCNP nanoplatform enabled remote control and real-time detection of osteogenic differentiation for OP treatment by NIR and could be a potential alternative to current OP treatment.

Non-destructive stem cell differentiation control and monitoring using UCNPs has also been studied for neural differentiation from MSCs. However, conventional UCNPs have shortcomings, such as low emission intensity due to undesirable energy transfer paths. Low power density excitations can minimise detrimental energy reverse transitions and produce bright visible emissions. Therefore, Rabie et al. [139] developed a core–shell–shell sandwich-structured UCNP with enhanced luminescent output relative to conventional UCNPs. This core–shell–shell UCNP was then used to construct a biosensor to detect DA released from stell cell-derived dopaminergic neurons (Figure 8). This UCNP detected DA released in vivo during the differentiation of stem cells into specific neurons at the single cell level in a highly selective, real-time, and non-invasive manner, with a sensitivity of at least three times higher than similarly designed systems. This sensor was demonstrated to detect DA at low concentrations. The developed NIR-based neurotransmitter detection method has significant potential for the diagnosis of diseases related to neurodegenerative diseases and stem cell treatment strategies.

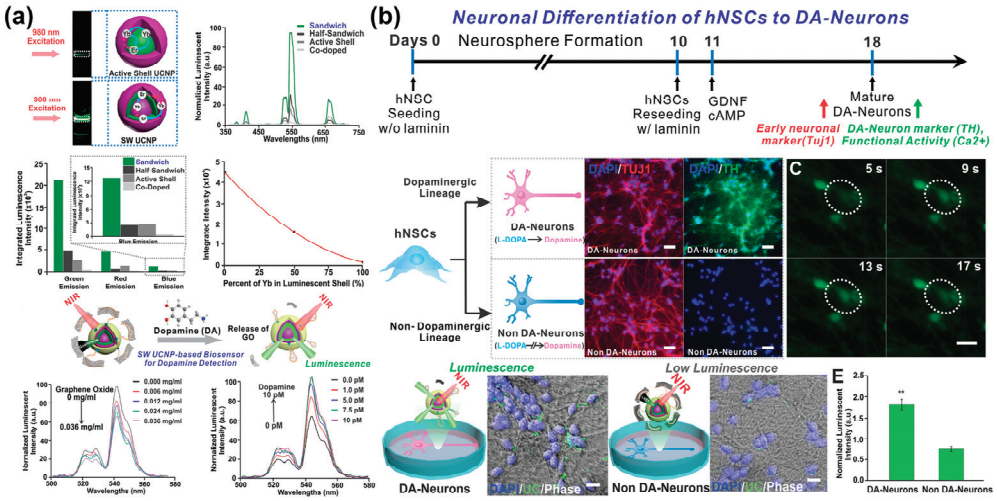

Figure 8. Upconversion nanoparticle-based optical sensor capable of monitoring neurogenesis. (**a**) Upconversion luminescence profiles and analysis of the operating mechanism and characteristics of UCNPs for each condition. (**b**) Monitoring of neuronal differentiation of hNSCs using the UCNPs-based optical sensor. Reprinted with permission from [139]. Copyright 2019, Wiley Online Library. cAMP, cyclic adenosine monophosphate; DA, dopamine; GDNF, neurotrophic factor; GO, graphene oxide; hNSCs, human neural stem cells; NIR, near-infrared; UCNPs, upconversion nanoparticles. ** $p < 0.01$.

The literature identified several UCNPs with high optical properties and low cytotoxicity. Moreover, UCNP-based sensors can monitor stem cell differentiation in real-time,

non-invasively, without a label. In addition to cell imaging, UCNPs are potential drug delivery systems to control stem cell differentiation.

3.3. Autofluorescence-Based Optical Sensors

Various biomaterials derived from cellular organisms have autofluorescence properties, which allows them the potential to be used in biosensors for invasive and label-free sensing to obtain information about cells and tissues [140]. Furthermore, autofluorescence techniques do not require treatment or fixing of specimens and can be performed in real-time. In addition, autofluorescence-based sensors can be applied to monitor stem cell differentiation with invasive optical sensing methods, such as Raman spectroscopy and NIR, because autofluorescence can indicate a specific cellular component [141,142]. Raman-based sensing applied with autofluorescence is especially advantageous to analyse information about intracellular dynamics, which can be utilised to investigate the intracellular changes during stem cell differentiation [103].

A label-free autofluorescence-based imaging system combining optical metabolic modelling with quantitative image analysis was developed by Qian et al. [143] for monitoring human PSC (hPSC) differentiation into cardiomyocytes (Figure 9). This study was based on the fact that hPSC-derived cardiomyocytes undergo significant metabolic changes during differentiation. Specifically, the amount or ratio of oxidised flavin adenine dinucleotide (FAD) and reduced nicotinamide adenine dinucleotide (phosphate) (NAD(P)H), both autofluorescence metabolic materials, is influenced by the cellular conditions and differentiation and can be imaged to collect metabolic information at the single cell level. Furthermore, the ratio of NAD(P)H to FAD provides information about the relative oxidative state of the cells. Therefore, cardiomyocytes differentiated from different hPSC lines were visualised with NAD(P)H and FAD autofluorescence probes. According to the autofluorescence imaging on the eighth day, the intensity of NAD(P)H autofluorescence differed depending on the differentiation efficiencies. In addition, the cardiomyocytes and non-cardiomyocytes showed different autofluorescence intensities. For instance, NAD(P)H and FAD fluorescence after 8 days was exhibited in 84.1% of the differentiated cells, compared with 0.3% in undifferentiated cells.

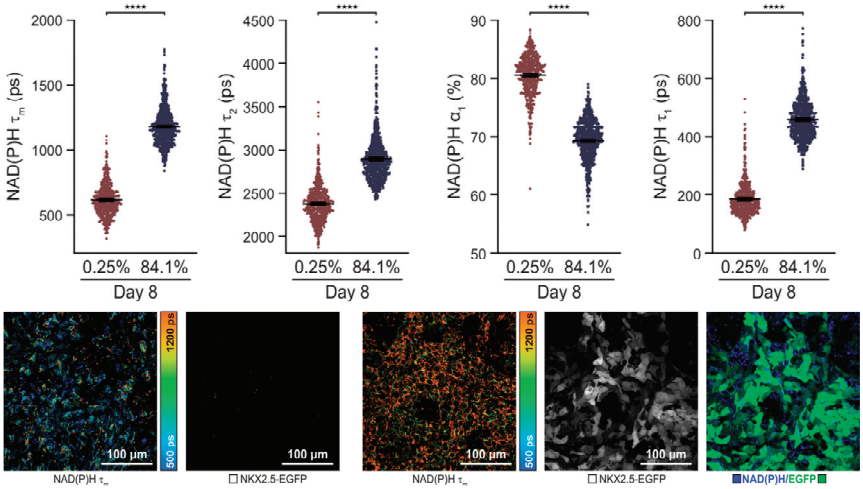

Figure 9. An autofluorescence imaging for monitoring of cardiomyocyte differentiation. Single-cell quantitative analysis of NAD(P)H during 8 days of the differentiation period. Reprinted with permission from [143]. Copyright 2019, Wiley Online Library. EGFP, enhanced green fluorescent protein; NAD(P)H, reduced nicotinamide adenine dinucleotide (phosphate); NKX2.5-EGFP, homeobox protein NKX2.5-EGFP.**** $p < 0.0001$.

In another study, Suhito et al. [144] reported on an autofluorescence-integrated Raman mapping analysis for label-free monitoring of adipogenic differentiation. Raman mapping analysis has the critical issue of long detection time, which results in cell apoptosis. To address this issue, these researchers developed a novel optical sensing method that enabled the rapid and non-destructive analysis of adipogenesis. The authors confirmed that the lipid droplets present in adipocytes were identified with the developed autofluorescence-integrated Raman sensing method; the Raman scattering of lipid droplets was aroused at 2850–2855 cm^{-1}. In addition, this method was utilised in the large-scale sensing analysis of multiple cells in culture plates by obtaining Raman mapping images at low magnification. Moreover, the analysis required a very short time (<20 min) and could scan 440 × 330 μm area per mapping image. Furthermore, the authors analysed in-batch and batch-to-batch variations of adipogenic differentiation throughout the autofluorescence-Raman imaging.

Similarly, Li et al. showed a label-free autofluorescence sensing system capable of monitoring of neurogenesis [145]. The optical sensor was based on tetrapod-shaped ZnO (t-ZnO) microparticles capable of label-free monitoring of neuronal differentiation. Specifically, this sensor formed 3D scaffolds that analysed DA released from neurons embedded on the surface using autofluorescence imaging. Interestingly, t-ZnO nanoparticles with four hexagonal arms were biocompatible and autofluorescence materials that fluoresced under UV light because they contained anion vacancies. The nanoparticles' autofluorescence was demonstrated to be very sensitive to hole scavengers, which was used for quantitative DA analysis. Furthermore, nanoparticles' autofluorescence acted as a quencher for the autofluorescence of the t-ZnO nanoparticles. Due to its 3D structures with high surface area and autofluorescence, the t-ZnO nanoparticles-based sensor showed a high sensing performance toward DA (LOD: 0.137 μM). Furthermore, DA was selectively datable in the presence of interfering molecules, including citric acid, glutamine, ascorbic acid, glucose, KCl and calcium chloride.

Autofluorescence-based optical sensing techniques were reported as suitable for non-invasive, non-destructive, and label-free monitoring of stem cell differentiation. Chronic lymphocytic leukaemia-derived autofluorescence could be utilised to analyse the biological changes in stem cell differentiation. Furthermore, most autofluorescence is biocompatible, which allows stem cells to be stably cultured and differentiated on the sensor for long time periods.

4. Conclusions and Future Perspectives

This review summarised recent progress in nano-biosensors for non-invasively monitoring of stem cell differentiation. Various nano- and micromaterials, such as AuNPs, AgNPs, UCNPs, autofluorescence probes, nucleic acids, microfluidic systems and microelectrode arrays, were reviewed and compared. Furthermore, their advantageous use to improve the biosensors' performance, including sensitivity and selectivity, for monitoring stem cell differentiation was appraised. In the case of electrochemical sensors, the electrochemically active surface area was found to be a crucial parameter; this is because the redox reaction of target analytes occurs on the electrode surface via electron transfer. Moreover, various nanomaterials were identified that could be applied to improve the electrochemically active surface. Furthermore, specific micro-scaled systems were identified that could be utilised to enhance the advantage of existing nanomaterials, providing more sensitive and selective sensing capabilities toward target molecules. The literature scrutinised supported that many nanomaterials have been applied in optical sensing to enhance the optical signal intensity to target analytes specifically or to make the analysis process simpler and faster. In addition to excellent sensing capabilities, various nano-biosensors have functioned as stem cell cultivation platforms by providing cell-friendly surfaces. In conclusion, electrochemical or optical nano-biosensors capable of monitoring stem cell differentiation in a non-invasive, non-destructive, and label-free sensing system could be used to control stem cell differentiation and develop practical and efficient stem cell therapies.

Table 1. Nano-Biosensors for Non-Invasive Monitoring of Stem Cell Differentiation.

Method	Material and Technique	Advantages	Limitations	Target/Sensitivity	Differentiation	Ref.
Electrochemical sensing	AuNPs	■ High biocompatibility towards hESC growth and adhesion ■ Label-free identification of differentiated cells	■ Insufficient sensitivity	Cells/12,500 cells	Epithelial differentiation	[59]
	AuNPs-nanoarray	■ Non-destructive and real-time sensing system for monitoring of osteogenic differentiation ■ Providing topographical cues favourable for stem cell differentiation	■ Low sensing performance at early differentiation stages	ALP/0.03 unit/mL	Osteogenic differentiation	[73]
	AuNPs-RGD-Fe_3O_4	■ Capable of regulation of mechanotransduction-mediated stem cell differentiation ■ In-situ time-resolved monitoring of osteogenic differentiation	■ Difficult analysis of early differentiation	ALP/-	Osteogenic differentiation	[74]
	AuNPs	■ Simultaneous electrochemical monitoring and kidney organoid generation on-a-chip ■ Electrical signal interpretation in multiple detection of kidney ■ organoid on-a-chip	■ Difficult to identify detailed cell subtypes	Cells/21,363 cells	Kidney organoids	[75]
	Aptamer-CPNTs	■ Highly sensitive and selective detection of DA ■ Non-destructive monitoring of exocytotic DA release from living neurons	■ Potential colouration effect and its poor stability	DA/100 pM	Neuronal differentiation	[89]
	Peptide-Oligonucleotide	■ Non-destructive detection of cardiomyogenic differentiation ■ Applicable to label-free drug screening	■ Insufficient selectivity for applications in cell culture environments	cTnI/0.42 pg/mL	Cardiomyocyte differentiation	[90]
	Aptamer-Pdots-microarray	■ High throughput DA sensing at the single cell level ■ Imaging of exocytotic DA release from living neurons	■ High variations in DA signals	DA/53 pM	Neuronal differentiation	[91]
	Aptamer	■ Based on a nanostructure suitable for excluding non-specific proteins as interfering molecules ■ Suitable to track in situ neurochemical flux in the complex cell media	■ Difficult sensor operation	5-HT/< 1 nM	Neuronal differentiation	[92]
	Graphene-	■ Simultaneously detection of DA and serotonin ■ Potential for multi-site neurotransmitter mapping with high spatial and temporal resolution	■ Platform not proven applicable to cell culture	DA/61.67 nM	Neuronal differentiation	[104]

Table 1. *Cont.*

Method	Material and Technique	Advantages	Limitations	Target/Sensitivity	Differentiation	Ref.
Electrochemical sensing	Pyrolytic carbon fibre	■ Real-time monitoring of exocytotic DA release ■ Multifunctional platform applicable to stem cell-based sensing and therapeutics	■ Insufficiently proven sensor selectivity	DA/-	Neuronal differentiation	[105]
	Carbon nanotube	■ Label-free and non-invasive evaluation of antipsychotic drugs on DA release from neuronal cells	■ Insufficient selectivity toward DA	DA/<10 nM	Neuronal differentiation	[106]
	Microfluidics	■ Label-free and non-invasive impedance measurements of single cells	■ Insufficient for practical applications in terms of throughput	-	Osteogenic differentiation	[113]
		■ Compartmentalised the neuronal culture into three distinct but axonally connected networks ■ Mimicking local and circuitry functionality of brain tissue	■ Includes complicated devices and procedures	-	Neuronal differentiation	[114]
		■ Non-invasive monitoring of cell-secreted multiple biomarkers in response to chemotherapeutic drugs ■ Contains 3D cardiac and BC spheroid-based microtissues with mechanical properties mimicking individual native tissues	■ Short-term (<6 days) analysis of differentiation	Troponin T and HER-2/<0.1 pg/mL	Cardiomyocyte differentiation	[115]
	Microelectrode array	■ Long-term (>100 days) monitoring of cardiomyocyte differentiation with 3D cultivation system	■ Signal variations during monitoring differentiation	E4031/<1 nM	Cardiomyocyte differentiation	[119]
		■ In vitro multi-site and long-term monitoring of bioelectrical activity changes in the neuronal network ■ Cross-correlation analysis between channels capable of evaluating the connection status in the neuronal networks	■ Insufficient biological validation	Glutamate and GABA/100 nM and 50 nM, respectively	Neuronal differentiation	[120]
	Microelectrode array-rGO	■ Stable monitoring of neuronal differentiation from long-term cultured neurons ■ Quantitative analysis of different types of DA vesicular exocytosis	■ Insufficient selectivity toward DA	DA/2 nM	Neuronal differentiation	[121]
Optical sensing	AuNPs-DNA	■ Long-term (>21 d) sensing of biomarkers involved in osteogenic differentiation ■ Label-free monitoring of osteogenic differentiation	■ Potential side effects of cellular uptake of AuNPs	miR-144-3p/13.6 aM	Osteogenic differentiation	[128]

Table 1. *Cont.*

Method	Material and Technique	Advantages	Limitations	Target/Sensitivity	Differentiation	Ref.
Optical sensing	AuNPs-BCIP	■ Label-free monitoring of osteogenic differentiation	■ Potential side effects of cellular uptake of AuNPs	ALP/1.0 U/L	Osteogenic differentiation	[129]
	AuStar-DTCC-Ag_2S	■ Depth-independent and high-resolution stem cell-tracking strategy ■ Real-time sensing of in vivo functionality of stem cells	■ Potential side effects of cellular uptake of AuNPs	Cells/<100 cells	Adipogenic differentiation Osteogenic differentiation Chondrogenic differentiation	[130]
	Au-Ni nanorods	■ Highly selective detection of stem cell differentiation ■ Applicable to in vitro and in vivo stem cell differentiation modulation	■ Potentially undesired effects of magnetic fields on cell behaviour	miR-124/<1 pM	Neuronal differentiation	[131]
	AuNPs-nanopore	■ Cost-effective and sensitive sensing method for detection of neuronal differentiation	■ Signal variations during monitoring differentiation	GDNF/<2 pg/mL	Neuronal differentiation	[132]
	AgNPs	■ Label-free sensing system for sensing multiple osteogenic differentiation-involved markers. ■ 3D culture system integrated-sensing system	■ Signal variations during monitoring differentiation	ALP, OC, and FN/-	Osteogenic differentiation	[133]
	AgNPs-Aptamer	■ Ultrasensitive and reliable detection of exocytotic DA release from living neurons ■ 3D culture system integrated-sensing system	■ Insufficient biological validation	DA/10 aM in PBS and 10 fM in serum	Neuronal differentiation	[135]
	UCNP	■ Simultaneous differentiation control and sensing of osteogenic differentiation ■ Label-free detection of osteogenic differentiation	■ Potential cytotoxicity by photothermal effect	MMP13/-	Osteogenic differentiation	[137]
		■ Simultaneous differentiation control and sensing of osteogenic differentiation ■ Applicable to in vitro and in vivo stem cell differentiation modulation	■ Potential cytotoxicity by photothermal effect	MMP13/-	Osteogenic differentiation	[138]
		■ Monitoring of neuronal differentiation at single-cell level ■ Real-time analysis of the function of DAnergic neurons	■ Potential cytotoxicity by photothermal effect	DA/<1 pM	Neuronal differentiation	[140]

Table 1. *Cont.*

Method	Material and Technique	Advantages	Limitations	Target/Sensitivity	Differentiation	Ref.
Optical sensing	Autofluorescence	■ Label-free monitoring of cardiomyocyte differentiation ■ Can predict the cardiomyocyte differentiation efficiency early in the differentiation process	■ Potential phototoxicity during imaging procedures	FAD and NAD(P)H/-	Cardiomyocyte differentiation	[143]
		■ Non-destructive and large-scale analysis (440 × 330 μm area) of adipogenic differentiation ■ Rapid visualisation (<20 min) of the cell morphology and cytosolic microstructure	■ Difficult to apply to multiple-cell analysis	Lipid droplets/-	Adipogenic differentiation	[144]
	t-ZnO	■ Utilisable directly without complicated probe immobilisation or modification ■ High resolution detection of DA release from neural tissue	■ Insufficient lifetime for living tissue cultivation	DA/0.137 μM	Neuronal differentiation	[145]

Note: 3D, three-dimensional; 5-HT, 5-hydroxytryptamine; AgNPs silver nanoparticles; Ag_2S, silver sulphide; ALP, alkaline phosphatase; AuNPs, gold nanoparticles; Au-Ni, gold-nickel; AuStar, gold nanostar; BC, breast cancer; BCIP, 5-bromo-4-chloro-3-indolyl phosphate; CPNTs, carboxylated polypyrrole nanotubes; cTnI, cardiac troponin I; DA, dopamine; DAnergic neurons, dopaminergic neurons; DNA, deoxyribonucleic acid; DTCC, disseminated tumour cell clusters; E4031, N-[4-[1-[2-(6-methylpyridin-2-yl)ethyl]piperidine-4-carbonyl]phenyl]; FAD, flavin ade-nine dinucleotide; Fe_3O_4, iron (II, III) oxide; FN, fibronectin; GABA, γ-aminobutyric acid; GDNF, glial cell-derived neurotrophic factor; HER-2, human epidermal growth factor receptor-2; miR, microRNA; MMP13, metalloproteinase 13; NAD(P)H, nicotinamide adenine dinucleotide (phosphate); OC, osteocalcin; Pdots, polymer dots, RGD, Arg-Gly-Asp ligand; rGO, reduced graphene oxide; t-ZnO, tetrapod zinc oxide; UCNPs, upconversion nanoparticles.

Author Contributions: M.-J.K., Y.-W.C. and T.-H.K. wrote and revised the manuscript. All authors have read and agreed to the published version of the manuscript.

Funding: This research was supported by the Chung-Ang University Graduate Research Scholarship in 2022 and by the National Research Foundation of Korea (NRF) grant funded by the Korean government (MSIT) (No. 2022R1A2C4002217).

Institutional Review Board Statement: Not applicable.

Informed Consent Statement: Not applicable.

Data Availability Statement: Not applicable.

Conflicts of Interest: The authors declare no conflict of interest.

References

1. Van der Kooy, D.; Weiss, S. Why stem cells? *Science* **2000**, *287*, 1439–1441. [CrossRef]
2. Cho, Y.-W.; Jee, S.; Suhito, I.R.; Lee, J.-H.; Park, C.G.; Choi, K.M.; Kim, T.-H. Single metal-organic framework–embedded nanopit arrays: A new way to control neural stem cell differentiation. *Sci. Adv.* **2022**, *8*, eabj7736. [CrossRef]
3. Slavin, S.; Nagler, A.; Naparstek, E.; Kapelushnik, Y.; Aker, M.; Cividalli, G.; Varadi, G.; Kirschbaum, M.; Ackerstein, A.; Samuel, S.; et al. Nonmyeloablative stem cell transplantation and cell therapy as an alternative to conventional bone marrow transplantation with lethal cytoreduction for the treatment of malignant and non-malignant hematologic diseases. *Blood* **1998**, *91*, 756–763. [CrossRef]
4. Kim, S.U.; De Vellis, J. Stem cell-based cell therapy in neurological diseases: A review. *J. Neurosci. Res.* **2009**, *87*, 2183–2200. [CrossRef]
5. Haas, S.; Weidner, N.; Winkler, J. Adult stem cell therapy in stroke. *Curr. Opin. Neurol.* **2005**, *18*, 59–64. [CrossRef]
6. Asahara, T.; Kalka, C.; Isner, J.M. Stem cell therapy and gene transfer for regeneration. *Gene Ther.* **2000**, *7*, 451–457. [CrossRef]
7. Zakrzewski, W.; Dobrzyński, M.; Szymonowicz, M.; Rybak, Z. Stem cells: Past, present, and future. *Stem Cell Res. Ther.* **2019**, *10*, 68. [CrossRef]
8. Golchin, A.; Farahany, T.Z. Biological products: Cellular therapy and FDA approved products. *Stem Cell Rev. Rep.* **2019**, *15*, 166–175. [CrossRef]
9. Müller, A.M.; Huppertz, S.; Henschler, R. Hematopoietic stem cells in regenerative medicine: Astray or on the path? *Transfus. Med. Hemotherapy* **2016**, *43*, 247–254. [CrossRef]
10. Mosaad, Y.M. Hematopoietic stem cells: An overview. *Transfus. Apher. Sci.* **2014**, *51*, 68–82. [CrossRef]
11. Herberts, C.A.; Kwa, M.S.; Hermsen, H.P. Risk factors in the development of stem cell therapy. *J. Transl. Med.* **2011**, *9*, 29. [CrossRef]
12. Trounson, A.; McDonald, C. Stem cell therapies in clinical trials: Progress and challenges. *Cell Stem Cell* **2015**, *17*, 11–22. [CrossRef]
13. Kang, S.K.; Shin, I.S.; Ko, M.S.; Jo, J.Y.; Ra, J.C. Journey of mesenchymal stem cells for homing: Strategies to enhance efficacy and safety of stem cell therapy. *Stem Cells Int.* **2012**, *2012*, 342968. [CrossRef]
14. Mastri, M.; Lin, H.; Lee, T. Enhancing the efficacy of mesenchymal stem cell therapy. *World J. Stem Cells* **2014**, *6*, 82–93. [CrossRef]
15. Cho, Y.-W.; Kim, D.-S.; Suhito, I.R.; Han, D.K.; Lee, T.; Kim, T.-H. Enhancing neurogenesis of neural stem cells using homogeneous nanohole pattern-modified conductive platform. *Int. J. Mol. Sci.* **2019**, *21*, 191. [CrossRef]
16. Lee, S.H.; Jeon, S.; Qu, X.; Kang, M.S.; Lee, J.H.; Han, D.-W.; Hong, S.W. Ternary MXene-loaded PLCL/collagen nanofibrous scaffolds that promote spontaneous osteogenic differentiation. *Nano Converg.* **2022**, *9*, 38. [CrossRef]
17. VanGuilder, H.D.; Vrana, K.E.; Freeman, W.M. Twenty-five years of quantitative PCR for gene expression analysis. *Biotechniques* **2008**, *44*, 619–626. [CrossRef]
18. Tokuyasu, K.T. Application of cryoultramicrotomy to immunocytochemistry. *J. Microsc.* **1986**, *143*, 139–149. [CrossRef]
19. Adan, A.; Alizada, G.; Kiraz, Y.; Baran, Y.; Nalbant, A. Flow cytometry: Basic principles and applications. *Crit. Rev. Biotechnol.* **2016**, *37*, 163–176. [CrossRef]
20. Mahmood, T.; Yang, P.C. Western blot: Technique, theory, and trouble shooting. *N. Am. J. Med. Sci.* **2012**, *4*, 429–434. [CrossRef]
21. Enzmann, G.U.; Benton, R.L.; Talbott, J.F.; Cao, Q.; Whittemore, S.R.; Zhang, Y.; Yang, J.; Zhang, P.; Liu, T.; Xu, J.; et al. Functional considerations of stem cell transplantation therapy for spinal cord repair. *J. Neurotrauma* **2006**, *23*, 479–495. [CrossRef]
22. Bonanos, N.; Steel, B.C.H.; Butler, E.P.; Macdonald, J.R.; Johnson, W.B.; Worrell, W.L.; Niklasson, G.A.; Malmgren, S.; Strømme, M.; Sundaram, S.K.; et al. Applications of Impedance Spectroscopy. In *Impedance Spectrophotometry: Theory, Experiment, and Applications*, 3rd ed.; Barsoukov, E., Macdonald, J.R., Eds.; John Wiley and Sons Inc.: Hoboken, NJ, USA, 2018; pp. 175–478. [CrossRef]
23. Katz, E.; Willner, I. Probing biomolecular interactions at conductive and semiconductive surfaces by impedance spectroscopy: Routes to impedimetric immunosensors, DNA-sensors, and enzyme biosensors. *Electroanalysis* **2003**, *15*, 913–947. [CrossRef]
24. Notingher, I.J. Raman spectroscopy cell-based biosensors. *Sensors* **2007**, *7*, 1343–1358. [CrossRef]
25. Shafer-Peltier, K.E.; Haynes, C.L.; Glucksberg, M.R.; Van Duyne, R.P. Toward a glucose biosensor based on surface-enhanced Raman scattering. *J. Am. Chem. Soc.* **2003**, *125*, 588–593. [CrossRef] [PubMed]

26. Zhang, Y.; Sun, J.; Liu, L.; Qiao, H. A review of biosensor technology and algorithms for glucose monitoring. *J. Diabetes Complicat.* **2021**, *35*, 107929. [CrossRef] [PubMed]
27. Wu, Y.; Ray, A.; Wei, Q.; Feizi, A.; Tong, X.; Chen, E.; Luo, Y.; Ozcan, A. Deep learning enables high-throughput analysis of particle-aggregation-based biosensors imaged using holography. *ACS Photon* **2019**, *6*, 294–301. [CrossRef]
28. Skládal, P. Advances in electrochemical immunosensors. *Electroanalysis* **1997**, *9*, 737–745. [CrossRef]
29. Felix, F.S.; Angnes, L. Electrochemical immunosensors—A powerful tool for analytical applications. *Biosens. Bioelectron.* **2018**, *102*, 470–478. [CrossRef]
30. Wu, Z.; Hu, J.; Zeng, T.; Zhang, Z.-L.; Chen, J.; Wong, G.; Qiu, X.; Liu, W.; Gao, G.F.; Bi, Y.; et al. Ultrasensitive Ebola virus detection based on electroluminescent nanospheres and immunomagnetic separation. *Anal. Chem.* **2017**, *89*, 2039–2048. [CrossRef]
31. Chen, D.; Zhang, M.; Zhou, F.; Hai, H.; Li, J. Ultrasensitive electroluminescence biosensor for a breast cancer marker microRNA based on target cyclic regeneration and multi-labeled magnetized nanoparticles. *Microchim. Acta* **2019**, *186*, 628. [CrossRef]
32. Roh, J.; Cho, Y.H.; Ahn, D.J. Sustainable colorimetric/luminescent sensors enabled by armored lipid nanoparticles. *Nano Converg.* **2022**, *9*, 42. [CrossRef]
33. Kweon, S.Y.; Park, J.P.; Park, C.Y.; Park, T.J. Graphene oxide-mediated fluorometric aptasensor for okadaic acid detection. *BioChip J.* **2022**, *16*, 207–213. [CrossRef]
34. Ronkainen, N.J.; Halsall, H.B.; Heineman, W.R. Electrochemical biosensors. *Chem. Soc. Rev.* **2010**, *39*, 1747–1763. [CrossRef] [PubMed]
35. Hammond, J.L.; Formisano, N.; Estrela, P.; Carrara, S.; Tkac, J. Electrochemical biosensors and nanobiosensors. *Essays Biochem.* **2016**, *60*, 69–80. [CrossRef]
36. Pohanka, M.; Skládal, P. Electrochemical biosensors—Principles and applications. *J. Appl. Biomed.* **2008**, *6*, 57–64. [CrossRef]
37. Jothimani, G.; Pathak, S.; Dutta, S.; Duttaroy, A.K.; Banerjee, A. A comprehensive cancer-associated microRNA expression profiling and proteomic analysis of human umbilical cord mesenchymal stem cell-derived exosomes. *Tissue Eng. Regen. Med.* **2022**, *19*, 1013–1031. [CrossRef]
38. Serafin, A.; Rubio, M.C.; Carsi, M.; Ortiz-Serna, P.; Sanchis, M.J.; Garg, A.K.; Oliveira, J.M.; Koffler, J.; Collins, M.N. Electroconductive PEDOT nanoparticle integrated scaffolds for spinal cord tissue repair. *Biomater. Res.* **2022**, *26*, 63. [CrossRef]
39. Azmi, N.E.; Rashid, A.H.A.; Abdullah, J.; Yusof, N.A.; Sidek, H. Fluorescence biosensor based on encapsulated quantum dots/enzymes/sol-gel for non-invasive detection of uric acid. *J. Lumin* **2018**, *202*, 309–315. [CrossRef]
40. Bantz, K.C.; Meyer, A.F.; Wittenberg, N.J.; Im, H.; Kurtuluş, O.; Lee, S.H.; Lindquist, N.C.; Oh, S.-H.; Haynes, C.L. Recent progress in SERS biosensing. *Phys. Chem. Chem. Phys.* **2011**, *13*, 11551–11567. [CrossRef]
41. Rachim, V.P.; Chung, W.-Y. Wearable-band type visible-near infrared optical biosensor for non-invasive blood glucose monitoring. *Sens. Actuators B Chem.* **2019**, *286*, 173–180. [CrossRef]
42. Eom, G.; Hang, A.; Kim, H.; Moon, J.; Kang, H.; Jung, J.; Lim, E.-K.; Jepng, J.; Park, H.G.; Kang, T. Ultrasensitive detection of ovarian cancer biomarker using Au nanoplate SERS immunoassay. *BioChip J.* **2021**, *15*, 348–355. [CrossRef]
43. Kim, H.; Han, Y.; Suhito, I.R.; Choi, Y.; Kwon, M.; Son, H.; Kim, H.-R.; Kim, T.-H. Raman spectroscopy-based 3D analysis of odontogenic differentiation of human dental pulp stem cell spheroids. *Anal. Chem.* **2021**, *93*, 9995–10004. [CrossRef] [PubMed]
44. Suhito, I.R.; Angeline, N.; Lee, K.-H.; Kim, H.; Park, C.G.; Luo, Z.; Kim, T.-H. A spheroid-forming hybrid gold nanostructure platform that electrochemically detects anticancer effects of curcumin in a multicellular brain cancer Model. *Small* **2021**, *17*, 2002436. [CrossRef] [PubMed]
45. Tenney, R.M.; Discher, D.E. Stem cells, microenvironment mechanics, and growth factor activation. *Curr. Opin. Cell Biol.* **2009**, *21*, 630–635. [CrossRef]
46. Pandey, P.; Datta, M.; Malhotra, B.D. Prospects of nanomaterials in biosensors. *Anal. Lett.* **2008**, *41*, 159–209. [CrossRef]
47. Naveen, M.H.; Gurudatt, N.G.; Shim, Y.-B. Applications of conducting polymer composites to electrochemical sensors: A review. *Appl. Mater. Today* **2017**, *9*, 419–433. [CrossRef]
48. Beaver, K.; Dantanarayana, A.; Minteer, S.D. Materials approaches for improving electrochemical sensor performance. *J. Phys. Chem. B* **2021**, *125*, 11820–11834. [CrossRef]
49. Chen, I.-J.; White, I.M. High-sensitivity electrochemical enzyme-linked assay on a microfluidic interdigitated microelectrode. *Biosens. Bioelectron.* **2011**, *26*, 4375–4381. [CrossRef]
50. Shin, S.R.; Zhang, Y.S.; Kim, D.J.; Manbohi, A.; Avci, H.; Silvestri, A.; Aleman, J.; Hu, N.; Kilic, T.; Keung, W.; et al. Aptamer-based microfluidic electrochemical biosensor for monitoring cell-secreted trace cardiac biomarkers. *Anal. Chem.* **2016**, *88*, 10019–10027. [CrossRef]
51. Sage, A.T.; Besant, J.D.; Lam, B.; Sargent, E.H.; Kelley, S.O. Ultrasensitive electrochemical biomolecular detection using nanostructured microelectrodes. *Acc. Chem. Res.* **2014**, *47*, 2417–2425. [CrossRef]
52. Toderas, F.; Baia, M.; Astilean, S. Controlling gold nanoparticle assemblies for efficient surface-enhanced Raman scattering and localized surface plasmon resonance sensors. *Nanotechnology* **2007**, *18*, 255702. [CrossRef]
53. Nie, Y.; Jin, C.; Zhang, J.X.J. Microfluidic in situ patterning of silver nanoparticles for surface-enhanced Raman spectroscopic sensing of biomolecules. *ACS Sens.* **2021**, *6*, 2584–2592. [CrossRef] [PubMed]
54. Widmann, K.; Ao, T.; Foord, M.E.; Price, D.F.; Ellis, A.D.; Springer, P.T.; Ng, A. Single-state measurement of electrical conductivity of warm dense gold. *Phys. Rev. Lett.* **2004**, *92*, 125002. [CrossRef]

55. Guo, S.; Wang, E. Synthesis and electrochemical applications of gold nanoparticles. *Anal. Chim. Acta* **2007**, *598*, 181–192. [CrossRef] [PubMed]
56. Yu, A.; Liang, Z.; Caruso, F. Nanostructured electrochemical sensor based on dense gold nanoparticle films. *Nano Lett.* **2003**, *3*, 1203–1207. [CrossRef]
57. Luo, X.; Morrin, A.; Killard, A.J.; Smyth, M.R. Application of nanoparticles in electrochemical sensors and biosensors. *Electroanalysis* **2006**, *18*, 319–326. [CrossRef]
58. El-Said, W.A.; Al-Bogami, A.S.; Alshitari, W.; El-Hady, D.A.; Saleh, T.S.; El-Mokhtar, M.A.; Choi, J.-W. Electrochemical microbiosensor for detecting COVID-19 in a patient sample based on gold microcuboids pattern. *BioChip J.* **2021**, *15*, 287–295. [CrossRef]
59. Suhito, I.R.; Kang, E.-S.; Kim, D.-S.; Baek, S.; Park, S.-J.; Moon, S.-H.; Luo, Z.; Lee, D.; Min, J.; Kim, T.-H. High density gold nanostructure composites for precise electrochemical detection of human embryonic stem cells in cell mixture. *Colloids Surf. B Biointerfaces* **2019**, *180*, 384–392. [CrossRef]
60. Kim, D.-S.; Kang, E.-S.; Baek, S.; Choo, S.-S.; Chung, Y.-H.; Lee, D.; Min, J.; Kim, T.-H. Electrochemical detection of dopamine using periodic cylindrical gold nanoelectrode arrays. *Sci. Rep.* **2018**, *8*, 14049. [CrossRef]
61. Koo, K.-M.; Kim, C.-D.; Kim, H.; Cho, Y.-W.; Suhito, I.R.; Kim, T.-H. Extracellularly detectable electrochemical signals of living cells originate from metabolic reactions. *Adv. Sci.* **2023**, *10*, e2207084. [CrossRef]
62. Ju, F.N.; Kim, C.-H.; Lee, K.-H.; Kim, C.-D.; Lim, J.; Lee, T.; Park, C.G.; Kim, T.-H. Gold nanostructure-integrated conductive microwell arrays for uniform cancer spheroid formation and electrochemical drug screening. *Biosens. Bioelectron.* **2023**, *222*, e115003. [CrossRef] [PubMed]
63. Koo, K.-M.; Go, Y.-H.; Kim, S.-M.; Kim, C.-D.; Do, J.T.; Kim, T.-H.; Cha, H.-J. Label-free and non-destructive identification of naïve and primed embryonic stem cells based on differences in cellular metabolism. *Biomaterials* **2023**, *293*, e121939. [CrossRef] [PubMed]
64. Chen, Y.; Xianyu, Y.; Jiang, X. Surface modification of gold nanoparticles with small molecules for biochemical analysis. *Acc. Chem. Res.* **2017**, *50*, 310–319. [CrossRef]
65. Perrault, S.D.; Chan, W.C.W. Synthesis and surface modification of highly monodispersed, spherical gold nanoparticles of 50−200 nm. *J. Am. Chem. Soc.* **2010**, *131*, 17042–17043. [CrossRef] [PubMed]
66. Zhu, T.; Vasilev, K.; Kreiter, M.; Mittler, S.; Knoll, W. Surface modification of citrate-reduced colloidal gold nanoparticles with 2-mercaptosuccinic Acid. *Langmuir* **2003**, *19*, 9518–9525. [CrossRef]
67. Connor, E.E.; Mwamuka, J.; Gole, A.; Murphy, C.J.; Wyatt, M.D. Gold nanoparticles are taken up by human cells but do not cause acute cytotoxicity. *Small* **2005**, *1*, 325–327. [CrossRef]
68. Baranes, K.; Shevach, M.; Shefi, O.; Dvir, T. Gold nanoparticle-decorated scaffolds promote neuronal differentiation and maturation. *Nano Lett.* **2016**, *16*, 2916–2920. [CrossRef]
69. Yi, C.; Liu, D.; Fong, C.-C.; Zhang, J.; Yang, M. Gold nanoparticles promote osteogenic differentiation of mesenchymal stem cells through p38 MAPK pathway. *ACS Nano* **2010**, *4*, 6439–6448. [CrossRef]
70. Ricles, L.M.; Nam, S.Y.; Sokolov, K.; Emelianov, S.Y.; Suggs, L.J. Function of mesenchymal stem cells following loading of gold nanotracers. *Int. J. Nanomed.* **2011**, *6*, 407–416. [CrossRef]
71. Silva, A.K.A.; Di Corato, R.; Pellegrino, T.; Chat, S.; Pugliese, G.; Luciani, N.; Gazeau, F.; Wilhelm, C. Cell-derived vesicles as a bioplatform for the encapsulation of theranostic nanomaterials. *Nanoscale* **2013**, *5*, 11374–11384. [CrossRef]
72. Zong, J.; Cobb, S.L.; Cameron, N.R. Peptide-functionalized gold nanoparticles: Versatile biomaterials for diagnostic and therapeutic applications. *Biomater. Sci.* **2017**, *5*, 872–886. [CrossRef] [PubMed]
73. Lee, J.-H.; Choi, H.K.; Yang, L.; Chueng, S.-T.D.; Choi, J.-W.; Lee, K.-B. Nondestructive real-time monitoring of enhanced stem cell differentiation using a graphene-Au hybrid nanoelectrode array. *Adv. Mater.* **2018**, *30*, e1802762. [CrossRef] [PubMed]
74. Lee, S.; Kim, M.S.; Patel, K.D.; Choi, H.; Thangam, R.; Yoon, J.; Koo, T.M.; Jung, H.J.; Min, S.; Bae, G.; et al. Magnetic control and real-time monitoring of stem cell differentiation by the ligand nanoassembly. *Small* **2021**, *17*, e2102892. [CrossRef] [PubMed]
75. Suhito, I.R.; Kim, J.W.; Koo, K.-M.; Nam, S.A.; Kim, Y.K.; Kim, T.-H. In situ detection of kidney organoid generation from stem cells using a simple electrochemical method. *Adv. Sci.* **2022**, *9*, e2200074. [CrossRef] [PubMed]
76. Saleh, J.; Mercier, B.; Xi, W. Bioengineering methods for organoid systems. *Biol. Cell* **2021**, *113*, 475–491. [CrossRef]
77. Rossi, G.; Manfrin, A.; Lutolf, M.P. Progress and potential in organoid research. *Nat. Rev. Genet.* **2018**, *19*, 671–687. [CrossRef]
78. Huch, M.; Knoblich, J.A.; Lutolf, M.P.; Martinez-Arias, A. The hope and the hype of organoid research. *Development* **2017**, *144*, 938–941. [CrossRef]
79. Watson, J.D.; Crick, F.H. Molecular structure of nucleic acids: A structure for deoxyribose nucleic acid. *Nature* **1953**, *171*, 737–738. [CrossRef]
80. Baeumner, A.J.; Pretz, J.; Fang, S. A universal nucleic acid sequence biosensor with nanomolar detection limits. *Anal. Chem.* **2004**, *76*, 888–894. [CrossRef]
81. Wang, J. Electrochemical nucleic acid biosensors. *Anal. Chim. Acta* **2002**, *469*, 63–71. [CrossRef]
82. Du, Y.; Dong, S. Nucleic acid biosensors: Recent advances and perspectives. *Anal. Chem.* **2017**, *89*, 189–215. [CrossRef] [PubMed]
83. Park, G.; Lee, M.; Park, C.; Min, J.; Lee, T. Selection of DNA aptamer and its application as an electrical biosensor for Zika virus detection in human serum. *Nano Converg.* **2022**, *9*, 41. [CrossRef] [PubMed]

84. Darmostuk, M.; Rimpelova, S.; Gbelcova, H.; Ruml, T. Current approaches in SELEX: An update to aptamer selection technology. *Biotechnol. Adv.* **2015**, *33*, 1141–1161. [CrossRef] [PubMed]
85. Gopinath, S.C.B. Methods developed for SELEX. *Anal. Bioanal. Chem.* **2007**, *387*, 171–182. [CrossRef]
86. Zhou, W.; Huang, P.-J.J.; Ding, J.; Liu, J. Aptamer-based biosensors for biomedical diagnostics. *Anal.* **2014**, *139*, 2627–2640. [CrossRef]
87. Kim, Y.S.; Raston, N.H.; Gu, M.B. Aptamer-based nanobiosensors. *Biosens. Bioelectron.* **2016**, *76*, 2–19. [CrossRef]
88. Song, S.; Wang, L.; Li, J.; Fan, C.; Zhao, J. Aptamer-based biosensors. *TrAC Trends Anal. Chem.* **2008**, *27*, 108–117. [CrossRef]
89. Park, S.J.; Lee, J.; Seo, S.E.; Kim, K.H.; Lee, S.H.; Ban, H.S.; Lee, B.D.; Song, H.S.; Kim, J.; Lee, C.S. High-performance conducting polymer nanotube-based liquid-ion gated field-effect transistor aptasensor for dopamine exocytosis. *Sci. Rep.* **2020**, *10*, 3772. [CrossRef]
90. Han, K.; Li, G.; Tian, L.; Li, L.; Shi, Y.; Huang, T.; Li, Y.; Xu, Q. Multifunctional peptide-oligonucleotide conjugate promoted sensitive electrochemical biosensing of cardiac troponin I. *Biochem. Eng. J.* **2021**, *174*, 108104. [CrossRef]
91. Wang, N.; Ao, H.; Xiao, W.; Chen, W.; Li, G.; Wu, J.; Ju, H. Confined electrochemiluminescence imaging microarray for high-throughput biosensing of single cell-released dopamine. *Biosens. Bioelectron.* **2022**, *201*, 113959. [CrossRef]
92. Nakatsuka, N.; Heard, K.J.; Faillétaz, A.; Momotenko, D.; Vörös, J.; Gage, F.H.; Vadodaria, K.C. Sensing serotonin secreted from human serotonergic neurons using aptamer-modified nanopipettes. *Mol. Psychiatry* **2021**, *26*, 2753–2763. [CrossRef] [PubMed]
93. Hajian, A.; Lindström, S.B.; Pettersson, T.; Hamedi, M.M.; Wågberg, L. Understanding the dispersive action of nanocellulose for carbon nanomaterials. *Nano Lett.* **2017**, *17*, 1439–1447. [CrossRef] [PubMed]
94. Teradal, N.L.; Jelinek, R. Carbon nanomaterials in biological studies and biomedicine. *Adv. Healthc. Mater.* **2017**, *6*, 1700574. [CrossRef] [PubMed]
95. Choi, H.K.; Kim, C.-H.; Lee, S.N.; Kim, T.-H.; Oh, B.-K. Nano-sized graphene oxide coated nanopillars on microgroove polymer arrays that enhance skeletal muscle cell differentiation. *Nano Converg.* **2021**, *8*, 40. [CrossRef]
96. Reaz, A.H.; Saha, S.; Roy, C.K.; Wahab, M.A.; Will, G.; Amin, M.A.; Yamauchi, Y.; Liu, S.; Kaneti, Y.V.; Hossain, M.S.; et al. Boosting capacitive performance of manganese oxide nanorods by decorating with three-dimensional crushed graphene. *Nano Converg.* **2022**, *9*, 10. [CrossRef]
97. Kim, H.; An, H.J.; Park, J.; Lee, Y.; Kim, M.S.; Lee, S.; Kim, N.D.; Song, J.; Choi, I. Ultrasensitive and real-time optical detection of cellular oxidative stress using graphene-covered tunable plasmonic interfaces. *Nano Converg.* **2022**, *9*, 23. [CrossRef]
98. Chae, S.Y.; Park, R.; Hong, S.W. Surface-mediated high antioxidant and anti-inflammatory effects of astaxanthin-loaded ultrathin graphene oxide film that inhibits the overproduction of intracellular reactive oxygen species. *Biomater. Res.* **2022**, *26*, 30. [CrossRef]
99. Kang, E.-S.; Kim, H.; Han, Y.; Cho, Y.-W.; Son, H.; Luo, Z.; Kim, T.-H. Enhancing osteogenesis of adipose-derived mesenchymal stem cells using gold nanostructure/peptide-nanopatterned graphene oxide. *Colloids Surf. B Biointerfaces* **2021**, *204*, 111807. [CrossRef]
100. Park, D.; Park, J.; Lee, J.; Shim, C.J.; Kim, M.S.; Lee, T.Y.; Lim, J.O. Fabrication and characterization of graphene oxide-coated plate for efficient culture of stem cells. *Tissue Eng. Regen. Med.* **2021**, *18*, 775–785. [CrossRef]
101. Kim, H.; Solak, K.; Han, Y.; Cho, Y.-W.; Koo, K.-M.; Kim, C.-D.; Luo, Z.; Son, H.; Kim, H.-R.; Mavi, A.; et al. Electrically controlled mRNA delivery using a polypyrrole-graphene oxide hybrid film to promote osteogenic differentiation of human mesenchymal stem cells. *Nano Res.* **2022**, *15*, 9253–9263. [CrossRef]
102. Kang, E.-S.; Song, I.; Kim, D.-S.; Lee, U.; Kim, J.-K.; Son, H.; Min, J.; Kim, T.-H. Size-dependent effects of graphene oxide on the osteogenesis of human adipose-derived mesenchymal stem cells. *Colloids Surf. B Biointerfaces* **2018**, *169*, 20–29. [CrossRef] [PubMed]
103. Gosnell, M.E.; Anwer, A.G.; Mahbub, S.B.; Perinchery, S.M.; Inglis, D.W.; Adhikary, P.P.; Jazayeri, J.A.; Cahill, M.A.; Saad, S.; Pollock, C.A.; et al. Quantitative non-invasive cell characterization and discrimination based on multispectral autofluorescence features. *Sci. Rep.* **2016**, *6*, 23453. [CrossRef] [PubMed]
104. Castagnola, E.; Garg, R.; Rastogi, S.K.; Cohen-Karni, T.; Cui, X.T. 3D fuzzy graphene microelectrode array for dopamine sensing at sub-cellular spatial resolution. *Biosens. Bioelectron.* **2021**, *191*, 113440. [CrossRef] [PubMed]
105. Vasudevan, S.; Kajtez, J.; Bunea, A.-I.; Gonzalez-Ramos, A.; Ramos-Moreno, T.; Heiskanen, A.; Kokaia, M.; Larsen, N.B.; Martínez-Serrano, A.; Keller, S.S.; et al. Leaky optoelectrical fiber for optogenetic stimulation and electrochemical detection of dopamine exocytosis from human dopaminergic neurons. *Adv. Sci.* **2019**, *6*, 1902011. [CrossRef]
106. Pham Ba, V.A.; Cho, D.-G.; Hong, S. Nafion-radical hybrid films on carbon nanotube transistors for monitoring antipsychotic drug effects on stimulated dopamine release. *ACS Appl. Mater. Interfaces* **2019**, *11*, 9716–9723. [CrossRef]
107. Whitesides, G.M. The origins and the future of microfluidics. *Nature* **2006**, *442*, 368–373. [CrossRef]
108. Liu, K.-K.; Wu, R.-G.; Chuang, Y.-J.; Khoo, H.S.; Huang, S.-H.; Tseng, F.-G. Microfluidic systems for biosensing. *Sensors* **2010**, *10*, 6623–6661. [CrossRef]
109. Rivet, C.; Lee, H.; Hirsch, A.; Hamilton, S.; Lu, H. Microfluidics for medical diagnostics and biosensors. *Chem. Eng. Sci.* **2011**, *66*, 1490–1507. [CrossRef]
110. Luka, G.; Ahmadi, A.; Najjaran, H.; Alocilja, E.; DeRosa, M.; Wolthers, K.; Malki, A.; Aziz, H.; Althani, A.; Hoorfar, M. Microfluidics integrated biosensors: A leading technology towards lab-on-a-chip and sensing applications. *Sensors* **2015**, *15*, 30011–30031. [CrossRef]
111. Rackus, D.G.; Shamsi, M.H.; Wheeler, A.R. Electrochemistry, biosensors and microfluidics: A convergence of fields. *Chem. Soc. Rev.* **2015**, *44*, 5320–5340. [CrossRef]

112. Karimi, M.; Bahrami, S.; Mirshekari, H.; Basri, S.M.M.; Nik, A.B.; Aref, A.R.; Akbari, M.; Hamblin, M.R. Microfluidic systems for stem cell-based neural tissue engineering. *Lab A Chip* **2016**, *16*, 2551–2571. [CrossRef] [PubMed]
113. Fan, W.; Chen, X.; Ge, Y.; Jin, Y.; Jin, Q.; Zhao, J. Single-cell impedance analysis of osteogenic differentiation by droplet-based microfluidics. *Biosens. Bioelectron.* **2019**, *145*, 111730. [CrossRef] [PubMed]
114. Pelkonen, A.; Mzezewa, R.; Sukki, L.; Ryynänen, T.; Kreutzer, J.; Hyvärinen, T.; Vinogradov, A.; Aarnos, L.; Lekkala, J.; Kallio, P.; et al. A modular brain-on-a-chip for modelling epileptic seizures with functionally connected human neuronal networks. *Biosens. Bioelectron.* **2020**, *168*, 112553. [CrossRef] [PubMed]
115. Lee, J.; Mehrotra, S.; Zare-Eelanjegh, E.; Rodrigues, R.O.; Akbarinejad, A.; Ge, D.; Amato, L.; Kiaee, K.; Fang, Y.; Rosenkranz, A.; et al. A heart-breast cancer-on-a-chip platform for disease modeling and monitoring of cardiotoxicity induced by cancer chemotherapy. *Small* **2021**, *17*, e2004258. [CrossRef] [PubMed]
116. Huang, X.-J.; O'Mahony, A.M.; Compton, R.G. Microelectrode arrays for electrochemistry: Approaches to fabrication. *Small* **2009**, *5*, 776–788. [CrossRef] [PubMed]
117. Farooqi, H.M.U.; Kang, B.; Khalid, M.A.U.; Salih, A.R.C.; Hyun, K.; Park, S.H.; Huh, D.; Choi, K.H. Real-time monitoring of liver fibrosis through embedded sensors in a microphysiological system. *Nano Converg.* **2021**, *8*, 3. [CrossRef] [PubMed]
118. Ino, K.; Shiku, H.; Matsue, K. Bioelectrochemical applications of microelectrode arrays in cell analysis and engineering. *Curr. Opin. Electrochem.* **2017**, *5*, 146–151. [CrossRef]
119. Fleischer, S.; Jahnke, H.-G.; Fritsche, E.; Girard, M.; Robitzki, A.A. Comprehensive human stem cell differentiation in a 2D and 3D mode to cardiomyocytes for long-term cultivation and multiparametric monitoring on a multimodal microelectrode array setup. *Biosens. Bioelectron.* **2019**, *126*, 624–631. [CrossRef]
120. Gao, F.; Gao, K.; Zhang, P.; Fu, Y.; Liu, X.; Bai, S.; Li, W.; Qian, Z. A biomimetic sensor using neurotransmitter detection to decode odor perception by an olfactory network. *Biosens. Bioelectron.* **2022**, *211*, 114391. [CrossRef]
121. He, E.; Zhou, Y.; Luo, J.; Xu, S.; Zhang, K.; Song, Y.; Wang, M.; Xu, S.; Dai, Y.; Yang, G.; et al. Sensitive detection of electrophysiology and dopamine vesicular exocytosis of hESC-derived dopaminergic neurons using multifunctional microelectrode array. *Biosens. Bioelectron.* **2022**, *209*, 114263. [CrossRef] [PubMed]
122. Yang, X.; Yang, M.; Pang, B.; Vara, M.; Xia, Y. Gold nanomaterials at work in biomedicine. *Chem. Rev.* **2015**, *115*, 10410–10488. [CrossRef]
123. Haiss, W.; Thanh, N.T.; Aveyard, J.; Fernig, D.G. Determination of size and concentration of gold nanoparticles from UV−Vis spectra. *Anal. Chem.* **2007**, *79*, 4215–4221. [CrossRef] [PubMed]
124. Evanoff, D.D., Jr.; Chumanov, G. Synthesis and optical properties of silver nanoparticles and arrays. *ChemPhysChem* **2005**, *6*, 1221–1231. [CrossRef] [PubMed]
125. Park, J.H.; Choe, H.-S.; Kim, S.-W.; Im, G.-B.; Um, S.H.; Kim, J.-H.; Bhang, S.H. Silica-capped and gold-decorated silica nanoparticles for enhancing effect of gold nanoparticle-based photothermal therapy. *Tissue Eng. Regen. Med.* **2022**, *19*, 1161–1168. [CrossRef] [PubMed]
126. Lee, W.-J.; Kim, K.-J.; Hossain, M.K.; Cho, H.-Y.; Choi, J.-W. DNA–gold nanoparticle conjugates for intracellular miRNA detection using surface-enhanced Raman spectroscopy. *BioChip J.* **2022**, *16*, 33–40. [CrossRef]
127. Michota, A.; Bukowska, J. Surface-enhanced Raman scattering (SERS) of 4-mercaptobenzoic acid on silver and gold substrates. *J. Raman Spectrosc.* **2003**, *34*, 21–25. [CrossRef]
128. Cao, X.; Wang, Z.; Bi, L.; Bi, C.; Du, Q. Gold nanocage-based surface-enhanced Raman scattering probes for long-term monitoring of intracellular microRNA during bone marrow stem cell differentiation. *Nanoscale* **2020**, *12*, 1513–1527. [CrossRef]
129. Sun, D.; Xu, W.; Liang, C.; Shi, W.; Xu, S. Smart surface-enhanced resonance Raman scattering nanoprobe for monitoring cellular alkaline phosphatase activity during osteogenic differentiation. *ACS Sens.* **2020**, *5*, 1758–1767. [CrossRef]
130. Hua, S.; Zhong, S.; Arami, H.; He, J.; Zhong, D.; Zhang, D.; Chen, X.; Qian, J.; Hu, X.; Zhou, M. Simultaneous deep tracking of stem cells by surface enhanced Raman imaging combined with single-cell tracking by NIR-II imaging in myocardial infarction. *Adv. Funct. Mater.* **2021**, *31*, 2100468. [CrossRef]
131. Lee, J.-H.; Choi, J.-H.; Chueng, S.-D.; Pongkulapa, T.; Yang, L.; Cho, H.-Y.; Choi, J.-W.; Lee, K.-B. Nondestructive characterization of stem cell neurogenesis by a magneto-plasmonic nanomaterial-based exosomal miRNA detection. *ACS Nano* **2019**, *13*, 8793–8803. [CrossRef]
132. Yang, R.; Boldrey, J.; Jiles, D.; Schneider, I.; Que, L. On chip detection of glial cell-derived neurotrophic factor secreted from dopaminergic cells under magnetic stimulation. *Biosens. Bioelectron.* **2021**, *182*, 113179. [CrossRef] [PubMed]
133. Ko, J.; Ham, J.; Lee, H.; Lee, K.; Koh, W.-G. Integration of a fiber-based cell culture and biosensing system for monitoring of multiple protein markers secreted from stem cells. *Biosens. Bioelectron.* **2021**, *193*, 113531. [CrossRef] [PubMed]
134. Li, L.; Lu, Y.; Qian, Z.; Yang, Z.; Yang, K.; Zong, S.; Wang, Z.; Cui, Y. Ultra-sensitive surface enhanced Raman spectroscopy sensor for in-situ monitoring of dopamine release using zipper-like ortho-nanodimers. *Biosens. Bioelectron.* **2021**, *180*, 113100. [CrossRef] [PubMed]
135. Wang, F.; Banerjee, D.; Liu, Y.; Chen, X.; Liu, X. Upconversion nanoparticles in biological labeling, imaging, and therapy. *Analyst* **2010**, *135*, 1839–1854. [CrossRef]
136. Guller, A.E.; Generalova, A.N.; Petersen, E.V.; Nechaev, A.V.; Trusova, I.A.; Landyshev, N.N.; Nadort, A.; Grebenik, E.A.; Deyev, S.M.; Shekhter, A.B.; et al. Cytotoxicity and non-specific cellular uptake of bare and surface-modified upconversion nanoparticles in human skin cells. *Nano Res.* **2015**, *8*, 1546–1562. [CrossRef]

137. Wang, K.; Wu, Q.; Wang, X.; Liang, G.; Yang, A.; Li, J. Near-infrared control and real-time detection of osteogenic differentiation in mesenchymal stem cells by multifunctional upconversion nanoparticles. *Nanoscale* **2020**, *12*, 10106–10116. [CrossRef]
138. Yan, R.; Guo, Y.; Wang, X.; Liang, G.; Yang, A.; Li, J. Near-infrared light-controlled and real-time detection of osteogenic differentiation in mesenchymal stem cells by upconversion nanoparticles for osteoporosis therapy. *ACS Nano* **2022**, *16*, 8399–8418. [CrossRef]
139. Rabie, H.; Zhang, Y.; Pasquale, N.; Lagos, M.J.; Batson, P.E.; Lee, K. NIR biosensing of neurotransmitters in stem cell-derived neural interface using advanced core–shell upconversion nanoparticles. *Adv. Mater.* **2019**, *31*, e1806991. [CrossRef]
140. Andersson, H.; Baechi, T.; Hoechl, M.; Richter, C. Autofluorescence of living cells. *J. Microsc.* **1998**, *191 Pt 1*, 1–7. [CrossRef]
141. Zhao, J.; Lui, H.; McLean, D.I.; Zeng, H. Automated autofluorescence background subtraction algorithm for biomedical Raman spectroscopy. *Appl. Spectrosc.* **2007**, *61*, 1225–1232. [CrossRef]
142. Paras, C.; Keller, M.; White, L.; Phay, J.; Mahadevan-Jansen, A. Near-infrared autofluorescence for the detection of parathyroid glands. *J. Biomed. Opt.* **2011**, *16*, 067012. [CrossRef] [PubMed]
143. Qian, T.; Heaster, T.M.; Houghtaling, A.R.; Sun, K.; Samimi, K.; Skala, M.C. Label-free imaging for quality control of cardiomyocyte differentiation. *Nat. Commun.* **2021**, *12*, 4580. [CrossRef] [PubMed]
144. Suhito, I.R.; Han, Y.; Ryu, Y.-S.; Son, H.; Kim, T.-H. Autofluorescence-Raman Mapping Integration analysis for ultra-fast label-free monitoring of adipogenic differentiation of stem cells. *Biosens. Bioelectron.* **2021**, *178*, 113018. [CrossRef] [PubMed]
145. Li, J.; Reimers, A.; Dang, K.M.; Brunk, M.G.K.; Drewes, J.; Hirsch, U.M.; Willems, C.; Schmelzer, C.E.H.; Growth, T.; Nia, A.S.; et al. 3D printed neural tissues with in situ optical dopamine sensors. *Biosens. Bioelectron.* **2023**, *222*, 114942. [CrossRef] [PubMed]

biosensors

MDPI

Review

Progress in Fluorescence Biosensing and Food Safety towards Point-of-Detection (PoD) System

Saloni Kakkar [1,2,†], Payal Gupta [2,†], Navin Kumar [2,*] and Krishna Kant [3,*]

[1] Institute of Microbial Technology (IMTECH), Council of Scientific and Industrial Research (CSIR), Chandigarh 160036, India
[2] Department of Biotechnology, Graphic Era (Deemed to be University), Dehradun 248002, India
[3] Biomedical Research Center (CINBIO), University of Vigo, 36310 Vigo, Spain
* Correspondence: navinkumar.bt@geu.ac.in (N.K.); krishna.kant@uvigo.es (K.K.)
† These authors contributed equally to this work.

Abstract: The detection of pathogens in food substances is of crucial concern for public health and for the safety of the natural environment. Nanomaterials, with their high sensitivity and selectivity have an edge over conventional organic dyes in fluorescent-based detection methods. Advances in microfluidic technology in biosensors have taken place to meet the user criteria of sensitive, inexpensive, user-friendly, and quick detection. In this review, we have summarized the use of fluorescence-based nanomaterials and the latest research approaches towards integrated biosensors, including microsystems containing fluorescence-based detection, various model systems with nano materials, DNA probes, and antibodies. Paper-based lateral-flow test strips and microchips as well as the most-used trapping components are also reviewed, and the possibility of their performance in portable devices evaluated. We also present a current market-available portable system which was developed for food screening and highlight the future direction for the development of fluorescence-based systems for on-site detection and stratification of common foodborne pathogens.

Keywords: food pathogen; microfluidic; biosensing; fluorescence microscopy; PoC device

Citation: Kakkar, S.; Gupta, P.; Kumar, N.; Kant, K. Progress in Fluorescence Biosensing and Food Safety towards Point-of-Detection (PoD) System. *Biosensors* **2023**, *13*, 249. https://doi.org/10.3390/bios13020249

Received: 20 December 2022
Revised: 26 January 2023
Accepted: 6 February 2023
Published: 9 February 2023

1. Introduction

Food safety is an assurance for access to healthy and safe food for sustaining life and good health. To ensure food safety, food hygiene must be undertaken in order to preserve the nutritional value of food and protect it from microbial attack from production to consumption. This food safety must ensure the nutritional requirement of the public and, at the same time, it must not expose them to any foodborne illness. Currently, malnutrition and foodborne disease are the major food-related concerns in global population. To avoid foodborne disease, timely detection of pathogens in the food responsible for toxin production and disease is necessary. Food may contain microbes in the form of bacteria, fungus, protozoa, or viruses that are responsible for causing hundreds of diseases from mild through to severe. The United States reported an outbreak of foodborne infections, particularly bacterial infections associated with fresh farm produce in multiple states from 2010 to 2017 [1]. Likewise, a retrospective study was performed to mark the status of foodborne diseases (involving enteric bacteria) in South Africa, from 2013 to 2017 where the presence of *Salmonella* species, *Escherichia coli*, *Bacillus cereus*, *Listeria monocytogenes*, and *Clostridium perfringens* were reported in food samples [2].

Foodborne diseases are consequences of harmful toxins or other chemical substances produced by naturally occurring microbes in the food material which, upon entering the host body, lead to digestive-system dysfunction [3]. The escalation in foodborne diseases and associated mortality is a result of the prevalence of harmful pathogens in food due to the evolution in agricultural practices, food production and storage methods, under-cooked animal products, ready-to-eat mixes, and, most importantly, globalization of the food

trade [4]. In pursuance of safe food supply and reduced incidence of foodborne diseases, an early, quick, and accurate detection of pathogens in food items is required [5]. A number of conventional methods for detection of foodborne pathogens are available. These are based on culturing microbes on differential media, biochemical characterization, sequencing, and characterization through HPLC, MS, PCR, etc. [6]. However, these methods are expensive, time-consuming, and unwieldy, thus restricting their use in point-of-care (PoC) applications [7]. In the food industry, rapid detection of microbes, even at very low numbers in food samples (both raw and processed), is of utmost importance in order to ensure the food quality and safety [8,9]. With the advancement in point-of-care detection methods, researchers have been now able to offer ASSURED (affordable, sensitive, specific, user-friendly, rapid and robust, equipment-free, and deliverable) technologies to the users [10]. The signals in PoC applications are usually fluorescence-, colorimetric-, or electrochemical-based and are simple and easy to interpret/read [11]. Nevertheless, PoC applications have evolved greatly, with advancements still continuing to address challenges in translation of methods from laboratory- into industrial-application detection systems. Some of the key challenges which need attention are sensitivity, multiplexing, quantification, and multi-functionality.

Indeed, rapid and sensitive detection methods have evolved greatly, and are still evolving, making them highly sensitive, compact, and reusable with almost no detection time. In the present review, we have summarized the fluorescence biosensing basics of a variety of fluorescence-sensing methods. The review describes fluorescence biosensing materials stretching from nano to molecular to protein-based biomolecules. Further, the different materials used for integrating fluorescence-biosensing and fabrication-detection systems are also been described. The various sequential aspects and approaches of fluorescent-based biosensors are summarized under the schematic presentation in Figure 1. The figure is a detailed flow-chart for detection of food microbes/toxins/ions with the help of bioreceptors such as DNA/proteins generated against these food analytes conjugated with fluorescent active bioprobes viz. nanoparticles/graphene/quantum dots, etc. The fluorescent signal output thus generated can be in the form of FCS, FRET, or FILM; each of these components is discussed in the following sections of the review.

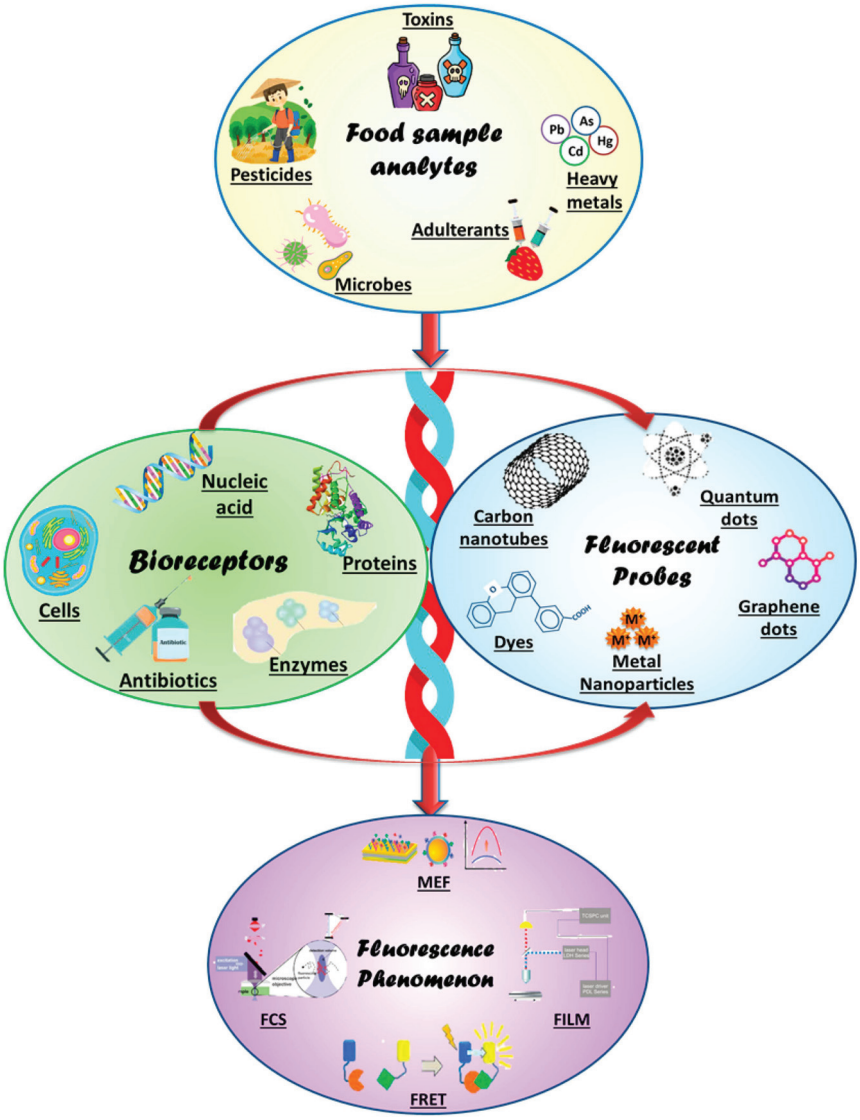

Figure 1. The schematic diagram presents the fundamental components for designing a fluorescence biosensing platform for food sensing. The food analytes (microbes, pesticides, adulterants, pollutants) are detected by using the specific bioreceptors (proteins, enzymes, cells, DNA) generated against various toxins/pesticides/adulterants, etc. These bioreceptors are coupled with bioprobes (nanoparticles, CNT, graphenes, quantum dots, etc.) that are fluorescently active to generate a fluorescent signal (MEF, FERT) response.

2. Fundamental Aspects of Fluorescence Biosensing

Among the variety of available sensing options, fluorescence biosensors are the most promising due to their high sensitivity and selectivity which extends their usefulness in biosensors for clinical and environmental monitoring. When a substance absorbs light of higher energy/shorter wavelength and emits low-wavelength light which is a very-short

lived (10^{-9} to 10^{-8} s), this light is called fluorescence [12]. Fluorescence-based detection in biosensors is beneficial for aspects such as sensitivity, signal detection limits, and accuracy.

Developments in nanotechnology have also revolutionized the field of fluorescence biosensing and improved the specificity and sensitivity of the analyte to nano-levels. An example of this is fluorescence-based detection using a cleavable hairpin beacon coupled with LAMP (loop-mediated isothermal amplification) to probe the presence of the *Borrelia burgdorferi* recA gene where the system showed a sensitivity of detecting nearly 100 copies of the gene in 25 min [13]. This sensitivity is many folds higher than that of traditional organic dyes and other fluorescent probes. Among the variety of nanomaterials, quantum dots and carbon nanotubes/carbon dots have gained special attention due to better compatibility, higher surface-to-volume ratio, better chemical and thermal stability, and faster detection. The carbon-nanoparticle-based fluorescence detection of ferrocyanide ion in food samples such as salted foods (radish, cucumber, cabbage) was achieved with a detection limit of as low as 3 ng/mL [14]. Another efficient and sensitive quantum dot (QD)-based fluorescent system to probe the presence of thiram in food samples was reported. The QD consisted of mesoporous silica loaded with a gold nanocluster with the LoD of 0.19 ng/mL [15]. All these features favor its application in point-of-detection (PoD) devices which have maximum demand in diagnostics where sensitivity, specificity, and user-friendly quick response are needed for analyte detection. To utilize these fluorescent labels in biosensing applications, the fluorescence measuring/sensing/estimating phenomenon also need to be understood, and this is elaborated in the following section.

3. Fluorescence Biosensing Materials

With the advancements in the field of nanobiotechnology, fluorescence-based detection methodologies have replaced conventional organic dyes with nanomaterials as detection labels due to their superior optical properties viz. a wide range of excitation and emission wavelengths and brighter fluorescence with better photostability [16]. Figure 2 summarizes a wide range of nanomaterials that are used for fluorescent based point-of-care biosensing of food analytes such as varied nanoparticles, graphene derivatives, metal organic frameworks, carbon-based nanomaterials, etc. Moreover, traditional fluorescence biosensors employing organic dyes do not offer low detection limits, hence compromising the sensitivity of the assay due to limited quantum yields and low receptor binding ratio of dyes. The potential biocompatibility of fluorescent nanomaterials owing to their physico-chemical properties enhances the performance of biosensors, delivering low-cost and portable point-of-care fluorescence sensing of food contamination. Additionally, these fluorescent nanomaterials will impart a solid support system for biosensing conjugated with multiple probes with high labeling ratio yielding high sensitivity [17]. Nanomaterials as fluorescent packets are advantageous in having tunable optical properties with greater quantum yield. Hence, considering the applications of fluorescent nanomaterials in food sensing, we will discuss the major advances and improvements of various nanomaterials that are currently being used for designing fluorescence biosensors. The applications of different nanomaterials and the enhancement of their limits of detection in the system are summarized in Table 1. A list of recent studies of metal nanomaterials and carbon-based nanomaterials along with some other nanomaterials is featured in the table with comparison between their limits of detection for analyzing a wide range of food analytes.

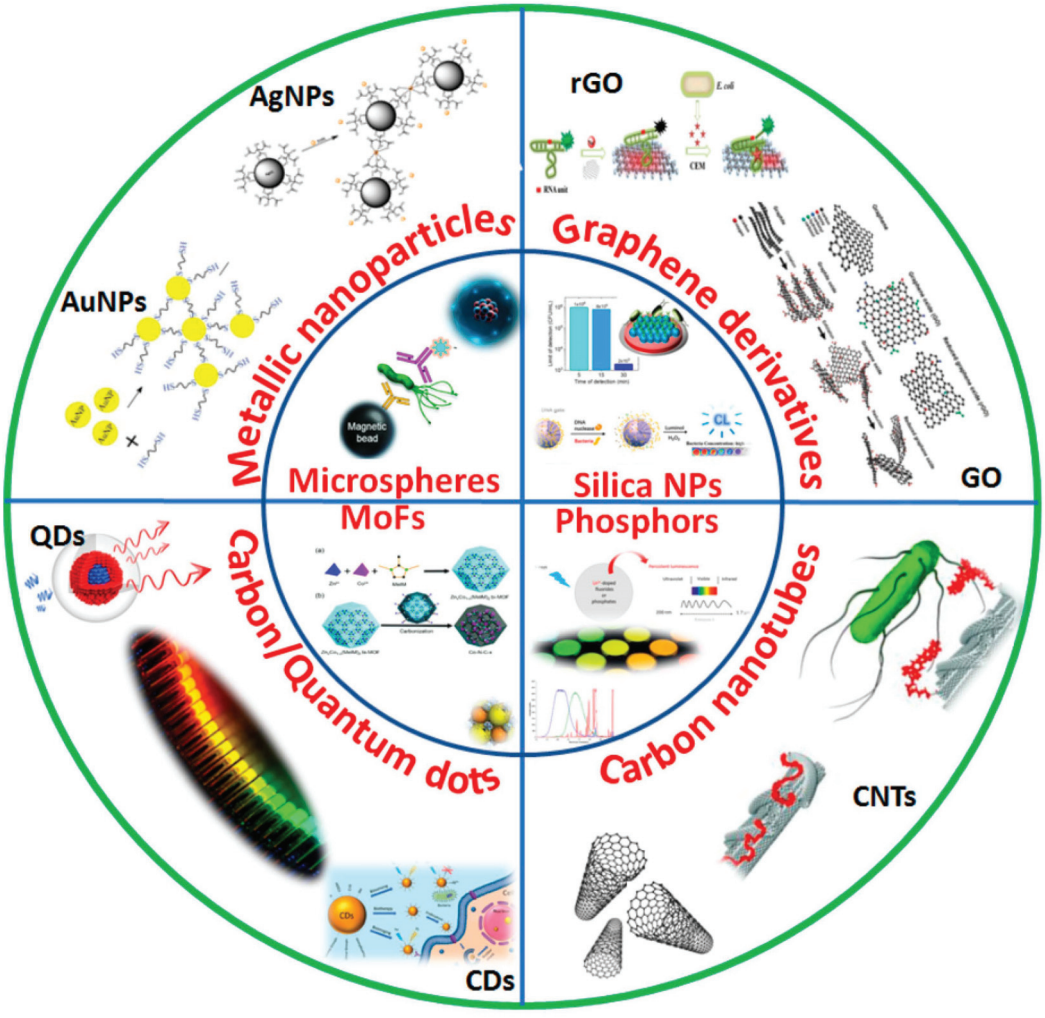

Figure 2. Variety of nanomaterials and their surface modifications used in biosensing of food toxins/pathogens like metallic nanoparticles such as AgNPs (Silver nanoparticles), AuNPs (Gold nanoparticles), carbon nanomaterials viz. QDs (Quantum Dots), GO/rGO (Graphene oxide), carbon nanotubes and other MoFs (Metal organic frameworks), Silica nanoparticles, Microspheres, Phosphors, etc. materials.

3.1. Nanomaterials

Metallic nanoparticles acquire quantum mechanical effects such as photoluminescence and the photobleaching resistance of gold nanoparticles encourages the development of in vivo fluorescence biosensors with less toxicity [17]. Gold nanoparticles are excellent FRET-quenchers due to their surface plasmon in visible range, which causes strong absorption and scattering with huge extinction coefficients [18]. A study has reported the gold-nanoparticle-based combined fluorometric and spectrophotometric biosensing of biogenic amines in poultry meat samples. The excitation and emission of histamine conjugated with gold nanoparticle was measured and showed 50 times enhanced fluorescence compared to histamine alone [19]. Silver nanoparticles are great substrates for metal-enhanced fluorescence (MEF) as they contribute towards enhanced fluorescence

signal intensity lowering the detection limit of bioassays. These particles are also known to be great acceptors in FRET, and they even promote the efficacy of the assays as FRET pair enhancers. A recent work published by Kato et al. demonstrated a one-pot method for stable coating of silver nanoparticles with a thiolated polymer to form polymeric shells that behaved as an excellent quencher. Great potential for increase in fluorescent plasmonics was observed along with efficient masking of fluorescence quenching with polymer-coated silver nanoparticles [20].

Carbon nanotubes (CNTs), which have a unique arrangement of sp2 hybridized carbon atoms that form a π-conjugated network, have been explored in depth in developing fluorescent biosensing assays. The ability of CNTs to quench the fluorescence of organic dyes or quantum dots in the NIR region is combined with photoluminescence properties through dynamic energy transfer [21]. Chen et al., reported on the development of an acetylcholine-based, cost-effective, and sensitive electrochemical sensor to detect pesticides in food samples. The assay used MWCNTs that increased surface area for effective electrochemical polymerization, yet maintained the enzymatic activity, exhibiting a stable response towards multiple real samples such as carbonated drinks, milk, orange juice, and beer [22].

Quantum dots (QDs), also known as semiconductor crystalline materials, are novel fluorescence materials with quantum confinement effect, good photostability, and effective biocompatibility, and they possess composition-based emission tunability [23]. With large Stokes shift and flexible fluorescence, their applications include biosensing, biomedicine, and optoelectronics [24]. QDs possess superior attributes of broader excitation with narrow emission spectra, longer time of fluorescence, and 100 times higher molar extinction coefficient than conventional organic dyes [25]. All these exceptional properties have led to the development of highly efficient and stable optical biosensing systems enabled via QD-based FRET systems. QDs directly enable the sensing phenomenon by enhancing or quenching via direct adsorption/chelation/interaction of specific conjugated bioreceptors or metal ions [26]. Many studies have reported the applicability of QDs and their conjugated derivatives in developing fluorescence-based platforms for pathogen sensing and food safety [27–29].

Graphene-based nanomaterials are graphene sheet, graphene oxide (GO), and a reduced form of graphene-oxide nanosheet (rGO). Graphene and its derivatives possess outstanding ability in quenching fluorescent dyes so they are used as potential energy acceptors in designing fluorescent sensors. They are often combined and conjugated with fluorophores such as QDs and UCNPs in the form of FRET pairs [30]. Various aspects of biomedical applications such as chemi-sensors, electrochemical sensors, and fluorescent biosensors serving either as quenchers or fluorophores have been explored [31]. A study reported a conjugated system of QD–aptamer–GO for detecting β-lactoglobulin in food samples [32]. Other nanomaterials, such as metal organic frameworks, up-conversion nanoparticles, silica nanoparticles, and phosphors, also contribute to the development of point-of-care fluorescent biosensing technologies for food safety. Various food analytes and the detection limit for these analytes are summarized in the Table 1. In conclusion, all these nanomaterials, with their advanced properties have resulted in the development of efficient fluorescent biosensors for food safety. Table 1 provides a comparative analysis of the bioreceptors employed for detection and their LoD. Although major nanomaterials exhibiting fluorescent properties have been discussed in this review, high-end nanohybrids incorporating conjugated nanomaterials, magnetic nanoparticles, and co-embedded manipulations that are easily fabricated have been reported to be upcoming substitutes. Moreover, depending upon the fluorescent phenomenon being used, such as quenching/masking or fluorescence enhancement involved in food sensing, the particular nanomaterial is selected for its respective application providing improved sensitivity compared to traditional dyes.

Table 1. List of food-analyte sensing by various types of nanomaterials (2018–2022).

Nanomaterial	Analyte	Biorecognition Element	LoD	Ref.
Metal Nanoparticles				
Gold nanoparticles	Salmonella typhimurium	DNA aptamer	36 CFU/mL	[33]
Gold nanoparticles	Dipicolinic acid	Eu^{3+} ion/gold nanocluster	0.8 μM	[34]
Gold nanoparticles	Histamine	Gold nanoparticles	2.04 nM	[35]
Silver nanoparticles	Melamine	Polyethyleneimine–silver nanobioprobe	132 nM	[36]
Silver nanoparticles	Staphylococcal enterotoxin A	DNA aptamer	0.3393 ng/mL	[37]
Silver nanoparticles	Fe^{+3} ions	Vitamin B12-functionalized biological silver nanoparticles (FAgNPs)	2 mg/L	[38]
Copper nanoparticles	Zearalenone	Antibodies	16.0 μg/kg	[39]
Platinum nanoparticles	Hypoxanthine	Platinum nanoparticles	2.88 μM	[40]
Tungsten nanoparticles	Maltose and sucrose	Fenugreek β-amylase functionalized tungsten disulfide nanoparticles	0.052 and 0.096 mM	[41]
Palladium nanoparticles	Tetracyclines	Graphene quantum dots/palladium nanoparticles	45 ng/mL	[42]
Carbon-based nanomaterials				
Carbon nanotubes	*Escherichia coli* O157:H7	Carbonyl iron powder/MWCNT-DNA aptamer	3.15×10^2 cfu/mL	[43]
Carbon nanotubes	Patulin mycotoxin	Carboxyfluorescein dye MWCNTs–DNA aptamer	0.13 μg/L	[44]
Carbon nanohorns	Fipronil	FAM–aptamer with oxidized single-walled carbon nanohorns	3 nM	[45]
Carbon dots	Tartrazine	Fluorescent carbon dots	12.4 nM	[46]
Carbon dots	Tetracyclines and Al^{3+}	Fluorescent carbon dots	0.057–0.23 μM and 0.091 μM	[47]
Carbon dots	Ascorbic acid	Carbon Dots/Fe^{3+} composite	3.11 μmol·L^{-1} μmol/L	[48]
Quantum dots	Acrylamide	DNA aptamer	2.41×10^{-8} M	[49]
Quantum dots	Histamine	Carbon quantum dots with peptide	13 μg/kg	[50]
Quantum dots	Biogenic amines	Carbon dots/yellow fluorescent CdTe quantum dots	1.259-5.428 μM	[51]
Graphene oxide	β-lactoglobulin	DNA aptamer	96.91 μg/L	[32]
Graphene quantum dots	Formaldehyde	Graphene quantum dots	0.0515 μg/mL	[52]
Graphene oxide	Zearalenone and ochratoxin A	Cy3 aptamer and Alexa Fluor 488 aptamer	1.797 ng/mL and 1.484 ng/mL	[53]
Other nanomaterials				
Silica nanoparticles	Thiram	Mesoporous silica with gold nanoparticles	0.19 ng/mL	[15]
Silica nanoparticles	Aflatoxin B_1	DNA aptamer	0.13 ng/mL	[54]
Up-conversion nanoparticles	Staphylococcus aureus	Aptamer-functionalized gold nanoparticles	10.7 CFU/mL	[55]
Up-conversion nanoparticles	Histamine	Up-conversion nanoparticles	7.34 mg/L	[56]
Metal organic frameworks (MOF)	Acrylamide	6-carboxyfluorescein-labeled aptamer (FAM-ssDNA)	1.9 nM	[57]
Metal organic frameworks	Tetracycline antibiotics	Luminescent MOF	0.28–0.30 μM	[58]
Metal organic frameworks	Ethanolamine	Zeolitic imidazolate framework-8/FAM-aptamer	17.86 pM	[59]
Phosphors	Zearalenone in cereals	Black phosphorus–gold nanocomposite	2 μg/kg	[60]

3.2. Nucleic-Acid-Based Molecular Markers

Fluorescent-based molecular markers such as DNA/mRNA covalently conjugated with fluorophore are used for sensing applications as they selectively bind to functional groups of target molecules [61]. Fluorescent DNA/RNA can also be generated by use of 2-aminopurine (for adenine) or isoxanthopterin (for guanine) nucleobase analogs and used as efficient molecular recognition elements (MREs) for developing target-detection systems [62]. Generally, fluorescent nucleic acids are classified based on their structures that begin with detecting SNP based on duplex formation. Another structural analysis of homoadenine and A-cluster systems demonstrated their applicability in three-way-junction (3WJ) probes for targeting miRNA. Moreover, G-quadruplexes with their G-rich sequences form fluorescent probes or detection of targets. Most important is the selectivity and specificity of a new group of fluorescent molecular beacon (MB) systems towards target sequence [63]. MBs are highly specific single-stranded DNA fluorescent probes that are dual modified at one end with fluorophore (F) and at the other end with a quencher (Q), leading to their applicability in detection systems [64]. An MB can acquire an open structural state where the quencher is away from the fluorophore, spatially restoring the fluorescence that generally happens in the presence of target and closed state where the fluorophore and quencher come into close proximity, diminishing the fluorescence. A recent study reported the detection of signature molecules of food-borne pathogens using the FRET mechanism of MBs, QDs, and nanoscale quenchers [65]. Moreover, MB-based multiplex real-time PCR studies have been reported for detection of various food pathogens [66–68]. Evolving from the inherent attribute of nucleic acid to form Watson–Crick duplex structures to detect complementary nucleic acid strands, there have been ground-breaking discoveries of generating affinity nucleic acids possessing specific binding properties [69]. Over the last decade, single-stranded DNA/RNA aptamers as a versatile class of bioreceptors, have been introduced. Their ease of synthesis and excellent biofunctionalization properties enable efficient fluorescent sensing [70,71]. The fluorophore is conjugated with an aptamer as a labeled/non-labeled moiety and target detection is determined by excitation-light interaction with the bioreceptor reflecting fluorescent intensity [72]. A recent study reported a signal-on fluorescent MB-aptamer-based sensor for rapid detection of mercury in food samples [73].

Comprehensively, as compared to the classical conventional bioreceptors for sensing applications, aptamers pave novel avenues for designing fluorescent detection strategies due to their exceptional properties that allow bioconjugation with a large variety of compounds. They offer high sensitivity for detection of target analytes enabling specific biorecognition abilities that promote potential sensing applications.

3.3. Antibodies

Fluorescent immunoassays generally use antibodies covalently linked with fluorochrome that absorbs light and emits at another wavelength as detection reagents. In point of fact, a few years ago, the novel concept of a fluorescent immunosensor, a Quenchbody, also known as a Q-body, was introduced by Ueda and colleagues. The key aspect of this technology comprises antibody-labeling of the N-terminal region/antigen-binding fragment (Fab) of an antibody with fluorescent dyes, delivering enhanced fluorescence when antibody–antigen interaction occurs [74,75]. Fluorescent dyes such as TAMARA, ATTO520, and rhodamine are conjugated with variable regions of antibodies via flexible linker peptides [76]. These fluorescent-labeled antibodies are utilized in designing lateral-flow test cards for sensing food contaminants. Alongside, smartphone integration with fluorescent detectors have been successfully used as efficient point-of-care systems for sensing pathogenic bacteria in food samples [7]. Huang et al., in 2017, reported a protein-sensing platform employing a combination of graphene-oxide sheets conjugated with antibodies that displayed quantitative quenching of fluorescent signals [77]. Another fluorescence-antibody-labeled sandwich immunoassay was reported using chitosan–cellulose nanocrystal membrane for rapid detection of *Listeria monocytogenes* in food samples [78]. Over the

recent years, the advancements in antibody-based detection techniques have increased due to immunological modifications, resulting in effective food-sensing applications.

3.4. Proteins/Enzymes

Several protein-based assays have employed studies of protein modification/interaction, kinase activity, time-bound fluorescent assays, detection of toxins/adulterants, identification of viral antigens/pathogens, etc. These have incorporated fluorescent dyes viz. Cy5, BEBO (cyanide dye), lanthanides (e.g., Eu^{3+}, Sm^{3+}, Tb^{3+} and Dy^{3+}), SYBR green, NanoOrange, and RiboGreen that have been utilized in fluorescent biomolecular assays such as bimolecular fluorescence complementation (BiFC), lanthanide fluorescent immunoassay, fluorescent-dye-based assay, chemifluorescent enzyme-linked immunosorbent assay (ELISA), real-time immuno-PCR, immuno-detection, and sandwich fluoroimmunoassay [79]. Green fluorescent protein (GFP) or yellow fluorescent protein (YFP) have quite often been used as reporter conjugates/markers in the detection of pathogens for food sensing, helping in enumerating/tracking of bacterial cells. For complex sample preparation, fluorescent proteins with their longer wavelengths avoid the limitation associated with fluorescent dyes. Along with GFP and YFP, R-phycoerythrin (PE) isolated from red algae is also used as stable fluorescent protein [80]. A study has reported a novel TurboGFP expression vector for labeling of Yersinia species *Y. enterocolitica* biovar 1A, biovar 2, biovar 4, and *Y. pseudotuberculosis.* After being transformed with the vector, these bacteria expressed fluorescence of bright green color that could be seen with the naked eye [81]. Similarly, a fiber-optic toxicity biosensor incorporating GFP label modification of *Escherichia coli* was designed for detection of hazardous heavy metals such as Cu(II), Cd(II), Pb(II), Zn(II), Cr(VI), Co(II), Ni(II), Ag(I), and Fe(III) and their toxicity in the samples [82]. Apart from proteins, certain enzyme-based sensors utilizing peroxidase (HRP), glucose oxidase, lactase, urease, alkaline phosphatase, etc., integrate fluorescent properties of coenzymes that absorb light or substrates for catalytic reactions play a crucial role in sensing of food, toxins, pathogens, etc. Enzymes, being different moieties than generalized bioreceptors, are not directly involved in detection of analytes but they amplify the signal by catalyzing certain reactions. Likewise the fact that they only need a substrates in order to work, but are not affected by the working medium/environment, makes them outstanding as potential substitutes for sensing and food-monitoring applications.

4. Integration of Fluorescence Biosensing for Microbe Detection

Over recent decades, development of fluorescence-based detection of pathogenic microbes has accelerated, with the development of direct and rapid point-of-care testing techniques that maintain proper safety assessments. Fluorescence biosensing has the well-established advantages of immediate response time, highly sensitive detection, easy labelling of fluorophore with functional groups, localized fluorescence signals that provides visible output using multicolor dyes, and multiplexed detection assays [83]. For decades culture-based methodology was the gold-standard. It offers low-cost, equipment-free, and easy-operational detection assays. However, its time constraint compromises rapid and on-site detection. Then, PCR (polymerase chain reaction) and LAMP (loop-mediated isothermal amplification) assays were developed, offering high sensitivity and rapid bacterial detection. However, several bottlenecks related to expensive instrumentation, false-positive results, and the need for trained manpower also restricted their applicability for point-of-care microbial detection systems. Moreover, immunological techniques, such as ELISA, that are increasingly recommended for pathogen detection due to their sensitive antigen–antibody interaction, also have shortcomings of cross-reactivity, longer durations for result processing, and complex sample processing [84]. Therefore, to avoid the limitations of the aforementioned methodologies, high-performance novel fluorescence-based biosensing techniques were introduced. These are sensitive up to an ultralow level microbial concentrations and satisfy the high demand for food safety. Here, we will focus upon

these fluorescence-based bioassays comprising microarray/biochip assays, microfluidics assays, paper-based hand-held devices, and lateral-flow devices.

4.1. Microarrays

Fluorescence-based microarrays comprise a microtiter plate, a glass slide onto which the sample protein is bound in an array, and fluorescently labelled probe molecules which are added to deliver chemiluminescence or a colorimetric signal readout. The fluorescence-labelled probe interacts with the immobilized protein samples releasing a fluorescent signal that is further scanned by laser for detection. The biochemical activity of protein-sensing is generally studied using three types of array—analytical, functional, and reverse-phase protein microarrays—that are consolidated for pathogen-sensing, ensuring food safety. Studies have shown that the bead/suspension array technique provides detection of bacterial/plant toxins, mycotoxins, and pesticides in food using microsphere beads conjugated with biomolecules such as DNA oligonucleotides/proteins labeled with fluorescent dye. The DNA microarray technique comprises immobilization of cDNA probes on a solid matrix onto which PCR-amplified fluorescent-labeled DNA molecules are hybridized. Their interaction generates a signal, allowing detection of known probes on the microarray. DNA-microarray-technology applications have been extended to a great extent for detection of food pathogens. Fluorophores that are generally incorporated for labeling of probes are Cyanine5/Alexa Fluor 647 (excitation at 650 nm/emission at 668 nm), Cyanine3/Alexa Fluor 555 (excitation/emission values at 550/568 nm), and bacterial-species-specific antibody-labeled and biotinylated DNA/RNA aptamers in combination with fluorescence-labeled streptavidin [85]. An in situ generated biochip was designed for detection of food pathogens present on freshly cut vegetables and fruits. Specific sequences of Vibrio *parahemolyticus*, *Escherichia coli* O157:H7, *Salmonella typhimurium*, *Staphylococcus aureus*, and *Listeria monocytogenes* were identified using tilling array probes in a hybridization array. The assay produced strong amplification signals with detection limit of 3log CFU/gm on freshly cut lettuce and cantaloupe in 24 h time detection [86]. Another work studying the amplification of foodborne-pathogen sensing on microarray comprised Cy5-dye-labeled double biotin DNA linkage and detection antibody as Cy5–Ab complex. Simultaneous detection of *Salmonella* and *E. coli* was achieved as visual screening followed by fluorescence-based quantification. A detection limit of 10^3 CFU/mL and 9 CFU/mL in buffer and real food was achieved via visual screening and quantification of fluorescence intensity [87].

4.2. Microfluidic Devices

Microfluidics technology is considered to be a multidisciplinary technique interlinking several aspects of science including biochemistry, fluid dynamics, material science, physics, engineering, nanotechnology, chemistry, microtechnology, and biotechnology. It has been introduced as a novel point-of-care testing device in biosensing, providing large surface-to-volume ratio and making it a portable technology [88]. Fluorescence-based detection on microfluidic chips comprises bioluminescence, laser-induced fluorescence, immunofluorescence technique, and chemiluminescence, and the unique combination of these biochips with fluorescence detectors efficiently promotes sensitive detection of food-borne pathogens [89].

The fabrication of microfluidic-based devices comprises manufacturing technologies using silicon, glass, polymer (polydimethylsiloxane:PDMS) and ceramic that employs a photolithography method integrating mass production by micro electro-mechanical systems (MEMS). Generally, there are three versions of microfluidics: (a) continuous-flow, (b) droplet-based, and (c) digital, and their fabrication employs wet-etching, molding, sanding, laser, and milling techniques. Microfluidic fluorescence sensors need to maintain excitation spectra slightly different to the emissions in order to obtain complex spatial arrangement in glass-based microfluidics, while polymer microsystems often use PDMS that incorporates molding, layer structuration, or 3D printing which is an inexpensive

method. Lastly, ceramic was primarily utilized in microelectronics due to its significant features of designing 3D structures in low-temperature cofired ceramic (LTCC) [90]. PDMS were also applied as the surface for capturing bacteria. A recent study presented a 3D PDMS sponge fabrication utilizing salt crystals as the scarifying mold and the inner surface of the PDMS sponge was functionalized by apolipoprotein-H (ApoH), as universal ligand to capture both Gram-positive (*L. monocytogenes*) and Gram-negative (*Salmonella* spp.) bacteria, in combination with a microfluidic bioreactor. The capture proficiency was found greater than 70% for both targeted pathogens with an LoD of 10^3 and 10^4 CFU/mL for *Salmonella* spp. and *L. monocytogenes*, respectively [91].

Microfluidic devices have facilitated lab-on-chip (LOC)-integrating micropores, mixers enhancing capture efficiency, micropillars, and microfilters as additional modules combining these analytical procedures onto the same chip. The miniaturization, portability, instant detection, automation, and high-throughput are key advantages offered by microfluidics that are widely applicative in sensitive detection of food pathogens and toxins [92]. Recently, many smartphone microfluidic platforms integrating immunomagnetic nanoparticles or urease enzyme or paper-based/impedance electrochemical measurements have been introduced, offering high-end food sensing with multiplexed and rapid detection of pathogens [93]. A study has reported QD fluorescent-probe-based readout integrated with manganese nanoflowers as QD nanocarriers for signal amplification to detect *Salmonella typhimurium*. The bacterial load was determined with a low detection limit of 43 CFU/mL in food samples such as chicken, depending on the fluorescent intensity of released QDs [94]. Another sensor introduced immunomagnetic separation with fluorescent-labeling and video-processing smartphone for detection of *Salmonella*. The immunomagnetic particles separated and concentrated *Salmonella* followed by labeling with immunofluorescent microspheres to form fluorescent bacteria. This fluorescent *Salmonella* was injected into a biochip integrated with a smartphone fluorescent microscopic system. A low detection limit of 58 CFU/mL *Salmonella* was obtained by online counting of fluorescent spots using a smartphone App. (as presented in Figure 3) [95]. Shin et al., recently proposed a lateral-flow assay for multiplexed detection of *E. coli*, *Salmonella typhimurium*, *Staphylococcus aureus*, and *Bacillus cereus* in contaminated lettuce samples (Figure 3c) [96].

Paper-based devices are facile and flexible analytical biosensors as they offer a wide range of advantages over microfluidic chips in being cost-effective, with easy fabrication, great biocompatibility and high capillary action [97]. Lateral-flow assays (LFAs) and microfluidic paper-based analytical devices (μPADs) are the most common type of paper-based devices. LFAs or dipsticks are known for their facile handling, and rapid and naked-eye-visible readout without any additional equipment. Their cost-effectiveness and versatility in assay formats and user-friendliness offer their wide applicability in point-of-care testing of food pathogens. LFAs simply comprise a sample pad where sample is added, a conjugate pad where the sample travels via capillary action activating the immobilized molecules, an absorbent pad, and a nitrocellulose membrane; all arranged on a plastic padding. The molecular components in the sample are separated as they travel across the membrane and produce a test line as positive-result output and a control line [98]. LFAs that are used for food-borne-pathogen detection incorporate monodispersed latex labels, gold colloid, and fluorescent/carbon tags for conjugate labeling. The colored particle, generally colloidal gold, binds to biomolecules (antigen/antibody/aptamer) immobilized onto test line that correlates with the amount of sample added [99,100]. Commercial LFA strips available in the market for bacterial sensing include *Listeria*-, *Salmonella*-, and *Escherichia coli* O157-Reveal test kits (Neogen®) Lansing, USA; *Listeria*, *Salmonella*- and *Escherichia coli*-VIP GOLD™ (BioControl Systems®) Bellevue, USA, and for *Listeria*, DuPont™ Lateral Flow System (DuPontQualicon) [4].

Paper-based μPADs generally utilize paper instead of chip microfluidics and are economical and efficient, removing the need for cleanroom facilities. Compared to silicon-based conventional biochips, paper-based chips are simple and highly porous, allowing physical absorption-generating devices that are easy to operate, modify and dispose of.

These μPADs perform liquid transport, reactions, and even reagent storage on the hydrophilic porous paper that promotes transfer of liquids in the device. In this way, the designed flow-channels obviate the requirement for an external pump for running the assay [98]. The major component of paper μPADs is cellulose. Being biocompatible and flexible, it somehow absorbs the reagents dried onto it and arranged this in a cartridge integrated to a fluid delivery system viz. a droplet dispenser. Only the template has to be added to the kit and the start button is pressed, triggering the fluid delivery into μPAD. The fabrication of paper pads is categorized as patterning of hydrophobic barriers onto paper such as wax/laser/inkjet printing and shaping techniques, for instance, paper cutting/laser etching [98]. A recent work has developed an aptasensor integrating microfluidics paper-based multiplexed detection of *E. coli* O157:H7 and *S. typhimurium* (as presented in Figure 4). This novel sensor comprises single-input detection of more than single whole-cell food pathogen providing a quantitative signal readout as image analysis with a low detection limit of 10^3 and 10^4 CFU/mL, respectively [101].

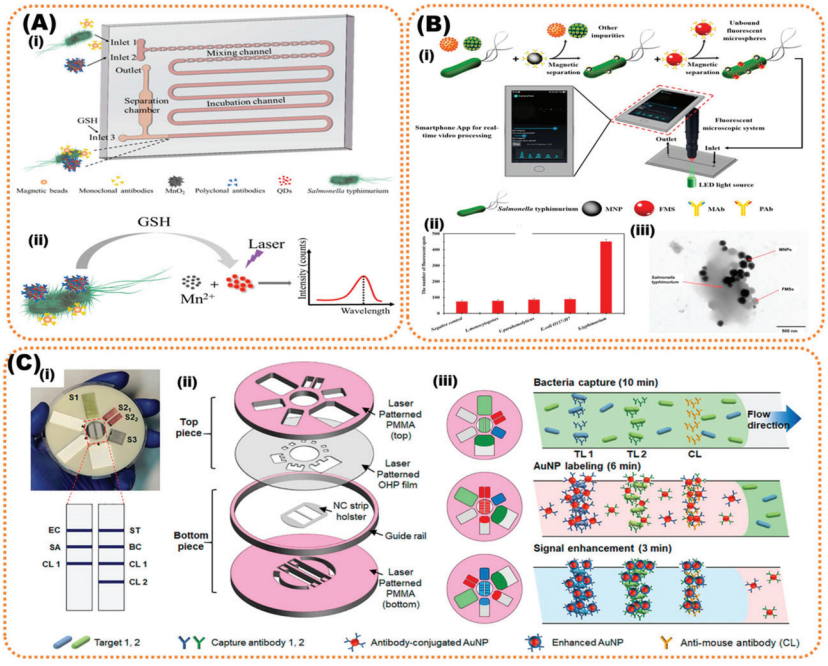

Figure 3. (**A**) PDMS microfluidic-platform-based study reports QD fluorescent-probe-based detection of *Salmonella typhimurium*. (**i**) Schematic presentation of microfluidic channel with inlet and outlet and presentation of the experimental process and (**ii**) the bacterial load was determined with LoD of 43 CFU/mL in food samples using the laser b. Copyright (2020), with permission from MDPI [94]. (**B**) Immunomagnetic separation with fluorescent-labeled sample and (**i**) video-processed using smartphone for detection of *Salmonella* with an LoD of 58 CFU/mL and (**ii**,**iii**) the efficiency of salmonella detection compared to other bacteria and bacterial-capturing mechanism with nanoparticle, respectively. Copyright (2019), with permission from Elsevier [95]. (**C**) Shin et al. presented a (**i**) CD-disk-type microfluidic system for lateral-flow assay, (**ii**) the assembly of lateral-flow assay, and (**iii**) multiplexed detection of *E. coli*, *Salmonella Typhimurium*, *Staphylococcus aureus*, and *Bacillus cereus* in contaminated lettuce samples. Copyright (2018), with permission from the American Chemical Society [96].

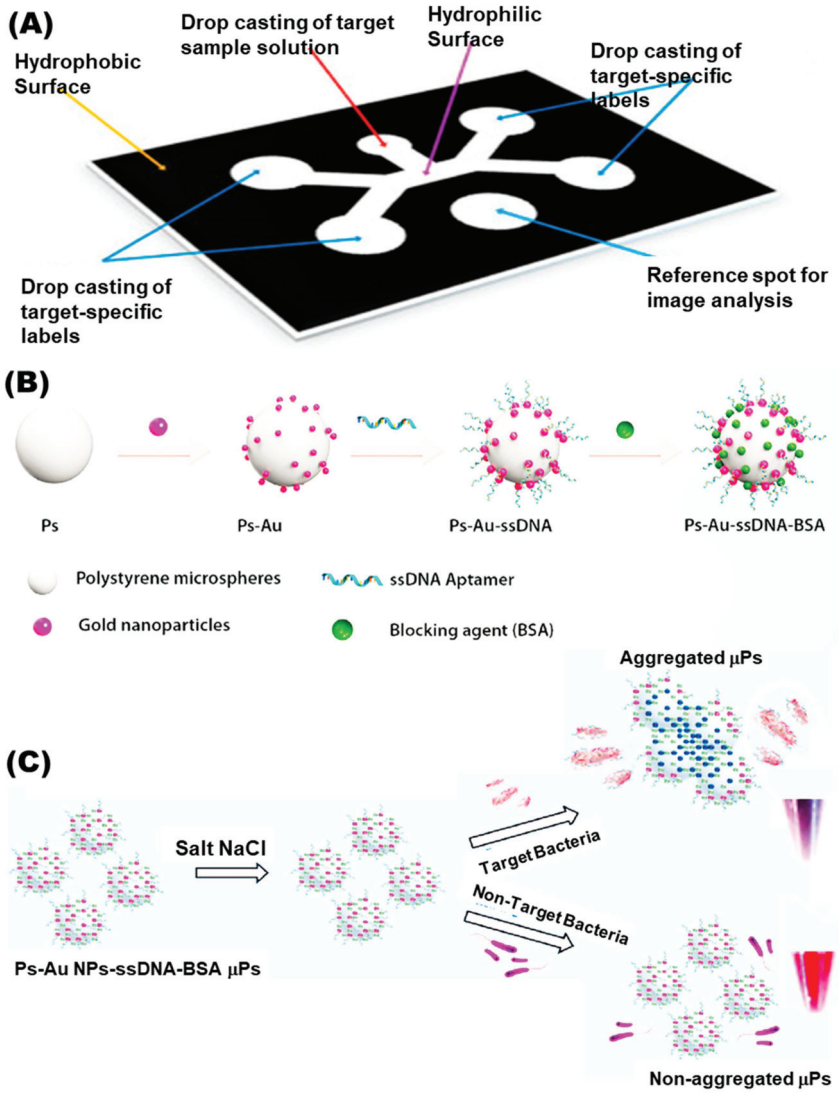

Figure 4. (**A**) Paper-based microfluidics assembly for multiplexed assay. (**B**) Nanoparticle surface modification and building with ssDNA and blocking BSA protein for detection of *E. coli* O157:H7 and *S. typhimurium*. (**C**) Sensor detecting whole-cell food pathogen with an LoD of 10^3 and 10^4 CFU/mL, respectively. Copyright (2022), with permission from Elsevier [101].

Finally, we can say that the traditional approaches, such as PCR-based techniques and fluorescence detection on the surface are time-consuming and require specialized instrumentation. The microfluidic-based biosensor has shown its potential in research into rapid and sensitive detection with a very high limit of detection. Above, we discussed some examples of microfluidic biosensors for the detection of food contaminants. As add-ons to microfluidic systems and in integration with these methods, nanomaterials have become attractive in attaining selectivity. Nanomaterial provides a large surface area for binding of recognition molecules and enhances the signal for fluorescence. The use of nanomaterials in these biosensors makes them easy to use and feasible for point-of-care

detection. In particular, the pros and cons of microfluidic-based biosensors include (i) high sensitivity in the analysis of small- and large-volume sample and (ii) high specificity and multiplexity to detect different analytes. In microfluidic systems, the challenges for food samples are is that some liquid samples are highly dense and cause blockage in the microfluidic device. Still, it is predicted that the future for microfluidic-based sensing of food samples is very promising.

5. Future Outlook

In this review, we have discussed the various research approaches, nanomaterials, and methodologies in fluorescent-based detection methods used for food safety. Traditionally, fluorescence-, and image-based biosensors are used to detect contamination in food and water. Food and water are very complex matrices, which not only include several diet elements (proteins, lipids, sugars, etc.), but also consist of parts such as additives. It is important to mention that fluorphores have the challenge of the aggregation-caused quenching (ACQ) effect, which restricts their function in sensing. The development of biosensors for food safety and their in-field application deal with issues pertaining to pre-treatment of complex samples such as the development of biosensors for food safety and their in-field application deal with issues pertaining to pre-treatment of complex food sample and maintain sensitivity. Moreover, a lower concentration of bacterial contamination in food samples is also challenging for target sensitivity and detection limits. Although microarrays are effective and accurate signal-producing technology, they require technical expertise and are expensive. Therefore, microfluidics or lab-on-chip devices hold great potential due to automation, miniaturization, and portability, and their ability to produce fast signal readout. However, certain limitations due to blockage of microfluidic channels or non-specific adsorption cause problems in complex sample analysis. In this context, signal-amplification methodologies, along with deep-learning strategies, can improve food-sensing fluorescent biosensing. Regardless of the performance of fluorescence- and image-based biosensors, they still have several challenges in real-world applications due to a high rate of false-negative or false-positive results and diet elements create autofluorescence and disrupt sensitivity and trigger false results. The nanomaterial-based fluorescent biosensors are able to address this problem. Although nano-biomaterials have benefits in operation, several parameters must be adjusted and need optimization. Extensive research, over several years, into sensing for food-safety purposes has shown that certain materials (e.g., graphene, metal nanoparticles) are usually preferred for fluorescence-sensing of food material. The advantage of using nanomaterials is the ability to achieve high signal intensity with selectivity. Nanomaterial-based biosensors have been successfully developed but suffer from constraints of stability, repeatability, and poor anti-interference ability. To overcome some major problems in fluorescence sensing, it is necessary to integrate and compare different methods to achieve optimum sensitivity. Chemometric, surface-enhanced Raman scattering (SERS), electrochemical sensing can also be used along with fluorescence for multiplexed sensing with high sensitivity. To date, fluorescent systems are in the experimental stage and practical functions of nanomaterial-based fluorescent biosensors in food matrices continue to remain under investigation. By implementing artificial intelligence and microfluidic systems for fluorescence biosensors we may achieve the goal of developing low-cost and real-time recognition of contaminants in food matrices. Recent research has shown the possibility of achieving sensitive and precise detection of food contaminants using the smartphone by enabling artificial intelligence for signal analysis without the requirement for sophisticated equipment. This development opens the door to a stand-alone, point-of-detection device for fluorescence-based detection, showing the possibility of detection of food contaminants outside the laboratory.

Author Contributions: Conceptualization, K.K. and N.K.; methodology, S.K.; resources, P.G.; data curation, P.G.; writing—original draft preparation, S.K. and P.G.; writing—review and editing, K.K. and N.K.; visualization, S.K. and K.K.; supervision, K.K. and N.K.; funding acquisition, K.K. All authors have read and agreed to the published version of the manuscript.

Funding: Krishna Kant acknowledges the European Union's Horizon 2020 research and innovation program under the Marie Sklodowska-Curie grant agreement no. (894227). Saloni Kakkar acknowledges the DST-INSPIRE fellowship for funding and CSIR-IMTECH for her carrying out PhD work. We also acknowledge University of Vigo, Spain and Graphic Era (Deemed to be University), Dehradun 248002, for providing facilities and computational resources.

Institutional Review Board Statement: Not applicable.

Informed Consent Statement: Not applicable.

Data Availability Statement: Not applicable.

Acknowledgments: We acknowledge University of Vigo, Spain, and Graphic Era (Deemed to be a University), Dehradun 248002, for providing facilities and computational resources.

Conflicts of Interest: The authors declare no conflict of interest.

References

1. Carstens, C.K.; Salazar, J.K.; Darkoh, C. Multistate Outbreaks of Foodborne Illness in the United States Associated with Fresh Produce from 2010 to 2017. *Front. Microbiol.* **2019**, *10*, 2667. [CrossRef]
2. Shonhiwa, A.M.; Ntshoe, G.; Essel, V.; Thomas, J.; McCarthy, K. A Review of Foodborne Diseases Outbreaks Reported to the Outbreak Response Unit, National Institute for Communicable Diseases, South Africa, 2013–2017. *Int. J. Infect. Dis.* **2019**, *79*, 73. [CrossRef]
3. Van der Fels-Klerx, H.J.; Van Asselt, E.D.; Raley, M.; Poulsen, M.; Korsgaard, H.; Bredsdorff, L.; Nauta, M.; D'agostino, M.; Coles, D.; Marvin, H.J.P. Critical Review of Methods for Risk Ranking of Food-Related Hazards, Based on Risks for Human Health. *Crit. Rev. Food Sci. Nutr.* **2018**, *58*, 178–193. [CrossRef]
4. Law, J.W.-F.; Ab Mutalib, N.-S.; Chan, K.-G.; Lee, L.-H. Rapid Methods for the Detection of Foodborne Bacterial Pathogens: Principles, Applications, Advantages and Limitations. *Front. Microbiol.* **2015**, *5*, 770. [CrossRef]
5. Campbell, V.R.; Carson, M.S.; Lao, A.; Maran, K.; Yang, E.J.; Kamei, D.T. Point-of-Need Diagnostics for Foodborne Pathogen Screening. *SLAS Technol.* **2021**, *26*, 55–79. [CrossRef]
6. Kant, K.; Ngo, T.A.; Matteucci, M.; Wolff, A. Fabrication of 3D Microstructure Array on Chip for Rapid Pathogen Detection. *Sensors Actuators B Chem.* **2019**, *281*, 774–782. [CrossRef]
7. Choi, J.R.; Yong, K.W.; Choi, J.Y.; Cowie, A.C. Emerging Point-of-Care Technologies for Food Safety Analysis. *Sensors* **2019**, *19*, 817. [CrossRef]
8. Vinayaka, A.C.; Ngo, T.A.; Kant, K.; Engelsmann, P.; Dave, V.P.; Shahbazi, M.-A.; Wolff, A.; Bang, D.D. Rapid Detection of Salmonella Enterica in Food Samples by a Novel Approach with Combination of Sample Concentration and Direct PCR. *Biosens. Bioelectron.* **2019**, *129*, 224–230. [CrossRef]
9. Mandal, P.K.; Biswas, A.K.; Choi, K.; Pal, U.K. Methods for Rapid Detection of Foodborne Pathogens: An Overview. *Am. J. Food Technol.* **2011**, *6*, 87–102. [CrossRef]
10. Valderrama, W.B.; Dudley, E.G.; Doores, S.; Cutter, C.N. Commercially Available Rapid Methods for Detection of Selected Food-Borne Pathogens. *Crit. Rev. Food Sci. Nutr.* **2016**, *56*, 1519–1531.
11. Choi, J.R.; Yong, K.W.; Tang, R.; Gong, Y.; Wen, T.; Li, F.; Pingguan-Murphy, B.; Bai, D.; Xu, F. Advances and Challenges of Fully Integrated Paper-Based Point-of-Care Nucleic Acid Testing. *TrAC Trends Anal. Chem.* **2017**, *93*, 37–50. [CrossRef]
12. Lakowicz, J.R. Fluorescence Sensing. In *Principles of Fluorescence Spectroscopy*; Springer: Berlin/Heidelberg, Germany, 1999; pp. 531–572.
13. Ding, X.; Yin, K.; Li, Z.; Pandian, V.; Smyth, J.A.; Helal, Z.; Liu, C. Cleavable Hairpin Beacon-Enhanced Fluorescence Detection of Nucleic Acid Isothermal Amplification and Smartphone-Based Readout. *Sci. Rep.* **2020**, *10*, 18819. [CrossRef] [PubMed]
14. Hu, Q.; Pan, Y.; Gong, X.; Rao, S.; Xiao, L.; Liu, L.; Yang, Z. A Sensitivity Enhanced Fluorescence Method for the Detection of Ferrocyanide Ions in Foodstuffs Using Carbon Nanoparticles as Sensing Agents. *Food Chem.* **2020**, *308*, 125590. [CrossRef] [PubMed]
15. Ren, H.X.; Qian, Z.J.; Li, M.; Peng, C.F.; Wang, Z.P.; Wei, X.L.; Xu, J.G. Mesoporous Silica-Loaded Gold Nanocluster with Enhanced Fluorescence and Ratiometric Fluorescent Detection of Thiram in Foods. *Mikrochim. Acta* **2021**, *188*, 363. [CrossRef]
16. Zhang, Y.; Tang, H.; Chen, W.; Zhang, J. Nanomaterials Used in Fluorescence Polarization Based Biosensors. *Int. J. Mol. Sci.* **2022**, *23*, 8625. [CrossRef]
17. Zhong, W. Nanomaterials in Fluorescence-Based Biosensing. *Anal. Bioanal. Chem.* **2009**, *394*, 47–59. [CrossRef]
18. Sapsford, K.E.; Berti, L.; Medintz, I.L. Materials for Fluorescence Resonance Energy Transfer Analysis: Beyond Traditional Donor–Acceptor Combinations. *Angew. Chemie Int. Ed.* **2006**, *45*, 4562–4589. [CrossRef]
19. El-Nour, K.M.A.; Salam, E.T.A.; Soliman, H.M.; Orabi, A.S. Gold Nanoparticles as a Direct and Rapid Sensor for Sensitive Analytical Detection of Biogenic Amines. *Nanoscale Res. Lett.* **2017**, *12*, 231. [CrossRef]
20. Kato, R.; Uesugi, M.; Komatsu, Y.; Okamoto, F.; Tanaka, T.; Kitawaki, F.; Yano, T.A. Highly Stable Polymer Coating on Silver Nanoparticles for Efficient Plasmonic Enhancement of Fluorescence. *ACS Omega* **2022**, *7*, 4286–4292. [CrossRef]

21. Cui, D.; Pan, B.; Zhang, H.; Gao, F.; Wu, R.; Wang, J.; He, R.; Asahi, T. Self-Assembly of Quantum Dots and Carbon Nanotubes for Ultrasensitive DNA and Antigen Detection. *Anal. Chem.* **2008**, *80*, 7996–8001. [CrossRef]
22. Chen, H.; Zuo, X.; Su, S.; Tang, Z.; Wu, A.; Song, S.; Zhang, D.; Fan, C. An Electrochemical Sensor for Pesticide Assays Based on Carbon Nanotube-Enhanced Acetycholinesterase Activity. *Analyst* **2008**, *133*, 1182–1186. [CrossRef]
23. Alivisatos, P. The Use of Nanocrystals in Biological Detection. *Nat. Biotechnol.* **2003**, *22*, 47–52. [CrossRef]
24. Reshma, V.G.; Mohanan, P.'V. Quantum Dots: Applications and Safety Consequences. *J. Lumin.* **2019**, *205*, 287–298. [CrossRef]
25. Li, J.; Zhu, J.J. Quantum Dots for Fluorescent Biosensing and Bio-Imaging Applications. *Analyst* **2013**, *138*, 2506–2515. [CrossRef]
26. Cardoso Dos Santos, M.; Algar, W.R.; Medintz, I.L.; Hildebrandt, N. Quantum Dots for Förster Resonance Energy Transfer (FRET). *TrAC—Trends Anal. Chem.* **2020**, *125*, 115819. [CrossRef]
27. Xiong, J.; Zhang, H.; Qin, L.; Zhang, S.; Cao, J.; Jiang, H. Magnetic Fluorescent Quantum Dots Nanocomposites in Food Contaminants Analysis: Current Challenges and Opportunities. *Int. J. Mol. Sci.* **2022**, *23*, 4088. [CrossRef]
28. Mohamadi, E.; Moghaddasi, M.; Farahbakhsh, A.; Kazemi, A. A Quantum-Dot-Based Fluoroassay for Detection of Food-Borne Pathogens. *J. Photochem. Photobiol. B Biol.* **2017**, *174*, 291–297. [CrossRef]
29. Sun, F.; Zhang, J.; Yang, Q.; Wu, W. Quantum Dot Biosensor Combined with Antibody and Aptamer for Tracing Food-Borne Pathogens. *Food Qual. Saf.* **2021**, *5*, fyab019. [CrossRef]
30. Yin, P.T.; Shah, S.; Chhowalla, M.; Lee, K.B. Design, Synthesis, and Characterization of Graphene-Nanoparticle Hybrid Materials for Bioapplications. *Chem. Rev.* **2015**, *115*, 2483–2531. [CrossRef]
31. Zheng, P.; Wu, N. Fluorescence and Sensing Applications of Graphene Oxide and Graphene Quantum Dots: A Review. *Chem. Asian J.* **2017**, *12*, 2343. [CrossRef]
32. Yang, J.; Zhang, Y.; Lu, Y. A Fluorescence Detection Method for the Determination of β-Lactoglobulin in Foods. *Anal. Methods* **2022**, *14*, 1872–1879. [CrossRef] [PubMed]
33. Chen, M.; Pan, L.; Tu, K. A Fluorescence Biosensor for Salmonella Typhimurium Detection in Food Based on the Nano-Self-Assembly of Alendronic Acid Modified Upconversion and Gold Nanoparticles. *Anal. Methods* **2021**, *13*, 2415–2423. [CrossRef] [PubMed]
34. Li, X.; Luo, J.; Jiang, X.; Yang, M.; Rasooly, A. Gold Nanocluster-Europium(III) Ratiometric Fluorescence Assay for Dipicolinic Acid. *Mikrochim. Acta* **2021**, *188*, 26. [CrossRef] [PubMed]
35. Bi, J.; Tian, C.; Zhang, G.L.; Hao, H.; Hou, H.M. Detection of Histamine Based on Gold Nanoparticles with Dual Sensor System of Colorimetric and Fluorescence. *Foods* **2020**, *9*, 316. [CrossRef]
36. Li, Z.; Li, Y.; Li, L.; Wang, T. Aquamarine Blue Emitting Silver Nanoparticles as Fluorescent Sensor for Melamine Detection. *Spectrochim. Acta Part A Mol. Biomol. Spectrosc.* **2019**, *217*, 51–59. [CrossRef]
37. Zhang, X.; Khan, I.M.; Ji, H.; Wang, Z.; Tian, H.; Cao, W.; Mi, W. A Label-Free Fluorescent Aptasensor for Detection of Staphylococcal Enterotoxin A Based on Aptamer-Functionalized Silver Nanoclusters. *Polymers* **2020**, *12*, 152. [CrossRef]
38. Harke, S.S.; Patil, R.V.; Dar, M.A.; Pandit, S.R.; Pawar, K.D. Functionalization of Biogenic Silver Nanoparticles with Vitamin B12 for the Detection of Iron in Food Samples. *Food Chem. Adv.* **2022**, *1*, 100017. [CrossRef]
39. Xuan, Z.; Wu, Y.; Liu, H.; Li, L.; Ye, J.; Wang, S. Copper Oxide Nanoparticle-Based Immunosensor for Zearalenone Analysis by Combining Automated Sample Pre-Processing and High-Throughput Terminal Detection. *Sensors* **2021**, *21*, 6538. [CrossRef]
40. Chen, J.; Lu, Y.; Yan, F.; Wu, Y.; Huang, D.; Weng, Z. A Fluorescent Biosensor Based on Catalytic Activity of Platinum Nanoparticles for Freshness Evaluation of Aquatic Products. *Food Chem.* **2020**, *310*, 125922. [CrossRef]
41. Agrawal, D.C.; Yadav, A.; Singh, V.K.; Srivastava, A.; Kayastha, A.M. Immobilization of Fenugreek β-Amylase onto Functionalized Tungsten Disulfide Nanoparticles Using Response Surface Methodology: Its Characterization and Interaction with Maltose and Sucrose. *Colloids Surf. B Biointerfaces* **2020**, *185*, 110600. [CrossRef]
42. Ahmed, S.R.; Kumar, S.; Ortega, G.A.; Srinivasan, S.; Rajabzadeh, A.R. Target Specific Aptamer-Induced Self-Assembly of Fluorescent Graphene Quantum Dots on Palladium Nanoparticles for Sensitive Detection of Tetracycline in Raw Milk. *Food Chem.* **2021**, *346*, 128893. [CrossRef]
43. Yang, T.; Yang, X.; Guo, X.; Fu, S.; Zheng, J.; Chen, S.; Qin, X.; Wang, Z.; Zhang, D.; Man, C.; et al. A Novel Fluorometric Aptasensor Based on Carbon Nanocomposite for Sensitive Detection of *Escherichia coli* O157:H7 in Milk. *J. Dairy Sci.* **2020**, *103*, 7879–7889. [CrossRef]
44. Khan, R.; Sherazi, T.A.; Catanante, G.; Rasheed, S.; Marty, J.L.; Hayat, A. Switchable Fluorescence Sensor toward PAT via CA-MWCNTs Quenched Aptamer-Tagged Carboxyfluorescein. *Food Chem.* **2020**, *312*, 126048. [CrossRef]
45. Zhang, J.; Feng, T.; Zhang, J.; Liang, N.; Zhao, L. Fluorescence Assay for the Sensitive Detection of Fipronil Based on an "on–off" Oxidized SWCNH/Aptamer Sensor. *Anal. Methods* **2021**, *13*, 3282–3291. [CrossRef]
46. Liu, L.; Sun, H.; Xiao, L.; Yang, Z.-q.; Han, J.; Gong, X.; Hu, Q. Development of a Highly Sensitive Fluorescence Method for Tartrazine Determination in Food Matrices Based on Carbon Dots. *Anal. Bioanal. Chem.* **2021**, *413*, 1485–1492. [CrossRef]
47. Jia, J.; Lu, W.; Cui, S.; Dong, C.; Shuang, S. Preparation of Yellow-Emitting Carbon Dots and Their Bifunctional Detection of Tetracyclines and Al3+ in Food and Living Cells. *Mikrochim. Acta* **2021**, *188*, 418. [CrossRef]
48. Wang, T.; Luo, H.; Jing, X.; Yang, J.; Huo, M.; Wang, Y. Synthesis of Fluorescent Carbon Dots and Their Application in Ascorbic Acid Detection. *Molecules* **2021**, *26*, 1246. [CrossRef]
49. Wei, Q.; Zhang, P.; Liu, T.; Pu, H.; Sun, D.W. A Fluorescence Biosensor Based on Single-Stranded DNA and Carbon Quantum Dots for Acrylamide Detection. *Food Chem.* **2021**, *356*, 129668. [CrossRef]

50. Shi, R.; Feng, S.; Park, C.Y.; Park, K.Y.; Song, J.; Park, J.P.; Chun, H.S.; Park, T.J. Fluorescence Detection of Histamine Based on Specific Binding Bioreceptors and Carbon Quantum Dots. *Biosens. Bioelectron.* **2020**, *167*, 112519. [CrossRef]
51. Yan, J.; Fu, Q.; Zhang, S.; Liu, Y.; Shi, X.; Hou, J.; Duan, J.; Ai, S. A Sensitive Ratiometric Fluorescent Sensor Based on Carbon Dots and CdTe Quantum Dots for Visual Detection of Biogenic Amines in Food Samples. *Spectrochim. Acta Part A Mol. Biomol. Spectrosc.* **2022**, *282*, 121706. [CrossRef]
52. Zhang, Y.; Qi, J.; Li, M.; Gao, D.; Xing, C. Fluorescence Probe Based on Graphene Quantum Dots for Selective, Sensitive and Visualized Detection of Formaldehyde in Food. *Sustainability* **2021**, *13*, 5273. [CrossRef]
53. Wang, Q.; Yang, Q.; Wu, W. Graphene-Based Steganographic Aptasensor for Information Computing and Monitoring Toxins of Biofilm in Food. *Front. Microbiol.* **2020**, *10*, 3139. [CrossRef] [PubMed]
54. Tan, H.; Ma, L.; Guo, T.; Zhou, H.; Chen, L.; Zhang, Y.; Dai, H.; Yu, Y. A Novel Fluorescence Aptasensor Based on Mesoporous Silica Nanoparticles for Selective and Sensitive Detection of Aflatoxin B1. *Anal. Chim. Acta* **2019**, *1068*, 87–95. [CrossRef] [PubMed]
55. Ouyang, Q.; Yang, Y.; Ali, S.; Wang, L.; Li, H.; Chen, Q. Upconversion Nanoparticles-Based FRET System for Sensitive Detection of Staphylococcus Aureus. *Spectrochim. Acta Part A Mol. Biomol. Spectrosc.* **2021**, *255*, 119734. [CrossRef] [PubMed]
56. Cao, Y.; Wang, X.; Feng, T.; Li, Z.; Xue, C.; Xu, J. Ratiometric Fluorescent Nanosystem Based on Upconversion Nanoparticles for Histamine Determination in Seafood. *Food Chem.* **2022**, *390*, 133194. [CrossRef]
57. Gan, Z.; Zhang, W.; Arslan, M.; Hu, X.; Zhang, X.; Li, Z.; Shi, J.; Zou, X. Ratiometric Fluorescent Metal-Organic Framework Biosensor for Ultrasensitive Detection of Acrylamide. *J. Agric. Food Chem.* **2022**, *70*, 10065–10074. [CrossRef]
58. Liu, Q.; Ning, D.; Li, W.J.; Du, X.M.; Wang, Q.; Li, Y.; Ruan, W.J. Metal-Organic Framework-Based Fluorescent Sensing of Tetracycline-Type Antibiotics Applicable to Environmental and Food Analysis. *Analyst* **2019**, *144*, 1916–1922. [CrossRef]
59. Khoshbin, Z.; Zamanian, J.; Davoodian, N.; Mohammad Danesh, N.; Ramezani, M.; Alibolandi, M.; Abnous, K.; Mohammad Taghdisi, S. A Simple and Ultrasensitive Metal-Organic Framework-Based Aptasensor for Fluorescence Detection of Ethanolamine. *Spectrochim. Acta. A. Mol. Biomol. Spectrosc.* **2022**, *267*, 120488. [CrossRef]
60. Li, S.; Zhang, F.; Wang, J.; Wen, W.; Wang, S. Black Phosphorus-Au Nanocomposite-Based Fluorescence Immunochromatographic Sensor for High-Sensitive Detection of Zearalenone in Cereals. *Nanophotonics* **2020**, *9*, 2397–2406. [CrossRef]
61. He, Y.; Li, Y. Fluorescent Markers. In *Encyclopedia of Systems Biology*; Springer: New York, NY, USA, 2013; pp. 746–748. [CrossRef]
62. Nutiu, R.; Billen, L.P.; Li, Y. Fluorescence-Signaling Nucleic Acid-Based Sensors. In *Nucleic Acid Switches and Sensors*; Springer: Boston, MA, USA, 2006; pp. 49–72. [CrossRef]
63. Podder, A.; Lee, H.J.; Kim, B.H. Fluorescent Nucleic Acid Systems for Biosensors. *Bull. Chem. Soc. Jpn.* **2020**, *94*, 1010–1035. [CrossRef]
64. Tyagi, S.; Kramer, F.R. Molecular Beacons: Probes That Fluoresce upon Hybridization. *Nat. Biotechnol.* **1996**, *14*, 303–308. [CrossRef]
65. Burris, K.P.; Wu, T.C.; Vasudev, M.; Stroscio, M.A.; Millwood, R.J.; Stewart, C.N. Mega-Nano Detection of Foodborne Pathogens and Transgenes Using Molecular Beacon and Semiconductor Quantum Dot Technologies. *IEEE Trans. Nanobiosci.* **2013**, *12*, 233–238. [CrossRef]
66. Vidic, J.; Vizzini, P.; Manzano, M.; Kavanaugh, D.; Ramarao, N.; Zivkovic, M.; Radonic, V.; Knezevic, N.; Giouroudi, I.; Gadjanski, I. Point-of-Need DNA Testing for Detection of Foodborne Pathogenic Bacteria. *Sensors* **2019**, *19*, 1100. [CrossRef]
67. Hadjinicolaou, A.V.; Demetriou, V.L.; Emmanuel, M.A.; Kakoyiannis, C.K.; Kostrikis, L.G. Molecular Beacon-Based Real-Time PCR Detection of Primary Isolates of Salmonella Typhimurium and Salmonella Enteritidis in Environmental and Clinical Samples. *BMC Microbiol.* **2009**, *9*, 97. [CrossRef]
68. Hu, Q.; Lyu, D.Y.; Shi, X.; Jiang, Y.; Lin, Y.; Li, Y.; Qiu, Y.; He, L.; Zhang, R.; Li, Q. A Modified Molecular Beacons-Based Multiplex Real-Time PCR Assay for Simultaneous Detection of Eight Foodborne Pathogens in a Single Reaction and Its Application. *Foodborne Pathog. Dis.* **2014**, *11*, 207–214. [CrossRef]
69. Su, X.; Xiao, X.; Zhang, C.; Zhao, M. Nucleic Acid Fluorescent Probes for Biological Sensing. *Appl. Spectrosc.* **2012**, *66*, 1249–1261. [CrossRef]
70. Ellington, A.D.; Szostak, J.W. In Vitro Selection of RNA Molecules That Bind Specific Ligands. *Nature* **1990**, *346*, 818–822. [CrossRef]
71. Tuerk, C.; Gold, L. Systematic Evolution of Ligands by Exponential Enrichment: RNA Ligands to Bacteriophage T4 DNA Polymerase. *Science* **1990**, *249*, 505–510. [CrossRef]
72. Hong, L.; Pan, M.; Xie, X.; Liu, K.; Yang, J.; Wang, S.; Wang, S. Aptamer-Based Fluorescent Biosensor for the Rapid and Sensitive Detection of Allergens in Food Matrices. *Foods* **2021**, *10*, 2598. [CrossRef]
73. Wang, L.; Chi, E.Z.; Zhao, X.H.; Zhang, Q. A Simple and Rapid "Signal On" Fluorescent Sensor for Detecting Mercury (II) Based on the Molecular Beacon Aptamer. *Foods* **2022**, *11*, 1847. [CrossRef]
74. Abe, R.; Ohashi, H.; Iijima, I.; Ihara, M.; Takagi, H.; Hohsaka, T.; Ueda, H. "quenchbodies": Quench-Based Antibody Probes That Show Antigen-Dependent Fluorescence. *J. Am. Chem. Soc.* **2011**, *133*, 17386–17394. [CrossRef] [PubMed]
75. Ueda, H.; Dong, J. From Fluorescence Polarization to Quenchbody: Recent Progress in Fluorescent Reagentless Biosensors Based on Antibody and Other Binding Proteins. *Biochim. Biophys. Acta Proteins Proteom.* **2014**, *1844*, 1951–1959. [CrossRef] [PubMed]
76. Dong, J.; Ueda, H. Recent Advances in Quenchbody, a Fluorescent Immunosensor. *Sensors* **2021**, *21*, 1223. [CrossRef] [PubMed]
77. Huang, A.; Li, W.; Shi, S.; Yao, T. Quantitative Fluorescence Quenching on Antibody-Conjugated Graphene Oxide as a Platform for Protein Sensing. *Sci. Rep.* **2017**, *7*, 40772. [CrossRef] [PubMed]

78. Capo, A.; D'Auria, S.; Lacroix, M. A Fluorescence Immunoassay for a Rapid Detection of Listeria Monocytogenes on Working Surfaces. *Sci. Rep.* **2020**, *10*, 21729. [CrossRef]
79. Nishi, K.; Isobe, S.I.; Zhu, Y.; Kiyama, R. Fluorescence-Based Bioassays for the Detection and Evaluation of Food Materials. *Sensors* **2015**, *15*, 25831. [CrossRef]
80. Wu, J.; Lu, Y.; Ren, N.; Jia, M.; Wang, R.; Zhang, J. DNAzyme-Functionalized R-Phycoerythrin as a Cost-Effective and Environment-Friendly Fluorescent Biosensor for Aqueous Pb^{2+} Detection. *Sensors* **2019**, *19*, 2732. [CrossRef]
81. Gensberger, E.T.; Kostić, T. Green Fluorescent Protein Labeling of Food Pathogens Yersinia Enterocolitica and Yersinia Pseudotuberculosis. *J. Microbiol. Methods* **2017**, *132*, 21–26. [CrossRef]
82. Futra, D.; Heng, L.Y.; Ahmad, A.; Surif, S.; Ling, T.L. An Optical Biosensor from Green Fluorescent *Escherichia coli* for the Evaluation of Single and Combined Heavy Metal Toxicities. *Sensors* **2015**, *15*, 12668–12681. [CrossRef]
83. Li, B.; Yu, Q.; Duan, Y. Fluorescent Labels in Biosensors for Pathogen Detection. *Crit. Rev. Biotechnol.* **2015**, *35*, 82–93. [CrossRef]
84. Huang, F.; Zhang, Y.; Lin, J.; Liu, Y. Biosensors Coupled with Signal Amplification Technology for the Detection of Pathogenic Bacteria: A Review. *Biosensors* **2021**, *11*, 190. [CrossRef] [PubMed]
85. Poltronieri, P.; Mezzolla, V.; Primiceri, E.; Maruccio, G. Biosensors for the Detection of Food Pathogens. *Foods* **2014**, *3*, 511. [CrossRef] [PubMed]
86. Sarengaowa; Hu, W.; Feng, K.; Jiang, A.; Xiu, Z.; Lao, Y.; Li, Y.; Long, Y. An in Situ-Synthesized Gene Chip for the Detection of Food-Borne Pathogens on Fresh-Cut Cantaloupe and Lettuce. *Front. Microbiol.* **2020**, *10*, 3089. [CrossRef] [PubMed]
87. Hormsombut, T.; Rijiravanich, P.; Surareungchai, W.; Kalasin, S. Highly Sensitive and Selective Antibody Microarrays Based on a Cy5-Antibody Complexes Coupling ES-Biochip for E. Coli and Salmonella Detection. *RSC Adv.* **2022**, *12*, 24760–24768. [CrossRef] [PubMed]
88. Luka, G.; Ahmadi, A.; Najjaran, H.; Alocilja, E.; Derosa, M.; Wolthers, K.; Malki, A.; Aziz, H.; Althani, A.; Hoorfar, M. Microfluidics Integrated Biosensors: A Leading Technology towards Lab-on-a-Chip and Sensing Applications. *Sensors* **2015**, *15*, 30011–30031. [CrossRef]
89. Bahavarnia, F.; Hasanzadeh, M.; Sadighbayan, D.; Seidi, F. Recent Progress and Challenges on the Microfluidic Assay of Pathogenic Bacteria Using Biosensor Technology. *Biomimetics* **2022**, *7*, 175. [CrossRef]
90. Nawrot, W.; Drzozga, K.; Baluta, S.; Cabaj, J.; Malecha, K. A Fluorescent Biosensors for Detection Vital Body Fluids' Agents. *Sensors* **2018**, *18*, 2357. [CrossRef]
91. Azinheiro, S.; Kant, K.; Shahbazi, M.A.; Garrido-Maestu, A.; Prado, M.; Dieguez, L. A Smart Microfluidic Platform for Rapid Multiplexed Detection of Foodborne Pathogens. *Food Control* **2020**, *114*, 107242. [CrossRef]
92. Kant, K.; Shahbazi, M.A.; Dave, V.P.; Ngo, T.A.; Chidambara, V.A.; Than, L.Q.; Bang, D.D.; Wolff, A. Microfluidic Devices for Sample Preparation and Rapid Detection of Foodborne Pathogens. *Biotechnol. Adv.* **2018**, *36*, 1003–1024. [CrossRef]
93. Mi, F.; Hu, C.; Wang, Y.; Wang, L.; Peng, F.; Geng, P.F.; Guan, M. Recent Advancements in Microfluidic Chip Biosensor Detection of Foodborne Pathogenic Bacteria: A Review. *Anal. Bioanal. Chem.* **2022**, *414*, 2883–2902. [CrossRef]
94. Hao, L.; Xue, L.; Huang, F.; Cai, G.; Qi, W.; Zhang, M.; Han, Q.; Wang, Z.; Lin, J. A Microfluidic Biosensor Based on Magnetic Nanoparticle Separation, Quantum Dots Labeling and MnO_2 Nanoflower Amplification for Rapid and Sensitive Detection of Salmonella Typhimurium. *Micromachines* **2020**, *11*, 281. [CrossRef]
95. Wang, S.; Zheng, L.; Cai, G.; Liu, N.; Liao, M.; Li, Y.; Zhang, X.; Lin, J. A Microfluidic Biosensor for Online and Sensitive Detection of Salmonella Typhimurium Using Fluorescence Labeling and Smartphone Video Processing. *Biosens. Bioelectron.* **2019**, *140*, 111333. [CrossRef]
96. Shin, J.H.; Hong, J.; Go, H.; Park, J.; Kong, M.; Ryu, S.; Kim, K.P.; Roh, E.; Park, J.K. Multiplexed Detection of Foodborne Pathogens from Contaminated Lettuces Using a Handheld Multistep Lateral Flow Assay Device. *J. Agric. Food Chem.* **2018**, *66*, 290–297. [CrossRef]
97. Fu, L.M.; Wang, Y.N. Detection Methods and Applications of Microfluidic Paper-Based Analytical Devices. *TrAC Trends Anal. Chem.* **2018**, *107*, 196–211. [CrossRef]
98. Wang, J.; Davidson, J.L.; Kaur, S.; Dextre, A.A.; Ranjbaran, M.; Kamel, M.S.; Athalye, S.M.; Verma, M.S. Paper-Based Biosensors for the Detection of Nucleic Acids from Pathogens. *Biosensors* **2022**, *12*, 1094. [CrossRef]
99. Ngom, B.; Guo, Y.; Wang, X.; Bi, D. Development and Application of Lateral Flow Test Strip Technology for Detection of Infectious Agents and Chemical Contaminants: A Review. *Anal. Bioanal. Chem.* **2010**, *397*, 1113–1135. [CrossRef]
100. Zhao, X.; Lin, C.W.; Wang, J.; Oh, D.H. Advances in Rapid Detection Methods for Foodborne Pathogens. *J. Microbiol. Biotechnol.* **2014**, *24*, 297–312. [CrossRef]
101. Somvanshi, S.B.; Ulloa, A.M.; Zhao, M.; Liang, Q.; Barui, A.K.; Lucas, A.; Jadhav, K.M.; Allebach, J.P.; Stanciu, L.A. Microfluidic Paper-Based Aptasensor Devices for Multiplexed Detection of Pathogenic Bacteria. *Biosens. Bioelectron.* **2022**, *207*, 114214. [CrossRef]

biosensors

MDPI

Review

Recent Advancements in Electrochemical Biosensors for Monitoring the Water Quality

Yun Hui [1], Zhaoling Huang [2], Md Eshrat E. Alahi [1,*], Anindya Nag [3,4], Shilun Feng [5,*] and Subhas Chandra Mukhopadhyay [6]

[1] Shenzhen Institute of Advanced Technology, Chinese Academy of Sciences, Shenzhen 518055, China; yun.hui@siat.ac.cn
[2] School of Mechanical and Electrical Engineering, Guilin University of Electronic Technology, Guilin 541004, China; zhaoling_huang@guet.edu.cn
[3] Faculty of Electrical and Computer Engineering, Technische Universität Dresden, 01062 Dresden, Germany; anindya.nag@tu-dresden.de
[4] Centre for Tactile Internet with Human-in-the-Loop (CeTI), Technische Universität Dresden, 01069 Dresden, Germany
[5] State Key Laboratory of Transducer Technology, Shanghai Institute of Microsystem and Information Technology, Chinese Academy of Sciences, Shanghai 200050, China
[6] The School of Science and Engineering, Macquarie University, Sydney 2109, Australia; subhas.mukhopadhyay@mq.edu.au
* Correspondence: md-eshrat-e-alahi.alahi1@hdr.mq.edu.au (M.E.E.A.); shilun.feng@mail.sim.ac.cn (S.F.)

Abstract: The release of chemicals and microorganisms from various sources, such as industry, agriculture, animal farming, wastewater treatment plants, and flooding, into water systems have caused water pollution in several parts of our world, endangering aquatic ecosystems and individual health. World Health Organization (WHO) has introduced strict standards for the maximum concentration limits for nutrients and chemicals in drinking water, surface water, and groundwater. It is crucial to have rapid, sensitive, and reliable analytical detection systems to monitor the pollution level regularly and meet the standard limit. Electrochemical biosensors are advantageous analytical devices or tools that convert a bio-signal by biorecognition elements into a significant electrical response. Thanks to the micro/nano fabrication techniques, electrochemical biosensors for sensitive, continuous, and real-time detection have attracted increasing attention among researchers and users worldwide. These devices take advantage of easy operation, portability, and rapid response. They can also be miniaturized, have a long-life span and a quick response time, and possess high sensitivity and selectivity and can be considered as portable biosensing assays. They are of special importance due to their great advantages such as affordability, simplicity, portability, and ability to detect at on-site. This review paper is concerned with the basic concepts of electrochemical biosensors and their applications in various water quality monitoring, such as inorganic chemicals, nutrients, microorganisms' pollution, and organic pollutants, especially for developing real-time/online detection systems. The basic concepts of electrochemical biosensors, different surface modification techniques, bio-recognition elements (BRE), detection methods, and specific real-time water quality monitoring applications are reviewed thoroughly in this article.

Keywords: biosensors; electrochemical detection; water quality monitoring; bio-recognition element; in-situ monitoring; surface modification

Citation: Hui, Y.; Huang, Z.; Alahi, M.E.E.; Nag, A.; Feng, S.; Mukhopadhyay, S.C. Recent Advancements in Electrochemical Biosensors for Monitoring the Water Quality. *Biosensors* **2022**, *12*, 551. https://doi.org/10.3390/bios12070551

Received: 26 June 2022
Accepted: 13 July 2022
Published: 21 July 2022

1. Introduction

Water is an essential part of all the living beings on earth, but in recent times, anthropogenic activities have increased immensely, which are the major causes of water pollution, disturbing the marine biodiversity and leading to a tremendous water shortage [1–3]. Even though the chemicals and water nutrients are crucial to our day-to-day lives, the excessive

amount threatens humans, aquatic life, and animals. The pollution of water and habitat degradation are the causes of the escalating water shortage and the reasons for the deterioration in marine biodiversity. Although freshwater accessibility has deteriorated over the past decades, water demand has risen, particularly in warm areas with minimal rainfall. Recently, 71% of the world's inhabitants, equal to 4.3 billion, were dealing with water shortages for several months [4]. Although water demand sharply increased, massive water pollution increased water scarcity and declining water quality in the past decades.

The characteristics of water pollution are comprised of their physical presence, chemical parameters, and richness of microorganisms. The concentration and composition of ingredients in water differ extensively. They can be categorized into four distinct classifications, such as (i) inorganic chemicals, (ii) nutrients, (iii) microorganisms' pollution, and (iv) organic pollutants. They can bring about harmful ecological consequences, for example, the interference of internal secretion and hormone systems, stimulation of genotoxicity and cytotoxicity, and hazardous effects [5]. The strength of ingredients in water is essential for selecting, designing, and operational treatment processes and recycling waste. The variable quantity of contaminants in effluent over time also increases the attention to emerging technologies for monitoring the water and applying reasonably priced and real-time approaches [6]. This review is mainly focused on monitoring heavy metals, nutrients, organic pollutants, biochemical oxygen demand, and microorganisms. Heavy metals in soil and water are considered environmental contaminants with elevated toxicity, easy accretion, and complicated degradation [7]. Nutrients bring about water eutrophication. Organic pollutants, particularly persistent organic pollutants (POPs), have harshly harmful impacts on human health and the environment with their complex degradation and potential bioaccumulation [8]. The biochemical oxygen demand (BOD) is the essential supervisory index to measure organic water contamination and demonstrate water quality [9,10]. Water quality monitoring is critical and closely related to our life and production.

Conventional analytical techniques or laboratory-based procedures, such as gas chromatography (GC), high-performance liquid chromatography (HPLC), atomic absorption spectroscopy (AAS), atomic fluorescence spectrometry (AFS), and inductively coupled plasma mass spectrometry (ICP-MS), are sensitive, precise, and consistent. They are regularly used to measure water parameters with the help of trained operators. However, they are involved with bulky and costly instrumentation, take much time for sample preparation, and are unsuitable for in situ measurements, especially requiring trained operators' help and transporting the water samples to laboratories for assessment [11–13]. Additionally, they cannot asses the accumulative toxicity or nutrient value of multiple chemicals or pollutants in a sample, which is a crucial objective of water quality monitoring applications [14]. Many property indicators are regularly used to determine the different qualities of water for settling or recycling. Many of them are laboratory-based techniques, which require complex pretreatment, and consequently, the methods are sluggish and expensive [1,15]. These characteristics encourage developing new technologies that are more low-cost, portable, sensitive, and efficient in the on-site real-time detection of multicontaminants containing a wide variety of materials [16,17]. The significant challenges of developing a portable biosensing device are inadequate sensitivity and poor selectivity during the on-site detection. The significant level of noises can come on chemical components level from the sampling field and ambient environments can be variable due to the harsh environments or diurnal variations. These are the major obstacles where the researchers are putting lot of attentions on how to avoid these for generating a reliable and portable biosensing output signal. The portable biosensing method is successfully utilized for other applications, such as pesticide residues in fruits and vegetables [18], POC Detection for biomedical application [19], chemical and biological pollutants in water [20].

In recent years, the advancement of electrochemical biosensors for detecting environmental pollutants has received considerable attention [21–25]. Biosensors have many advantages over the conventional lab-based method, including low costs, portability, fast response time, less usage of reagents, and the capability to continuous monitor the complex

wastewater [26–28]. Such sensors significantly benefit from sensing the minimum level in polluted water, such as wastewater. Biosensors are also compact and miniaturized devices that facilitate the advancement of portable sensing systems to monitor on-site effluents [29]. Bearing in mind the wide range of bio-recognition elements (including enzymatic, immunochemical, non-enzymatic receptor, whole-cell and DNA elements, and molecularly imprinted polymer (MIP)), the various types of biosensors can be classified as (i) electrochemical [30], (iii) piezoelectric [31], (ii) optical [32], and (iv) thermal biosensors [33] based on their working principles and transducing mechanisms [34], but the current review paper will cover the topics which are related to electrochemical biosensing. An electrochemical biosensor is based on the interactions between the immobilized bio-recognition element on its surface with binding molecules (the analyte of interest) and generating the changes in electrochemical properties, further translating into a meaningful electrical signal. The electrochemical methods offer rapid detection, fabrication, excellent sensitivity, and low cost.

Moreover, by operating at a wide range of potential, it is possible to simultaneously determine multiple analytes with different electrochemical potentials. Electrochemical biosensors' efficiency in monitoring water pollutants' presence relied on bio-recognition elements, transducers, and immobilization techniques, which offer us the classification criterion. In comparison with optical methods, electrochemical transduction has advantages for analyzing turbid samples because it is non-sensitive to light. For optical sensing, they are likely to be interference from environmental effects, costly, and susceptible to physical damage.

This review provides an overview of recent progress in developing electrochemical biosensors for water quality detection, focusing on the last decade. Some older publications are cited to support and build up the critical concepts of electrochemical biosensors. We expect this critical review will help those working in ecological toxicant analysis in water, some scientists who might be unaware of electroanalytical chemistry and biosensors.

2. Electrochemical Biosensors

Electrochemistry is essential for achieving the biosensing process in various biomarker analyses. Thus, electrochemical biosensing has attracted widespread attention in various applications due to its considerable advantages. Electrochemical biosensors react with the analyte of interest or molecules to produce an electrical signal proportionate to the analyte concentration. A conventional electrochemical biosensor comprises a reference electrode and a sensing electrode (working electrode) separated by an electrolyte. In most applications, the electrochemical biosensors consist of a three-electrode system with the reference electrode connected to a potentiostat, and the circuit can be completed by adding a counter electrode for flowing the current. These sensing devices are inexpensive, low-cost electrochemical cells that can be produced, portable, and easy to use, and can be operated with reduced power consumption. It requires electronic components for detecting the target analytes, unlike optical sensors. The following sections describe a range of elements and techniques of the electrochemical biosensor for biosensing applications.

3. Surface Modification Technique

Surface chemistry plays a considerable role in electrochemical biosensors to link the biological recognition element (BRE) on top of the sensing surface and prevent the substrate electrode from nonspecific interactions. In addition, the functionalization of the surface is conducive to noise control and sensitivity enhancement. BRE used in electrochemical sensors mainly consists of enzymes, antibodies, DNA/RNA, aptamers, and whole cells [22], which define a biosensor's sensitivity and selectivity. Immobilization techniques, such as adsorption, encapsulation in polymers or gel, chemical crosslinking, self-assembled monolayer, covalent linking, affinity, and electrodeposition, have been widely investigated for detecting various analysts in complex water samples. The surface modification of BRE on the electrodes usually involves one or more strategies.

3.1. Adsorption

Adsorption is a straightforward method of modifying the surface of the electrode to a specific recognition element in an entirely arbitrary way. Every biological recognition element needs to achieve the best conditions. Most proteins usually achieve the best surface coverage on uncharged surfaces under the neutral pH and functional ionic strength, using a specific 5−20 μg/mL concentration [35]. Yang et al. [36] have developed an impedimetric-based immunosensor by the adsorption method of anti-*E. coli* antibodies against the integrated microelectrode arrays for detecting the *E. coli* O157:H7. Surface modification of the surface receptor proteins G and A can be produced by many bacterial strains that can promote receptor binding. Each protein, such as A and G, can certainly be capable of binding 4 and 2 molecules of IgG. An analogous method utilizes or takes advantage of the strong binding of the glycoprotein avidin for biotin-functionalizing the receptors due to the intense alienation of the avidin/biotin complex. The detection level of *E. coli* was 1.3×10^{-15} M, which was as low as 10−100 CFU mL^{-1} in concentration. It may be identified on the avidin-modified developed electrodes using biotinylated anti-*E. coli* as the targeted recognition ligand.

3.2. Self-Assembled Monolayers (SAMs)

Self-Assembled Monolayers (SAMs) are chemisorbed and ordered with various layers formed by the natural arrangement of thiolated molecules on the location of metallic interfaces. The most extensively used methods consist of SAMs with n-alkanethiols on noble metals [37], SAMs with carboxylate on the oxide surfaces [38], and SAMs with silane on the glass/silicon surfaces [39]. Xia et al., immersed the sidewall of the silica core into AuNSM colloid, forming a self-assembled AuNSM monolayer for sensitive wavelength-modulated localized surface plasmon resonance (LSPR) for detecting the mercury (II) [40]. The label-free sensor obtained a very low LOD of 0.7 nM owing to the near field coupling improvement by the proximity distance of two types of gold nanoparticles-DNA conjugates.

3.3. Covalent Attachment

Covalent attachment is another approach for the covalent coupling to the ligand recognitions to electrochemical biosensor's interfaces, and improvements from the arrays of protein help form the most favorable conditions. A commonly used crosslinking molecule is carboxylic acid (C(=O) OH) groups on the electrode's surface as the biorecognition element with amine functional groups for exploiting the amide bond formation using the techniques of EDC/NHS chemistry. Likewise, this coupling approach has been effectively applied in various three-dimensional supports, such as agarose, aldehyde−agarose, and carboxymethylated dextran-based modified electrodes [41]. Carbon-based materials that reduce graphene oxide and carbon nanotubes can be adjusted with carboxylic acid through $\pi-\pi$ stacking interaction. Furthermore, some researchers have lately proposed integrating covalent functional groups using diazonium chemistry [42].

3.4. Electrodeposition

The electrochemical deposition was crucial in preparing nanomaterials reliably and cost-effectively with mild physicochemical conditions. Furthermore, noble metals, mixed metal oxides, carbon materials, or conducting polymers can be deposited on the electrode with high deposition speed, straightforward scale-up techniques and commercial feasibility with standard maintenance. This method helps form the hybrid films with the controlled thickness and morphology, modifying the process parameters, controlling the bath conditions (solvent, pH, temperature), and effectively regulating the electrolyte formula [43]. For example, new properties immediately stand out when poly(3,4-ethylenedioxythiophene) associates with one or more components deposited as films [44]. Table 1 shows the various characteristics of the surface modification techniques for the BRE in electrochemical biosensors.

Table 1. Surface modification techniques of BRE in electrochemical biosensors.

Surface Modification Technique	Immobilization Site	Spatial Orientation	Accessibility	Advantage	Disadvantage	Ref.
Adsorption	random	random	low	simple and direct	low immobilization efficiency	[45,46]
Encapsulation in polymers or gel	random	random	low	abundant BRE	necessary surface treatment and low immobilization efficiency	[47]
Chemical crosslinking	random	random	low	simple and high stability	the strict control of conditions and nonspecific interaction	[48]
Self-assembled monolayers	active terminal	orientation	high	simple and controllable BRE density	possible nonspecific interaction	[49]
Covalent linking	terminal activation	orientation	high	high stability	necessary surface treatment and low immobilization efficiency	[50]
Affinity	biotinylated terminal	orientation	high	simple and high stability	necessary surface treatment and possible nonspecific interaction	[51]
Electrodeposition	random	random	high	Reliable, cost-effective, and easy fabrication and maintenance	possible nonspecific interaction	[52]

4. Biorecognition Elements

Biorecognition elements (Figure 1) are the most critical part of the electrochemical biosensor, shouldering specific pollutants' specific recognition in a complex matrix. The effective immobilization of biorecognition elements, including enzymes, antibodies, DNA/RNA, aptamers, and whole cells, facilitates their binding to a noticeably broad range of the target species or analyte of interest. As is shown in Table 2, different kinds of recognition elements were summarized, as well as the analytes, electrodes, type of transducers, and the response of various electrochemical biosensors. Apart from conserving the functionality of the bio-recognition elements, e.g., specific enzymatic activities, it is critical to ensure the biomaterials' accessibility to target analytes. The vicinity between the biomaterials and the solid or metallic electrode surface is also preferred for achieving a fast and effective electron transfer. Several techniques have been suggested, including physical (e.g., electrostatic adsorption), chemical (e.g., self-assembled monolayers, covalent bonding, avidin-biotin binding, hybridization), and electrochemical (e.g., electrochemical adsorption) methods, but the optimal configuration for the biorecognition elements depends on the biomaterial and the modified electrode materials and interface. Besides the immobilization strategies, nonspecific adsorptions that mostly lead to high baseline signals and delayed responses should also be considered. Generally, various highly hydrophilic composites, for instance, poly (ethylene glycol) (PEG) and bovine serum albumin (BSA) and can be considered as additional elements for eliminating the nonspecific binding sites at the electrode and solution interface.

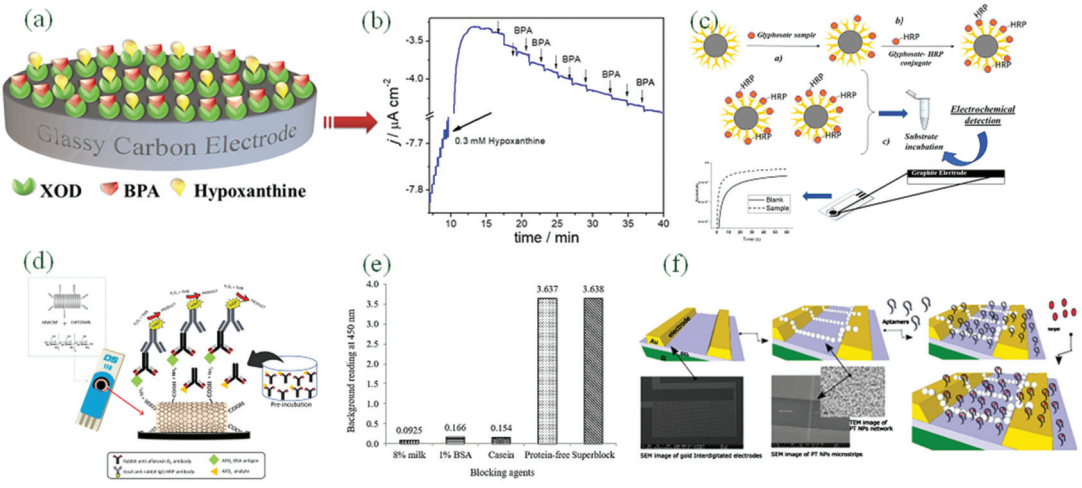

Figure 1. (**a**,**b**) Amperometric response of B.P.A. at XOD/GCE in the presence of 0.3 mM hypoxanthine (Reproduced with the permission from [53]); (**c**) Schematic of magnetic beads (MBs) for the analyte and its capturing technique on the electrode surface (Reproduced with the permission from [54]); (**d**) The complete schematic diagram of the nanomaterial-based immunosensor based on ELISA indirect competitive format (Reproduced with the permission from [55]); (**e**) Effect of various blocking agents on background reading by eight percent skimmed milk, one percent BSA, casein, protein-free, and superblock (Reproduced with the permission from [56]); (**f**) Schematic representation, SEM and EIS responses of the fabricated aptasensor (Reproduced with the permission from [57]).

4.1. Enzyme-Based Bio-Recognition Materials

Enzym electrodes have been widely studied for the superior catalytic activity of inclusiveness of the enzymes and are commercially accessible. Regarding the electrochemical detection of water pollutants with enzymes, in some cases, they are converted to indirect detection of corresponding substrates by inhibiting enzyme activity. The biotransformation

of various compounds can catalyze these enzymes through oxidation–reduction reactions (REDOX). The amperometric biosensors' electrical responses of Oxidase/Peroxidase have electrical responses to a specific substrate that can be measured either by two different methods, such as direct or indirect methods [58]. Enzymes can be immobilized by physical adhesion or entrapped by the process of electrochemical techniques. According to the Michaelis–Menten equation, the enzymatic sensor's detection limit depends on the enzyme's activity. Thus, accommodating proper conditions (desirable temperature and buffer pH, etc.) for the development of the biosensor throughout the experiment is significant.

Ayenimo et al., rapidly developed a reliable, sensitive amperometric glucose biosensor to rapidly determine Hg^{2+}, Cu^{2+}, Pb^{2+}, and Cd^{2+}. A conductive ultrathin polypyrrole (PPy) film where the thickness was 55 nm thick was utilized to entrap glucose oxidase (GOx) with a fast response time. Upon exposure to trace metals, a more robust inhibition of GOx activity led to reduced glucose amperometric response [59]. Messaoud et al., have used fixed potential amperometry to determine bisphenol A (BPA), based on xanthine oxidase (XOD) enzymatic inhibition hypoxanthine as enzyme substrate, as is shown in Figure 1a,b. The mechanism of enzyme inhibition was estimated from the Cornish–Bowden and Dixon plots that were reversible with the competitiveness. An extremely low detection limit of 1.0 nM was achieved with excellent repeatability and reproducibility. The biosensor water samples' selectivity, stability, and practical tests were also investigated [60].

4.2. Antibody

Immunoassay is based on detecting antigen–antibody conjugates or excessive other reagents (e.g., enzyme-labelled second antibody). Furthermore, it can be divided into competitive mode and non-competitive mode based on whether the analyte competes for a restricted number of binding antibody sites with the labelled analyte (e.g., indirect competitive immunoassay) or not (e.g., sandwich format) [61]. Immunoassays can also be classified as homogeneous and heterogeneous assays. Antibodies and antigens move freely from a complex immune situation to the solution phase in a homogenous format. However, it can be seen differently in a heterogeneous structure where the antibodies (or sometimes antigens) can be immobilized on a solid support to form the complex. Both types have been widely investigated, but homogeneous assays benefit from the possibility of multiplexing the complex format and separations are fast.

In contrast, the heterogeneous structure takes advantage of the elevated ratio of surface area to volume, which provides an additional higher sensitivity. Electrochemical immune sensors exhibit high sensitivity and selectivity compared to redox detection, which is extremely important in detecting various pesticides to decrease their mutual interference. The detection principle is mainly based on the current or impedance changes induced by antibody–antigen interaction, including chronoamperometry (CA) and electrochemical impedance spectroscopy (EIS).

A non-competitive immunoassay combined the with magneto-electrochemical immune sensors. It was developed to detect herbicide atrazine, one of the most used pesticides globally [62]. It is based on the recombinant M13 phage particles that bear a molecule named peptide. It is recognized explicitly as the immune complex of atrazine with an anti-atrazine monoclonal antibody. However, it is worth mentioning that each phage bore thousands of HRP Molecules, indicating the increased activity of pyrocatechol oxidation in the presence of hydrogen peroxide (H_2O_2). The phage anti-immunocomplex electrochemical immunosensor (PhAIEI) had dominant features, which provided a 200-fold improvement in sensitivity and a 10-fold wide linear working range compared with previous work with the same monoclonal antibody and anti-immunocomplex peptide. By chronoamperometry (CA), the fabricated PhAIEI was successfully applied in untreated river samples with excellent recoveries.

The leucomalachite green and malachite green in the water from a fish farm were detected by a BSA-decorated gold nanocluster (BSA-AuNC) with antibody composite film using the electrochemical impedance spectroscopy (EIS) method. The film was modified

by a glassy carbon electrode (GCE). The modification was carried out due to the potential hazards to the human immune system and the human reproductive system [63]. Moreover, the BSA-AuNCs interface's stability was improved via a diazotization method, and the antibody against leucomalachite green was chemically connected with the interface under the optimum conditions. After two weeks, the EIS immunosensor showed acceptable repeatability and stability with a negligible impedance reduction. A low LOD of 0.03 ng/mL was also obtained and compared with the ELISA method.

Azri et al., have developed an ultrasensitive electrochemical immunosensor for the detection of aflatoxin B1 (AFB1) based on an indirect competitive enzyme-linked immunosorbent assay (ELISA) to study the antigen–antibody interaction and optimize the optimum parameters of the assay [55]. The immunosensor demonstrated an excellent duplicability (RSD of 9%), and the response was logarithmic, where the detection range of 50–10,000 pM of IMD under the optimal conditions. The sensor was developed with the combination of BSA-labelled antigen and enzymatic tags. Compared with standard analytical methods, the developed sensor demonstrated a more comprehensive lower detection limit and a comprehensive range of responses which satisfied the detection requirements considering the European Union legislation. Saravanan et al., proposed a simple, disposable, and low-cost, paper-based immunosensor to detect bacteria in water [64]. The screen-printed fabrication technique was used for printing a conductive carbon electrode onto a commercial hydrophobic paper. Carboxyl groups were utilized for functionalization with the lectin Concanavalin A, which was covalently immobilized as the selective coating for biorecognition element for interacting with mono- and oligosaccharides. A linear calibration curve was developed for bacterial concentrations ranging from 10^3~10^6 CFU mL^{-1}, with the projected lower detection limit of 1.9×10^3 CFU mL^{-1}.

Immunomagnetic assays with the introduction of magnetic beads (MBs) are particularly effective for enhancing the analytical performance. A huge surface area allows them to be utilized in immobilization of biomolecules, such as enzymes, DNA, and antibodies. Chemical and physical stability, low toxicity, and high biocompatibility make them suitable for the immobilization of biomolecules. Efficient dispersing ability enables them to shorten the reaction time between dissolved species and biomolecules [54]. The electrochemical glyphosate (N-(phosphonomethyl)glycine) biosensor has been developed with a disposable screen-printed electrochemical cell and applied to the analysis of spiked beer samples based on the competitive assay, as is shown in Figure 1c [54]. With tetramethylbenzidine (TMB) as the enzymatic substrate, the affinity reaction's scope has been achieved by monitoring the current (A) due to reducing the enzymatic effect. The concentration range was found as 0–10,000 ng, where the detection limit was 5 ng/L and the quantification limit was 30 ng/L. An indirect competitive ELISA was exhibited in Figure 1d [55], competition occurred between aflatoxin B1-bovine serum albumin (AFB1–BSA) and free AFB1 (in peanut sample and standard) for the binding site of a fixed amount of anti-AFB1 antibody on the multiwalled carbon nanotubes/chitosan/screen-printed carbon electrode (MWCNTs/CS/SPCE). Figure 1e showed the effect of various blocking agents on background reading by eight percent skimmed milk, one percent BSA, casein, protein-free, and superblock [55].

4.3. Nucleic Acid-Based Bio-Recognition Materials

Compared with enzyme and antibody, nucleic acid (DNA or RNA)-based electrochemical biosensor was reported later, but their various applications are increased exponentially due to their multiple advantages. Their conformation is more robust than antibodies or enzymes. They can be entrapped in the biosensor assembly and bind with a wide range of specific targets with elevated affinity and sensitivity [65]. The interaction between immobilized nucleic acid and the analyte can change structures and electrochemical properties. One of the analytes are aptamers, which have artificial functional single-stranded DNA or RNA structures that can bind various target molecules, such as amino acids, small molecules, proteins, and cells, with high specificity affinity [66]. Aptamers can be obtained through an in the vitro selection procedure, followed by the classical methodology of

systematic evolution of ligands by exponential enrichment (SELEX). Tuerk and Gold first proposed it in 1990 [67]. Figure 1f showed a highly sensitive impedimetric aptasensor for the selective detection of acetamiprid and atrazine [57].

Many nucleic acid-based electrochemical biosensor configurations have been extensively studied in gene analysis, clinical diagnostics, and environmental monitoring due to their fast, low-cost, sensitive, and selective responses to numerous analytes [68]. The most crucial step in preparing the nucleic acid-based electrochemical biosensor is the surface immobilization of the oligonucleotide strands. A terminal modification (sulfhydryl and amino groups) is the most common method to immobilise nucleic acid. Its most significant advantage lies in efficiently achieving directional and stable fixation. It is easy to prepare DNA arrays and realize high-throughput determination combined with lab-on-a-chip technology. The electrochemical detection of nucleic acid can be divided into direct and indirect methods. The electroactivity of oligonucleotide strands can be changed in the direct methods, which also changes the interfacial properties of the oligonucleotide strands-modified electrode in terms of conductivity, capacitance, or impedance. The indirect methods depend on the usage of electrochemical active nucleic acid labels [69] or intercalators [70] (e.g., methylene blue) [71].

Nucleic acids have been most widely used in metal ion detection, mainly consisting of the following four types: metal ion-specific DNAs, aptamers, DNAzymes, and guanine (G)-rich oligonucleotides, which can be related to G-quadruplexes [72]. Heavy metal ions can generate the partial disordering of oligonucleotide strands and reduce base stacking and base pairing after forming a metal–base complex. DPV studied the evaluation of the interaction of Pb^{2+}, Cd^{2+}, Ni^{2+}, and Pd^{2+} with dsDNA, including hydrogen bonding cleavage, double helix conformation, and oxidative damage to DNA bases at GCE. [73]. Hg^{2+} can combine with two thymine bases (T) and mediate T–T mismatch to form a stable T–Hg^{2+}–T structure which is more durable than the natural adenine–thymine (A–T) base pair with a binding constant close to 10^6 M^{-1} [74]. Ag^+ can selectively interact with cytosine (C)-rich oligonucleotide strands to form C–Ag^+–C mismatch [75]. These impressive mismatches belong to coordination bonds, and on these principles, significant efforts have been made for high selectivity and sensitivity to determine Hg^{2+} [40,76] and Ag^+ [77,78]. As for the detection of Pb^{2+} ion, the G-rich DNA sequences are widely used due to their ability to fold to form a most compact G-quadruplex structure, especially in the presence of Pb^{2+} ion [79]. For example, the simultaneous detection and determination of mercury (II) and lead (II) ions were implemented by Wang et al. [80]. The biosensor functionality was improved by placing the amino-modified reduced graphene oxide (NH_2-rGO) nanofilm on a gold electrode as an excellent anchorage for the DNAzyme and the DNA strands. The presence of target ions could be recognized through the difference in charge-transfer resistance values before and after DNA interactions with Hg^{2+} and Pb^{2+} ions.

4.4. Whole Cell-Based Bio-Recognition Materials

Whole cells or microorganisms used for environmental biosensing can be classified as bacteria, yeasts, and fewer algae. The whole cell-based biosensor combines cells and transducers, generating a measurable electrical signal against the specific or target analytes [81]. In recent years, the whole cell has become an excellent alternative to the traditional bio-recognition elements due to their easy cultivation and manipulation, hosting many enzymes to catalyze reactions and good compatibility with various types of transducers. Substantial efforts have been made, from commercial to well-characterized cells with robust and specific enzymatic properties [82]. Moreover, they can give information on the pollutants' bioavailability and toxicity toward eukaryotic or prokaryotic cells [83].

Whole cells played an essential role in detecting heavy metal ions as the carrier to adsorb, precipitate or metabolize heavy metal ions. The whole cell was integrated into biosensors for low cost, low toxicity, high adsorption, and feasible fabrication based on the complexation, ion exchange, and physical adsorption between the whole cell and metal

ions. Alpat et al., used green microalgae (Tetraselmis chuii) for the biosorption, preconcentration, and determination of Cu^{2+} in an easy, inexpensive, sensitive, and effective way [84]. The working electrode was fabricated by mixing green microalgae and carbon paste. Different pulse cathode differential voltammetry showed good linearity in the range of 5.0×10^{-8}–1.0×10^{-6} M with the L.O.D. of 4.6×10^{-10} mol L^{-1}. A Phormidium sp. modified voltammetric sensor for Pb^{2+} detection from aqueous solutions was also developed. Possible functional groups involved in Pb^{2+} accumulation were carboxyl, sulphoxide, and alcoholic groups. The developed microbial biosensor's analytical properties and selectivity were investigated comprehensively, with a detection limit of 2.5×10^{-8} M [85].

The oxygen consumption estimates the biological oxygen demand (BOD) during the biodegradation with the aerobic whole cells as the catalysts. It is known that the biosensors need biorecognition elements with minimal selectivity and high activity of bio-oxidation for a wide range of organics, which ensures their application in the practical water samples containing water nutrients and complex organics. Xia's group developed the fast detection method of BOD by selecting the Bacillus subtilis as a biorecognition element for its resistance in extreme conditions. They created a single-microbial-layered structure on the gold surface where the Bacillus subtilis bonded covalently. However, the conductivity was low due to the microbial electrode, and the biocompatibility was also poor [86]. In a second study, they improved the performance by creating the rough electrode surface with the microbial layer, and the carboxyl graphene and Au nanoparticles' electrodeposition was used for creating this roughness [87]. In a third study, they used magnetite-functionalized Bacillus subtilis as the element of this BOD microsensor that can be regenerated and immobilized on an ultramicroelectrode array (UMEA). Modification and regeneration of the electrodes array are controlled magnetically. The assay can be performed in a short time (5 min) with vastly improved sensitivity. The calibration plot is linear in 2–15 mg·L^{-1}. The developed biosensor was also applied successfully to determine BOD in spiked water samples [88]. Khor et al., constructed a two-electrode sensor system using calcium alginate to immobilize microorganisms for BO detection [89]. Ferrocyanide can dissolve in the carrier solution and be fixed into the membrane to participate in a biochemical reaction. Ultramicroelectrode has the advantages of small size, fast diffusion and mass transfer, and a fast, stable state. In the combination of optimized microbial-sensitive film thickness, the rapid detection of BOD is realized.

Table 2. Summary of recognition elements, analyte, electrode, type of transducers, the limit of detection, and the response of various electrochemical biosensors.

Recognition Element	Analyte/Pollutant	Electrode/Sensing Material	Type of Transducers	Limit of Detection	Response Time	Response Range	References
An enzyme (HRP)	phenol	electrochemically reduced graphene oxide/glass carbon electrode	differential pulse voltammetry	2.19 μM	-	3.0–100.0 μM	[90]
Enzyme (BChE)	paraoxon	Prussian Blue Nanoparticles/screen-printed electrodes	amperometric	1 μg L^{-1}	10 min	2.0–10 μg L^{-1}	[91]
Enzyme (AChE)	Chlorpyrifos	ZrO_2/RGO/ITO glass electrode	amperometric	100 fM	-	0.1–1000 pM	[92]
An enzyme (tyrosinase)	PhOH	ZnO Nanoparticles/screen-printed carbon electrodes	amperometric	19.8 nM	<10 s	0.1–14 μM	[93]
Antibodies (anti-Microcystin-leucine arginine)	Microcystin-leucine arginine	cysteamine/gold electrode	electrochemical impedance spectroscopy	570 pg L^{-1}	-	3.3×10^{-4}–10^{-7} g L^{-1}	[94]
Antibodies (anti-alkylphenols)	4-nonylphenol	single-walled carbon nanotubes/gold electrode	field effect transistors	5 μg L^{-1}	-	5–500 μg L^{-1}	[21]
Aptamers	atrazine	platinum nanoparticles microwires	electrochemical impedance spectroscopy	10 pM	10 min	100 pM–1 μM	[57]
Aptamers	Vibrio alginolyticus	magnetic beads with a solid-contact polycation-sensitive membrane	potentiometric	10 CFU mL^{-1}	1 min	10–100 CFU mL^{-1}	[95]
Whole cell (Shewanella cells)	riboflavin	Shewanella oneidensis MR-1	amperometric	0.85 ± 0.09 nM	-	2–100 nM	[96]

5. Type of Transducers

A transducer is considered a significant part of the biosensor. It can convert the physical change of the surroundings to suitable electrical signals, which a reaction could cause. Biological or bio-recognition elements can be associated with or integrated with a transducer. The bio-recognition elements can be incorporated with chemical and physical bounding on the surface of the transducer, which also depends on the immobilization methods [97]. Significant electrochemical transducers are available, such as amperometric or voltammetric, impedimetric, capacitive, potentiometric, and ion-selective field-effect transistors. The following sections summarise these transducers for water quality detections in various applications. As is shown in Table 3, various types of transducers and characteristics were summarized.

5.1. Voltammetric/Amperometric Biosensors

The method is based on the current detection technique, either by ramping up the working electrode's potential at a given rate or keeping the potential constant compared to the reference electrode. The system's response would be observed in both methods [65]. An amperometric biosensor (Figure 2) is based on the current generated from any electrochemical oxidation and reduction mechanisms of any electroactive species. It consists of a three-electrode system where a time-dependent excited potential is applied to the working electrode-changing the potential which is also relative to the fixed potential to the reference electrode. A current flows between the working electrode and the auxiliary electrode (nA to μA), where it is correlated with a bulk concentration of the electroactive species or the construction and expenditure rate within the adjoining biocatalytic layer. Platinum wire can be used as auxiliary electrode and an Ag/AgCl electrode can be used as reference electrode.

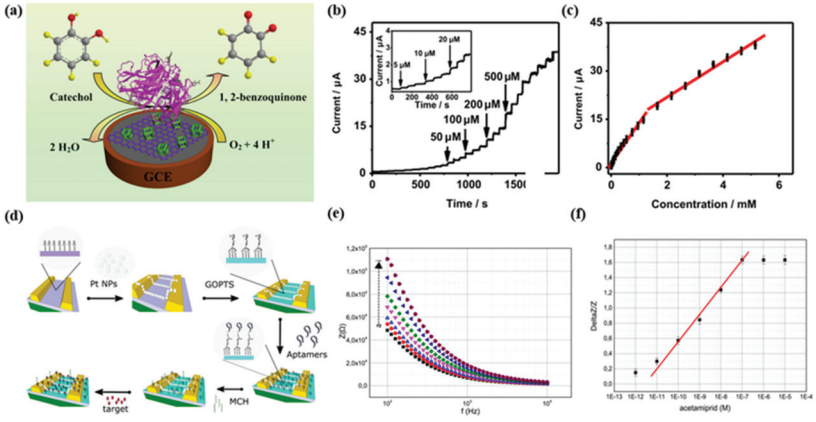

Figure 2. (**a**) Schematic design of the catalyzed oxidation on the catechol (analyte) electrode surface by laccase. (**b**) The proposed calibration curves of the catalytic currents vs. catechol (analyte) concentrations; and (**c**) calibration curve (Adapted from [98]) based on amperometric responses; (**d**) Schematic design of surface functionalization, where the Thiol-modified aptamers are bonded covalently and immobilized on the surfaces; (**e**) The Bode plots of the functionalized sensors; (**f**) The calibration curves are obtained for pesticides, such as acetamiprid (reproduced with the permission of [57]).

In 1956, Leland C. Clark introduced the oxygen probe, the simplest form of an amperometric biosensor. The oxygen probe measures the dissolved oxygen during the electrochemical reduction of oxygen. The associated electrolyte current is considered a response signal. This method can suit affinity sensors, which provide the electrochemically active compound as the recognition material and electrochemical labelling. Some electrochemically active

nucleobases are included in the nucleic acid structure and are used for monitoring the recognition of hybridization. A new design [99] of biosensor strips was integrated with a conducting copper track and a graphite–epoxy composite for pesticide analysis. It was applied by screen-printing, and the enzyme (AChE or BChE) was immobilized manually by crosslinking with glutaraldehyde. Micaela Badea et al. [100] have reported modified platinum electrodes with a cellulose acetate membrane to fabricate rapid amperometric detection of nitrites and nitrates in water. The developed method is simple, fast, and does not need an extra reagent for nitrite detection.

Biagiotti, Vanessa, et al. [101] have reported a platinum electrode modified by electropolymerized films and polymer nanotubule nets. They tried several analytical parameters; among them, poly(1,3-DAB) film showed the best performance for nitrite detection in drinking water. The electrode was characterized electrochemically by cyclic voltammetry and amperometry coupled to flow injection analysis (FIA). It has shown the linear range of concentration (10–1000 μM), LOD (2 μM), and good reproducibility (R.S.D.%: 0.4). Stoytcheva, Margarita, et al. [102] undertook a work to determine the enzymatic phenols by developing polymer film formation on the working electrode. Pan, Yanhui, et al. [103] developed an electrochemical biosensor that was constructed by nitrogen-doped graphene nanoribbons (NGNRs) and ionic liquid (IL). The molecularly imprinted polymer (MIP) was used to develop the composite film to determine 4-nonyl-phenol (NP), and the determination of concentration range was 0.04–6 μM. They obtained satisfactory results from real samples with high sensitivity, selectivity, and stability.

Table 3. Various types of transducers and characteristics.

Characteristics	Bio-Recognition Element	Detection Range	LOD	Response Time	Application	Ref
indium tin oxide (ITO) nanoparticles, hexaammineruthenium (III) chloride (RUT), and chitosan (CH) modified glassy carbon electrode (GCE)	horseradish peroxidase (HRP) enzyme	0.009–0.301 M (Pb^{2+}), 0.011–0.368 M (Ni^{2+}), and 0.008–0.372 M (Cd^{2+}).	8 nM (Pb^{2+}), 3 nM (Ni^{2+}), and 1 nM (Cd^{2+})	10 s	Heavy metal detection in water, with good selectivity, stability, and reproducibility	[104]
glassy carbon electrode with gold nanoparticles	Pb (II)-DNAzyme	1 pM–1000 nM	0.42 pM	-	Heavy metal detection in water. High sensitivity, excellent specificity, good stability and acceptable reproducibility	[105]
glassy carbon electrode	*E. coli* cells immobilization using bovine serum albumin (BSA)	4.99×10^{-10} to 4.99×10^{-3} mol/L for mercury, 8.89×10^{-10} mol/L to 8.89×10^{-3} mol/L for cadmium, and 15.29×10^{-10} mol/L to 15.29×10^{-3} mol/L for zinc.	$5.58 \times 10^{(-11)}$ mol/L for mercury ion, $5.10 \times 10^{(-10)}$ mol/L for cadmium ion, and $1.38 \times 10^{(-9)}$ mol/L for zinc ion.	-	Heavy metal detection in water and lowcost and easy availability	[106]
glassy carbon electrode (GCE) modified with multiwalled carbon nanotubes (MWCNT)	choline oxidase enzyme	0.1 to 1.0 nM (Pb^{2+})	0.04 nM	5 min	Heavy metal detection in tap water	[107]
Pt/CeO_2/urease electrode	ceria (CeO_2) nano-interface	0.5–2.2 (Pb^{2+}) and 0.02–0.8 μM (Hg^{2+})	0.019 ± 0.001 μM (Pb^{2+}) and 0.018 ± 0.003 μM (Hg^{2+})	<1 s	Heavy metal detection in river water and good repeatability and reproducibility	[108]

5.2. Impedimetric Biosensors

An impedimetric biosensor (Figure 2) was fabricated by immobilizing the bio recognition elements onto the surface of the electrode. Different bio-recognition elements can detect nutrients, heavy metals, or waterborne pathogens. The targeted analyte can be measured through the output of an electrical impedance signal made proportional to activity of the analyte. It is a two-electrode system where the alternating voltage can be applied with a few to 100 mV amplitude. The impedance (Z), or the components of resistance (R) and capacitance (C), can be changed due to the behaviour of the material. The applied voltage frequency can be scanned over various frequencies to get the corresponding impedance and characterize the sensor for specific material. The equivalent circuit parameters are also used for impedance spectra for characterization purposes. For developing an impedimetric biosensor, the prerequisite condition is the reproducible ability of the immobilizing bio-recognition molecules onto the sensor surface with the possession of their biological activity [109].

The impedance spectrum can be displayed in Nyquist or Bode plots. The plot is a semicircle region lying on the axis, followed by a straight line. Usually, electrochemical impedance spectroscopy (EIS) is used to investigate the properties of bio-recognition events at the modified surface.

An impedimetric biosensor was reported [110] with highly conductive tantalum silicide ($TaSi_2$) to detect and quantify *E. coli* O157:H7 in drinking water. The developed biosensor shows a linear response with a concentration of 101–105 CFU mL^{-1} and a sensitivity of 2.6 ± 0.2 kΩ. It can avoid interference which also confirms the excellent selectivity. The developed biosensor can be used multiple times with good repeatability. Hnaien, M. et al. have reported [111] a bacterial impedimetric biosensor for trichloroethylene (T.C.E.) detection in drinking water. Gold microelectrodes were used with single-wall carbon nanotubes, further linking with anti-Pseudomonas antibodies. It also showed a good linear response with the T.C.E. concentration up to 150 μg L^{-1} and a low L.O.D. (20 μg L^{-1}). It also showed excellent stability and recovery in real sample water. Lin, Zhenzhen et al. [112] have reported a biosensor for simultaneous detection of metal ions, such as Pb^{2+}, Ag^{+}, and Hg^{2+} in lake water. The DNA-based bio-recognition element was immobilized on the working gold electrodes. The developed biosensor had high sensitivity and selectivity, which were evaluated using the charge transfer resistance (RCT) difference before and after the immobilized DNA interactions with Pb^{2+}, Ag^{+}, and Hg^{2+}. Madianos, L. et al. [113] developed a biosensor to detect acetamiprid and atrazine (pesticides) in natural water. The e-beam lithography technique deposited platinum nanoparticles (Pt NPs) between the interdigitated electrodes (IDEs) to create a bridge structure. The aptamer was chemically used to functionalize the Pt N.P.s on the sensing surface. The developed biosensor was highly sensitive and selective and also showed excellent linear response in the range of 10 pM to 100 nM for acetamiprid and 100 pM to 1 μM for atrazine.

5.3. Capacitive Biosensors

Capacitive biosensors consider be the group of affinity biosensors that operate by the direct binding between the surface of the sensor surface and the target molecule. It measures the variations in the dielectric properties and/or the thickness of the dielectric layer at the electrolyte/electrode interface location. A conventional electrical plate capacitor contains two conductive metal plates with specific dielectric properties separated by a certain distance. The following relations can express the:

$$C = \frac{€A}{d} \quad (1)$$

where € is the permittivity of the dielectric material, A is the area of the plate, and d is the distance between them. Therefore, when there is a change in the properties of the materials, a change in capacitance can be measured by the above equation. The second type of capacitive biosensor depends on the theory of electrical double-layer. The electrodes

submerged in an electrolyte solution can resemble a capacitor for storing charge where an insulating layer covers the surface. The specific biorecognition element can be immobilized on top of this layer. The solvated ions and water molecules create a capacitance near the electrode surface.

N. V. Beloglazova et al. [114] reported a capacitive biosensor to detect benzo(a)pyrene (BaP) in river water. MIPs and monoclonal antibodies (mAb) are used as recognition elements on the electrode. The sensor is validated in a contaminated water sample from different places in Ghent, Belgium. Graniczkowska et al. [115] reported the development of a capacitive biosensor to monitor an amphetamine as a trace amount in water samples. The gold sensing electrode is immobilized with MIPs for creating sensing elements. Samuel M. Mugo et al. [116] reported a pathogen imprinted polymer for detecting *Escherichia coli* in water. The conducting electrode is based on multi-walled carbon nanotubes (CNT), and nitrocellulose (CNC) films, which were integrated with polyaniline (PANI) doped phenylboronic acid (PBA). The proposed sensor used both the capacitive and impediometric method for detecting the *E. coli* with a rapid response of $\leq$5 μmin.

5.4. Conductometric Biosensors

Conductometric biosensors measure the conducting current between the electrodes and reference electrodes where the analyte or the medium plays a vital role. Usually, a differential measurement is performed between the working electrode with an enzyme and an identical reference electrode without an enzyme in a biosensor. The sensitivity of the sample amount is hampered by the parallel conductance of the target solution. The technique is significantly like conventional conductometers. An alternating current with the operating frequency is applied to the active electrodes to measure the potential. Conductance is measured by using both the current and voltage. Glucose, urea, creatinine acetaminophen, and phosphate are reported as different analytes to be determined using conductometric biosensors [117].

G. A. Zhalyak et al. [118] reported an alkaline phosphate-based conductometric biosensor for assessing the heavy metal ions in water. Gold-based electrode and residual enzyme activity measured in tris-nitrate buffer without metal preincubation. Various metal toxicity can be measured in the range as follows: $Cd^{2+} > Co^{2+} > Zn^{2+} > Ni^{2+} > Pb^{2+}$. A similar method (Figure 3) is reported [119] to identify the heavy metals in water. The alkaline phosphate activity (APA) was collected from cyanobacterium to immobilize directly on the substrate by physical absorption. The response time was 12 s. Other works [120–122] are also reported for heavy metal detection in water.

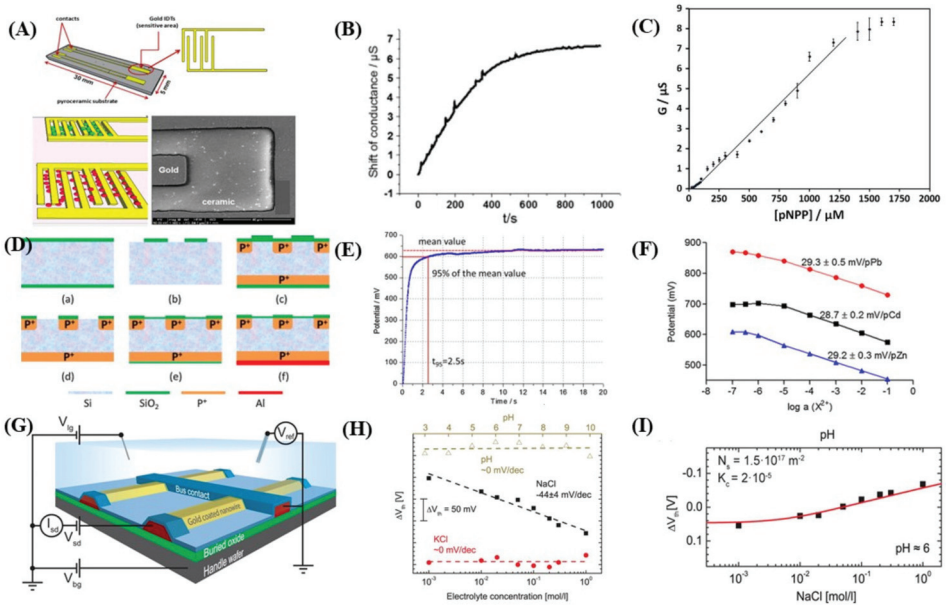

Figure 3. (**A**) Schematic of the microelectrodes with the gold electrode, the working electrode is immobilized with Spirulina cells, the reference electrode is immobilized with inhibited APA, which also includes Spirulina cells, and S.E.M. image of spirula cells with the gold electrodes of interdigitated transducers. (**B**) The real-time response of the conductometric transducer. (**C**) Standard calibration curve for the detection of the alkaline phosphatase activity (reproduced with the permission from [119]). (**D**) Fabrication process. (**E**) the response time of the sample solution. (**F**) The averaged calibration curve (reproduced with the permission from [123]). (**G**) Schematics of the measurement setup of the FET sensor. (**H**) Differential threshold voltage (ΔV_{th}) measurement of the gold-coated NWs vs concentration of the electrolyte and pH. (**I**) Response of the ionic strength of the gold-coated NW fitted with a blended site-binding model for deprotonation, protonation, and Cl– adsorption (reproduced with the permission from [124]).

In this work [125], the proposed biosensor was developed to determine the organic matter in water by immobilizing the enzyme bilayer with bovine serum albumin in glutaraldehyde vapour. It can detect the protein as a biomarker in water to identify urban pollution. The proposed method shows excellent sensitivity, reproducibility, and a long lifetime. C. Chouteau et al. [126] reported the whole cell *Chlorella vulgaris* microalgae as a bioreceptor on the interdigitated conductometric electrodes for detecting the toxic compounds in aquatic habitats. N. Kolahchi et al., proposed a fast, sensitive miniaturized conductometric biosensor for determining the phenol in water. *Pseudomonas* sp. (GSN23) bacteria were immobilized on the gold interdigitated microelectrodes to create the sensor assembly to determine phenol in river water.

5.5. Potentiometric Biosensors

A potentiometric biosensor works on the principle of potential difference between the working electrode and the reference electrode. The measured analytes are not consumed in the same way as in the amperometric biosensor. In this biosensing method, two electrodes galvanic cells immersed in the electrolyte solution generate the electromotive force (e.m.f.) measured by a high impedance voltmeter [127]. One electrode is used as a working electrode, and another is used as a reference electrode. The e.m.f. value is determined by the potential difference between the two electrodes. The analyte's concentration and

the potential difference is measured by the Nernst equation [128], which is explained as follows:

$$E_{cell} = E_0 - \frac{RT}{zF} lnQ \quad (2)$$

where E_{cell} is the e.m.f., E_0 is the potential of the standard electrode, R is the gas constant, T is the temperature in Kelvin, z is no of charge of the electrode reaction, F is the Faraday constant, and Q is ion concentration ratio of the anode to cathode.

Huang, Mei Rong et al. [129] have reported a membrane based on semi-conducting poly(phenylenediamine) microparticles for Pb^{2+} detection in natural water. The electrode is selective towards the Pb^{2+} with the concentration range 3.16×10^{-6} to 0.0316 M with a high sensitivity displaying a near-Nernstian slope of 29.8 mV decade^{-1}. The proposed electrode showed a long lifetime of 5 months, where the short response time was 14 s. Thayyath S. Anirudhan, and S. Alexander [130] have developed a modified multiwalled carbon nanotube (MWCNT) based imprinting polymer for the determination of pesticide 2,4-D (2,4-dichlorophenoxyacetic acid) in natural water. The sensor responds in the range of 1×10^{-9}–1×10^{-5} M, where the detection limit is 1.2×10^{-9} M. The developed sensor is stable and can be reusable many times in the first 3 months. Mashhadizadeh, Mohammad Hossein et al. [131] have reported a newly modified carbon electrode to determine the Cu^{2+} with the presence of other interfering ions. The proposed potentiometric sensor showed a Nernstian slope of 30 ($\pm$0.5) mV/decade over a concentration range from 1.0×10^{-8}–1.0×10^{-2} mol L^{-1}. The LOD was 7.0×10^{-9} mol L^{-1} and the response time was 30 s, which can be used for at least 3 months without sacrificing any quality of the sensor's response without any considerable divergence in responses.

5.6. Ion-Selective Field-Effect Transistors (ISFET) Based Biosensors

The last few years saw a significant change in ion-sensitive field-effect transistor (ISFET)-based devices, a principle initially proposed in the 1970s by Bergveld et al. [132]. This revolutionized the technology at a nanoscale level. These types of prototypes formed using silicon nanowire FETs (SiNWFETs) have been used for a wide range of applications, including pH sensing [133–135], chemical [136–139], and label-free biosensing [133,140–143] applications. The downscaling of these devices has been done by determining the kinetic studies on receptor binding [144] and intracellular recordings of action potentials [145]. The working mechanism is based on the adsorption of charged species on the sensing surface, causing variation in the surface potential and, thus, the current in the FET channel. These devices provide an additional attribute over the conventional ion-selective electrodes by transforming the high-impedance input signal into a low-impedance output signal. The probability of downscaling the dimension and conjugation them with conditioning circuits to detect multifunctional parameters [146] highlights the ability of SiNWFETs to operate as low-cost, efficient, and robust devices.

In one of the examples, the selectivity of the sensing surface is induced to deduce species other than protons. This was carried out to achieve high sensitivity by absorbing the target analyte. The covalent bonding of the linked molecules to perform chemical anchoring has been more than a viable method. The linker binding sites of the self-assembled monolayers (SAMs) are situated in the proximity of the FET surface at a higher density. The topic of SAMs has extensively been studied [49]. In ISFET systems, a technique related to self-assembly of silane monolayers has been used to alter the surfaces of the oxides [133,136,147].

Ion-sensitive field-effect transistors that use silicon nanowires have high dielectric constant gate oxide layers formed with Al_2O_3 or H_2O_2. These devices exhibit responses that are sensitive to pH variations and ions present in the electrolyte due to the presence of hydroxyl groups. The complexity of the oxide surface due to its intrinsic non-selective nature makes it challenging to sense ionic species other than protons. The modification of the individual nanowires has been done with thin gold films to increase the specificity via functionalization. It has also been shown that the sodium ion (Na^+) detection using SAM

of thiol-modified crown ethers has been done, where a response of ≈−44 mV per decade was achieved for the sodium ions in a NaCl solution. The testing process was carried out in the presence of various ions like protons (H^+), potassium (K^+), and chloride (Cl^-) ions, where the voltage difference between the gold-coated nanowire functionalized by the SAM (active) and a gold-coated nanowire was determined. It was seen that the functional SAM was unable to obtain any output from the bare gold-coated nanowire concerning pH and background ionic species. This response increases the credibility of gold in comparison to oxide surfaces when the devices are used for differential measurements.

6. Signal Amplification Strategy

One of the critical capabilities of a biosensor lies in its enhanced performance in terms of the morphological, structural, and electrochemical characteristics of the considered nanostructured material. In normal terms, the sensors are characterized using X-ray diffraction, confocal microscopy, transmission electron microscopy, and voltammetric techniques. The hybrid prototypes used for biosensing applications constitute combined attributes that have generated high sensitivity, selectivity, and rapid and stable response during the detection water pollutants. The synergy observed between the processed materials improved the electrochemical activity, stability of the immobilization of bioreceptor, electron transfer rate and surface area of the electrodes, thus obtaining a high magnitude of the peak current during the detection of different analytes as a typical signal amplification strategy.

The use of metallic nanoparticles with a large electroactive surface area has been employed for electrochemical biosensing applications due to their high electrical conductivity, catalytic properties, fast electron transfer, biocompatible nature, and easy incorporation with different kinds of nanomaterials. Zeinab et al., showcased the use of an ultrasensitive electrochemical aptasensor for quantitative detection of bisphenol A (B.P.A.) via signal amplification strategy

The use of gold-platinum nanoparticles (Au-PtNPs) was carried out by electrodepositing them on acid-oxidized carbon nanotubes (CNTs-COOH)-modified glassy carbon (GC) electrodes. Then, acriflavine was immobilized by covalent bonds at the surface to capture BPA-aptamer by forming phosphoramidite bonds. The aptamer's conformational change occurred once the B.P.A. interacted with the aptamer. Thus, the retardation was carried out for the interfacial electron transfer of acriflavine as a probe. The LOD for this technique was calculated to be as low as 0.035 pM, which resulted from high-density Au-PtNPs and superior electron transfer of acriflavine. The resulting aptasensor also exhibited reasonable specificity, stability, and reproducibility.

Recently, the application of conducting polymer-based materials were made in biosensors for two particular areas, including enhancing the affinity of these sensors as backbone or side groups and using them as immobilization matrices for the bioreceptors with high electrical conductivity and fast electron transfer [44]. Disposable nitrate biosensors were used as nanoarrays to detect nitrate reductase as a target analyze. Bio-recognition element was immobilized within a poly (3, 4-ethylenedioxythiophene) (PEDOT) matrix to produce a quantifiable amperometric response. Superior analytical performance and quick fabrication process, and easy operating principle were obtained with this PEDOT/nitrate reductase nanowire sensor [148].

Dendrimers are synthetic three-dimensional macromolecule polymers with well-defined, highly branched, globular-shaped molecular structures [149]. Poly (propylene imine) dendrimer PPI has been popularized for biosensing applications due to its high biocompatibility and compatibility with host–guest chemistry. Due to the disastrous effects of cholera infection resulting in watery diarrhoea with severe dehydration and death, Tshikalaha et al., developed biosensors to detect cholera toxins in the water. The sensors are operated by co-electrodepositing PPI dendrimer and AuNPs on glassy carbon electrodes. The probe of the anti-cholera toxin was dropped on GCE/PPI/AuNPs and finally blocked with B.S.A. to reduce nonspecific binding[150]. A LOD of 7.2×10^{-13} and 4.2×10^{-13} g mL^{-1} were obtained from SWV and EIS analysis.

Another significant strength in improving electrochemical signals is the core-shell or core-satellite nanostructures. These nanomaterials can be loaded to the core nanoparticle via surface functionalization in chemical ways. For example, heterogeneous magnetic nanoparticles [151] and Mesoporous silica [152] have attracted increasing attention due to their easy magnetic separation with labelled bio-receptors and easy encapsulation of enormous materials in their structural pores, respectively. Ultrasensitive electrochemical biosensors used to detect Ag^+ ions were constructed using magnetic Fe_3O_4@gold core–shell nanoparticles (Fe_3O_4@Au NPs) for labelling with H.C.R. product and enrichment on the surface of the magnetic gold electrodes [153]. The prototypes showed high selectivity due to their duplex-like DNA. scaffolds structure with specific C–Ag^+–C base pairing. They also had attributes like high sensitivity, low LOD of 0.5 fM and a wide dynamic range of 1 fM–100 pM. Marcos et al. [154] reported a new hybrid nanomaterial platform that included MWCNT and haemoglobin-functionalized mesoporous silica particles with highly sensitive quantification of nitrite and trichloroacetic acid as processed materials. The efficient electron transfer between haemoglobin and the electrode surface can be attributed to certain factors, including the high surface area and protein loading capacity of the mesoporous silica nanoparticles as well as the increased surface area and catalytic properties of MWCNTs.

In regards to the porous materials, metal–organic frameworks (MOFs) are another interesting class of porous crystalline inorganic–organic hybrid materials, as Fe(III)-based MOF (Fe-MOF) was reported [155] to have an excellent stability and redox activity when used as the prime electrode materials [156]. As is shown in Figure 4, a core–shell nanostructured Fe(III)-based metal–organic framework (Fe-MOF) and mesoporous Fe_3O_4@C nanocapsules (denoted as Fe-MOF@mFe_3O_4@mC)-based aptasensor was constructed [155]. The EIS was used for detecting the responses, where an advantage of the conformational transition interaction took place. This phenomenon was caused due to two factors: the formation of the G-quadruplex between a single-stranded aptamer and a highly heavy metal ion of Fe-MOF. The proposed aptasensor showcased a decent linear relationship with the logarithm of heavy metals and a low LOD of 2.27 and 6.73 pM toward the detection of metallic ions of Pb^{2+} and As^{3+}, respectively.

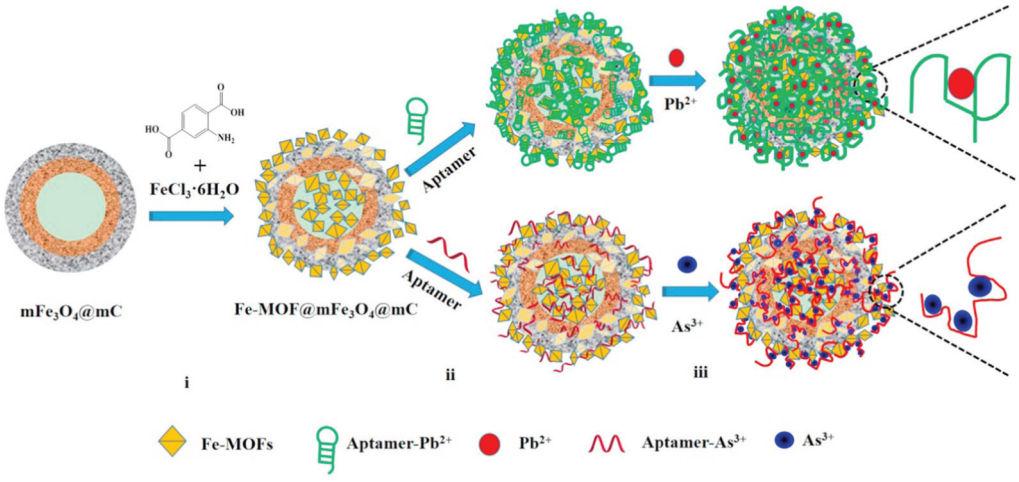

Figure 4. Schematic diagram of the preparation process of nanocomposite and its related aptasensor for detecting Pb^{2+} and As^{3+} via electrochemical techniques, including (**i**) the preparation of the nanocomposite, (**ii**) the immobilization, and (**iii**) the determination of the heavy metal ions, (reproduced with the permission from [155]).

7. In Situ Monitoring System

The recent development of various biosensors recommends excellent potential for monitoring water quality in the other treatment water recourses due to their simple, compact design, dispensability, and cheapness. In situ can be considered as online monitoring and offline or portable monitoring. Online monitoring defines as real-time in situ measurements of any sampling for analysis and provides on-field sampling data compared to conventional methods. It is incredibly challenging to monitor water contaminants, primarily chemical pollutants, in online monitoring. It is a more flexible approach and can be conducted from remote locations. An online monitoring system can be constructed utilizing a wireless sensor network (WSN) or an Internet of Things (IoT)-enabled network [25,157,158]. Simultaneous data collections, higher detection, easy monitoring, and sufficient data are the significant advantages of constructing the WSN network for monitoring purposes. Low power consumption and energy harvesting options are essential for developing an online monitoring network.

Pasternak et al., reported [136] a biological oxygen demand (BOD) biosensor, which was self-powered and autonomous for water quality measurement. The energy harvesting system, data logger, and sensing unit were developed continuously to monitor the sample in water (Figure 5). This biosensor can detect urine contamination in water, and the system can run autonomously for five months.

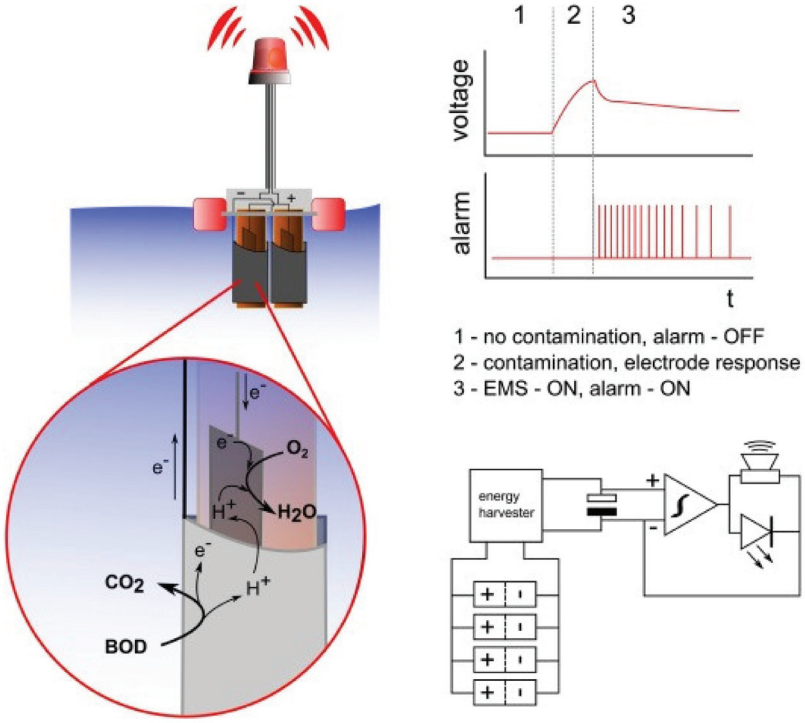

Figure 5. Schematic representation of the sensor's proposed biosensor and operating principle. The block diagram of the system shows the energy harvester charging/discharging repeatedly (reproduced with the permission of [159]).

Quek et al. [160] reported an assimilable organic carbon (AOC) based amperometric biosensor for detecting marine microbial fuel cell (MFC) in marine water, where the system was tested for 36 days. The response time, the reproducibility of the signal, and recovery time were good, which are essential for developing an online monitoring system.

Bio-recognition elements play a crucial role in developing robust biosensors, which could be helpful for online monitoring. Among the many bio-recognition features, the enzymatic biosensors method is used widely for electrochemical detection, as they have high sensitivity for distinguishing the target elements from interference elements [161]. However, they are a costly method, have an increased duration of immobilization procedure, and have poor durability and stability, which is ascribed to the loss of enzyme activity during the onsite monitoring [82]. Therefore, MFC biosensors are widely used for various target analytes with an extensive range of cells [162]. They have mainly been installed to monitor water quality, but very few commercial prototypes are available for monitoring water toxicity. They can survive under harsh conditions, such as high and low pH, unusual temperature, and salinity [161].

Figure 6 has shown the portable electrochemical EIS based system for monitoring samples from water. Figure 7 shows the schematic block diagram of a standard electrochemical biosensor monitoring system. The sensing parameters would be capacitance, impedance, current, or voltage based on the characteristics of the electrochemical biosensor. The impedance analyzer relates to the sensor to collect the sensor data. It also provides sufficient energy to the sensor. The microcontroller unit manages all the sensing data, sends the data to the cloud server through the base station or the internet and manages the operating condition of the complete sensing system. The energy harvesting unit connects with the power management unit to supply continuous energy to the sensing unit. The microcontroller unit also connects with the wireless communication module, another crucial module for developing an online monitoring system. Different wireless communication modules are available, such as Bluetooth low energy, low power wide area network (LPWAN) wireless modules, SigFox modules, WiFi modules, and ZigBee modules. The modules are characterized based on their bandwidth, data transmission capability, power consumption, and communication range. The communication module solely depends on the installation duration of the network, the number of sensing systems, the content of coverage regions of the networks, and the application.

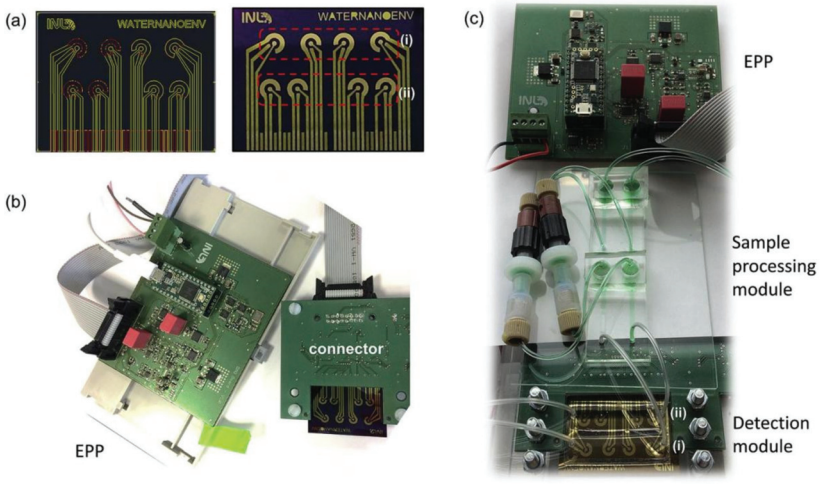

Figure 6. (**a**) Design and fabrication of electrochemical-cell-chips development; (**b**) electrochemical impedance portable platform for EIS measurements; and (**c**) complete portable system for automatic detection (reproduced with the permission of [94]).

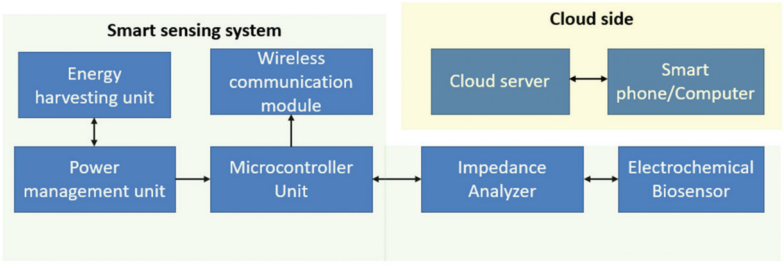

Figure 7. Schematic diagram of an online monitoring system.

8. Challenges and Future Work

Although much work has been carried out to detect water quality using electrochemical biosensors, some bottlenecks still need to be addressed. Some challenges in microbial biosensors' detection process are low recognition limits, limited specificity, and high contamination. It also has limitations in mass transmission due to the subsequently limited penetration of substrates and products throughout the cells [163]. These bottlenecks primarily exist and limit the sensitivity during these biosensors' real-time application. These prototypes can only detect certain microorganisms and limited chemicals present in water, thus making them unsuitable for the in situ monitoring of unanticipated shocks in wastewater [164,165]. Additionally, there is currently no verification on the immobilization of enzymes or microorganisms on the surfaces of biosensors during their deployment in harsh environments. They also have low durability, primarily when operated over several hours [165–167]. This makes these prototypes unsuitable for long-term operations during wastewater treatment. Other issues are the requirement of external power sources and additional dissolved oxygen (DO) that deters the exact conductivity and pH probes to measure various parameters [168,169]. These problems lead to the deterioration of their performance over a prolonged period. The real-time monitoring has also been challenging due to the delay in the response of these biosensors, thus hindering the timely action from overcoming the shock effects. For example, when anaerobic granule biosensors were used for the early alarm to detect copper and phenol in the wastewater [170], the delay (6–20 h) in the response time created problems in the practical application and of these prototypes.

Generally, electrochemical sensors have specific attributes like lower detection limit of detection than colourimetric and fluorescent sensors (pvalue $\ll$0.05, d-value >0.8) [171]. Some of the primary characteristics of the electrochemical biosensors are their compatibility with modern microfabrication technologies, low input power, roll-to-roll fabrication, and the independence of sample turbidity and colour [172].

Even though the fabricated sensors have been used for multifunctional applications, most focus on the detection criteria lying on the sampled genre like heavy metal ions. Rarely have the sensors been used to detect some multi-analytes like antibiotics, small molecules, and metal ions. Julius et al. [173] displayed the development and implementation of a cell-free in vitro transcription system that deploys RNA output sensors activated by ligand induction (ROSALIND) to detect specific contaminants based on aptamer transcription and fluorescent signal analysis. Importantly, easy storage and distribution can also be carried out with the ROSALIND system, thus making it easier to deploy. This assists in determining their capability to test municipal water supplies and demonstrate their use for monitoring water quality.

9. Conclusions

There is continuous fear about the risks caused by contaminations or pollutants to human health and marine ecosystems. However, standard analytical techniques are sensitive, accurate, laborious, expensive, and unsuitable for on-site monitoring with complex water sample pretreatment requirements before testing under the guidance of trained personnel.

This review assessed the recent progress in developing electrochemical biosensors for water quality sensing applications over the current time. Many of them also have certain advantages over the other methods in detecting the aggregate outcomes of multiple pollutants in water samples. Although electrochemical biosensors have great potential and are very sensitive and cost-effective compared to the standard analytical methods, they still need to reduce their cost and response time performance compared to the other sensors. The research will likely continue by modifying the electrode surfaces and innovative biorecognition elements, using various nanomaterials, conducting polymers, etc., and improving the surface-by-surface modification techniques to enhance electrochemical biosensor sensitivity and selectivity and the quick response. Further integration with intelligent electronics and wireless technologies will significantly benefit the development of biosensors for remote sensing applications or in situ measurements. However, the stability of the electrochemical biosensor remains a challenge that needs additional research to explore and to extend its shelf life. Finally, this review outlines the current methods and technologies in electrochemical biosensors for water quality sensing applications. We think that this review article will be helpful for beginners and a helpful guide that will enhance the awareness of the role that electrochemical biosensors can play in protecting our environment and most valuable water resources.

Author Contributions: Conceptualization, Y.H. and M.E.E.A.; resources, Z.H. and A.N.; data curation, Z.H. and A.N.; writing—original draft preparation, Y.H. and M.E.E.A.; writing—review and editing, Y.H., M.E.E.A., S.F. and S.C.M.; supervision, M.E.E.A., S.F. and S.C.M.; project administration, S.F. and M.E.E.A.; funding acquisition, S.F. All authors have read and agreed to the published version of the manuscript.

Funding: This work was funded by the National Natural Science Foundation of China (No. 62001460), the Natural Science Foundation of Guizhou (Grant No. Qiankehe-ZK[2 022]KEY002), and Shenzhen Key technology projects (JSGG20201103153801005), Shenzhen Municipal Science and Technology Innovation Commission (JCYJ20210324101611031).

Institutional Review Board Statement: Not applicable.

Informed Consent Statement: Not applicable.

Data Availability Statement: Not applicable.

Acknowledgments: The authors are thankful to their respective institutions/universities for providing valuable support and funding to conduct this research works.

Conflicts of Interest: The authors declare no conflict of interest.

References

1. Ejeian, F.; Etedali, P.; Mansouri-Tehrani, H.-A.; Soozanipour, A.; Low, Z.-X.; Asadnia, M.; Taheri-Kafrani, A.; Razmjou, A. Biosensors for wastewater monitoring: A review. *Biosens. Bioelectron.* **2018**, *118*, 66–79. [CrossRef] [PubMed]
2. W.H. Organization. Water, Sanitation and Hygiene (WASH). Available online: https://www.who.int/health-topics/water-sanitation-and-hygiene-wash (accessed on 10 May 2022).
3. Bereza-Malcolm, L.T.; Mann, G.L.; Franks, A.E. Environmental sensing of heavy metals through whole cell microbial biosensors: A synthetic biology approach. *ACS Synth. Biol.* **2015**, *4*, 535–546. [CrossRef] [PubMed]
4. Mekonnen, M.M.; Hoekstra, A.Y. Sustainability: Four billion people facing severe water scarcity. *Sci. Adv.* **2016**, *2*, 1–7. [CrossRef] [PubMed]
5. Korostynska, O.; Mason, A.; Al-Shamma'a, A. Monitoring Pollutants in Wastewater: Traditional Lab Based versus Modern Real-Time Approaches. In *Smart Sensors for Real-Time Water Quality Monitoring*; Springer: Berlin/Heidelberg, Germany, 2013; pp. 1–24.
6. Michael-Kordatou, I.; Iacovou, M.; Frontistis, Z.; Hapeshi, E.; Dionysiou, D.; Fatta-Kassinos, D. Erythromycin oxidation and ERY-resistant *Escherichia coli* inactivation in urban wastewater by sulfate radical-based oxidation process under UV-C irradiation. *Water Res.* **2015**, *85*, 346–358. [CrossRef]
7. Sun, J.; Gan, Y.; Liang, T.; Zhou, S.; Wang, X.; Wan, H.; Wang, P. Signal enhancement of electrochemical DNA biosensors for the detection of trace heavy metals. *Curr. Opin. Electrochem.* **2019**, *17*, 23–29. [CrossRef]
8. Uniyal, S.; Sharma, R.K. Technological advancement in electrochemical biosensor based detection of Organophosphate pesticide chlorpyrifos in the environment: A review of status and prospects. *Biosens. Bioelectron.* **2018**, *116*, 37–50. [CrossRef]

9. Jouanneau, S.; Recoules, L.; Durand, M.; Boukabache, A.; Picot, V.; Primault, Y.; Lakel, A.; Sengelin, M.; Barillon, B.; Thouand, G. Methods for assessing biochemical oxygen demand (BOD): A review. *Water Res.* **2014**, *49*, 62–82. [CrossRef]
10. Akhter, F.; Nag, A.; Alahi, M.E.E.; Liu, H.; Mukhopadhyay, S.C. Electrochemical detection of calcium and magnesium in water bodies. *Sens. Actuators A Phys.* **2020**, *305*, 111949. [CrossRef]
11. Yang, Y.; Fang, D.; Liu, Y.; Liu, R.; Wang, X.; Yu, Y.; Zhi, J. Problems analysis and new fabrication strategies of mediated electrochemical biosensors for wastewater toxicity assessment. *Biosens. Bioelectron.* **2018**, *108*, 82–88. [CrossRef]
12. Justino, C.I.; Duarte, A.C.; Rocha-Santos, T.A. Recent progress in biosensors for environmental monitoring: A review. *Sensors* **2017**, *17*, 2918. [CrossRef]
13. Ge, L.; Li, S.-P.; Lisak, G. Advanced sensing technologies of phenolic compounds for pharmaceutical and biomedical analysis. *J. Pharm. Biomed. Anal.* **2020**, *179*, 112913. [CrossRef]
14. Hassan, S.H.; Van Ginkel, S.W.; Hussein, M.A.; Abskharon, R.; Oh, S.-E. Toxicity assessment using different bioassays and microbial biosensors. *Environ. Int.* **2016**, *92*, 106–118. [CrossRef]
15. Yang, P.; Xia, J.; Zhan, C.; Qiao, Y.; Wang, Y. Monitoring the spatio-temporal changes of terrestrial water storage using GRACE data in the Tarim River basin between 2002 and 2015. *Sci. Total Environ.* **2017**, *595*, 218–228. [CrossRef]
16. Asadnia, M.; Myers, M.; Akhavan, N.D.; O'Donnell, K.; Umana-Membreno, G.A.; Mishra, U.; Nener, B.; Baker, M.; Parish, G. Mercury (II) selective sensors based on AlGaN/GaN transistors. *Anal. Chim. Acta* **2016**, *943*, 1–7. [CrossRef]
17. Biswas, P.; Karn, A.K.; Balasubramanian, P.; Kale, P.G. Biosensor for detection of dissolved chromium in potable water: A review. *Biosens. Bioelectron.* **2017**, *94*, 589–604. [CrossRef]
18. Umapathi, R.; Ghoreishian, S.M.; Sonwal, S.; Rani, G.M.; Huh, Y.S. Portable electrochemical sensing methodologies for on-site detection of pesticide residues in fruits and vegetables. *Coord. Chem. Rev.* **2022**, *453*, 214305. [CrossRef]
19. Dou, Y.; Li, Z.; Su, J.; Song, S. A Portable Biosensor Based on Au Nanoflower Interface Combined with Electrochemical Immunochromatography for POC Detection of Prostate-Specific Antigen. *Biosensors* **2022**, *12*, 259. [CrossRef]
20. Sohrabi, H.; Hemmati, A.; Majidi, M.R.; Eyvazi, S.; Jahanban-Esfahlan, A.; Baradaran, B.; Adlpour-Azar, R.; Mokhtarzadeh, A.; de la Guardia, M. Recent advances on portable sensing and biosensing assays applied for detection of main chemical and biological pollutant agents in water samples: A critical review. *TrAC Trends Anal. Chem.* **2021**, *143*, 116344. [CrossRef]
21. Belkhamssa, N.; da Costa, J.P.; Justino, C.I.; Santos, P.S.; Cardoso, S.; Duarte, A.C.; Rocha-Santos, T.; Ksibi, M. Development of an electrochemical biosensor for alkylphenol detection. *Talanta* **2016**, *158*, 30–34. [CrossRef]
22. Arduini, F.; Cinti, S.; Caratelli, V.; Amendola, L.; Palleschi, G.; Moscone, D. Origami multiple paper-based electrochemical biosensors for pesticide detection. *Biosens. Bioelectron.* **2019**, *126*, 346–354. [CrossRef]
23. Adekunle, A.; Raghavan, V.; Tartakovsky, B. A comparison of microbial fuel cell and microbial electrolysis cell biosensors for real-time environmental monitoring. *Bioelectrochemistry* **2019**, *126*, 105–112. [CrossRef]
24. Zheng, H.; Yan, Z.; Wang, M.; Chen, J.; Zhang, X. Biosensor based on polyaniline-polyacrylonitrile-graphene hybrid assemblies for the determination of phenolic compounds in water samples. *J. Hazard. Mater.* **2019**, *378*, 120714. [CrossRef]
25. Nag, A.; Alahi, M.E.E.; Feng, S.; Mukhopadhyay, S.C. IoT-based sensing system for phosphate detection using Graphite/PDMS sensors. *Sens. Actuators A Phys.* **2019**, *286*, 43–50. [CrossRef]
26. Khanmohammadi, A.; Jalili Ghazizadeh, A.; Hashemi, P.; Afkhami, A.; Arduini, F.; Bagheri, H. An overview to electrochemical biosensors and sensors for the detection of environmental contaminants. *J. Iran. Chem. Soc.* **2020**, *17*, 2429–2447. [CrossRef]
27. Guo, J. Uric acid monitoring with a smartphone as the electrochemical analyzer. *Anal. Chem.* **2016**, *88*, 11986–11989. [CrossRef]
28. Guo, J.; Ma, X. Simultaneous monitoring of glucose and uric acid on a single test strip with dual channels. *Biosens. Bioelectron.* **2017**, *94*, 415–419. [CrossRef]
29. Tsopela, A.; Laborde, A.; Salvagnac, L.; Ventalon, V.; Bedel-Pereira, E.; Séguy, I.; Temple-Boyer, P.; Juneau, P.; Izquierdo, R.; Launay, J. Development of a lab-on-chip electrochemical biosensor for water quality analysis based on microalgal photosynthesis. *Biosens. Bioelectron.* **2016**, *79*, 568–573. [CrossRef]
30. Xiao, G.; Song, Y.; Zhang, Y.; Xing, Y.; Zhao, H.; Xie, J.; Xu, S.; Gao, F.; Wang, M.; Xing, G. Microelectrode arrays modified with nanocomposites for monitoring dopamine and spike firings under deep brain stimulation in rat models of parkinson's disease. *ACS Sens.* **2019**, *4*, 1992–2000. [CrossRef]
31. Tian, Y.; Zhu, P.; Chen, Y.; Bai, X.; Du, L.; Chen, W.; Wu, C.; Wang, P. Piezoelectric aptasensor with gold nanoparticle amplification for the label-free detection of okadaic acid. *Sens. Actuators B Chem.* **2021**, *346*, 130446. [CrossRef]
32. Yang, F.; Chang, T.-L.; Liu, T.; Wu, D.; Du, H.; Liang, J.; Tian, F. Label-free detection of *Staphylococcus aureus* bacteria using long-period fiber gratings with functional polyelectrolyte coatings. *Biosens. Bioelectron.* **2019**, *133*, 147–153. [CrossRef]
33. Khorshid, M.; Sichani, S.B.; Cornelis, P.; Wackers, G.; Wagner, P. The hot-wire concept: Towards a one-element thermal biosensor platform. *Biosens. Bioelectron.* **2021**, *179*, 113043. [CrossRef] [PubMed]
34. Turner, A.P. Biosensors—Sense and sensitivity. *Science* **2000**, *290*, 1315–1317. [CrossRef] [PubMed]
35. Amiri, M.; Bezaatpour, A.; Jafari, H.; Boukherroub, R.; Szunerits, S. Electrochemical methodologies for the detection of pathogens. *ACS Sens.* **2018**, *3*, 1069–1086. [CrossRef] [PubMed]
36. Yang, L.; Li, Y.; Erf, G.F. Interdigitated array microelectrode-based electrochemical impedance immunosensor for detection of *Escherichia coli* O157: H7. *Anal. Chem.* **2004**, *76*, 1107–1113. [CrossRef]
37. Bhadra, P.; Shajahan, M.; Bhattacharya, E.; Chadha, A. Studies on varying n-alkanethiol chain lengths on a gold coated surface and their effect on antibody–antigen binding efficiency. *RSC Adv.* **2015**, *5*, 80480–80487. [CrossRef]

38. Lu, Z.; Zhao, W.; Wu, L.; He, J.; Dai, W.; Zhou, C.; Du, H.; Ye, J. Tunable electrochemical of electrosynthesized layer-by-layer multilayer films based on multi-walled carbon nanotubes and metal-organic framework as high-performance electrochemical sensor for simultaneous determination cadmium and lead. *Sens. Actuators B Chem.* **2021**, *326*, 128957. [CrossRef]
39. Konishi, T.; Hashimoto, T.; Sato, N.; Nakajima, K.; Yamaguchi, K. Substituent effects at the benzyl position and aromatic ring of silane-coupling agents containing 2-nitrobenzyl esters on photosensitivity and hydrophobic surface of a self-assembled monolayer (SAM). *Bull. Chem. Soc. Jpn.* **2016**, *89*, 125–134. [CrossRef]
40. Jia, S.; Bian, C.; Sun, J.; Tong, J.; Xia, S. A wavelength-modulated localized surface plasmon resonance (LSPR) optical fiber sensor for sensitive detection of mercury (II) ion by gold nanoparticles-DNA conjugates. *Biosens. Bioelectron.* **2018**, *114*, 15–21. [CrossRef]
41. Bizid, S.; Mlika, R.; Said, A.H.; Chemli, M.; Youssoufi, H.K. Investigations of poly (p-phenylene) modified with ferrocene and their application in electrochemical DNA sensing. *Sens. Actuators B Chem.* **2016**, *226*, 370–380. [CrossRef]
42. Lian, Y.; He, F.; Wang, H.; Tong, F. A new aptamer/graphene interdigitated gold electrode piezoelectric sensor for rapid and specific detection of *Staphylococcus aureus*. *Biosens. Bioelectron.* **2015**, *65*, 314–319. [CrossRef]
43. Rahmanian, R.; Mozaffari, S.A. Electrochemical fabrication of ZnO-polyvinyl alcohol nanostructured hybrid film for application to urea biosensor. *Sens. Actuators B Chem.* **2015**, *207*, 772–781. [CrossRef]
44. Hui, Y.; Bian, C.; Xia, S.; Tong, J.; Wang, J. Synthesis and electrochemical sensing application of poly(3,4-ethylenedioxythiophene)-based materials: A review. *Anal. Chim. Acta* **2018**, *1022*, 1–19. [CrossRef]
45. Armistead, P.M.; Thorp, H.H. Modification of indium tin oxide electrodes with nucleic acids: Detection of attomole quantities of immobilized DNA by electrocatalysis. *Anal. Chem.* **2000**, *72*, 3764–3770. [CrossRef]
46. Azek, F.; Grossiord, C.; Joannes, M.; Limoges, B.; Brossier, P. Hybridization assay at a disposable electrochemical biosensor for the attomole detection of amplified human cytomegalovirus DNA. *Anal. Biochem.* **2000**, *284*, 107–113. [CrossRef]
47. Schöning, M.J.; Wagner, T.; Poghossian, A.; Miyamoto, K.; Werner, C.; Krause, S.; Yoshinobu, T. Light-Addressable Potentiometric Sensors for (Bio-) Chemical Sensing and Imaging. In *Encyclopedia of Interfacial Chemistry: Surface Science and Electrochemistry*; Elsevier: Amsterdam, The Netherlands, 2018; pp. 295–308.
48. Evtugyn, G. *Biosensors: Essentials*; Springer: Berlin/Heidelberg, Germany, 2014; Volume 84.
49. Ulman, A. Formation and structure of self-assembled monolayers. *Chem. Rev.* **1996**, *96*, 1533–1554. [CrossRef]
50. Jijie, R.; Kahlouche, K.; Barras, A.; Yamakawa, N.; Bouckaert, J.; Gharbi, T.; Szunerits, S.; Boukherroub, R. Reduced graphene oxide/polyethylenimine based immunosensor for the selective and sensitive electrochemical detection of uropathogenic *Escherichia coli*. *Sens. Actuators B Chem.* **2018**, *260*, 255–263. [CrossRef]
51. Jain, A.; Cheng, K. The principles and applications of avidin-based nanoparticles in drug delivery and diagnosis. *J. Control. Release* **2017**, *245*, 27–40. [CrossRef]
52. Chen, X.; Feng, M.; Yan, H.; Sun, W.; Shi, Z.; Lin, Q. Fabrication of myoglobin-sodium alginate-graphene composite modified carbon ionic liquid electrode via the electrodeposition method and its electrocatalysis toward trichloroacetic acid. *Int. J. Electrochem. Sci.* **2017**, *12*, 11633–11645. [CrossRef]
53. Ben Messaoud, N.; Ghica, M.E.; Dridi, C.; Ben Ali, M.; Brett, C.M. A novel amperometric enzyme inhibition biosensor based on xanthine oxidase immobilised onto glassy carbon electrodes for bisphenol A determination. *Talanta* **2018**, *184*, 388–393. [CrossRef]
54. Bettazzi, F.; Romero Natale, A.; Torres, E.; Palchetti, I. Glyphosate determination by coupling an immuno-magnetic assay with electrochemical sensors. *Sensors* **2018**, *18*, 2965. [CrossRef]
55. Azri, F.A.; Sukor, R.; Selamat, J.; Abu Bakar, F.; Yusof, N.A.; Hajian, R. Electrochemical immunosensor for detection of aflatoxin B_1 based on indirect competitive ELISA. *Toxins* **2018**, *10*, 196. [CrossRef] [PubMed]
56. Pérez-Fernández, B.; Mercader, J.V.; Checa-Orrego, B.I.; De La Escosura-Muñiz, A.; Costa-García, A. A monoclonal antibody-based immunosensor for the electrochemical detection of imidacloprid pesticide. *Analyst* **2019**, *144*, 2936–2941. [CrossRef] [PubMed]
57. Madianos, L.; Tsekenis, G.; Skotadis, E.; Patsiouras, L.; Tsoukalas, D. A highly sensitive impedimetric aptasensor for the selective detection of acetamiprid and atrazine based on microwires formed by platinum nanoparticles. *Biosens. Bioelectron.* **2018**, *101*, 268–274. [CrossRef] [PubMed]
58. Campaña, A.L.; Florez, S.L.; Noguera, M.J.; Fuentes, O.P.; Ruiz Puentes, P.; Cruz, J.C.; Osma, J.F. Enzyme-based electrochemical biosensors for microfluidic platforms to detect pharmaceutical residues in wastewater. *Biosensors* **2019**, *9*, 41. [CrossRef]
59. Ayenimo, J.G.; Adeloju, S.B. Rapid amperometric detection of trace metals by inhibition of an ultrathin polypyrrole-based glucose biosensor. *Talanta* **2016**, *148*, 502–510. [CrossRef]
60. Ghanavati, M.; Azad, R.R.; Mousavi, S.A. Amperometric inhibition biosensor for the determination of cyanide. *Sens. Actuators B Chem.* **2014**, *190*, 858–864. [CrossRef]
61. Hervas, M.; Lopez, M.A.; Escarpa, A. Electrochemical immunosensing on board microfluidic chip platforms. *Trends Anal. Chem.* **2012**, *31*, 109–128. [CrossRef]
62. González-Techera, A.; Zon, M.A.; Molina, P.G.; Fernández, H.; González-Sapienza, G.; Arévalo, F.J. Development of a highly sensitive noncompetitive electrochemical immunosensor for the detection of atrazine by phage anti-immunocomplex assay. *Biosens. Bioelectron.* **2015**, *64*, 650–656. [CrossRef]
63. Zhu, D.; Li, Q.; Pang, X.; Liu, Y.; Wang, X.; Chen, G. A sensitive electrochemical impedance immunosensor for determination of malachite green and leucomalachite green in the aqueous environment. *Anal. Bioanal. Chem.* **2016**, *408*, 5593–5600. [CrossRef]
64. Rengaraj, S.; Cruz-Izquierdo, Á.; Scott, J.L.; Di Lorenzo, M. Impedimetric paper-based biosensor for the detection of bacterial contamination in water. *Sens. Actuators B Chem.* **2018**, *265*, 50–58. [CrossRef]

65. Tan, A.; Lim, C.; Zou, S.; Ma, Q.; Gao, Z. Electrochemical nucleic acid biosensors: From fabrication to application. *Anal. Methods* **2016**, *8*, 5169–5189. [CrossRef]
66. Hayat, A.; Marty, J.L. Aptamer based electrochemical sensors for emerging environmental pollutants. *Front. Chem.* **2014**, *2*, 41. [CrossRef]
67. Tuerk, C.; Gold, L. Systematic evolution of ligands by exponential enrichment: RNA ligands to bacteriophage T4 DNA polymerase. *Science* **1990**, *249*, 505–510. [CrossRef]
68. Huang, Y.; Xu, J.; Liu, J.; Wang, X.; Chen, B. Disease-related detection with electrochemical biosensors: A review. *Sensors* **2017**, *17*, 2375. [CrossRef]
69. Díaz-Serrano, M.; Rosado, A.; Del Pilar, J.; Vega, E.Z.; Guadalupe, A.R. Synthesis, Characterization and Use of Ru-Fc Intercalation Complex as an Electrochemical Label for the Detection of Pathogen-DNA. In *ECS Meeting Abstracts*; IOP Publishing: Bristol, UK, 2013.
70. Lv, X.; Ge, W.; Li, Q.; Wu, Y.; Jiang, H.; Wang, X. Rapid and ultrasensitive electrochemical detection of multidrug-resistant bacteria based on nanostructured gold coated ITO electrode. *ACS Appl. Mater. Interfaces* **2014**, *6*, 11025–11031. [CrossRef]
71. Ligaj, M.; Tichoniuk, M.; Gwiazdowska, D.; Filipiak, M. Electrochemical DNA biosensor for the detection of pathogenic bacteria *Aeromonas hydrophila*. *Electrochim. Acta* **2014**, *128*, 67–74. [CrossRef]
72. Zhan, S.; Wu, Y.; Wang, L.; Zhan, X.; Zhou, P. A mini-review on functional nucleic acids-based heavy metal ion detection. *Biosens. Bioelectron.* **2016**, *86*, 353–368. [CrossRef]
73. Chiorcea-Paquim, A.M.; Corduneanu, O.; Oliveira, S.C.B.; Diculescu, V.C.; Oliveira-Brett, A.M. Electrochemical and AFM evaluation of hazard compounds-DNA interaction. *Electrochim. Acta* **2009**, *54*, 1978–1985. [CrossRef]
74. Torigoe, H.; Ono, A.; Kozasa, T. Hg^{II} ion specifically binds with T:T mismatched base pair in duplex DNA. *Chem. Eur. J.* **2010**, *16*, 13218–13225. [CrossRef]
75. Xiao, Z.; Meng, H.; Qin, X.; Sang, X.; Zhang, Y.; Yuan, Y. The functionalization of gold nanoparticles as a novel platform for the highly efficient electrochemical detection of silver ions. *Analyst* **2021**, *146*, 597–604. [CrossRef]
76. Xu, G.; Huo, D.; Hou, C.; Zhao, Y.; Bao, J.; Yang, M.; Fa, H. A regenerative and selective electrochemical aptasensor based on copper oxide nanoflowers-single walled carbon nanotubes nanocomposite for chlorpyrifos detection. *Talanta* **2018**, *178*, 1046–1052. [CrossRef]
77. Lan, L.; Liu, Y.; Chen, X.; Zhang, T.; Dong, N.; Miao, P. Preparation of a novel iron cryptate as an electrochemical probe for biosensing. *Electrochem. Commun.* **2019**, *98*, 92–95. [CrossRef]
78. Hu, Y.; Zhang, Q.; Guo, Z.; Wang, S.; Du, C.; Zhai, C. In situ grown DNA nanotail-templated silver nanoclusters enabling label-free electrochemical sensing of terminal deoxynucleotidyl transferase activity. *Biosens. Bioelectron.* **2017**, *98*, 91–99. [CrossRef]
79. Khoshbin, Z.; Housaindokht, M.R.; Verdian, A.; Bozorgmehr, M.R. Simultaneous detection and determination of mercury (II) and lead (II) ions through the achievement of novel functional nucleic acid-based biosensors. *Biosens. Bioelectron.* **2018**, *116*, 130–147. [CrossRef]
80. Wang, M.; Zhang, S.; Ye, Z.; Peng, D.; He, L.; Yan, F.; Yang, Y.; Zhang, H.; Zhang, Z. A gold electrode modified with amino-modified reduced graphene oxide, ion specific DNA and DNAzyme for dual electrochemical determination of Pb (II) and Hg (II). *Microchim. Acta* **2015**, *182*, 2251–2258. [CrossRef]
81. Saini, R.; Hegde, K.; Brar, S.K.; Verma, M. Advances in Whole Cell-Based Biosensors in Environmental Monitoring. In *Tools, Techniques and Protocols for Monitoring Environmental Contaminants*; Elsevier: Amsterdam, The Netherlands, 2019.
82. Lagarde, F.; Jaffrezic-Renault, N. Cell-based electrochemical biosensors for water quality assessment. *Anal. Bioanal. Chem.* **2011**, *400*, 947–964. [CrossRef]
83. Gutiérrez, J.C.; Amaro, F.; Martín-González, A. Microbial Biosensors for Metal(loid)s. In *Microbial Ecotoxicology*; Springer: Cham, Switzerland, 2017.
84. Alpat, Ş.; Alpat, S.K.; Çadirci, B.H.; Yaşa, I.; Telefoncu, A. A novel microbial biosensor based on *Circinella* sp. modified carbon paste electrode and its voltammetric application. *Sens. Actuators B Chem.* **2008**, *134*, 175–181. [CrossRef]
85. Yüce, M.; Nazir, H.; Dönmez, G. An advanced investigation on a new algal sensor determining Pb(II) ions from aqueous media. *Biosens. Bioelectron.* **2010**, *26*, 321–326. [CrossRef]
86. Li, Y.; Sun, J.; Wang, J.; Bian, C.; Tong, J.; Li, Y.; Xia, S. A single-layer structured microbial sensor for fast detection of biochemical oxygen demand. *Biochem. Eng. J.* **2016**, *112*, 219–225. [CrossRef]
87. Li, Y.; Sun, J.; Wang, J.; Bian, C.; Tong, J.; Li, Y.; Xia, S. A microbial electrode based on the co-electrodeposition of carboxyl graphene and Au nanoparticles for BOD rapid detection. *Biochem. Eng. J.* **2017**, *123*, 86–94. [CrossRef]
88. Wang, J.; Li, Y.; Bian, C.; Tong, J.; Fang, Y.; Xia, S. Ultramicroelectrode array modified with magnetically labeled *Bacillus subtilis*, palladium nanoparticles and reduced carboxy graphene for amperometric determination of biochemical oxygen demand. *Microchim. Acta* **2017**, *184*, 763–771. [CrossRef]
89. Hooi, K.B.; Ismail, A.K.; Ahamad, R.; Shahir, S. A redox mediated UME biosensor using immobilized *Chromobacterium violaceum* strain R1 for rapid biochemical oxygen demand measurement. *Electrochim. Acta* **2015**, *176*, 777–783. [CrossRef]
90. Kaffash, A.; Zare, H.R.; Rostami, K. Highly sensitive biosensing of phenol based on the adsorption of the phenol enzymatic oxidation product on the surface of an electrochemically reduced graphene oxide-modified electrode. *Anal. Methods* **2018**, *10*, 2731–2739. [CrossRef]

91. Arduini, F.; Neagu, D.; Scognamiglio, V.; Patarino, S.; Moscone, D.; Palleschi, G. Automatable flow system for paraoxon detection with an embedded screen-printed electrode tailored with butyrylcholinesterase and prussian blue nanoparticles. *Chemosensors* **2015**, *3*, 129–145. [CrossRef]
92. Mogha, N.K.; Sahu, V.; Sharma, M.; Sharma, R.K.; Masram, D.T. Biocompatible ZrO_2-reduced graphene oxide immobilized AChE biosensor for chlorpyrifos detection. *Mater. Des.* **2016**, *111*, 312–320. [CrossRef]
93. Haddaoui, M.; Raouafi, N. Chlortoluron-induced enzymatic activity inhibition in tyrosinase/ZnO NPs/SPCE biosensor for the detection of ppb levels of herbicide. *Sens. Actuators B Chem.* **2015**, *219*, 171–178. [CrossRef]
94. Dos Santos, M.B.; Queirós, R.B.; Geraldes, Á.; Marques, C.; Vilas-Boas, V.; Dieguez, L.; Paz, E.; Ferreira, R.; Morais, J.; Vasconcelos, V. Portable sensing system based on electrochemical impedance spectroscopy for the simultaneous quantification of free and total microcystin-LR in freshwaters. *Biosens. Bioelectron.* **2019**, *142*, 111550. [CrossRef]
95. Zhao, G.; Ding, J.; Yu, H.; Yin, T.; Qin, W. Potentiometric aptasensing of *Vibrio alginolyticus* based on DNA nanostructure-modified magnetic beads. *Sensors* **2016**, *16*, 2052. [CrossRef]
96. Yu, Y.-Y.; Wang, J.-X.; Si, R.-W.; Yang, Y.; Zhang, C.-L.; Yong, Y.-C. Sensitive amperometric detection of riboflavin with a whole-cell electrochemical sensor. *Anal. Chim. Acta* **2017**, *985*, 148–154. [CrossRef]
97. Bozal-Palabiyik, B. Foodborne Diseases | | Biosensor-Based Methods for the Determination of Foodborne Pathogens. Available online: https://www.sciencedirect.com/science/article/pii/B9780128114445000129 (accessed on 10 May 2022).
98. Mei, L.; Feng, J.; Wu, L.; Zhou, J.; Chen, J.; Wang, A. Novel phenol biosensor based on laccase immobilized on reduced graphene oxide supported palladium-copper alloyed nanocages. *Biosens. Bioelectron.* **2015**, *74*, 347–352. [CrossRef]
99. Albareda-Sirvent, M.; Merkoçi, A.; Alegret, S. Pesticide determination in tap water and juice samples using disposable amperometric biosensors made using thick-film technology. *Anal. Chim. Acta* **2001**, *442*, 35–44. [CrossRef]
100. Badea, M.; Amine, A.; Palleschi, G.; Moscone, D.; Curulli, A. New electrochemical sensors for detection of nitrites and nitrates. *J. Electroanal. Chem.* **2001**, *509*, 66–72. [CrossRef]
101. Biagiotti, V.; Valentini, F.; Tamburri, E.; Terranova, M.L.; Moscone, D.; Palleschi, G. Synthesis and characterization of polymeric films and nanotubule nets used to assemble selective sensors for nitrite detection in drinking water. *Sens. Actuators B Chem.* **2007**, *122*, 236–242. [CrossRef]
102. Stoytcheva, M.; Zlatev, R.; Gochev, V.; Velkova, Z.; Montero, G.; Beleno, M.T. Amperometric biosensors precision improvement. Application to phenolic pollutants determination. *Electrochim. Acta* **2014**, *147*, 25–30. [CrossRef]
103. Pan, Y.; Shang, L.; Zhao, F.; Zeng, B. A novel electrochemical 4-nonyl-phenol sensor based on molecularly imprinted poly (o-phenylenediamine-co-o-toluidine)—Nitrogen-doped graphene nanoribbons—Ionic liquid composite film. *Electrochim. Acta* **2015**, *151*, 423–428. [CrossRef]
104. Dalkıran, B. Amperometric determination of heavy metal using an HRP inhibition biosensor based on ITO nanoparticles-ruthenium (III) hexamine trichloride composite: Central composite design optimization. *Bioelectrochemistry* **2020**, *135*, 107569. [CrossRef]
105. Mu, Q.; Liu, G.; Yang, D.; Kou, X.; Cao, N.; Tang, Y.; Miao, P. Ultrasensitive Detection of DNA Based on Exonuclease III-Assisted Recycling Amplification and DNAzyme Motor. *Bioconjugate Chem.* **2018**, *29*, 3527–3531. [CrossRef]
106. Han, X.; Li, C.; Yong, D. Microbial Electrode Sensor for Heavy-metal Ions. *Sens. Mater.* **2019**, *31*, 4103–4111. [CrossRef]
107. Magar, H.S.; Ghica, M.E.; Abbas, M.N.; Brett, C.M.A. Highly Sensitive Choline Oxidase Enzyme Inhibition Biosensor for Lead Ions Based on Multiwalled Carbon Nanotube Modified Glassy Carbon Electrodes. *Electroanalysis* **2017**, *29*, 1741–1748. [CrossRef]
108. Gumpu, M.B.; Krishnan, U.M.; Rayappan, J.B.B. Design and development of amperometric biosensor for the detection of lead and mercury ions in water matrix—A permeability approach. *Anal. Bioanal. Chem.* **2017**, *409*, 4257–4266. [CrossRef]
109. Rezaei, B.; Askarpour, N.; Ensafi, A.A. A novel sensitive doxorubicin impedimetric immunosensor based on a specific monoclonal antibody—Gold nanoparticle—Sol—Gel modified electrode. *Talanta* **2014**, *119*, 164–169. [CrossRef]
110. Brosel-Oliu, S.; Ferreira, R.; Uria, N.; Abramova, N.; Gargallo, R.; Muñoz-Pascual, F.-X.; Bratov, A. Novel impedimetric aptasensor for label-free detection of *Escherichia coli* O157: H7. *Sens. Actuators B Chem.* **2018**, *255*, 2988–2995. [CrossRef]
111. Hnaien, M.; Bourigua, S.; Bessueille, F.; Bausells, J.; Errachid, A.; Lagarde, F.; Jaffrezic-Renault, N. Impedimetric microbial biosensor based on single wall carbon nanotube modified microelectrodes for trichloroethylene detection. *Electrochim. Acta* **2011**, *56*, 10353–10358. [CrossRef]
112. Lin, Z.; Li, X.; Kraatz, H.B. Impedimetric immobilized DNA-based sensor for simultaneous detection of Pb^{2+}, Ag^{+}, and Hg^{2+}. *Anal. Chem.* **2011**, *83*, 6896–6901. [CrossRef]
113. Xu, Y.; Zhang, W.; Shi, J.; Li, Z.; Huang, X.; Zou, X.; Tan, W.; Zhang, X.; Hu, X.; Wang, X.; et al. Impedimetric aptasensor based on highly porous gold for sensitive detection of acetamiprid in fruits and vegetables. *Food Chem.* **2020**, *322*, 126762. [CrossRef]
114. Beloglazova, N.V.; Lenain, P.; De Rycke, E.; Goryacheva, I.Y.; Knopp, D.; De Saeger, S. Capacitive sensor for detection of benzo (a) pyrene in water. *Talanta* **2018**, *190*, 219–225. [CrossRef]
115. Graniczkowska, K.; Pütz, M.; Hauser, F.M.; De Saeger, S.; Beloglazova, N.V. Capacitive sensing of N-formylamphetamine based on immobilized molecular imprinted polymers. *Biosens. Bioelectron.* **2017**, *92*, 741–747. [CrossRef]
116. Mugo, S.M.; Lu, W.; Dhanjai, D. A pathogen imprinted hybrid polymer capacitive sensor for selective *Escherichia coli* detection. *Med. Devices Sens.* **2020**, *3*, e10071. [CrossRef]
117. Razavi, H.; Janfaza, S. Medical nanobiosensors: A tutorial review. *Nanomed. J.* **2015**, *2*, 74–87.

118. Zhylyak, G.; Dzyadevich, S.; Korpan, Y.; Soldatkin, A.; El'Skaya, A. Application of urease conductometric biosensor for heavy-metal ion determination. *Sens. Actuators B Chem.* **1995**, *24*, 145–148. [CrossRef]
119. Tekaya, N.; Saiapina, O.; Ouada, H.B.; Lagarde, F.; Ouada, H.B.; Jaffrezic-Renault, N. Ultra-sensitive conductometric detection of heavy metals based on inhibition of alkaline phosphatase activity from *Arthrospira platensis*. *Bioelectrochemistry* **2013**, *90*, 24–29. [CrossRef] [PubMed]
120. Soldatkin, O.; Kucherenko, I.; Pyeshkova, V.; Kukla, A.; Jaffrezic-Renault, N.; El'Skaya, A.; Dzyadevych, S.; Soldatkin, A. Novel conductometric biosensor based on three-enzyme system for selective determination of heavy metal ions. *Bioelectrochemistry* **2012**, *83*, 25–30. [CrossRef] [PubMed]
121. Upadhyay, L.S.B.; Verma, N. Alkaline phosphatase inhibition based conductometric biosensor for phosphate estimation in biological fluids. *Biosens. Bioelectron.* **2015**, *68*, 611–616. [CrossRef] [PubMed]
122. Wang, X.; Dzyadevych, S.V.; Chovelon, J.-M.; Renault, N.J.; Chen, L.; Xia, S.; Zhao, J. Development of a conductometric nitrate biosensor based on Methyl viologen/Nafion®composite film. *Electrochem. Commun.* **2006**, *8*, 201–205. [CrossRef]
123. Ha, D.; Hu, N.; Wu, C.; Kirsanov, D.; Legin, A.; Khaydukova, M.; Wang, P. Novel structured light-addressable potentiometric sensor array based on PVC membrane for determination of heavy metals. *Sens. Actuators B Chem.* **2012**, *174*, 59–64. [CrossRef]
124. Wipf, M.; Stoop, R.L.; Tarasov, A.; Bedner, K.; Fu, W.; Wright, I.A.; Martin, C.J.; Constable, E.C.; Calame, M.; Schonenberger, C. Selective sodium sensing with gold-coated silicon nanowire field-effect transistors in a differential setup. *ACS Nano* **2013**, *7*, 5978–5983. [CrossRef]
125. Khadro, B.; Namour, P.; Bessueille, F.; Leonard, D.; Jaffrezic-Renault, N. Validation of a conductometric bienzyme biosensor for the detection of proteins as marker of organic matter in river samples. *J. Environ. Sci.* **2009**, *21*, 545–551. [CrossRef]
126. Chouteau, C.; Dzyadevych, S.; Chovelon, J.-M.; Durrieu, C. Development of novel conductometric biosensors based on immobilised whole cell *Chlorella vulgaris* microalgae. *Biosens. Bioelectron.* **2004**, *19*, 1089–1096. [CrossRef]
127. Fabry, P.; Siebert, E. The CRC Handbook of Solid State Electrochemistry. In *Electrochemical Sensors*; CRC Press: Boca Raton, FL, USA, 1997; pp. 329–365.
128. Compton, R.G.; Banks, C.E. *Understanding Voltammetry*; World Scientific: London, UK, 2018.
129. Huang, M.R.; Rao, X.W.; Li, X.G.; Ding, Y.B. Lead ion-selective electrodes based on polyphenylenediamine as unique solid ionophores. *Talanta* **2011**, *85*, 1575–1584. [CrossRef]
130. Alexander, S. Multiwalled carbon nanotube based molecular imprinted polymer for trace determination of 2,4-dichlorophenoxyaceticacid in natural water samples using a potentiometric method. *Appl. Surf. Sci.* **2014**, *303*, 180–186.
131. Mashhadizadeh, M.H.; Khani, H.; Shockravi, A. Used a new aza-thia-macrocycle as a suitable carrier in potentiometric sensor of copper (II). *J. Incl. Phenom. Macrocycl. Chem.* **2010**, *68*, 219–227. [CrossRef]
132. Bergveld, P. Development of an ion-sensitive solid-state device for neurophysiological measurements. *IEEE Trans. Biomed. Eng.* **1970**, *1*, 70–71. [CrossRef]
133. Cui, Y.; Wei, Q.; Park, H.; Lieber, C.M. Nanowire nanosensors for highly sensitive and selective detection of biological and chemical species. *Science* **2001**, *293*, 1289–1292. [CrossRef]
134. Knopfmacher, O.; Tarasov, A.; Fu, W.; Wipf, M.; Niesen, B.; Calame, M.; Schonenberger, C. Nernst limit in dual-gated Si-nanowire FET sensors. *Nano Lett.* **2010**, *10*, 2268–2274. [CrossRef]
135. Chen, S.; Bomer, J.G.; Carlen, E.T.; van den Berg, A. Al_2O_3/silicon nanoISFET with near ideal Nernstian response. *Nano Lett.* **2011**, *11*, 2334–2341. [CrossRef]
136. Sudhölter, E.; Van der Wal, P.; Skowronska-Ptasinska, M.; Van den Berg, A.; Reinhoudt, D. Ion-sensing using chemically-modified ISFETs. *Sens. Actuators* **1989**, *17*, 189–194. [CrossRef]
137. Rocher, V.; Jaffrezic-Renault, N.; Perrot, H.; Chevalier, Y.; Le Perchec, P. Nitrate-sensitive field-effect transistor with silica gate insulator modified by chemical grafting. *Anal. Chim. Acta* **1992**, *256*, 251–255. [CrossRef]
138. Reinhoudt, D.N.; Engbersen, J.F.; Brzozka, Z.; van der Vlekkert, H.H.; Honig, G.W.; Holterman, H.A.; Verkerk, U.H. Development of durable K+-selective chemically modified field effect transistors with functionalized polysiloxane membranes. *Anal. Chem.* **1994**, *66*, 3618–3623. [CrossRef]
139. Park, L.-S.; Hur, Y.-J.; Sohn, B.-K. Effect of membrane structure on the performance of field-effect transistor potassium-sensitive sensor. *Sens. Actuators A Phys.* **1996**, *57*, 239–243. [CrossRef]
140. Gao, A.; Lu, N.; Wang, Y.; Dai, P.; Li, T.; Gao, X.; Wang, Y.; Fan, C. Enhanced sensing of nucleic acids with silicon nanowire field effect transistor biosensors. *Nano Lett.* **2012**, *12*, 5262–5268. [CrossRef]
141. Zheng, G.; Patolsky, F.; Cui, Y.; Wang, W.U.; Lieber, C.M. Multiplexed electrical detection of cancer markers with nanowire sensor arrays. *Nat. Biotechnol.* **2005**, *23*, 1294–1301. [CrossRef]
142. Stern, E.; Klemic, J.F.; Routenberg, D.A.; Wyrembak, P.N.; Turner-Evans, D.B.; Hamilton, A.D.; LaVan, D.A.; Fahmy, T.M.; Reed, M.A. Label-free immunodetection with CMOS-compatible semiconducting nanowires. *Nature* **2007**, *445*, 519–522. [CrossRef]
143. Stern, E.; Vacic, A.; Rajan, N.K.; Criscione, J.M.; Park, J.; Ilic, B.R.; Mooney, D.J.; Reed, M.A.; Fahmy, T.M. Label-free biomarker detection from whole blood. *Nat. Nanotechnol.* **2010**, *5*, 138–142. [CrossRef]
144. Duan, X.; Li, Y.; Rajan, N.K.; Routenberg, D.A.; Modis, Y.; Reed, M.A. Quantification of the affinities and kinetics of protein interactions using silicon nanowire biosensors. *Nat. Nanotechnol.* **2012**, *7*, 401–407. [CrossRef]
145. Duan, X.; Gao, R.; Xie, P.; Cohen-Karni, T.; Qing, Q.; Choe, H.S.; Tian, B.; Jiang, X.; Lieber, C.M. Intracellular recordings of action potentials by an extracellular nanoscale field-effect transistor. *Nat. Nanotechnol.* **2012**, *7*, 174–179. [CrossRef]

146. Rothberg, J.M.; Hinz, W.; Rearick, T.M.; Schultz, J.; Mileski, W.; Davey, M.; Leamon, J.H.; Johnson, K.; Milgrew, M.J.; Edwards, M. An integrated semiconductor device enabling non-optical genome sequencing. *Nature* **2011**, *475*, 348–352. [CrossRef]
147. Luo, L.; Jie, J.; Zhang, W.; He, Z.; Wang, J.; Yuan, G.; Zhang, W.; Wu, L.C.M.; Lee, S.-T. Silicon nanowire sensors for Hg^{2+} and Cd^{2+} ions. *Appl. Phys. Lett.* **2009**, *94*, 193101. [CrossRef]
148. Gokhale, A.A.; Lu, J.; Weerasiri, R.R.; Yu, J.; Lee, I. Amperometric Detection and Quantification of Nitrate Ions Using a Highly Sensitive Nanostructured Membrane Electrocodeposited Biosensor Array. *Electroanalysis* **2015**, *27*, 1127–1137. [CrossRef]
149. Astruc, D.; Boisselier, E.; Ornelas, C. Dendrimers designed for functions: From physical, photophysical, and supramolecular properties to applications in sensing, catalysis, molecular electronics, photonics, and nanomedicine. *Chem. Rev.* **2010**, *110*, 1857–1959. [CrossRef]
150. Tshikalaha, P.; Arotiba, O.A. Dendrimer supported electrochemical immunosensor for the detection of cholera toxin in water. *Int. J. Electrochem. Sci.* **2015**, *10*, 10083–10092.
151. Salihov, S.V.; Ivanenkov, Y.A.; Krechetov, S.P.; Veselov, M.S.; Sviridenkova, N.V.; Savchenko, A.G.; Klyachko, N.L.; Golovin, Y.I.; Chufarova, N.V.; Beloglazkina, E.K.; et al. Recent advances in the synthesis of Fe_3O_4@AU core/shell nanoparticles. *J. Magn. Magn. Mater.* **2015**, *394*, 173–178. [CrossRef]
152. Kholafazad Kordasht, H.; Pazhuhi, M.; Pashazadeh-Panahi, P.; Hasanzadeh, M.; Shadjou, N. Multifunctional aptasensors based on mesoporous silica nanoparticles as an efficient platform for bioanalytical applications: Recent advances. *TrAC Trends Anal. Chem.* **2020**, *124*, 115778. [CrossRef]
153. Zhang, Y.; Li, H.; Chen, M.; Fang, X.; Pang, P.; Wang, H.; Wu, Z.; Yang, W. Ultrasensitive electrochemical biosensor for silver ion based on magnetic nanoparticles labeling with hybridization chain reaction amplification strategy. *Sens. Actuators B Chem.* **2017**, *249*, 431–438. [CrossRef]
154. Eguílaz, M.; Villalonga, R.; Rivas, G. Electrochemical biointerfaces based on carbon nanotubes-mesoporous silica hybrid material: Bioelectrocatalysis of hemoglobin and biosensing applications. *Biosens. Bioelectron.* **2018**, *111*, 144–151. [CrossRef]
155. Zhang, Z.; Ji, H.; Song, Y.; Zhang, S.; Wang, M.; Jia, C.; Tian, J.Y.; He, L.; Zhang, X.; Liu, C.S. Fe(III)-based metal–organic framework-derived core–shell nanostructure: Sensitive electrochemical platform for high trace determination of heavy metal ions. *Biosens. Bioelectron.* **2017**, *94*, 358–364. [CrossRef]
156. Hod, I.; Sampson, M.D.; Deria, P.; Kubiak, C.P.; Farha, O.K.; Hupp, J.T. Fe-Porphyrin-Based Metal-Organic Framework Films as High-Surface Concentration, Heterogeneous Catalysts for Electrochemical Reduction of CO_2. *ACS Catal.* **2015**, *5*, 6302–6309. [CrossRef]
157. Alahi, M.E.E.; Xie, L.; Mukhopadhyay, S.; Burkitt, L. A temperature compensated smart nitrate-sensor for agricultural industry. *IEEE Trans. Ind. Electron.* **2017**, *64*, 7333–7341. [CrossRef]
158. Alahi, M.E.E.; Mukhopadhyay, S.C.; Burkitt, L. Imprinted polymer coated impedimetric nitrate sensor for real-time water quality monitoring. *Sens. Actuators B Chem.* **2018**, *259*, 753–761. [CrossRef]
159. Pasternak, G.; Greenman, J.; Ieropoulos, I. Self-powered, autonomous Biological Oxygen Demand biosensor for online water quality monitoring. *Sens. Actuators B Chem.* **2017**, *244*, 815–822. [CrossRef]
160. Quek, S.B.; Cheng, L.; Cord-Ruwisch, R. Microbial fuel cell biosensor for rapid assessment of assimilable organic carbon under marine conditions. *Water Res.* **2015**, *77*, 64–71. [CrossRef]
161. Wang, X.; Lu, X.; Chen, J. Development of biosensor technologies for analysis of environmental contaminants. *Trends Environ. Anal. Chem.* **2014**, *2*, 25–32. [CrossRef]
162. Verma, N.; Kaur, H.; Kumar, S. Whole cell based electrochemical biosensor for monitoring lead ions in milk. *Biotechnology* **2011**, *10*, 259–266. [CrossRef]
163. Perumal, V.; Hashim, U. Advances in biosensors: Principle, architecture and applications. *J. Appl. Biomed.* **2014**, *12*, 1–15. [CrossRef]
164. Abdulhalim, I.; Karabchevsky, A.; Patzig, C.; Rauschenbach, B.; Fuhrmann, B.; Eltzov, E.; Marks, R.; Xu, J.; Zhang, F.; Lakhtakia, A. Surface-enhanced fluorescence from metal sculptured thin films with application to biosensing in water. *Appl. Phys. Lett.* **2009**, *94*, 63106. [CrossRef]
165. Woznica, M.; Kowalska, P.; Lysek, R.; Masnyk, M.; Gorecki, M.; Kwit, M.; Furche, F.; Frelek, J. Stereochemical assingment of β-lactam antibiotics and their analogues by electronic circular dichroism spectroscopy. *Curr. Org. Chem.* **2010**, *14*, 1022–1036. [CrossRef]
166. McAuley, J.; Daly, P.; Curtis, C. A preliminary investigation of a novel design of visual cue glasses that aid gait in Parkinson's disease. *Clin. Rehabil.* **2009**, *23*, 687–695. [CrossRef]
167. An, F.; Bai, J.; Balantekin, A.; Band, H.; Beavis, D.; Beriguete, W.; Bishai, M.; Blyth, S.; Boddy, K.; Brown, R. Observation of electron-antineutrino disappearance at Daya Bay. *Phys. Rev. Lett.* **2012**, *108*, 171803. [CrossRef]
168. Kumlanghan, A.; Kanatharana, P.; Asawatreratanakul, P.; Mattiasson, B.; Thavarungkul, P. Microbial BOD sensor for monitoring treatment of wastewater from a rubber latex industry. *Enzym. Microb. Technol.* **2008**, *42*, 483–491. [CrossRef]
169. Kang, J.H.; Lee, S.I.; Lim, D.; Park, K.; Oh, S.; Kwon, H.; Hwang, I.; Lee, S.; Nam, E.; Shin, D. Salvage chemotherapy for pretreated gastric cancer: A randomized phase III trial comparing chemotherapy plus best supportive care with best supportive care alone. *J. Clin. Oncol.* **2011**, *30*, 1513–1518. [CrossRef]
170. Liu, E.; He, W.; Yan, C. 'White revolution' to 'white pollution'—Agricultural plastic film mulch in China. *Environ. Res. Lett.* **2014**, *9*, 91001. [CrossRef]

171. Akki, S.U.; Werth, C.J. Critical review: DNA aptasensors, are they ready for monitoring organic pollutants in natural and treated water sources? *Environ. Sci. Technol.* **2018**, *52*, 8989–9007. [CrossRef]
172. Mohanty, S.P.; Kougianos, E. Biosensors: A tutorial review. *IEEE Potentials* **2006**, *25*, 35–40. [CrossRef]
173. Jung, J.K.; Alam, K.K.; Verosloff, M.S.; Capdevila, D.A.; Desmau, M.; Clauer, P.R.; Lee, J.W.; Nguyen, P.Q.; Pastén, P.A.; Matiasek, S.J. Cell-free biosensors for rapid detection of water contaminants. *Nat. Biotechnol.* **2020**, *38*, 1451–1459. [CrossRef]

MDPI
St. Alban-Anlage 66
4052 Basel
Switzerland
www.mdpi.com

Biosensors Editorial Office
E-mail: biosensors@mdpi.com
www.mdpi.com/journal/biosensors

Academic Open
Access Publishing

mdpi.com

ISBN 978-3-0365-9513-9